Université Fédérale

Toulouse Midi-Pyrénées

# THÈSE

**En vue de l'obtention du**

## DOCTORAT DE L'UNIVERSITÉ DE TOULOUSE

**Délivré par :**

Institut Supérieur de l'Aéronautique et de l'Espace

---

**Présentée et soutenue par :**
**Johannes WOLF**

**le** mercredi 14 décembre 2016

**Titre :**

Traitement numérique de la fissuration dans les matériaux structuraux ductiles sous l'effet de sollicitations sévères

Numerical treatment of crack propagation in ductile structural materials under severe conditions

---

**École doctorale et discipline ou spécialité :**

ED MEGeP : Génie mécanique, mécanique des matériaux

**Unité de recherche :**

Institut Clément Ader

**Directeur(s) de Thèse :**

M. Patrice LONGERE (directeur de thèse)
M. Jean-Marc CADOU (co-directeur de thèse)

**Jury :**

André DRAGON Directeur de recherche CNRS émérite, Pprime - Président
Alain COMBESCURE Professeur émérite, INSA, Lyon - Rapporteur
Laurent STAINIER Professeur, ECN, Nantes - Rapporteur
Milan JIRASEK Professeur, CTU, Prague Examinateur
Hélène WELEMANE Maître de conférences, ENI, Tarbes Examinatrice
Patrice LONGERE Professeur, ISAE-SUPAERO, Toulouse - Directeur de thèse
Jean-Marc CADOU Maître de conférences, UBS, Lorient - Co-directeur de thèse

*Für meine Eltern*

## Abstract

The present work aims at numerically predicting the current residual strength of large engineering structures made of ductile metals regarding accidental events, e.g. ships collision or bird strike in aviation, which may potentially lead to failure. With this aim in view, the challenge consists in reproducing within a unified finite element (FE)-based methodology the successive steps of micro-voiding-induced damage, strain localization and crack propagation, if any.

A key ingredient for a predictive ductile fracture model is the proper numerical treatment of the critical transition phase of damage-induced strain localization inside a narrow band. For this purpose, three different viewpoints in terms of displacement field across the localization band are proposed involving a strong, weak and (non-linearly) regularized discontinuity, respectively.

A consistent variational framework is elaborated for each of the three methods, whereby the enriched kinematics is embedded into the FE formulation using the eXtended FEM. Then, within a comparative procedure, the performance of these methods is assessed regarding their ability of modeling the transition phase between diffuse damage (continuum mechanics framework) and crack propagation (fracture mechanics framework), always in the context of ductile materials.

According to the aforementioned analyses, the combination of the strong discontinuity cohesive model and the X-FEM appears to be the most promising of the three studied approaches to bring together physics and numerics. The development of such a model is discussed in detail. Finally, two supplementary criteria are defined: the first one for the passage from diffuse damage to the cohesive band model and the second one for the passage from the cohesive band model to the crack.

## Résumé

Le travail présenté a pour objectif la prédiction numérique de la résistance résiduelle de grandes structures vis-à-vis d'évènements accidentels, tels que ceux rencontrés p. ex. dans le cas de la collision de navires ou d'impact d'oiseaux en aéronautique. Ces évènements peuvent dans certain cas conduire à la rupture, qui est ici considérée ductile. La difficulté de cette étude, consiste à reproduire dans une méthodologie unifiée basée sur la méthode des éléments finis les étapes successives menant à la ruine ultime de la structure. Ces étapes sont : l'endommagement ductile, la localisation de la déformation et la propagation de la fissure.

Un élément essentiel pour la conception d'un modèle de fissuration ductile prédictif est le traitement numérique de la phase transitoire critique de localisation de la déformation induite par l'endommagement dans une bande de matière étroite. A cet effet, trois points de vue différents en termes de champ de déplacement à travers la bande de localisation sont proposés. Ces trois approches se distinguent par le type de discontinuité considérée : forte, faible et régularisée (expression non linéaire).

Un cadre variationnel consistant est élaboré pour chacune des trois approches. Ainsi la cinématique enrichie est incorporée dans la formulation de l'élément fini en utilisant la méthode des éléments finis enrichis (X-FEM). Puis, la performance de ces méthodes est évaluée vis-à-vis de leur capacité à modéliser la phase transitoire entre endommagement diffus (mécanique des milieux continus) et propagation de fissure (mécanique de la rupture). Ces travaux sont réalisés dans le contexte de matériaux ductiles.

D'après les analyses réalisées, la combinaison du modèle de 'discontinuité forte cohésive' et la X-FEM semble être la plus prometteuse des trois approches étudiées pour allier physique et numérique. Le développement d'un tel modèle est discuté en détail. Enfin, deux critères supplémentaires sont définis : le premier pour le passage de l'endommagement diffus au modèle de bande cohésive et un deuxième pour le passage du modèle de bande cohésive à la rupture.

# Contents

# Nomenclature

ASB Adiabatic Shear Band

Dof Degree of freedom

E-FEM Embedded Finite Element Method

FEM Finite Element Method

GP Gauss Point

GTN Gurson-Tvergaard-Needleman (model)

RVE Representative Volume Element

X-FEM Extended Finite Element Method

# Chapter I

# Introduction

## Contents of chapter I

# I.1 General context of the study

## I.1.1 Industrial context

The present work deals with the design of large engineering structures made of ductile metals regarding accidental events, e.g. ships collision, bird strike/ingestion in aviation or automotive crashworthiness, which may potentially lead to failure. Consider for example the structural effects of the oil tanker Limburg after being exposed to a terrorist attack, see figure (Fig.) I.1. An explosive-loaded boat provoked a detonation close to the vessel and teared a large hole into the hull causing an immense oil leak into the sea.

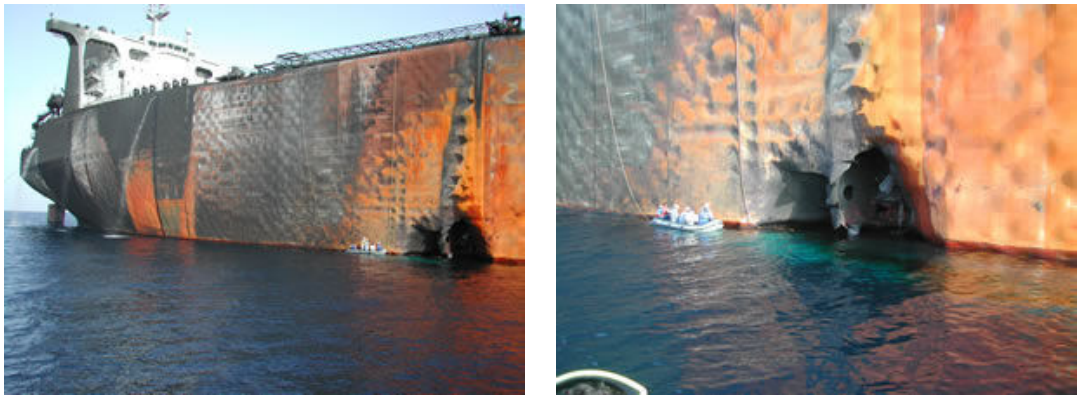

a) b)

Figure I.1 – Oil tanker Limburg after terrorist attack: a) damaged oil tanker [38] and b) close-up view [38]

A frequently reported case of damage in aviation is the ingestion of birds into the jet engines causing severe plastic deformation and cracking of the fan blades, see Fig. I.2. Such events have already been precursor of numerous plane crashes.

A *local* defect can have catastrophic consequences on the *global* scale of the structure. Predicting the current residual strength of the overloaded structure is of major interest for preserving the main functions and the integrity of the sensitive areas. Realizing large-scale experiments is associated with unacceptable costs. Instead, it is more favorable to analyze *small-scale* specimens (coupons) extracted from the *large-scale* structure which are exposed to similar conditions and to identify the underlying mechanisms which lead to the propagation of a crack. Based on the experimental findings and by making fundamental hypotheses, a numerical model is then expected to be set up.

**This work is concerned with the development of a physics-motivated numerical model allowing for the virtual testing of failure events using**

a) b)

Figure I.2 – Multiple bird strike in jet engines causing damage of the fan blades: a) Multiple cracks in fan blades [125] and b) large plastic deformation [125]

**the Finite Element Method (FEM).**

## I.1.2 Previous works

The complexity of setting up a numerical model of ductile fracture with a strong industrial focus has given rise to many research works. Among them and particularly relevant for this thesis are the three PhD works of Geffroy, Crété and Jan which will be roughly outlined below and related to this present work.

### I.1.2.1 Modeling of the structural failure caused by contact explosion

The PhD thesis of Geffroy [57] (LIMATB, UBS), see also [58], contributes to the numerical analysis of the crack arrest capability of ship hull materials subjected to contact explosion as it occurs in a terroristic attack. For the behavior of the undamaged material the effects of strain and strain rate hardening and thermal softening were taken into account. The author evidenced the interest of using an advanced damage-plasticity material model, namely a modified version of the well-known Gurson-Tvergaard-Needleman (GTN) model, to reproduce the evolution of more or less diffuse damage what is in accordance with microstructural observations. The constitutive model was implemented as user material (VUMAT) within the industrial finite element software Abaqus (explicit integration, 3D, dynamic loading). The developed material model showed satisfactory agreement in reproducing the material response before crack onset.

Crack propagation is treated by means of an empirical method: the crack is assumed to initiate as soon as the critical porosity is attained. Using the classical FEM, the element which meets the initiation criterion (critical porosity) is deleted

(element erosion method). A comparison between experimental and numerical results of an air-blast experiment is shown in Fig. I.3.

However by using the critical porosity criterion, the specific phenomena which lead to the formation of a macro-crack are not represented. Furthermore, the element erosion method has the inconvenience that the structural response is strongly sensitive with respect to the FE mesh size and orientation (see also Song [160]). This is reflected e.g. in that the crack path can not be properly captured (see Fig. I.3) and in that the crack propagates too fast compared to the experimental results (as stated in [57]). That gives rise to the conclusion that the residual strength of the structure after failure can not be reliably predicted, thus demanding for a more precise modeling of the failure response.

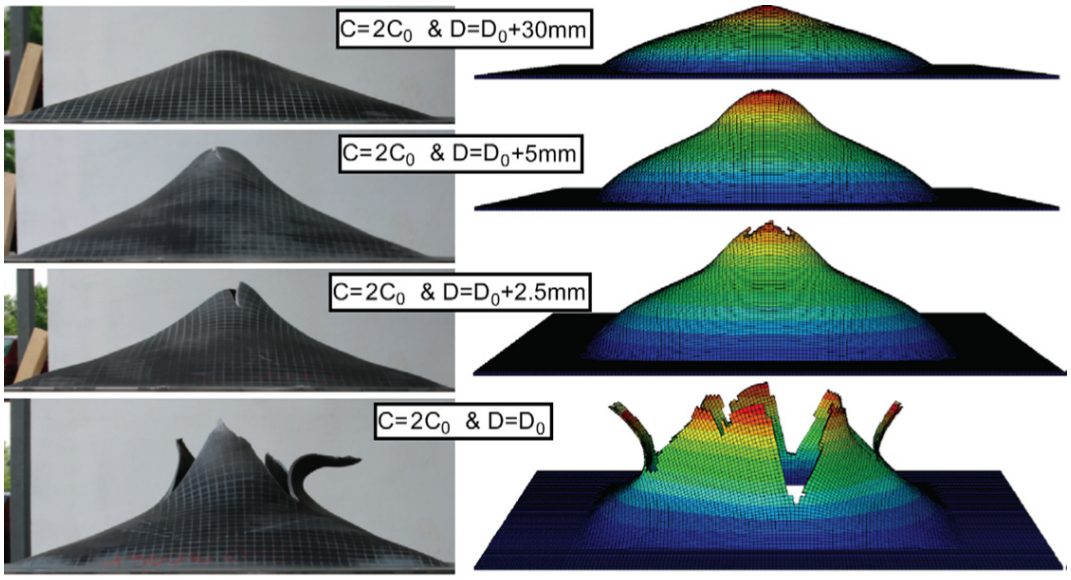


(a) Experimental results. (b) Numerical results.

Figure I.3 – Comparison between experimental (a) and numerical (b) results of air-blast experiments using four different distances between the specimen and the explosive charge [58]

### I.1.2.2 Modeling of the crack propagation in ductile plate structures using X-FEM

To this end, the thesis of Crété [45] (ICA, ISAE and LIMATB, UBS) was launched to focus on the numerical treatment describing the formation and propagation of a macro-crack involving the damage-plasticity pre-crack model developed by Geffroy. Due to the limitations of the standard FEM to reproduce crack propagation (mesh dependence, see above), the eXtended Finite Element Method (X-FEM) was

applied to describe the kinematic consequences of crack propagation across the mesh. Moreover, a direct coupling method between the more or less diffuse damage and the enriched FE technology was elaborated - without taking into account the transition phase of strain localization. The crack propagation relies on three elements:

- an initiation criterion,
- the determination of the crack direction and
- the computation of the crack length within one time increment.

The crack is assumed to propagate as soon as a critical stored energy is attained. The direction of propagation is evaluated based on the bifurcation analysis. The criteria involve the application of an averaging technique to reduce the mesh sensitivity in the softening regime.

The numerical model was implemented as user element (UEL) in Abaqus (implicit integration, 2D plane strain, dynamic loading). Virtual tests of a plate with pre-existing cracks have shown that the physical crack path can be well reproduced, see Fig. I.4. However, irrespective of the choice of the critical stored energy, the structural response deviates from the experimental curve in that the force abruptly drops as soon as the crack starts to propagate (Fig. I.4, rightmost) - a prediction which is indeed too conservative (i.e. too pessimistic). The sudden drop in load can potentially be traced back to the neglect of the phase of strain localization as a precursor of crack formation.

#### I.1.2.3 Modeling of the crack propagation in ductile shell structures using X-FEM

The PhD thesis of Jan [80] (LaMCoS, INSA de Lyon) is involved in the same industrial context of military vulnerability with the aim to numerically analyze the residual strength of ships exposed to extreme loads. Therein, a promising numerical approach is proposed capable of coupling the shell element formulation with the X-FEM in order to represent a propagating crack within the ship hull. This coupling pursues the objectives to reduce the model size as well as to handle the pathologic mesh dependence. The adopted crack propagation criterion is based on the (stress-based) approach by Haboussa [68] for the case of an elasto-plastic material behavior. However, the author states that - although this criterion is efficient and simple to implement - it must still be improved to better reproduce ductile materials. In the course of the degradation of the material resistance (stress

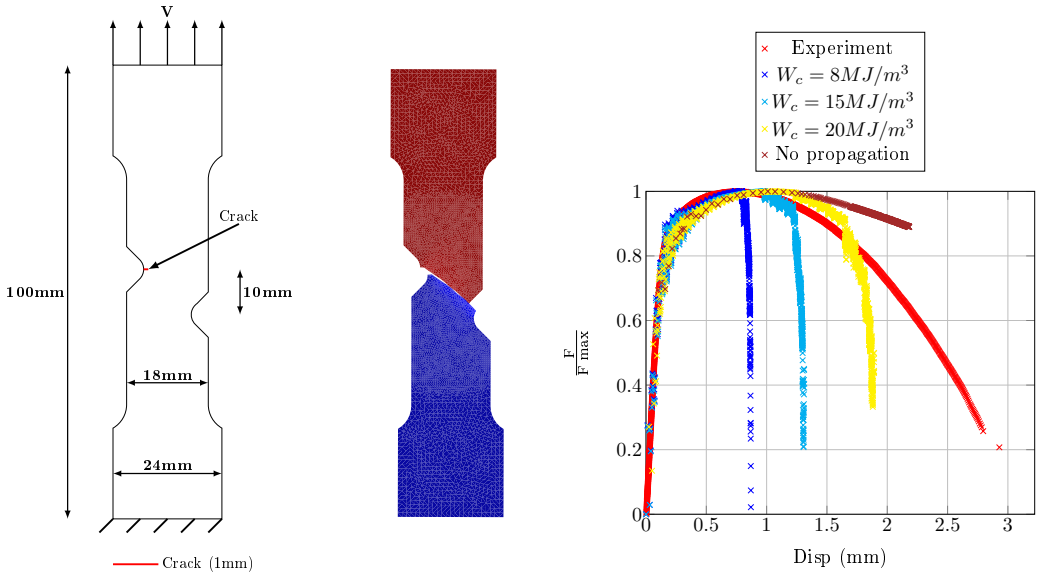


Figure I.4 – Simulation of a tensile test with a pre-cracked, double-notched specimen: Model (left), numerical result (center), comparison of experiment with simulation using different propagation criteria (right) (from [45])

softening) the risk is to not attain the yield stress at all.

The numerical model was implemented in the calculation code Europlexus (EPX) of the Commissariat à l'Energie Atomique (CEA) (explicit integration, 3D, dynamic loading). A comparison between experiments and numerical tests shows promising results when using very fine meshes. Therefore, this work constitutes another significant building brick towards a numerical model of the entire ductile failure process under highly dynamic loading.

**In the present work another point of view of the industrial problem combining numerical and physical considerations at the same time is studied. The objective is to propose methods aiming at a smooth transition from diffuse damage to crack propagation providing a unified model of ductile failure.**

## I.2 Problem statement and scientific challenges

Describing the overall process of deformation until fracture in ductile materials implies accounting for several interacting mechanisms whose comprehension remains - to this very day - imperfect. One can typically distinguish the following successive steps (often dealt with independently): plastic deformation, diffuse damage, damage

concentration (void coalescence) and strain localization and finally crack formation and propagation, see Fig. I.5. The ultimate purpose is to bring them together within a unified model which is to be numerically implemented into a commercial FE computation code.

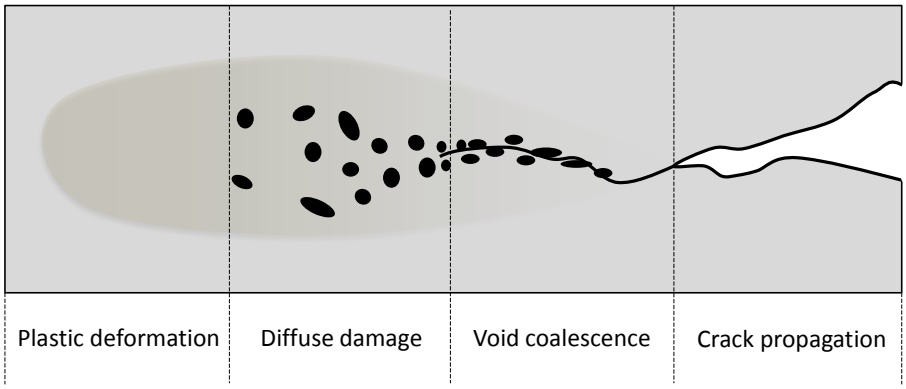


Figure I.5 – Main steps of ductile failure

## I.2.1 Modeling and numerical issues

### I.2.1.1 Diffuse damage and mesh dependence

As a result of void growth induced (diffuse) damage, the material properties are subjected to a progressive degradation. In order to reproduce these effects of ductile damage, several constitutive models have been proposed, e.g. by Gurson [66], Lemaitre [92], Rousselier [142] and also Longère [97]. At an advanced stage of damage evolution, the global structural response migrates to a softening regime (in lieu of the preceding hardening regime). This softening behavior goes along with the concentration of plastic deformation and damage within a narrow band.

When using the standard FEM, strain localization manifests itself in a spurious mesh dependence of the structural response. Due to this pathologic behavior, a reliable prediction of the residual strength of the structure after failure can not be provided. Aiming at an estimation which is less conservative and mesh-dependent, the complementary modeling of the post-localization phase is inevitable.

### I.2.1.2 Damage concentration and strain localization

The local material models fail to describe the damage concentration and strain localization in a narrow band and the potential crack propagation. A corrective approach consists in controlling the numerical strain localization in the FE mesh

in order to allow for capturing the genuine physical strain localization. The mesh dependence resulting from strain localization can be coped with by introducing a characteristic length into the formulation which serves as localization limiter. Non-local techniques (e.g. Bažant [17], Pijaudier-Cabot [127]) can be applied to attenuate the pathology, but accurate results require a very fine mesh and thus a big computational effort for large structures. Moreover, the physical strain localization itself as possible precursor of crack formation can not be properly represented.

A promising approach consists in using comparably large FEs and embedding the thin band of highly localized strain into the FE, e.g. by enriching the kinematic FE formulation (Ortiz [119], Belytschko [20]) or the material model (Longère [95]). **The development of an appropriate (embedded-band) method capable of reproducing the physical localization band and reducing the mesh sensitivity to a minimum is a significant objective of this dissertation.**

#### I.2.1.3 Crack formation and propagation

The standard FEM is not suitable to reproduce the discontinuous kinematics of a crack. Complementary techniques as the element deletion method (Song [160], Autenrieth [11]) and the inter-element crack method (Xu [182]) may be used to describe the crack propagation but they suffer from mesh dependence. Adaptive remeshing techniques have been shown to better reproduce the crack propagation, see e.g. Bouchard [31], yet requiring a huge computational effort.

Similar to the embedded-band approach to treat the (numerical and physical) strain localization, the crack can be embedded within the finite element by correspondingly enriching the kinematic FE formulation, as e.g. done in the eXtended FEM (X-FEM) (Belytschko [18]). Works devoted to show the performance of the X-FEM to reproduce the failure of elastic-(quasi-)brittle structures are numerous in literature (Moës [106], Dumstorff [50]), whereas works dealing with ductile, strongly nonlinear structures are still remarkably scarce (Crété [46], Broumand [32]). This method of embedded finite elements moreover allows for using a coarser mesh and is accordingly more suitable for large structures.

### I.2.2 Towards a unified approach

The challenge consists in reproducing within a unified methodology the successive steps of diffuse damage, strain localization and crack propagation leading to the ultimate ruin of the structure. That requires the definition of specific kinematics and

physics motivated criteria for the passage from one step to the other as compatible as possible. **For this purpose, we are studying here the ability of three different embedded-band FE methods to model the critical transition phase between diffuse damage (continuum mechanics framework) and crack propagation (fracture mechanics framework), namely the strain localization. The most promising of the three studied approaches is then elaborated in detail and appropriate physics-based criteria are proposed to pass from diffuse damage to strain localization, then from strain localization to crack propagation.**

## I.3 Main hypotheses for numerical treatment

Beforehand, the most significant hypotheses which are assumed for the developments in this work are listed:

- The focus of this work is set on the strain localization phenomenon which is initiated by void growth induced damage.
- The loading will be assumed monotonically increasing and quasi-static. So the influences of temperature and strain rate are tentatively neglected. Moreover this implies that any unloading phase will not be considered.
- The structural domain is discretized using 2D plane strain finite elements.
- It is assumed that the deformation remains infinitely small, although we are conscious about the fact that ductile fracture involves also large local strains.

## I.4 Outline of the dissertation

The second chapter gives an overview of the entire ductile failure process regarding physical mechanisms and their numerical treatment. Different concepts from the literature to reproduce the failure steps of diffuse damage, strain localization and crack propagation and overcome related numerical difficulties are introduced - always with regards to strongly non-linear ductile materials. Furthermore, appropriate approaches to describe numerically and physically the transition between diffuse damage and strain localization, then between strain localization and crack propagation are reviewed and discussed.

In the third chapter three embedded-band FE approaches to model the phase of strain localization in ductile materials are elaborated and studied from different

viewpoints. These methods consist in enriching the displacement field within the FE by, respectively, a strong, weak or (non-linearly) regularized discontinuity. Based on a profound discussion, the strong discontinuity approach using a cohesive band model appears to be the most promising to bring together physics and numerics.

In the fourth chapter a unified, physics-based model is elaborated treating successively the phases of plasticity-diffuse damage, localization followed by cracking. Thereby, the particular interest is on the coupling of the cohesive band model with the X-FE formulation. This approach allows passing progressively from the phase of void-growth induced damage to crack propagation in ductile materials. Finally an application with a plane specimen is analyzed, based on a propagation method which is elaborated in detail. This allows the evaluation of the unified failure model.

Concluding remarks and perspectives are presented in the last part of this dissertation.

This PhD thesis has been financially supported by the Direction Générale de l'Armement (DGA) and the French region Midi-Pyrénées. The work has been mainly realized at the Institut Clément Ader (UMR CNRS 5312) in Toulouse and involved short-term research stays at the IRDL (FRE CNRS 3744) (formerly LIMATB) in Lorient and at the tribology laboratory QUARTZ (EA 7393) in Saint-Ouen.

# Chapter II

# Overview of ductile fracture

## Contents of chapter II

## II.1 Introduction

The phenomenon of strain localization plays an important role in the ductile failure process, an insight which is by and by recognized in the research of failure. This appears to be mainly due to the increasing interest of the industry to be less conservative in the numerical prediction of structural ruin. This requires to reliably capture the mechanism of strain localization itself and to describe its relationship towards the precedent (diffuse damage) and subsequent (crack propagation) phase of failure.

In order to reproduce the strain localization in the context of a unified (physics-based) model, a background of ductile fracture physics and modeling is necessary. Therefore, an overview of ductile failure is given in this chapter. For a better understanding of the subsequent considerations, it is given in Fig. II.1 a concise illustration of the physical and numerical hypotheses used in this thesis which will be elaborated in the following (where that graphic will serve as reference). The modeling of the strain localization phase and its combination with the other processes will be part of chapters III and IV, so that the red boxes - left empty for now - will be filled out step by step.

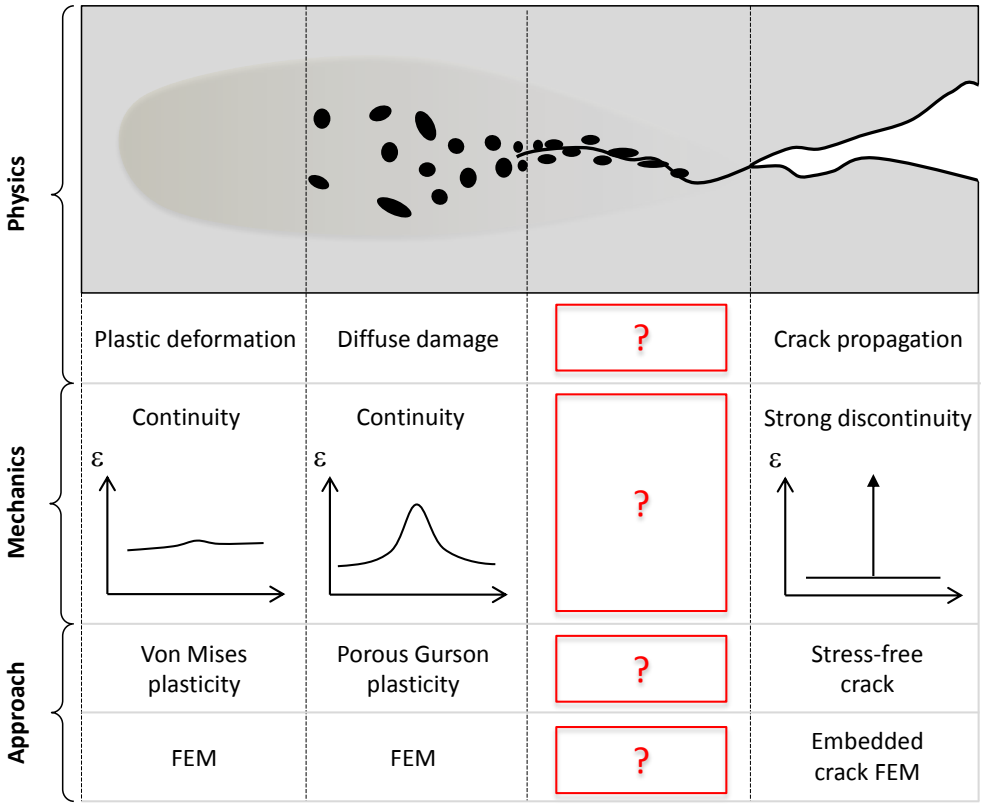


Figure II.1 – Tentative physical, mechanical and numerical model of ductile failure

# II.2 Physical aspects of ductile failure

In this section, the complex physics of ductile failure is reviewed. Based on experimental observations ([70], [56], [97], [179]) the failure process is divided into successive steps which are characteristic of their distinct physical mechanisms and kinematic fields.

## II.2.1 Experimental evidence

From a macroscopic point of view, ductile failure can be observed as a progressive loss of the overall material properties. After an initial phase of purely elastic behavior, the material undergoes combined elastic and intense plastic deformation which extends diffusely over the entire specimen. Then, the evolution of ductile damage gradually weakens the structure and leads to a softening behavior of the global response[1]. Softening goes along with the local concentration of damage in a narrow zone triggered by geometrical or material defects - an effect which will be referred to as strain localization. For a long time, damage has been regarded as a precursor of strain localization. Recent researches involving sophisticated X-ray tomography studies, see e.g. Maire [100] and Morgeneyer [109], have revealed that damage can also be preceded by strain localization. **In this study, the most observed phenomenon of damage-induced strain localization is treated, see Fig. II.2.**

The crack, which is visible to the naked eye (also referred to as macro-crack), is the result of successive though interdependent physical mechanisms at smaller scales. Detailed information on the underlying microscopic damaging process can e.g. be obtained from tensile tests which are interrupted at different stages of the failure process (yet often difficult to realize due to the high velocity of crack propagation throughout the structure) and analyzed using a scanning electron microscope (SEM). Consider in Fig. II.3 such a microscopic analysis of a notched plane specimen made from mild steel.

At the tip of the macro-crack, a fine, tortous crack (which is also referred to as *meso-crack*) can be identified. A closer look to the front and the vicinity of the meso-crack reveals the presence of micro-voids. Induced by internal necking, these cavities then progressively coalesce and initiate the meso-crack.

[1] It should be noted that there exist also other sources of softening, e.g. unstable phase transformation in shape memory alloys (see e.g. Ahmadian [2]), quasi-adiabatic heating under highly dynamic loading (see e.g. Recht [134] and Longère [96]) and dynamic recrystallization (see e.g. Roucoules [141]).

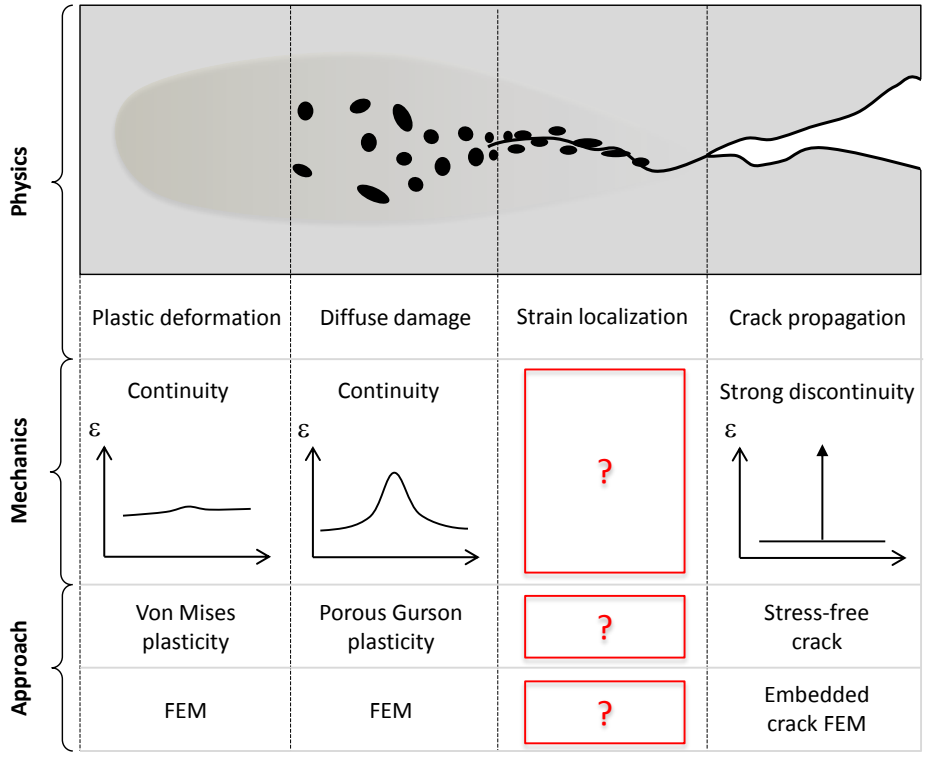


Figure II.2 – Updated failure process scheme taking into account the mechanism 'strain localization'

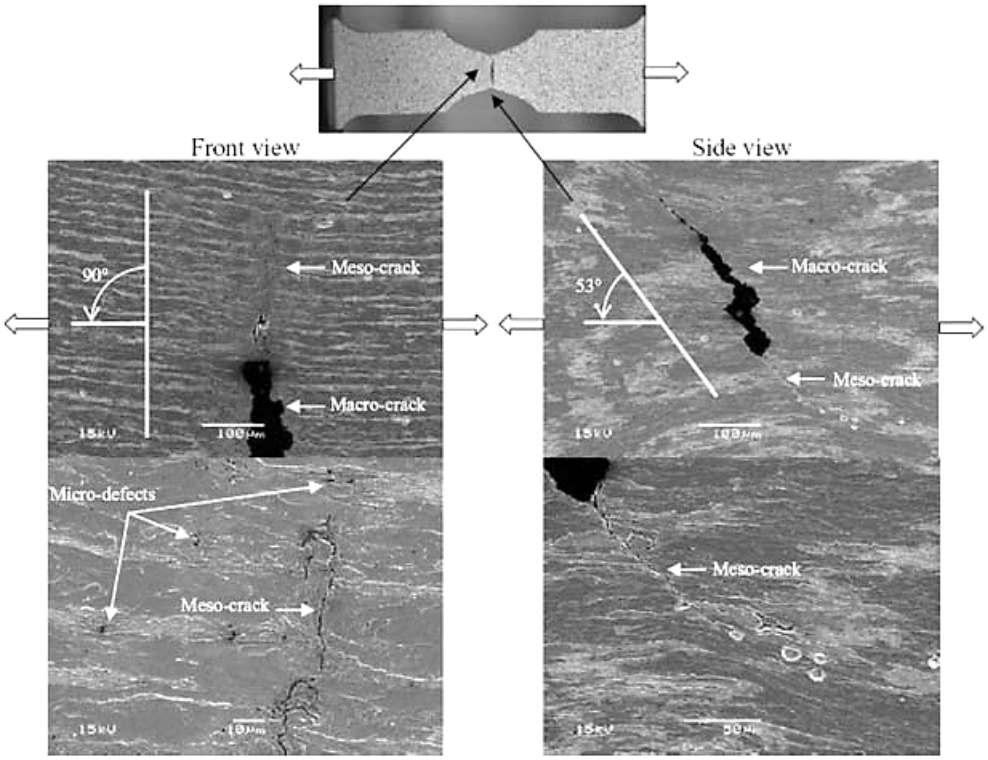


Figure II.3 – Experimental observation of the void-induced damage process in a notched plane specimen (DH36 steel) subjected to tensile loading [97]

**In this work, ductile failure is considered to originate from void accumulation in a band of localized damage.**

## II.2.2 Physical mechanisms considered

### II.2.2.1 Ductile failure - a multi-scale problem

The degradation process during ductile failure can be divided into four successive steps, which correspond to the illustration in Fig. II.2:

- homogeneous (undamaged) material undergoing plastic deformation,
- diffuse damage induced by the nucleation of micro-cavities followed by their growth due to ongoing microplastic flow,
- localization of plastic deformation and damage in a narrow band driven by void coalescence (progressive decohesion of the inter-cavity bonds) and
- formation and propagation of a macro-crack which may lead to the ruin of the structure if not arrested.

As these steps take place on different length scales, the fracture process is also referred to as a **multi-scale process**. To give an idea of the involved sizes (referring to the microscopic analysis in Fig. II.3): the diameter of the micro-voids amounts to $0.5 - 2\mu m$ in average, the mesocrack extends to $225\mu m$, whereas the macro-crack is in the order of some $mm$ to $cm$. However, with regard to rupture in large structures of some hundreds of meters length, the crack may extend over several meters, revealing the **challenge of setting up a model which enables to capture the small-scale as well as large-scale effects of ductile failure**.

One major challenge is to model each of these steps, another significant task is to treat the transition between each of the phases. **In the present work, the focus is on the phase of strain localization (the third step in Fig. II.2) and the transition (i) from the precedent stage of more or less diffuse damage to strain localization and (ii) from strain localization to the subsequent crack formation.**

### II.2.2.2 Characteristics of the kinematic fields across the failure zone

A characteristic evolution of the *macroscopic* strain field across the zone of failure can be identified (refer to the row 'Mechanics' in Fig. II.2, and also to Jirásek [83]). In the first two steps of ductile failure both the displacement and the strain

field remain continuous[2]. The ongoing dissipation effects gradually localize within a thin zone of finite width. The concentration of micro-voids in this zone goes along with a highly localized plastic deformation, what can also be identified with the appearance of a fine crack on the meso-scale (meso-crack). **Three different strain profiles across this localization zone will be proposed later on in chapter III, the most promising will be analyzed afterwards in chapter IV.** The final material separation at crack propagation corresponds to a strong discontinuity of the displacement field and a Dirac-type strain field across the crack.

It is important to underline the difficulty to cope with a continuous displacement field at the early stages of the failure process and a discontinuous displacement field once the crack initiates and propagates. This duality leads to numerical challenges what makes the transition from a continuous to a discontinuous field in a unified model a main focus of this thesis.

## II.3 Modeling of ductile failure and numerical issues

In the following part suitable approaches in modeling the successive ductile failure steps and the associated numerical issues are discussed. It is also given an overview on appropriate criteria indicating the onset of each phase so as to pass from one step to the other - an indispensable ingredient of an unified failure model.

### II.3.1 Damage-induced softening

In the following, any type of metals and alloys is considered which exhibits a distinct ductile behavior with a remarkable phase of plastic deformation and damage evolution before rupture, as e.g. the mild steel DH36 which is notably used in the shipbuilding industry (this material was considered in the theses of Geffroy [57] and Crété [45]).

#### II.3.1.1 Local modeling of ductile damage

Many models have been proposed so far to describe the constitutive consequences of void growth-induced damage of ductile materials. According to [57], these can be classified into dilatant (Gurson [66], Perzyna [126], Rousselier [142], Longère

[2]From a microscopical point of view, the presence of micro-cracks can be regarded as strong discontinuities. However, in this work, the mechanics is considered phenomenologically and in a macroscopic way.

[97]) and non-dilatant models (Lemaitre [92], Johnson-Cook [86]) according to their consideration (or neglecting) of the volumetric plastic deformation due to void growth.

Lemaitre [92] assumes that the ductile damage is directly related to the degradation of the elastic properties via a scalar macroscopic damage variable $D$. The material is supposed to be undamaged if $D = 0$, damaged if $0 < D < 1$ and completely damaged if $D = 1$. This phenomenological representation of damage can be thought of the surface density of micro-voids and -cracks in the material. Then, the model relies on the introduction of the effective stress tensor

$$\tilde{\underset{\sim}{\sigma}} = \frac{\underset{\sim}{\sigma}}{1 - D}. \tag{II.1}$$

Likewise, damage evolution corresponds to the deterioration of the elastic material properties (Young's modulus). According to the strain equivalence principle, for a fixed damage $D$, the damaged material with the elastic modulus behaves equivalent to an undamaged material with the effective elastic modulus $\tilde{E} = (1 - D)E$.

As opposed to the Lemaitre model, the micromechanics-based Gurson model considers the relationship between the volumetric deformation of the bulk and the void growth. The ductile damage corresponds to the expansion of small spherical voids which are surrounded by a perfectly plastic bulk. The damage is assumed to be diffusely distributed in the material, giving rise to the fundamental analysis of a statistically representative volume element (RVE). Then, the damage variable $f$ (porosity) defines the void density within the RVE. In her thesis, Geffroy [57] suggests to use the Gurson model. This choice was motivated by the intention to approach as close as possible to the physical observations. Another aspect was that in experiments with specimens made from DH36, Geffroy found out that the elastic properties do not degrade significantly, giving thus less interest to the Lemaitre model. And last but not least, the Gurson model is by far one of the most frequently used ductile model, having led to many extensions since its development.

In the following section, the applied Gurson-type model is described which is used later for the numerical studies.

#### II.3.1.2 Considered material model

As the focus of this work is not to set up a constitutive model, only the main ingredients of the material model are provided here. The presented model is described

in detail in [57], [97] and Crété [45].

In order to take into account effects of nucleation and growth of micro-voids and get better accordance with experiments, the micro-porous Gurson model was extended by Tvergaard and Needleman (see e.g. [168], [170]). This improved model is called GTN-model (abbreviation for Gurson-Tvergaard-Needleman). The plastic potential of GTN-model reads

$$\Phi_G = \left(\frac{\sigma_{eq}}{\sigma_y}\right)^2 + 2q_1 f \cosh\left(-\frac{3}{2}q_2\frac{p_m}{\sigma_y}\right) - 1 - (q_1 f)^2 = 0 \tag{II.2}$$

where $q_1$ and $q_2$ are material constants, $f$ is the porosity and $\sigma_{eq}$ denotes the equivalent stress

$$\sigma_{eq} = \sqrt{\frac{3}{2}\underset{\sim}{s} : \underset{\sim}{s}}. \tag{II.3}$$

Therein, $\underset{\sim}{s}$ is the deviatoric part of the Cauchy stress tensor $\underset{\sim}{\sigma}$ ($\underset{\sim}{\sigma} = \underset{\sim}{s} - p_m\underset{\sim}{\delta}$ with the mean pressure $p_m$ and the identity tensor $\underset{\sim}{\delta}$). The yield stress $\sigma_y$ in equation (Eq.) (II.2) is computed from the assumption that only a quasi-static loading is considered so that the effects of viscoplasticity and thermal softening are tentatively neglected in this study. A Voce-type strain hardening law is used, as proposed in [97]

$$\sigma_y = r_0 + \underbrace{r_{\text{inf}}\left[1 - \exp(-k\kappa)\right]^{\beta}}_{r(\kappa)}, \tag{II.4}$$

where $(r_0, r_{\text{inf}}, k, \beta)$ are material constants related to the hardening behavior, $\kappa$ is the accumulated plastic deformation and $r(\kappa)$ is the exponential hardening function.

The GTN potential equation reveals the dependence of the yield surface on the mean pressure and thus the void growth, which is an experimentally observed characteristic of the ductile materials treated in this study. It should be noted here, that Longère [97] proposed an advanced formulation of the plastic potential in order to take into account the experimentally observed void growth under pure shear loading. A comparison of the yield surfaces between the von Mises and the Gurson model is shown in Fig. II.4. This comparison emphasizes the independence of the von Mises law (no damage) on the hydrostatic stress, whereas the GTN yield surface depends on both the hydrostatic and deviatoric stresses.

The evolution of the accumulated plastic deformation is determined from the equality of the macroscopic plastic power with the microscopic one (see Gurson

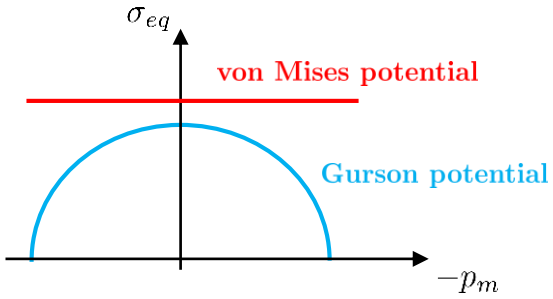


Figure II.4 – Comparison of the plastic potentials of the von Mises material model and the Gurson material model

[66]) as follows

$$\dot{\kappa} = \frac{\underset{\sim}{\sigma} : \dot{\underset{\sim}{\varepsilon}}^p}{(1-f)\sigma_y}, \tag{II.5}$$

where the plastic strain rate is computed from the normality rule

$$\dot{\underset{\sim}{\varepsilon}}^p = \dot{\lambda}\frac{\partial \Phi}{\partial \underset{\sim}{\sigma}} = \dot{\varepsilon}^{pD}\underset{\sim}{\mathcal{N}} + \frac{1}{3}\dot{\varepsilon}^{pM}\underset{\sim}{\delta}, \tag{II.6}$$

where $\dot{\varepsilon}^{pD} = \dot{\lambda}\frac{\partial \Phi}{\partial \sigma_{eq}}$ and $\dot{\varepsilon}^{pM} = -\dot{\lambda}\frac{\partial \Phi}{\partial p_m}$ represent, respectively, the distortional and dilatational parts of the plastic strain rate $\dot{\underset{\sim}{\varepsilon}}^p$, $\underset{\sim}{\mathcal{N}} = \frac{3}{2}\frac{\underset{\sim}{S}}{\sigma_{eq}}$ is the direction of isochoric plastic flow and $\dot{\lambda}$ is the rate of the plastic multiplier. The porosity is assumed to evolve from the superposed effects of the growth of existing voids ($\dot{f}_g$) and the nucleation of new voids ($\dot{f}_n$): $\dot{f} = \dot{f}_g + \dot{f}_n$. The growth of voids can be computed from the hydrostatic plastic deformation

$$\dot{f}_g = (1-f)\dot{\varepsilon}^{pM} \tag{II.7a}$$

$$\dot{f}_g(0) = f_0 \tag{II.7b}$$

The nucleation of new voids is described by a probabilistic function using the Gaussian-type distribution of Chu [43]:

$$\dot{f}_n = A_n\dot{\kappa}; \quad A_n = \frac{f_N}{s_N\sqrt{2\pi}}\exp\left[-\frac{1}{2}\left(\frac{\kappa-\kappa_N}{s_N}\right)^2\right] \tag{II.8a}$$

$$\dot{f}_n(0) = 0 \tag{II.8b}$$

with $\{f_N, s_N, \kappa_N\}$ being material parameters. The porosity is also influenced by the coalescence of voids by localized shearing which induces a strong degradation of the material properties. In fact, this physically complex phenomenon is difficult to characterize and to derive the parameters from experiments, so that the decision has been made to not model this effect explicitly. A phenomenologic description of

void coalescence was proposed e.g. by Tvergaard and Needleman [174].

The presented GTN model is not able to describe void growth (and thus also ductile damage) in the case of pure shear loading, i.e. if $\sigma_m = 0$. This is a consequence of Eq. (II.7). This is however in contradiction to experimental observations, see e.g. [57]. One possible extension of the GTN model to reduce this deficit has been proposed by Longère [97] which is also used here. Therein, a variable equivalent to a kinematic pressure $p_r$ is introduced into the GTN potential. Instead of using a logarithmic function, here a linear function is proposed in order to improve the numerical stability

$$p_r = b(q_1 f - 1), \tag{II.9}$$

with $b$ being a positive material constant. This variable provokes a shift of the yield surface towards positive pressures so that the modified potential takes the form

$$\Phi_G^{mod} = \left(\frac{\sigma_{eq}}{\sigma_y}\right)^2 + 2q_1 f \cosh\left(-\frac{3}{2}q_2\frac{p_m + p_r}{\sigma_y}\right) - 1 - (q_1 f)^2 = 0 \tag{II.10}$$

The GTN model involving isotropic strain hardening is numerically integrated using the radial return algorithm, see Aravas [7]. The integration is based on a separate consideration of the deviatoric and the hydrostatic part. Details are found in the appendix B.

#### II.3.1.2.1 Numerical treatment of volumetric locking

Volumetric locking is a numerical issue which occurs in low-order finite elements during (isochoric) plastic deformation leading to spurious pressure stresses at the integration points and results in a wrong estimation of the structural response. Locking occurs e.g. for a von Mises material where the plastic flow is only influenced by the deviatoric stresses, not by the hydrostatic stresses (thus behaving quasi-incompressible). Also the Gurson model is reported to suffer from locking when the porosity is still very small, see e.g. Zhang [187]. In this work, the B-Bar approach (see Hughes [76]) is applied to prevent volumetric locking in the pre-localization phase. More considerations on this topic are discussed in the appendix C.

## II.3.2 Numerical vs. physical strain localization

The coalescence of micro-voids, i.e. the necking of the ligament between voids, progressively leads to the concentration of voids and plastic deformation into a (more or less well-defined) localization band. Inside this narrow band large strains evolve and finally lead to crack propagation. Due to the incapability of the local material model to reproduce the strain localization, the post-localization response strongly depends on the FE mesh size and orientation.

### II.3.2.1 Numerical modeling of localization

The mechanical consequences of void coalescence and localization in the softening regime of the material can be incorporated into the constitutive law, see Thomason [166], Benzerga [27] and Tvergaard [174] for approaches in the context of the Gurson model. Such extensions show improvements in the softening response of the material, but their use beyond the incipience of localization is accompanied with a (mathematical-founded) loss of ellipticity of the governing differential equations. In a finite element mesh, this results in a severe mesh dependence of the structural response in the post-localization phase (further considerations on mesh sensitivity can be found in the appendix A).

In order to obtain reliable results which are not affected by that spurious mesh dependence, for a long time, the failure of the structure had been assumed to occur at the onset of localization. However, soon the demand for a resolution of the post-localization behavior of softening materials and structures came up. Non-local models have been developed to reduce the mesh sensitivity of the (local) continuum model by introducing an intrinsic length scale into the problem formulation. This length limits the size of the localization band when the mesh size is reduced. These non-local techniques are capable of alleviating the mesh-sensitivity in the post-localization regime, but cannot reproduce (and did not target at reproducing) the genuine (physical) localization band.

### II.3.2.2 Physical modeling of localization: Embedded band methods

The localization band can be resolved in a FE mesh using very small elements (where the band width is equal to or a multiple of the element size) which are aligned according to the boundary of the band (see Needleman [111]). Though with respect to the microscopically thin band, an excessive number of elements is required leading to a high computational effort.

In the eighties the idea came up to use comparably large finite elements and embed the strain localization band into the FE formulation[3]. The work of Belytschko [20] (based on the seminal paper of Ortiz [119]) was the first to capture the kinematical consequences of a localization band within a single FE by enriching its strain field formulation, see Fig. II.5.

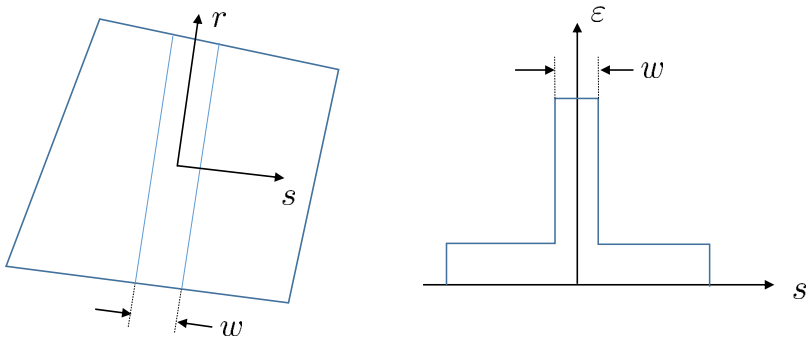


Figure II.5 – Embedded localization band inside a finite element (left) and strain field (right) (adapted from Belytschko [20])

The approach consists in controlling/fixing the band width of the localized zone in order to alleviate the mesh dependence problem - but more important - to reproduce the accumulation of a highly localized strain in a more or less defined band. The method can be well explained by means of a 2-node one-dimensional bar element with an embedded localization zone, see Fig. II.6.

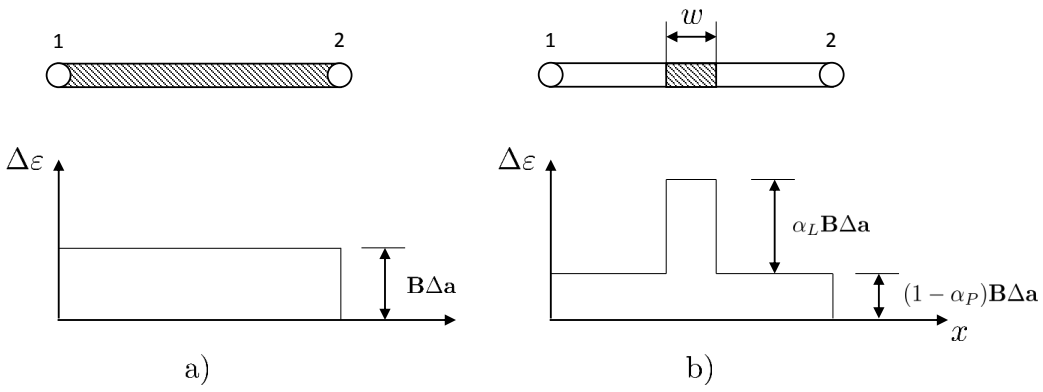


Figure II.6 – Principle of Belytschko's embedded band method: a) Constant-strain bar element. b) Bar element with localized band (adapted from Belytschko [20])

The left figure shows a constant strain field of the element modeled with the

[3]To mutually distinguish these methods from non-local methods, Belytschko [20] has introduced the apropos terms *super-h* and *sub-h* method in order to designate the extension size of the strain localization with respect to the element size. In super-h methods, the localization band width is larger than an element (what is usually the case for non-local methods) whereas in sub-h methods, it is smaller than an element and hence embedded into the element.

standard FEM. The idea of Belytschko was to divide the element into a localized and a non-localized zone (Fig. II.6b), where the strain field in both domains is assumed to be constant. These strain fields are determined by the parameters $\alpha_L$ and $\alpha_P$, which can be derived from two conditions: the strain compatibility condition inside the element and the assumption of stress continuity which is enforced at the interface between the localized and the non-localized domain ($\Delta\sigma_L - \Delta\sigma_N = 0$). This implies that the stress in the non-localized zone $\sigma_N$ undergoes elastic unloading, where the stress in the localized zone $\sigma_L$ is subjected to ongoing softening. The same idea of reproducing a band of highly localized strain and damage in an FE was followed by Huespe [74], but here the localization band is introduced by modifying the shape functions (in the context of the Strong Discontinuity Approach). This concept will be discussed in detail in chapter III.

In the previous approaches, the localization zone is considered as a band which is bounded by two sharp interfaces (between the localized and the non-localized domain), so that the band width is explicitly given. The displacement across these interfaces is weakly discontinuous. In other approaches, the sharp boundaries of the band are dispersed resulting in a smoothed (regularized) strain field across the localized zone. An appropriate (X-FE) framework in the context of shear band modeling was developed by Areias [8], [9]. The displacement field across the shear band is assumed to have a tanh-profile, see Fig. II.7.

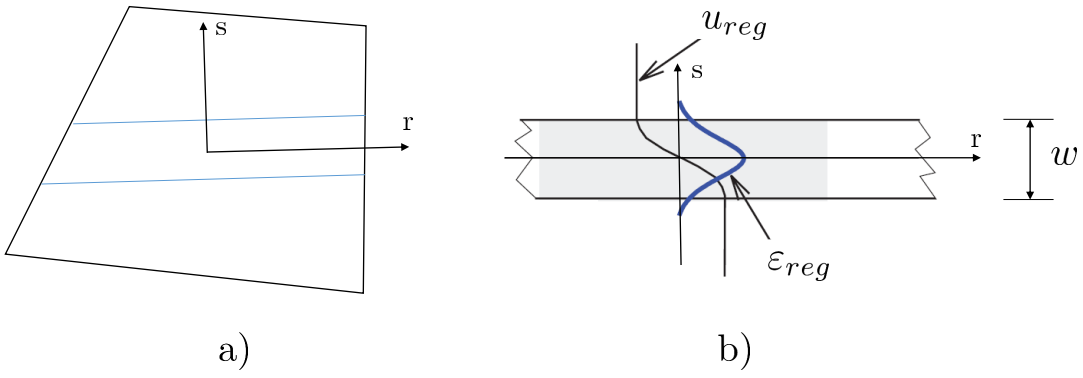


Figure II.7 – Principle of Areias' embedded band method: a) Embedded-band element b) Regularized displacement and strain field (adapted from Areias [8])

Similar regularization functions have been proposed e.g. by Patzák and Jirásek [124] (polynomial regularization function) to resolve the process zone in quasi-brittle materials or also Benvenuti [25] (exponential regularization function) in the context of elasto-damaging materials. It should be noted that these two methods seek not so much to reproduce the strain localization band itself than to model a smooth

transition from a damage model to crack propagation.

In the context of adiabatic shear banding (ASB), which appears in highly dynamic loading in ductile materials, Longère [95], [96] proposed to define an RVE into which the ASB is incorporated by associating it to an anisotropy damage-like tensor $D_{ij}$

$$D_{ij} = d \cdot N_{ij} \text{ , with } \quad N_{ij} = n_i n_j, \tag{II.11}$$

where $d$ is the scalar ASB-intensity and $\underline{n}$ characterizes the orientation of the band. In this approach, the width of the localization band is introduced implicitly.

Existing models which consist in embedding a localization band into a finite element, are mainly applied to quasi-brittle and elasto-plastic materials, but their ability to be applied to strongly non-linear ductile materials still remains a less discussed topic. Thus three embedded-band methods to reproduce the strain localization band are discussed in chapter III.

#### II.3.2.3 Onset of strain localization

The transition of more or less diffuse damage to the formation of a strain localization band requires specific conditions that indicate the initiation and orientation of the localization band.

Recalling that the strain localization is the precursor of the crack initiation, the classical criteria used in fracture mechanics (Griffith theory [63], critical stress intensity factor [79], J-integral [139], etc.) do not provide reliable measures to indicate the onset of localization. Especially, they do not capture the physical nature of strain localization which can be traced back to the appearance of an inhomogeneity (strain and damage concentration within a narrow band) within a - until then - homogeneous material. Under which conditions does the homogeneous material lose its stability so that a strain localization band can form? In the following, two methods to investigate the onset of strain localization - bifurcation analysis and perturbation analysis - are outlined.

##### II.3.2.3.1 Bifurcation analysis

Bifurcation analysis provides a condition for the spontaneous occurrence of an inhomogeneous strain mode within a homogeneous material. The elaboration of such a condition is the fruit of the early works of Hadamard [69], Thomas [165], Hill [71] and Mandel [101]. Later, analytical expressions for elasto-plastic materials

were developed by Rudnicki [144] and Ottosen [121] and finally also for ductile materials by Yamamoto [184] and others. In the following, the fundaments of bifurcation analysis are presented and the evaluation of the condition in the context of a GTN material are elaborated.

### General theory

The localization discontinuity can be suitably represented as a strain rate discontinuity across the plane of the band (see Rudnicki [144] and Rice [140]). In this concern, the discontinuity surface divides the solid into two subdomains $\Omega^+$ and $\Omega^-$. Considering the traction continuity of the stress/strain jump and the displacement continuity of the strain rate jump across the discontinuity, the following compatibility condition can be derived (see Thomas [165] and Jirásek [84] for a detailed derivation)

$$\left(\frac{\partial \dot{\underline{u}}}{\partial \underline{x}}\right)^{+} - \left(\frac{\partial \dot{\underline{u}}}{\partial \underline{x}}\right)^{-} = \underline{c} \otimes \underline{n}, \tag{II.12}$$

where $\underline{c}$ can be written in the form $\underline{c} = \dot{e}\underline{m}$, with $\dot{e} = \|\underline{c}\|$ representing the magnitude of the jump and $\underline{m} = \underline{c}/\|\underline{c}\|$ denoting the direction of the displacement jump, called the polarization vector. The vector $\underline{n}$ characterizes the orientation of the jump across the band, which is described by the left hand side of the Eq. (II.12)[4]. By means of the two vectors $\underline{m}$ and $\underline{n}$ the failure mode along the discontinuity is described completely:

- Tensile splitting (mode I) if $\underline{m} \parallel \underline{n}$, i.e. $\underline{m} \cdot \underline{n} = 1$ (Fig. II.8b) and
- shear slip (mode II) if $\underline{m} \perp \underline{n}$, i.e. $\underline{m} \cdot \underline{n} = 0$ (Fig. II.8c).

Together with the constitutive law in rate form $\dot{\underset{\sim}{\sigma}} = \underset{\approx}{D}^t : \dot{\underset{\sim}{\varepsilon}}$, where $\underset{\approx}{D}^t$ is the elastic-plastic tangent operator (tensor of fourth order), the strain-displacement-relation of the small-strain hypothesis and some mathematical considerations, one arrives at the general description of the weak discontinuity

$$\left(\underline{n} \cdot \underset{\approx}{D}^{t+} \cdot \underline{n}\right) \cdot \dot{e}\underline{m} = \underline{n} \cdot \left(\underset{\approx}{D}^{t-} - \underset{\approx}{D}^{t+}\right) : \dot{\underset{\sim}{\varepsilon}}^{-}. \tag{II.13}$$

The distinction between $\underset{\approx}{D}^{t+}$ and $\underset{\approx}{D}^{t-}$ is important with regard to the fact that the tangent operator depends on the strain rate and can thus vary between the two sides of the discontinuity surface. With the simplification of rate-independent

[4] The jump across the discontinuity can also be written as $[[\nabla \dot{\underline{u}}]]$.

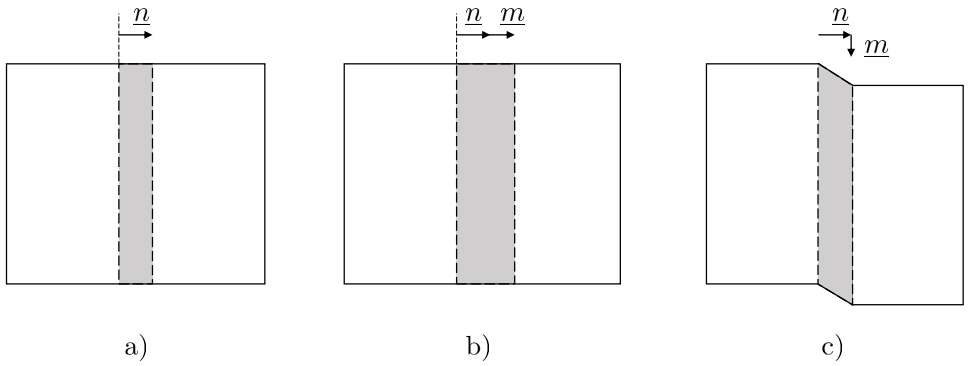


Figure II.8 – a) Body with a localization band, b) tensile splitting (mode I), c) shear slip (mode II) (adapted from Jirásek [84])

materials ($\underset{\sim}{D}^{t+} = \underset{\sim}{D}^{t-} = \underset{\sim}{D}^{t}$), this equation can be reduced to

$$\left(\underline{n} \cdot \underset{\sim}{D}^{t} \cdot \underline{n}\right) \cdot \underline{m} = 0. \tag{II.14}$$

In fact, the second-order tensor $\underset{\sim}{Q} = \underline{n} \cdot \underset{\sim}{D}^{t} \cdot \underline{n}$ is called localization tensor and becomes singular at the release of a localization band leading to the classical localization condition (eigenvalue problem):

$$\det \underset{\sim}{Q}(\underline{n}) = \det(\underline{n} \cdot \underset{\sim}{D}^{t} \cdot \underline{n}) = 0, \tag{II.15}$$

which is also named Mandel-Rice criterion [101]. Due to its characteristics, the tensor $\underset{\sim}{Q}$ is also called *acoustic tensor* as it defines the condition of propagation of elastic acceleration waves (in elastodynamics) propagating in direction $\underline{n}$ with speed $\underline{U}$ [72]. If the bifurcation criterion (singularity of the acoustic tensor for a normal vector $\underline{n}$) is satisfied, a localization band with normal $\underline{n}$ can emerge within the homogeneous material. Therefore this condition represents an indicator for both the onset *and* the orientation of strain localization. It should be noted that the criterion is a necessary but not sufficient condition since it is evaluated locally at a material point irrespective of the material behavior in the neighborhood. Also it is not valid for rate-dependent materials for which the acoustic tensor remains positive definite.

### Localization analysis of the GTN-model

Bifurcation analysis consists in searching for the normal vector $\underline{n}$ which renders the acoustic tensor singular for the first time in the load history. Mathematically, the roots of Eq. (II.15) have to be found which can be determined numerically

(for any kind of rate-independent material) or analytically for certain materials. The numerical approach (which was implemented here) is explained below. An analytical expression for the GTN-model can be derived (and may be implemented for future works), but the reader is referred to the appendix D.2 to regard the detailed set of equations.

The localization analysis relies on an accurate computation of the continuum tangent operator $\underset{\approx}{D}^t$ which is derived in the appendix D.1.

According to the paper of Ortiz [119], the determinant of the acoustic tensor in the 2D case (where the acoustic tensor is a 2x2 matrix) can be written as

$$\det \underset{\approx}{Q}(\underline{n}) = a_0 n_1^4 + a_1 n_1^3 n_2 + a_2 n_1^2 n_2^2 + a_3 n_1 n_2^3 + a_4 n_2^4 \tag{II.16}$$

where

$$\begin{aligned}
a_0 &= D_{1111}D_{1212} - D_{1112}D_{1211}, \\
a_1 &= D_{1111}D_{1222} + D_{1111}D_{2212} - D_{1112}D_{2211} - D_{1122}D_{1211}, \\
a_2 &= D_{1111}D_{2222} + D_{1112}D_{1222} + D_{1211}D_{2212} - D_{1122}D_{1212} - \\
&\quad D_{1122}D_{2211} - D_{1212}D_{2211}, \\
a_3 &= D_{1112}D_{2222} + D_{1211}D_{2222} - D_{1122}D_{2212} + D_{1222}D_{2211}, \\
a_4 &= D_{1212}D_{2222} - D_{2212}D_{1222}.
\end{aligned} \tag{II.17}$$

Setting $\underline{n} = [\cos\theta, \sin\theta]$ and $x = \tan\theta$, the condition becomes

$$f(x) = a_4 x^4 + a_3 x^3 + a_2 x^2 + a_1 x + a_0 = 0, \tag{II.18}$$

which is a polynomial of fourth order. If the minima of the function switch the sign from positive to negative, the localization is initiated. The minima occur at the roots of the first derivative $f'(x)$ which can be computed using Cardan's formulae.

#### II.3.2.3.2 Linear perturbation stability analysis

In rate-dependent materials which are subjected to high strain rates, the material instability is rather governed and controlled by an increasing effect of local heat accumulation provoking an increasing thermal softening which overcomes the plastic strain hardening (see e.g. [12] and [180]). It is important to note that

the constitutive formulations of such materials remain elliptic and the speed of acceleration waves remains positive [190]. Therefore the bifurcation analysis can not be applied to viscous materials. For this reason, Clifton [44], Bai [12], Molinari [108] and others applied the linear perturbation stability analysis to viscoplastic materials, which goes back to works of Rabotnov and Shesterikov [133].

The perturbation analysis permits to provide an analytical condition for the onset of an instability, which is however a necessary but not sufficient condition for a localization. This method is based on the analysis of the stability of the homogeneous solution $\underline{u}_0$ after superposing a small linear perturbation $\delta\underline{u}$ on the set of homogeneous solutions (see also Longère [95]):

$$\underline{u} = \underline{u}^0 + \delta\underline{u}, \tag{II.19}$$

where $\underline{u}$ represents the perturbed solution. Let the perturbation have a wave-like form:

$$\delta\underline{u} = \underline{\hat{u}} \exp(\omega t + ik\underline{n}\underline{x}), \tag{II.20}$$

where $\underline{\hat{u}}$ represents the perturbation magnitude, $\omega$ the wave pulsation, $k$ the wave number and $\underline{n}$ the wave vector. The wave pulsation can be further split into a real part $\omega_R = Re(\omega)$ and an imaginary part $\omega_I = Im(\omega)$:

$$\delta\underline{u} = \underline{\hat{u}} \exp(\omega_R t) \exp(ik(ct + \underline{n}\underline{x})), \tag{II.21}$$

where $c = \omega_I/k$ is the wave velocity. The behavior of the real part $\omega_R$ indicates the transition between the stable and unstable state:

- if $\omega_R > 0$, the perturbation increases over time;
- if $\omega_R < 0$, the perturbation decreases over time.

The objective of the analysis consists in finding the condition for which the solution turns from a stable state to an instable state, i.e. for the wave pulsation to turn from a negative to a positive value.

### II.3.3 Crack formation and propagation

The representation of a disconinuity in the finite element mesh requires a special numerical treatment and has thus given birth to many different methods. In the following, an overview of commonly used approaches within the FEM-framework is

given[5].

#### II.3.3.1 Crack propagation using standard FEM

There are three common methods to reproduce the crack propagation in the context of the standard FEM: element deletion method, adaptive remeshing technique and the inter-element crack method (cohesive element method).

##### II.3.3.1.1 Element deletion method

The element deletion method (Besson [29], Autenrieth [11]) is particularly simple to implement and therefore a preferred method in basic failure simulations. As soon as an initiation criterion is met, the stresses in the cracked element are set to zero. However, that method suffers from severe mesh dependence of the structural response. Moreover the geometric crack path can not be properly captured as the crack is represented as a sequence of elements.

##### II.3.3.1.2 Adaptive remeshing techniques

Remeshing methods (Bouchard [31], Carter [35]) capture the crack path geometrically, however it has severe disadvantages [85]:

- for nonlinear materials (history-dependent state variables) it is necessary to project results between different meshes many times (Réthoré [138])
- output of time histories at selected points is more difficult;
- the entire data management becomes more difficult because the problem is associated with many meshes.

Thus, remeshing techhniques can be computationally demanding and are not easy to implement.

##### II.3.3.1.3 Inter-element crack method

Another approach consists in using interface elements (Needleman [110], Ortiz [118]). The displacement jump is represented by incorporating elements of zero

[5]For the sake of completeness, other numerical methods of crack representation can be cited, e.g. Boundary Element Method (Yan [185], Portela [128]), Smoothed Particle Hydrodynamics (Gray [62]), Element-free Galerkin Method (Belytschko [21], Simkins [155]), Phase Field Method (Ambati [5], Ulmer [175]), Thick Level Set Method (Moës [107]).

width in between the finite elements. However, several disadvantages make cohesive elements rather unattractive:

- The discontinuity path is determined by the mesh structure. Interface elements are therefore restricted to applications in which the crack path is known in advance (from experimental observations or if the crack path is prescribed by the material structure, e.g. for delamination in composite materials). Then, the mesh lay-out has to be arranged such that the crack path coincides with the element boundaries.

- If the crack path is not known a priori, cohesive elements can be introduced between each element, as proposed by Xu [182]. Yet also this approach goes along with mesh-dependent results.

- The requirement to assign these interface elements an infinite elastic stiffness to model a perfect bond (leading to difficulties in the implementation as badly conditioned stiffness matrices, stress oscillations, etc. and thus to an erroneous crack pattern).

#### II.3.3.2 Embedded finite element methods

Alternatively, the crack can be reproduced numerically by using enriching techniques. These are based on an enrichment of the finite element formulation such that a prescribed displacement or strain field can be represented.

##### II.3.3.2.1 Classification of embedded-discontinuity FEM in terms of kinematic and static aspects

Following the systematic classification of Jirásek [81], three basic techniques can be found to embed the enriched displacement or strain field (be it a strong, weak or regularized discontinuity) into the element:

- *Statically optimal symmetric (SOS) formulation:* Although the stress continuity across the crack is naturally satisfied, the kinematics of a discontinuity is not properly represented (stress locking). Examples from the literature are the works of Belytschko [20], Larsson [91], Berends [28] and Armero [10].

- *Kinematically optimal symmetric (KOS) formulation:* Contrarily to the SOS, the kinematics of a discontinuity is well captured, but the stress continuity condition is not satisfactory. Examples from the literature are the works of Lotfi [98], Moës [106], [105] and Remmers [136].

- *Statically and kinematically optimal nonsymmetric (SKON) formulation:* This approach combines the advantages of the SOS and the KOS formulations implying that both the stress continuity and the kinematic aspects are reasonably reproduced. Examples from the literature are the works of Dvorkin [52], Klisinski [88], Oliver [112] and Huespe [74].

A more detailed description of these three classes is given in Jirásek [81].

#### II.3.3.2.2 Node enrichment vs. element enrichment

The embedded-discontinuity FEM are characterized in that the discontinuity is inserted into the structure irrespective of the FE mesh boundaries. There are basically two different ways to introduce a discontinuity into the finite element, either by node enrichment or by element enrichment.

**Node enrichment**

This type of embedded-discontinuity FEM is based on the partition of unity concept, see Melenk [103]. In the context of the FEM, the displacement field can be enhanced by a product of the standard shape functions (having the property of the partition of unity) with a priori known enrichment functions. The enriched displacement field $u(x)$ is then written as follows

$$u(x) = \sum_{i=1}^{n} N_i(x) \left( a_i + \sum_{j=1}^{m} G^j(x) b_i^j \right) \tag{II.22}$$

where $N_i$ is the $i$-th standard FE shape function, $n$ the number of nodes, $a_i$ the $i$-th standard displacement degree of freedom, $G_j$ is the $j$-th global enrichment function, $m$ the number of enrichment functions and $b_i^j$ the $i$-th additional degree of freedom associated to the $j$-th enrichment function. The multiplication of the enrichment functions $G_j$ with the standard FE shape functions has the advantage that they share the same support, i.e. the nodes of the element.

The enrichment functions can be chosen according to the physical problem. The displacement jump across the discontinuity can then be simply described by using a Heaviside (step) function. The singular displacement field at the crack tip can be reproduced by using a set of four asymptotic functions, see Belytschko [18]. These enrichment functions are jointly used in the generalized FEM [55] or also the extended FEM (X-FEM), see e.g. Moës [106].

**Element enrichment**

This type of embedded-discontinuity FEM is based on the concept of assumed enhanced strain, see Simo [158]. As opposed to node enrichment methods, it relies on the insertion of the enriching discontinuity mode on the element level (in the following referred to as the commonly used abbreviation E-FEM). Thus, the additional degrees of freedom are element-wise constant and can be statically condensed from the governing equations so that the computational effort can be reduced. The main idea of this approach is going back to works of Ortiz [119] and Belytschko [20] and was further extended by Simo [157] and Oliver [112] (Strong Discontinuity Approach, SDA), Feist [54] and Huespe [74], to name a few.

**Illustration of the difference between element and node enrichment**

This section is thought to illustrate the fundamental difference between node (referred to as X-FEM) and element (referred to as E-FEM) enrichment.

Consider the crack in Fig. II.9 which passes through the two neighboring finite elements e1 (nodes $1, 2, 3, 4$) and e2 (nodes $1', 2', 3', 4'$). The crack direction is indicated by the normal vector $\underline{n}$. At point $x$ the crack cuts the edge $\overline{23}$.

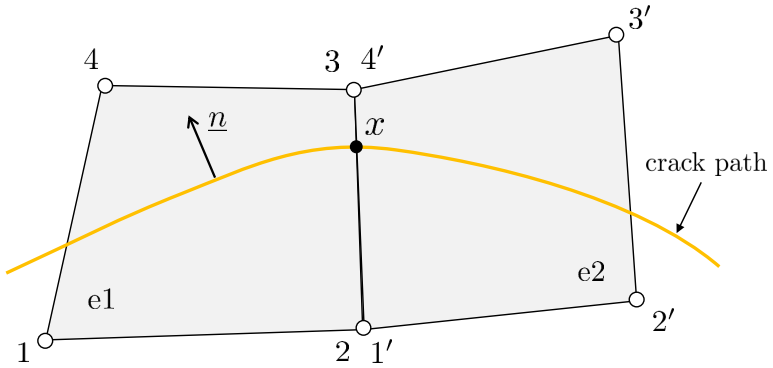


Figure II.9 – Illustration of a geometric crack path through two elements e1 and e2

In the following the displacement jump $[\![u]\!]$ across the crack line at point $x$ is computed both with the node and element enrichment formulations. The discretized (discontinuous) displacement field of the X-FEM can be written as follows

$$u(x) = \sum_{i=1}^{4} N_i(x) a_i + \sum_{j=1}^{4} N_j(x) \left(H(x) - H_j\right) b_j, \tag{II.23}$$

being $H$ the Heaviside function, which equals to 1, if a point is located at the

'positive' side of the crack and 0 if it is located on the 'negative' side (the normal vector is defined to point into the 'positive' sense). The discretized displacement field of the E-FEM reads

$$u(x) = \sum_{i=1}^{4} N_i(x) a_i + \left( \sum_{j=1}^{4} N_j(x) \left( H(x) - H_j \right) \right) b. \tag{II.24}$$

By using here the 'shifted basis' formulation (involving the Heaviside functions at the nodes $H_j$), the enrichment of the nodes of the element which is cut by the crack does not influence the neighboring elements.

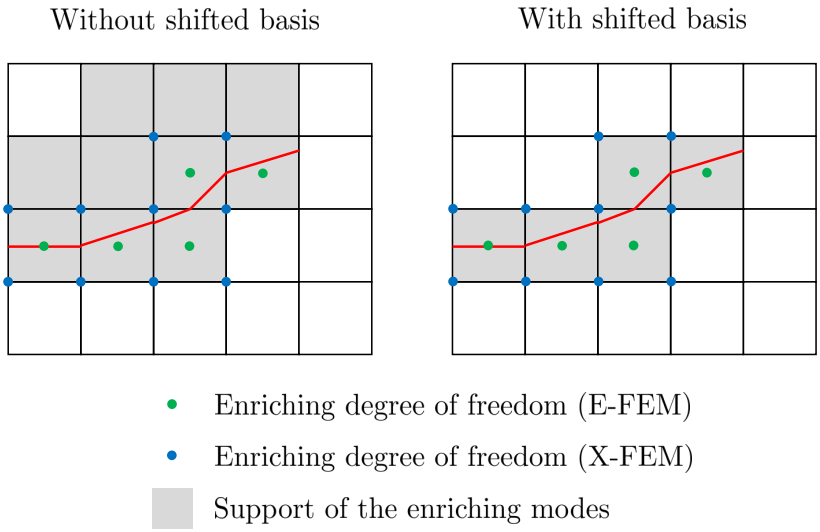


Figure II.10 – Effect of using the shifted basis formulation (or not) on the support of the enriched modes in the E-FEM and X-FEM

The main difference between the two formulations can be carved out when regarding the appearance of the enriching dof's $b$. The X-FEM expression involves eight enriching dof's, where there are only two in the E-FEM. This has far-rancing consequences, which are discussed below.

First of all, the displacement jump at point $x$ is computed with the X-FEM from the viewpoint of element e1:

$$[\![u]\!]^{e1}(x) = u(x^+) - u(x^-) \tag{II.25}$$

$$= \sum_{i=1}^{4} N_i(x^+) a_i + \sum_{j=1}^{4} N_j(x^+) \left( H(x^+) - H_j \right) b_j \tag{II.26}$$

$$- \sum_{i=1}^{4} N_i(x^-) a_i - \sum_{j=1}^{4} N_j(x^-) \left( H(x^-) - H_j \right) b_j. \tag{II.27}$$

Noting that $H(x^+) = 1$, $H(x^-) = 0$, $H_j = \{0; 0; 1; 1\}$ for $j = \{1, 2, 3, 4\}$ and $N_i(x^+) = N_i(\mathbf{x}^-) = N_i(x)$ and $N_i(x) = \{0; N_2(x); N_3(x); 0\}$ yields

$$[\![u]\!]^{e1}(x) = N_2 b_2 + N_3 b_3. \tag{II.28}$$

Thus, the displacement jump is computed from a linear interpolation of the enriching dof's through the shape functions. This allows for a good approximation of the jump throughout the finite element. In the same manner, the jump calculated within the element e2 reads

$$[\![u]\!]^{e2}(x) = N_{1'} b_{1'} + N_{3'} b_{3'} \tag{II.29}$$

what is the same expression as in Eq. (II.28), i.e. $[\![u]\!]^{e1}(x) = [\![u]\!]^{e2}(x)$. This implies that the displacement field and the jump between two neighboring (cut) elements are conforming.

Likewise, the displacement jump at $x$ is computed in the E-FEM framework

$$[\![u]\!]^{e1}(x) = \sum_{i=1}^{4} N_i(x^+) a_i + \left( \sum_{j=1}^{4} N_j(x^+) \left( H(x^+) - H_j \right) \right) b \tag{II.30}$$

$$- \sum_{i=1}^{4} N_i(x^-) a_i - \left( \sum_{j=1}^{4} N_j(x^-) \left( H(x^-) - H_j \right) \right) b \tag{II.31}$$

$$= \left( \sum_{j=1}^{4} N_j(x) \right) b \tag{II.32}$$

$$= b. \tag{II.33}$$

Thus, the jump equals to the enriching dof $b$ which is in fact constant within the element. This is an important difference to the X-FEM in that the displacement jump of the crack within the element is reduced to one constant displacement jump vector. The jump at $x$ 'seen' from the element e2 yields as well

$$[\![u]\!]^{e2}(x) = b, \tag{II.34}$$

but the jump variables (normally) differ between the elements, so that $b^{e1} \neq b^{e2}$. Therefore the conformity of the jump from one to another cut element can not be ensured. The different representations of the crack with line segments using the X-FEM and the E-FEM are compared in Fig. II.11. As opposed to the X-FEM, the E-FEM is not capable of reproducing a conforming displacement field.

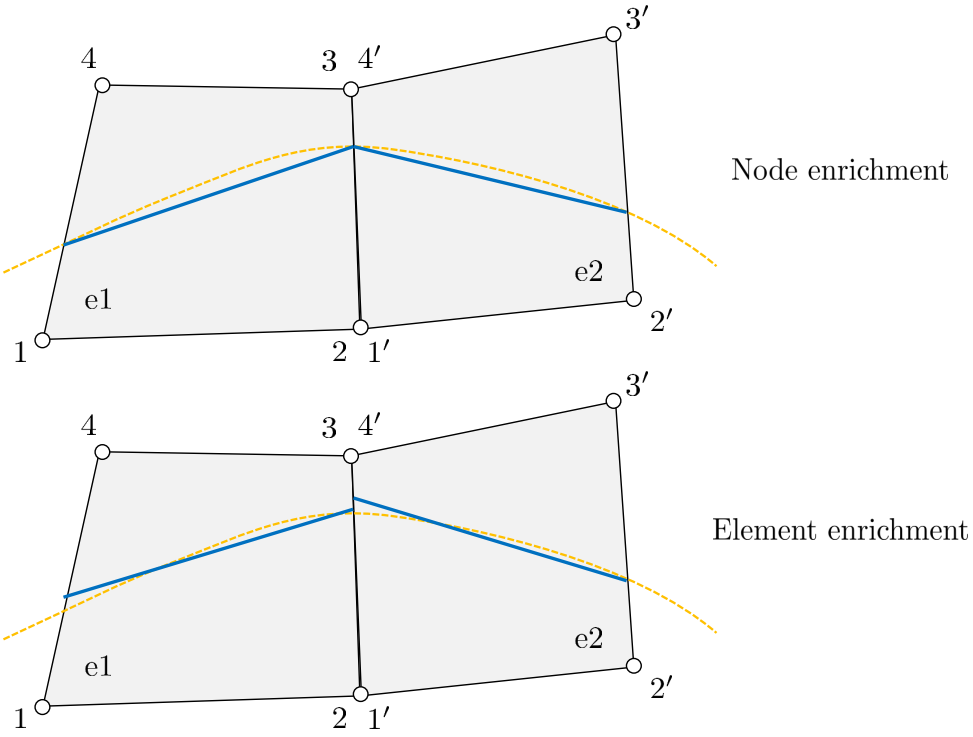


Figure II.11 – Comparison between node and element enrichment with regard to their discretization of the crack discontinuity

**Summary**

A comprehensive comparison of these two enrichment formulations applied to strong discontinuities is done extensively in articles of Jirásek [85] and Oliver [117]. In the end there is no superior method, but both have their advantages and disadvantages compared to the other method.

First of all the attention should be concentrated on the hint that representative approaches of the E-FEM have been proposed from all the three classes SOS, KOS and SKON. However - and this is rarely discussed in literature - the X-FEM has been mainly used in the KOS formulation, what is also emphasized in the paper of Wu [181]. This clarification plays an important role in the considerations conducted in chapter IV.

As already carved out, the added dof's are internal/elemental in the E-FEM, but global in the X-FEM. Moreover, the dof's are associated with the elements in the E-FEM, but with the nodes in the X-FEM. Although this seems to be a trivial fact, it has several consequences. First of all, the displacement approximation in the E-FEM is non-conforming (although recently, the consideration of non-conforming

discontinuity modes have led to conforming E-FEM, see e.g. Alfaiate [3] and Dias-da-Costa [47], [48]), whereas the displacement across the element boundary is conforming in the X-FEM. Then, in the E-FEM the additional degrees of freedom can be statically condensed from the governing equations (as they are element-wise constant), but this is not the case in X-FEM. Therefore, the E-FEM goes along with a smaller computational cost compared to the X-FEM, where the additional degrees of freedom appear in the global system of equations.

It should be noted, that - depending on the formulation (SOS, KOS, SKON) - the global stiffness matrix in the E-FEM can be non-symmetric, whereas in X-FEM it is mostly symmetric - due to the fact that the X-FEM is only used in the KOS formulation. Furthermore, the implementation effort for X-FEM is larger than for E-FEM, especially with regard to the implementation into an existing FEM software. Oliver [117] reports, that the accuracy is higher for the E-FEM compared to the X-FEM when applied to a coarse FE mesh.

So all these conclusions seem to indicate many differences between the two enrichment techniques, but in the end it turns out that the fundamental difference lies in their capabilities of capturing the enriching displacement field. The X-FEM provides more dof's in representing that relative displacement field than the E-FEM, so that **the X-FEM can be understood as a generalized (enhanced) formulation of the E-FEM** with all the resulting numerical pros and cons.

Finally, a summary is given in Tab. II.1.

Table II.1 – Comparison between E-FEM and X-FEM (Jirásek [85])

| Property of comparison | E-FEM | X-FEM |
|---|---|---|
| added degrees of freedom | internal | global |
| dof associated with | elements | nodes |
| displacement approximation | non-conforming | conforming |
| stiffness matrix | always non-symmetric | can be symmetric |
| strains in separated parts | partially coupled | independent |
| implementation effort | smaller | greater |
| computational cost | lower | higher |
| numerical robustness | limited | good |
| accuracy (Oliver [117]) | higher (coarse meshes) | lower |

#### II.3.3.3 Onset of crack propagation

In the case of brittle materials, criteria from linear elastic fracture mechanics can be applied to indicate the initiation of a crack as e.g. the (global) energy release rate by Griffith [63] or the (local) critical value of the stress intensity factor by Irwin [79]). However, these criteria do not apply to ductile materials exhibiting a distinct phase of plastic deformation and showing a strongly non-linear behavior. The use of the J-integral (Rice [139] and Cherepanov [42]) as propagation criterion does not apply for damage-induced softening behavior and non-proportional loading.

In the following, two indicators for crack initiation in ductile materials are considered: a critical value of an internal variable and use of a measure which is obtained from averaging a variable (stress, strain, etc.) over a patch at the crack tip.

##### II.3.3.3.1 Critical value of an internal variable

More adapted to the type of materials used in this work is to track a locally evaluated internal variable of the constitutive model close to the crack tip and check if it attains a critical limit, see e.g. Lievers [94] choosing a critical plastic shear strain. Geffroy [57] proposed to use a critical (failure) porosity, which is based on the observation that voids accumulate and coalesce in front of the crack tip. However, the porosity, which is defined macroscopically in the context of a homogeneous material, is used to conclude on microscopic processes in front of the crack tip, what is not realistic. Another issue is the question on how to quantify the critical value. There exist many empirical studies on this topic in the context of ductile materials, e.g. Xue [183] proposed a function where the rupture strain depends on the hydrostatic stress and the Lode angle. Komori [89] elaborated a function between the plastic strain at failure and the porosity obtained from the void coalescence criterion of Thomason [166]. Though, in the context of the FEM, this type of criteria is confronted with the spurious mesh sensitivity of the numerical result, see Fig. II.12.

##### II.3.3.3.2 Averaging of a variable over a crack-tip patch

In order to reduce the mesh dependence of the crack propagation indicator, an alternative way is to delocalize the fracture criterion over an area in front of the crack tip. Wells [178] and Remmers [135] proposed an averaging technique where a disk is inserted at the crack tip whose size equals to three times of the element size

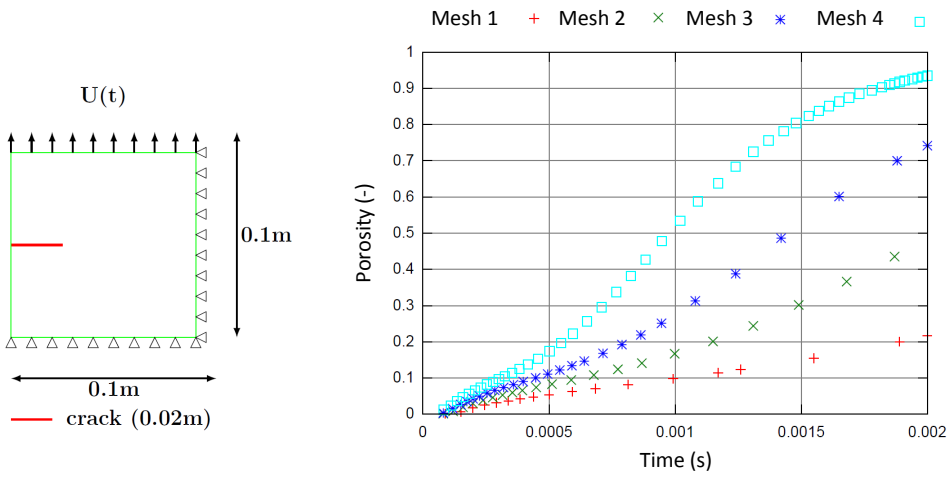


Figure II.12 – Demonstration of the mesh dependency (mesh 1 coarse to mesh 4 fine) when using a critical porosity criterion evaluated in the crack-tip element in the case of a tensile test (leftmost), adapted from [45]

(see Fig. II.13).

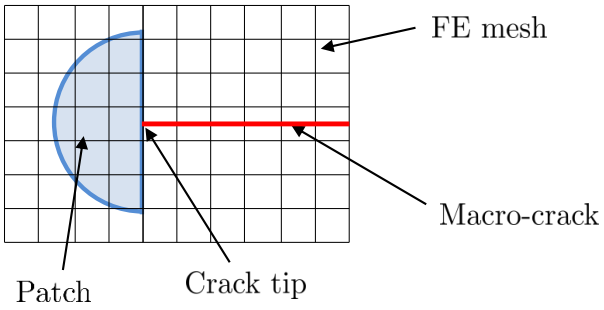


Figure II.13 – Half-circle patch inserted at the crack tip

Every integration point which is located within the patch, is weighted according to its distance to the crack tip, using a Gauss distribution function. By integrating over the entire patch, an averaged stress tensor is computed and by using a representative stress meausure it can be compared to a critical stress limit indicating the onset of crack propagation. Likewise, the maximal principal stress is computed from the averaged stress tensor and compared to a critical stress as applied in many papers, e.g. Prabel [130], Menouillard [104], Haboussa [67] and Jan [80]. These models however use an elasto-plastic constitutive material model including strain hardening with a positive hardening modulus. Yet a stress-based criterion is not adapted to the damage-induced strain softening behavior of the model used in this study. Instead, Crété [45] rather recommends for such type of materials to use the

stored plastic energy averaged over the patch

$$W_{Patch} = \frac{\sum_{i=1}^{p} \omega_s^i A^i}{\sum_{i=1}^{p} A^i} \tag{II.35}$$

where $p$ is the number of elements that are either completely or partially part of the patch, $A_i$ is the patch area of the i-th element, $\omega_s^i$ is the stored plastic energy of the i-th element averaged over the Gauss points which can be computed from integration of the exponential hardening law $r(\kappa)$, see Eq. (II.4), over the accumulated plastic strain $\kappa$

$$\omega_s = \int_0^{\kappa} r(\kappa) \mathrm{d}\kappa. \tag{II.36}$$

The crack propagates if the $W_{Patch}$ reaches a critical stored energy value. However, from his study it is unclear how to determine the critical stored energy directly from experiments. Also a main difficulty of using a patch is to quantify the radius of the patch which is usually a function of the FE mesh (and thus mesh dependent). The smaller the patch radius, the more the failure criterion depends on the crack-near field and inversely.

## II.4 Summary

In this chapter, the challenges of the physical and numerical modeling of the ductile failure process have been pointed out. The discussion of the modeling of the entire failure process has emphasized the objective to set up a unified model of ductile fracture. The focus of this work being on the modeling of the strain localization and its embedding into the failure process (transition conditions), it has required to adopt a constitutive model and crack propagation framework and modify them so as to attain some harmony with the strain localization.

The failure of a ductile material (e.g. DH36) was shown to result from void nucleation, growth and coalescence. The occurrence of damage at a very small (micro-)scale contrasts with the propagation of a (macro-)crack which may extend over meters in a large-scale structure (e.g. a ship of a length of several hundred meters). Mastering a high fidelity resolution of the local crack propagation and a low fidelity computation of the global structural response in one simulation (see Fig. II.14) constitutes a main challenge in predicting the residual structural strength after failure.

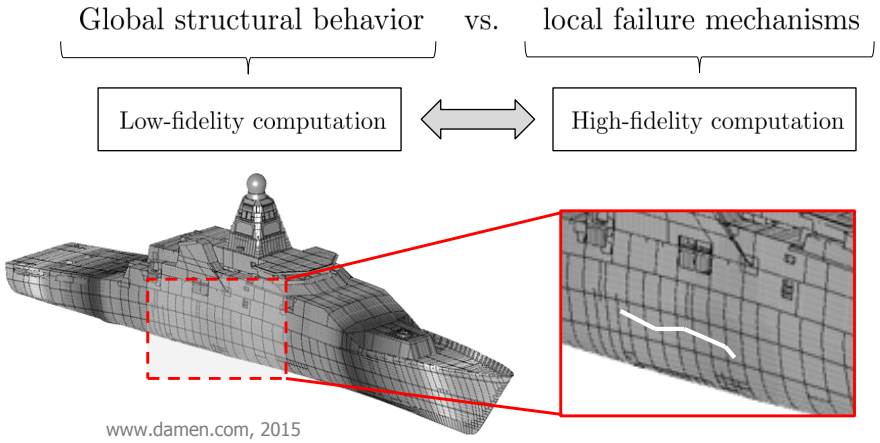


Figure II.14 – High fidelity vs. low fidelity computation (the FE model was taken from www.damen.com)

### II.4.1 Damage-induced softening

In a first step, a material model for the pre-localization response was elaborated. A summary is given in Tab. II.2. The effect of strain hardening is considered, yet the influences of viscoplasticity and thermal softening are tentatively neglected. The damage-induced softening can be described either by dilatant or non-dilatant models. The first class takes into account the effect of void growth on the volumetric plastic deformation of the surrounding matrix, whereas the second class does not. Motivated by the objective to stick as close as possible to the physical observations, a Gurson-type model was chosen, see Tab. II.2. The physical consequences of void coalescence is not explicitly introduced in the material model, but is rather involved in the modeling of strain localization.

There are two main challenges to deal with: volumetric locking and mesh dependence. Volumetric locking can potentially arise in the early phase of damage evolution. In order to prevent the simulation from volumetric locking, the B-Bar approach [76] is used. Mesh dependence of the structural response is a problem which comes up in the post-localization regime of softening materials or structures. It can be attributed to the non-existence of a characteristic length scale in the local material model to prevent pre-localization in a band of finite elements. Non-local regularization methods provide a means to reduce the issue, but they require to use a very fine mesh to capture the (micro-scale) localization effects and they do not aim at reproducing the appearance of a (more or less sharply bounded) localization band.

Table II.2 – Summary : Damage-induced softening

| | |
|---|---|
| Modified plastic potential of the damaged material (GTN-model) | • $\Phi_G^{mod} = \left(\frac{\sigma_{eq}}{\sigma_y}\right)^2 + 2q_1 f \cosh\left(-\frac{3}{2}q_2\frac{p_m+p_r}{\sigma_y}\right) - (1+(q_3 f)^2) = 0$ |
| Numerical modeling | • Standard FEM |
| Numerical issues | • Volumetric locking (B-Bar approach)<br>• Mesh dependence in the softening regime |

## II.4.2 Numerical vs. physical localization

Reducing the mesh dependence in the softening regime of the material is one issue, but capturing the damage concentration and strain localization inside a narrow band is another one. Embedding the localization band into the finite element efficiently allows for combining these two objectives in one approach. The enrichment techniques of Belytschko [20] and Huespe [74] provide an idea of how a sharply bounded band can be embedded into the FE. The kinematic field across the band can be as well conceived in a dispersed manner and has given rise to propose different displacement profiles, e.g. using a tanh, polynomial or exponential shape - to name a few. Incorporating the band kinematics into the FE requires enriching the nodal or elemental basis of the FE (the same concept is used for introducing a discontinuity during crack propagation). A different point of view was elaborated by Longère [95] in the context of adiabatic shear banding which induces an anisotropy of the material.

The transition from (more or less) diffuse damage to localization relies on the finding a condition for when the homogeneous material loses its stability. Two common methods have been discussed: bifurcation analysis and linear perturbation analysis. Bifurcation analysis is limited to rate-independent materials and consists in evaluating the orientation of the localization band for which the determinant of the acoustic tensor equals to zero (or numerically negative). The perturbation analysis is based on assessing the condition of stability of a homogeneous solution after having been disturbed by a small wave-like perturbation. In this work, the bifurcation analysis is used due to the fact that viscoplasticity is tentatively ne-

glected, see Tab. II.3.

Modeling this step is essential for an accurate prediction of the structural failure response. Neglecting this transition phase between diffuse damage and crack propagation can result in tremendous inaccuray, as it has been a meaningful outcome of the thesis of Crété (recall Fig. I.4). Studying three different embedded-band methods capable of reproducing the localization band and treating the passage between the other stages of ductile failure will be the topic of the next chapter.

Table II.3 – Summary : Strain localization

| | |
|---|---|
| Onset of strain localization | • Bifurcation analysis: $\det(\underline{n} \cdot \underset{\sim}{D}^t \cdot \underline{n}) = 0$<br>• Numerical computation of the criterion (Ortiz [119]) |
| Challenges | • Reduction of the mesh dependence in the post-localization phase<br>• Physical description of the damage concentration and strain localization in a (more or less well-defined) narrow band<br>• Application of the criteria and methods for a strongly non-linear ductile material |
| Numerical modeling | • Incorporation of the strain localization band into the FEM<br>• **Numerical method to be discussed in the next chapters** |

### II.4.3 Crack propagation

The third important step of failure modeling discussed in this chapter is the formation and propagation of a macro-crack. Similar to the localization phase, the challenge here consists in capturing the (stress-free) crack discontinuity in the FE mesh. Three different methods in the context of the FEM have been proposed,

however they turned out to suffer from mesh dependence and thus do not really provide a reliable means of numerical modeling. Rather, the discontinuous displacement field is embedded into the FE by enhancing its kinematic formulation. In the last decades, many such embedded crack methods have been proposed. They can be classified into the SOS, KOS and SKON formulation depending on whether the kinematic representation of the discontinuity, the static continuity across the crack or both are satisfied. Apart from this classification, it can be distinguished the type of FE enrichment: either the nodal (X-FEM) or elemental (E-FEM) basis is enriched. Both enriching techniques have advantages and drawbacks compared to the other. A strong feature of the X-FEM is that it allows for a more precise approximation of the crack path. The E-FEM stands out in terms of lower computational cost and a higher accuracy for coarse meshes. Also there are methods of the SOS, KOS and SKON class, whereas the X-FEM so far can be only found in the KOS formulation. The choice of method is made in connection with the choice of the localization method in the next two chapters, see Tab. II.4.

The crack initiation can be indicated by calculating a (local) critical value of an internal variable (plastic strain, porosity, etc.), which suffers from mesh sensitivity issues, or by averaging a variable (stress, plastic strain, etc.) over a crack-tip patch and comparison to a critical value. The second approach is the most promising in the context of ductile materials and allows to reduce the mesh dependence problem. Yet, no particular method has been chosen so far as its choice depends on the method used for localization modeling, see the next two chapters.

Table II.4 – Summary : Crack propagation

| | |
|---|---|
| Onset of crack propagation | • Depends on the modeling of the strain localization phase (see next chapters) |
| Challenges | • Reduction of the mesh dependence in the crack propagation phase<br>• Numerical modeling of the crack discontinuity |
| Numerical modeling | • Incorporation of the crack into the FE<br>• Enrichment of the kinematics of the FE (node or element enrichment, depends on the method used for localization band modeling)<br>• **Numerical method to be discussed in the next chapters** |

# Chapter III

# Performance of selected methods to describe strain localization in ductile materials

## Contents of chapter III

# III.1 Introduction

In the previous chapter, appropriate methods for treating each step of ductile failure in a physical and numerical manner as well as physics-motivated transition criteria between these steps have been evoked. In this part, we are studying the performance of three different embedded-band FE methods to model the phase of strain localization in ductile materials. The most promising of these studied approaches is then discussed in detail in chapter IV.

Basically there is no consensus in the literature on how to model the critical phase of strain localization. Continuum approaches attempt to describe the effects of void coalescence on the (continuum) material, see e.g. the works of Pardoen ([122], [123]), Benzerga ([26], [27]) and Tvergaard ([169], [171]). An alternative way consists in reproducing the kinematic consequences of the narrow band of highly localized strain, an approach which is applied in the following.

By definition, a strong discontinuity involves a discontinuity of the displacement/velocity field, whereas a weak discontinuity involves a discontinuity of the displacement/velocity *gradient* field.

# III.2 Preliminary considerations

In this section, three localization methods using different kinematic representations are assessed. In view of comparing the methods in question at the end of this chapter, common notations and methods are defined here. Therefore, the different kinematic fields are discussed and the principle of virtual work is stated which the three methods are derived from. Moreover the enrichment method and transition criteria which are used for all three methods are specified. Then, in the subsequent sections, the localization methods are described one after the other.

## III.2.1 Kinematic modeling of the localization band

The continuous displacement field $\hat{u}(x)$ is assumed to be enriched by a discontinuous field $\tilde{u}(x)$ which is supposed to represent the characteristic kinematics of the localization band. The superposition of these two fields yields the total displacement field $u(x)$

$$u(x) = \hat{u}(x) + H_w(s)\tilde{u}(x) \tag{III.1}$$

where the function $H_w(s)$ is an adapted version of the classical Heaviside (step)

function; $s$ is the signed distance function with respect to the center line of the band (see Fig. III.1). The sign of the distance function is determined in accordance with the orientation of the normal vector of the localization band. For now, the normal vector is assumed to be arbitrary, but it can be evaluated e.g. from stability analysis, see section II.3.2.3 and chapter IV for further details.

The advantage of using the discontinuous enrichment formulation is that any arbitrary profile of the displacement field across the band can be prescribed. Depending on the different viewpoints (discussed below), the displacement field may be described by a strong, weak[1] or (non-linearly) regularized discontinuity. Possible mathematical formulations are the following, where the limit values of the Heaviside functions have been chosen to be $-1$ and $+1$[2]:

- Strong discontinuity: $$H_w(s) = \begin{cases} 1 & s \geq 0 \\ -1 & s < 0 \end{cases} \tag{III.2}$$

- Weak discontinuity: $$H_w(s) = \begin{cases} 1 & s \geq \frac{w}{2} \\ \frac{2}{w}s & -\frac{w}{2} \leq s < \frac{w}{2} \\ -1 & s < -\frac{w}{2} \end{cases} \tag{III.3}$$

- Regularized discontinuity: $$H_w(s) = \begin{cases} 1 & s \geq \frac{w}{2} \\ \tanh(\frac{4}{w}s) & -\frac{w}{2} \leq s < \frac{w}{2} \\ -1 & s < -\frac{w}{2} \end{cases} \tag{III.4}$$

where $w$ is the characteristic (explicitly indicated) width of the localization band. These functions are qualitatively visualized in a common graph in Fig. III.1. The Heaviside function of the strong discontinuity can be identified as step function across the band, the one of the weak discontinuity as linear function and the one of the regularized discontinuity as tanh nonlinear function, which were originally proposed (in similar formulation) by, respectively, Moës [106], Huespe [74] and Areias [8].

[1] It should be noted that the weak discontinuity is a special type of regularization of the strong discontinuity. However, in this work the class of 'weak discontinuity' is regarded as being different from the class of 'regularized discontinuity' which is referred to as non-linearly distributed (continuous) profile.

[2] Alternative formulations, which can be found in the literature, are functions bounded by 0 and $+1$ or also by $-0.5$ and $+0.5$.

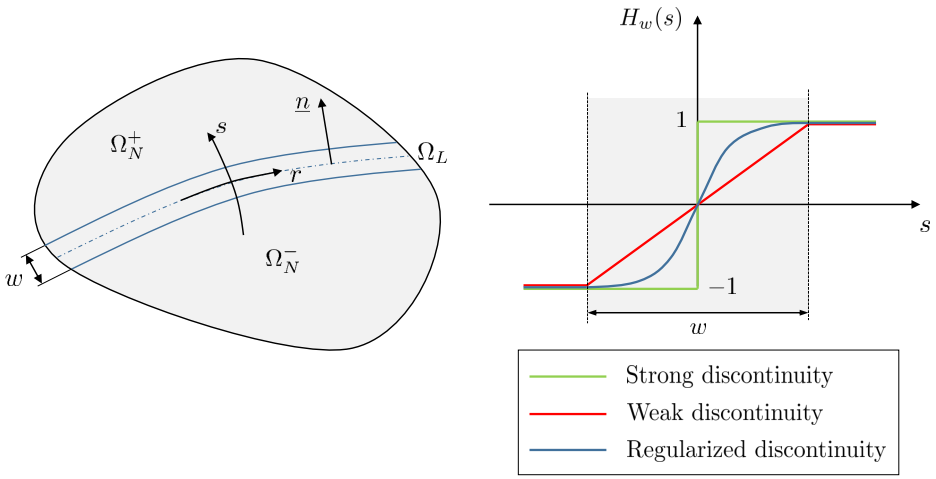


Figure III.1 – Qualitative comparison of the strong, weak and regularized (displacement) discontinuity field

Based on the enriched displacement field, the strain field is computed as follows

$$\varepsilon(x) = \nabla^s u = \nabla^s \hat{u}(x) + H_w(s)\nabla^s \tilde{u} + (\tilde{u}(x) \otimes \nabla H_w(s))^s. \tag{III.5}$$

Using $\nabla H_w(s) = \frac{\partial H_w}{\partial s}\nabla s = \delta_w \underline{n}$, where $\delta_w$ denotes an adapted version of the classical Dirac's delta distribution, yields

$$\varepsilon(x) = \underbrace{\underbrace{\nabla^s \hat{u}(x)}_{\varepsilon_{cont}} + H_w(s)\nabla^s \tilde{u}}_{\varepsilon_{bulk}} + \underbrace{\delta_w(\tilde{u}(x) \otimes \underline{n})^s}_{\varepsilon_{loc}}. \tag{III.6}$$

Here, $\varepsilon_{cont}$ denotes the continuous strain which prevails before the onset of localization, $\varepsilon_{bulk}$ the bulk strain and $\varepsilon_{loc}$ the localization strain, which is large compared to the bulk strain and includes contributions normal and tangential to the band, namely $\varepsilon_{loc} = \delta_w[(\tilde{u}_n \cdot \underline{n}) \otimes \underline{n} + (\tilde{u}_m \otimes \underline{n})^s]$ where the scalar $\tilde{u}_n$ and the vector $\tilde{u}_m$ are parts of the decomposition $\tilde{u} = \tilde{u}_n \cdot \underline{n} + \tilde{u}_m$. This results in different characteristic strain profiles across the localization band, see Fig. III.2, which shows a single bar element submitted to a symmetric displacement, with a constant strain (no discontinuity), and a strong, weak and regularized discontinuity, respectively.

These three conceptually different displacement and resulting strain profiles come from different physical interpretations of the mechanism of strain localization:

- *Strong discontinuity:* The complex micro-mechanisms which take place during strain localization can be assumed to be collapsed into a surface which corresponds to the experimental observation of the presence of a meso-

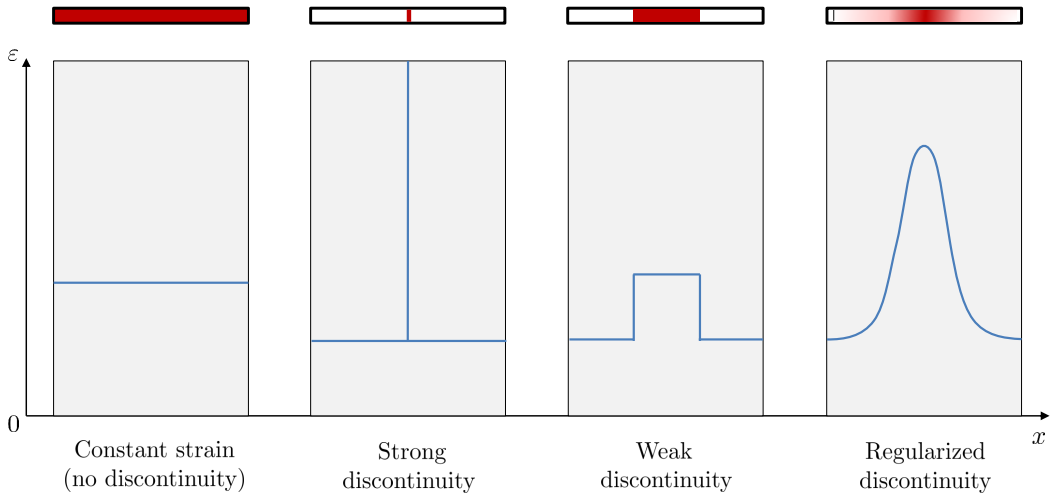


Figure III.2 – Different strain field profiles across the localization band

crack. In contrast to the macro-crack which is also represented by a strong discontinuity, the meso-crack is not continuous along its propagation path as it is interrupted by zones of material cohesion (see the micrograph in Fig. II.3) and it can thus be assumed to still carry stresses. In a similar context, e.g. when it is about to describe the progressive transition from damage to fracture, there are e.g. the works of Dvorkin [52], Moës [105], Oliver [112] and Remmers [136].

- *Weak discontinuity:* Strain localization is shown to go along with void coalescence which occurs in a narrow zone. This band of physically non-zero width accommodates large portions of damage and plastic deformation. Examples from the literature are the works of Belytschko [20], Huespe [74], Ortiz [119] and Sluys [159].

- *Regularized discontinuity:* Considering that strain localization cannot appear in a sharply confined band, the strain field across the band is rather seen in a continuous (smooth) manner. Thus, the strain is highly concentrated in a thin zone and the maximal strain is found in the very center of the band. A similar perception can be found in the modeling of shear bands. Examples from the literature are the works of Abbas [1], Areias [8], Benvenuti [25] and Su [162].

These different viewpoints of the localization band are studied successively in the following. As a means of comparison, an appropriate discretization framework is elaborated, computational issues are discussed and capabilities for describing the transition from continuum mechanics and towards fracture mechanics are assessed.

### III.2.2 Principle of virtual work

Consider the two-dimensional body $\Omega$ in Fig. III.3 which contains a localization band $\Omega_L$. Its orientation is indicated by its normal vector $\underline{n}$. The band divides the domain into two parts $\Omega_N^+$ and $\Omega_N^-$, which form together the continuous domain $\Omega_N$. The interfaces between the localized and non-localized domain are denoted as $\Gamma_D^+$ and $\Gamma_D^-$[3]. External traction forces $\underline{t}^*$ are applied at the boundary $\Gamma_t$. External displacements $\underline{u}^*$ are imposed at the boundary $\Gamma_u$.

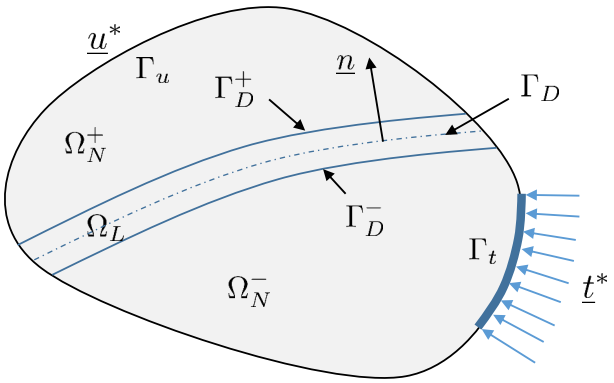


Figure III.3 – 2D domain $\Omega$ crossed by a localization band $\Omega_L$

Assuming quasi-static loading (thus neglecting inertia and body forces), the balance of linear momentum in $\Omega$ can be written by $\nabla \cdot \underset{\sim}{\sigma} = 0$. Furthermore, the traction continuity condition $\underset{\sim}{\sigma} \cdot \underline{n} = \underline{t}$ applies along $\Gamma_D^+$ and $\Gamma_D^-$. Introducing any admissible virtual variation of displacements $\delta u$ and applying the divergence theorem yields the principle of virtual work

$$\int_\Omega \nabla^S(\delta u) : \underset{\sim}{\sigma} \, \mathrm{d}\Omega = \int_{\Gamma_t} \delta u \cdot \underline{t}^* \, \mathrm{d}\Gamma. \tag{III.7}$$

Then, using the Bubnov-Galerkin approach, i.e. the test functions are chosen from the same space as the trial functions, see Eq. (III.1), yields

$$\delta u = \delta \hat{u} + H_w \delta \tilde{u}. \tag{III.8}$$

Note that this equation involves the decomposition of the displacement field into a coarse scale $\delta \hat{u}$ and a fine scale $H_w \delta \tilde{u}$. Thus it can also be understood as a formulation of the variational multi-scale method which was originally developed

[3]The indices 'L', 'N' and 'D' refer to 'Localized', 'Non-localized' and 'Discontinuity', respectively.

by Hughes [77]. The variational strain field derives from the displacement field

$$\nabla^S(\delta u) = \nabla^S(\delta \hat{u}) + H_w \nabla^S(\delta \tilde{u}) + \delta_w(\delta \tilde{u} \otimes \underline{n})^S. \tag{III.9}$$

Later in this chapter, the three methods will be derived from the weak equilibrium equation (III.7) using the variations of the displacement in Eq. (III.8) and strain field in Eq. (III.9) with the corresponding $H_w$ and $\delta_w$ functions.

### III.2.3 Enrichment method considered

Representing the different viewpoints of kinematics of the localization band in the FE requires an appropriate discretization method. The sections II.3.2.2 and II.3.3.2 have evidenced the interest to use the embedded-band FEM to capture a discontinuity - or more generally: an arbitrary displacement profile - in the FE mesh. Therein, two possible enrichment techniques were presented: E-FEM (element enrichment) and X-FEM (node enrichment). Here, the X-FEM is chosen against the E-FEM to incorporate the strong, weak and regularized discontinuity into the element. The choice is based on the following considerations:

- The X-FEM provides a more accurate displacement approximation due to the higher number of enriching dof's.

- As opposed to the X-FEM, the E-FEM is reported to suffer from severe stability and robustness issues under certain conditions (see Jirásek [82], Oliver [115]). Cumbersome workarounds, as the implicit-explicit integration scheme (Oliver [116], Sanchez [147]), have to be applied in order to prevent the numerical simulation from failing.

- The X-FEM has already been successfully applied to ductile materials in the framework of the PhD thesis of Crété [45] - although without considering the phase of strain localization. His methods and his implementation in a user element in Abaqus serve as helpful support for this work.

The displacement and strain fields and their variations are interpolated as follows (using matrix notation from now on)

$$\begin{aligned} \hat{\mathbf{u}} &= \mathbf{N}\mathbf{a} & \delta\hat{\mathbf{u}} &= \mathbf{N}\mathbf{a}' \\ \tilde{\mathbf{u}} &= \mathbf{N}\mathbf{b} & \delta\tilde{\mathbf{u}} &= \mathbf{N}\mathbf{b}' \\ \nabla^{\mathbf{s}}\hat{\mathbf{u}} &= \mathbf{B}\mathbf{a} & \nabla^{\mathbf{s}}(\delta\hat{\mathbf{u}}) &= \mathbf{B}\mathbf{a}' \\ \nabla^{\mathbf{s}}\tilde{\mathbf{u}} &= \mathbf{B}\mathbf{b} & \nabla^{\mathbf{s}}(\delta\tilde{\mathbf{u}}) &= \mathbf{B}\mathbf{b}' \end{aligned} \tag{III.10}$$

The **B**-matrix contains the spatial derivatives of the shape functions **N**, i.e. $\mathbf{B} = \mathbf{LN}$ with **L** being the matrix differential operator

$$\mathbf{L} = \begin{bmatrix} \partial/\partial x & 0 \\ 0 & \partial/\partial y \\ \partial/\partial y & \partial/\partial x \end{bmatrix}. \tag{III.11}$$

As opposed to the examples shown in chapter II, in this chapter the shifted basis formulation $H^*(x) = H(x) - H(x_k)$ will not be used for the sake of simplicity. The displacement field then reads

$$\mathbf{u} = \mathbf{Na} + H_w\mathbf{Nb}, \tag{III.12}$$

where the modified Heaviside function $H_w$ is used according to the characteristic kinematics, i.e. Eqs. (III.2), (III.3) and (III.4). The discretized strain field then is

$$\boldsymbol{\varepsilon} = \mathbf{Ba} + H_w\mathbf{Bb} + (\delta_w\mathbf{n})\mathbf{Nb}. \tag{III.13}$$

## III.2.4 Criteria for the transitions

Here, the common features for the transition criteria, i.e. the passage from diffuse damage to localization and from localization to crack propagation, are briefly presented. The discussion of the detailed transition methods is not the focus of this chapter and is therefore put off to chapter IV.

### III.2.4.1 Diffuse damage to localization

It is assumed in this chapter that, without going into the detail, the criteria for the onset of localization and the orientation of the band are derived from (see the literature review in section II.3.2.3):

- Bifurcation analysis for rate-independent materials
- Linear perturbation method for rate-dependent materials

At the onset of localization the band is inserted into the element and the enriching dof's in the context of the X-FEM are activated.

### III.2.4.2 Localization to crack propagation

Due to the attractiveness of the X-FEM to reproduce the relative opening and sliding of two (meso-crack) surfaces in an element, it is desirable to not only use it

to describe localization but also to represent crack propagation. By maintaining the same formulation, the transition from localization to crack propagation can take place naturally and without modifications. Such a smooth passage demands for finding a criterion which permits to progressively cancel the stresses in the localization band in order to avoid jumps which may cause numerical problems. Then, in the limit case where the stresses in the localization band become zero, the contribution of the localized domain to the global system of equations vanishes and the classical (traction-free) X-FEM is obtained.

## III.3 Method 1: Strong discontinuity

The important damage mechanisms take place on a very small scale compared to the structural dimensions. This method thus consists in a macro-mechanical representation of the degradation process within the localization band with a cohesive surface approach.

### III.3.1 Concept

The damage mechanisms inside the localization band are lumped into a crack-like surface (3D) in front of the crack tip. As the (volumetric) constitutive (stress-strain) law describing the bulk material does not apply anymore, an additional (surfacic) constitutive relation is needed. This idea is realized in cohesive zone models (Barenblatt [15], Dugdale [49], Hillerborg [73]), where a (softening) traction-separation ($t$-$[\![u]\!]$) law is introduced, see Fig. III.4 for the case of a mode-I opening. Thus, the damage-induced softening behavior within the localization band can be reproduced.

Stating that ductile damage is driven by void coalescence in the form of void impingement (favored by hydrostatic tension) and/or localized shearing (favored by a deviator), the propagation of the process of localization involves a cohesive law which accounts for a normal ($[\![u]\!]_n = [\![u]\!] \cdot \underline{n}$) and also a tangential component ($[\![u]\!]_m = [\![u]\!] \cdot \underline{m}$).

The introduced cohesive traction can be interpreted as the ongoing decohesion induced by internal necking of the inter-void material during void coalescence. The opening and sliding of the cohesive 'band' can be thought as an abstraction of the experimentally observed meso-crack, which is not entirely discontinuous in its propagation in contrast to the macro-crack, but exhibits zones of material cohesion, see Fig. II.3. Simultaneously the cohesive law provides for a smooth passage from

diffuse damage to crack propagation.

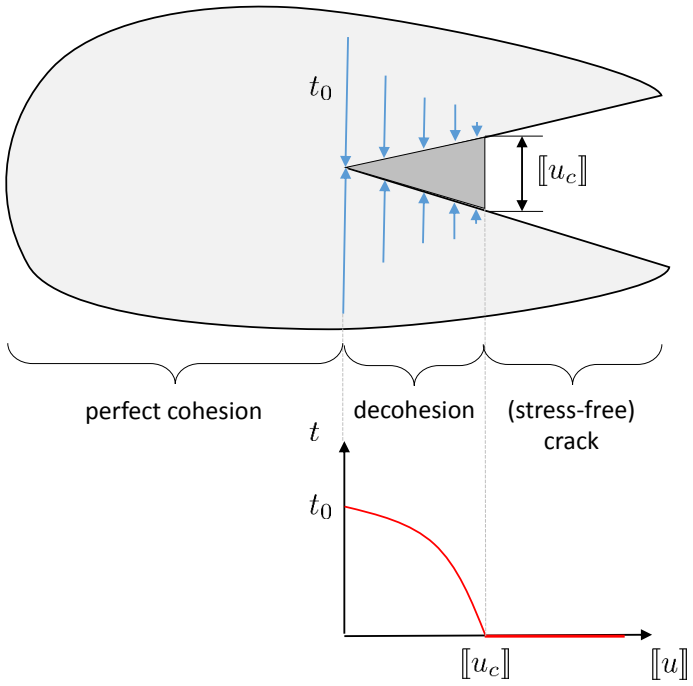


Figure III.4 – Cohesive zone model for mode I

Cohesive cracks have been embedded within the X-FEM e.g. by Moës [105] and Wells [178] in the context of quasi-brittle materials and by Seabra [150] and Simatos [154] for ductile materials. A similar point of view is represented by Samaniego [146] in the context of shear banding.

### III.3.2 Variational and finite element formulations

The elaborations of Wells [178] are used here to derive the variational and finite element formulations.

The kinematic field of a strong discontinuity implies using the following formulations, see also Eq. (III.2)

$$H_w(s) = \begin{cases} 1 & s \geq 0 \\ -1 & s < 0 \end{cases} \quad ; \quad \delta_w(s) = \frac{\partial H_w}{\partial s} = 2\delta_{\Gamma_D} \tag{III.14}$$

where $H_w$ coincides with the classical Heaviside (step) function and $\delta_{\Gamma_D}$ is the Dirac's delta distribution centered at the discontinuity $\Gamma_D$ (see Fig. III.3). The factor 2 in the delta function appears due to the fact that the Heaviside

function is spanned between $-1$ and 1. The Dirac's delta function has for a given continuous function $\Phi$ the following property (a relation which is needed for subsequent derivations)

$$\int_\Omega \Phi(\mathbf{x})\delta(\mathbf{x})\,\mathrm{d}\Omega = \int_{\Gamma_D} \Phi(\mathbf{p})\,\mathrm{d}\Gamma, \tag{III.15}$$

where $\mathbf{p}$ refers to all points along the discontinuity $\Gamma_D$.

Before being able to compute the nodal displacements and strains in a finite element mesh, the following derivations have to be employed. First of all, inserting the variations of the displacement in Eq. (III.8) and strain in Eq. (III.9) into the virtual work in Eq. (III.7) gives

$$\begin{aligned}\int_\Omega \nabla^S(\delta\hat{u}) : \underset{\sim}{\sigma}\,\mathrm{d}\Omega + \int_\Omega H_w \nabla^S(\delta\tilde{u}) : \underset{\sim}{\sigma}\,\mathrm{d}\Omega + \int_\Omega \delta_w(\delta\tilde{u}\otimes\underline{n})^S : \underset{\sim}{\sigma}\,\mathrm{d}\Omega \\ = \int_{\Gamma_t} (\delta\hat{u} + H_w\delta\tilde{u})\cdot\underline{t}^*\,\mathrm{d}\Gamma.\end{aligned} \tag{III.16}$$

Then, exploiting the property of the Dirac's delta in Eq. (III.15) allows to write

$$\int_\Omega \delta_w(\delta\tilde{u}\otimes\underline{n})^S : \underset{\sim}{\sigma}\,\mathrm{d}\Omega = \int_{\Gamma_D} \delta\tilde{u}\cdot\underline{t}\,\mathrm{d}\Gamma, \tag{III.17}$$

where $\underline{t}$ is the (cohesive) traction force along the strong discontinuity surface $\Gamma_D$, see Fig. III.3. As a consequence, the traction force has contributions normal and tangential to the band. Here, the switchover of a continuum (volumetric) stress state $\underset{\sim}{\sigma}$ in the pre-localization formulation to a traction $\underline{t}$ acting on the cohesive surface becomes obvious. By the independency of the variations $\delta\hat{u}$ and $\delta\tilde{u}$, see also Zienkiewicz [189], and using the discretized variations of the displacements and strains in Eq. (III.10), two separate weak equilibrium equations are obtained

$$\int_\Omega \mathbf{B}^T\boldsymbol{\sigma}\,\mathrm{d}\Omega = \int_{\Gamma_t} \mathbf{N}^T\mathbf{t}^*\,\mathrm{d}\Gamma \tag{III.18a}$$

$$\int_\Omega H_w\mathbf{B}^T\boldsymbol{\sigma}\,\mathrm{d}\Omega + 2\int_{\Gamma_D} \mathbf{N}^T\mathbf{t}\,\mathrm{d}\Gamma = \int_{\Gamma_t} H_w\mathbf{N}^T\mathbf{t}^*\,\mathrm{d}\Gamma \tag{III.18b}$$

The first equation constitutes the equilibrium in the continuous field (bulk material). The second equation describes the traction continuity across the discontinuity in a weak sense, where continuity is established between the integral over the entire continuous domain $\Omega_N$, i.e. $\Omega_N^+ \cup \Omega_N^-$, and the integral over the cohesive surface, what is typical of KOS formulations. So the traction continuity appears as a result of the consequent application of the principle of virtual work and is not

imposed as an additional equation. This is in contrast to the SOS ([20], [119]) and SKON formulations ([74], [112]) in the context of the E-FEM, where the traction continuity condition is explicitly imposed at the interface and thus allows for a more accurate stress computation.

To determine the state of equilibrium involving a non-linear material behavior, an incremental-iterative solution procedure is used. Therefore, the stress-strain and traction-jump relationships have to be brought into a rate form. The bulk stress rate is computed using the continuum tangent modulus $\mathbf{D^t}$

$$\dot{\boldsymbol{\sigma}} = \mathbf{D^t}\dot{\varepsilon} = \mathbf{D^t}(\mathbf{B}\dot{\mathbf{a}} + H_w\mathbf{B}\dot{\mathbf{b}}), \tag{III.19}$$

where $\dot{\mathbf{a}}$ and $\dot{\mathbf{b}}$ represent, respectively, the regular and enhanced nodal velocities, see Eq. (III.10). In the same way, the traction rate of the cohesive law reads (in the local coordinate system $\{\mathbf{n}, \mathbf{m}\}$)

$$\dot{\boldsymbol{t}} = \mathbf{T}[\![\dot{\boldsymbol{u}}]\!], \tag{III.20}$$

where $\mathbf{T}$ is the cohesive tangent modulus. A link between the enriching degrees of freedom of the X-FEM and the displacement jump can be made

$$\begin{aligned}
[\![\dot{u}]\!](x) &= \dot{u}(x^+) - \dot{u}(x^-) \\
&= \sum_{i\in I} \dot{u}_i N_i(x^+) + \sum_{j\in J} \dot{b}_j N_j(x^+) H_w(x^+) \\
&- \left( \sum_{i\in I} \dot{u}_i N_i(x^-) + \sum_{j\in J} \dot{b}_j N_j(x^-) H_w(x^-) \right),
\end{aligned} \tag{III.21}$$

where $x$ is an arbitrary point located on the cohesive surface, $x^+$ is the projection of $x$ to the positive face and $x^-$ accordingly to the negative face. Noting that $N_i(x^+) = N_i(x^-) = N_i(x)$ and $H_w(x^+) = -H_w(x^-) = 1$ results in

$$[\![\dot{u}]\!](x) = 2\sum_{j\in J} \dot{b}_j N_j(x). \tag{III.22}$$

Finally, Eqs. (III.19), (III.20) and (III.22) can be inserted into Eq. (III.18) so that the following set of discrete linearized equations involving the incremental displacements d$a$ and d$b$ is obtained

$$\begin{bmatrix} \mathbf{K}_{aa} & \mathbf{K}_{ab} \\ \mathbf{K}_{ba} & \mathbf{K}_{bb} \end{bmatrix} \begin{Bmatrix} \mathrm{d}a \\ \mathrm{d}b \end{Bmatrix} = \begin{Bmatrix} \mathbf{f}_a^{ext} \\ \mathbf{f}_b^{ext} \end{Bmatrix} - \begin{Bmatrix} \mathbf{f}_a^{int} \\ \mathbf{f}_b^{int} \end{Bmatrix}, \tag{III.23}$$

where the stiffness matrix $\mathbf{K}$ is computed as follows

$$\mathbf{K} = \begin{bmatrix} \int_\Omega \mathbf{B}^T \mathbf{D}^\mathbf{t} \mathbf{B} \, \mathrm{d}\Omega & \int_\Omega H_w \mathbf{B}^T \mathbf{D}^\mathbf{t} \mathbf{B} \, \mathrm{d}\Omega \\ \int_\Omega H_w \mathbf{B}^T \mathbf{D}^\mathbf{t} \mathbf{B} \, \mathrm{d}\Omega & \int_\Omega \mathbf{B}^T \mathbf{D}^\mathbf{t} \mathbf{B} \, \mathrm{d}\Omega + 4 \int_{\Gamma_D} \mathbf{N}^T \mathbf{T} \mathbf{N} \, \mathrm{d}\Gamma \end{bmatrix} \tag{III.24}$$

and the internal and external force vectors are calculated from

$$\mathbf{f}_a^{ext} = \int_{\Gamma_t} \mathbf{N}^T \mathbf{t}^* \, \mathrm{d}\Gamma \tag{III.25a}$$

$$\mathbf{f}_b^{ext} = \int_{\Gamma_t} H_w \mathbf{N}^T \mathbf{t}^* \, \mathrm{d}\Gamma \tag{III.25b}$$

$$\mathbf{f}_a^{int} = \int_\Omega \mathbf{B}^T \boldsymbol{\sigma} \, \mathrm{d}\Omega \tag{III.25c}$$

$$\mathbf{f}_b^{int} = \int_\Omega H_w \mathbf{B}^T \boldsymbol{\sigma} \, \mathrm{d}\Omega + 2 \int_{\Gamma_D} \mathbf{N}^T \mathbf{t} \, \mathrm{d}\Gamma. \tag{III.25d}$$

It can be seen that the stiffness matrix is symmetric if the matrices $\mathbf{D}^\mathbf{t}$ and $\mathbf{T}$ are symmetric as well, what is assumed here. A symmetric global stiffness matrix has computational advantages in the solution procedure [178].

### III.3.3 Computational issues

The incorporation of a discontinuity into the element using X-FEM requires the application of special integration techniques to evaluate the integrals at the Gauss points in the continuum bulk. The widely used subtriangulation method of Moës [106] is not adapted to ductile materials for which the history-dependent variables need to be tracked. Thus it is rather advantageous to use the approach of Crété [46] where the 2D element is subdivided into 16 rectangles which are each integrated by the 4-point Gauss rule (64 Gauss points in total), see Fig. III.5. This method is discussed in detail in chapter IV.

The contributions of the cohesive tractions to the elemental equations, that is the line integrals along $\Gamma_D$ in $\mathbf{K}_{bb}$ and $\mathbf{f}_b^{int}$, can be evaluated by using 2 additional (standard) Gauss points, see e.g. Wells [178]. These are positioned along the 1D cohesive segment within the localized element, see Fig. III.5.

According to Wells [178], the convergence rate appears to be optimal and the simulation is very robust, if the cohesive band is introduced at the end of an increment.

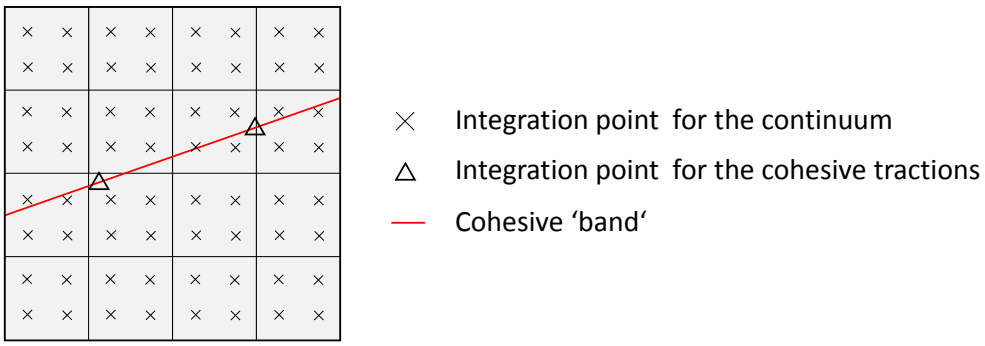


Figure III.5 – Integration scheme for a 2D quadrilateral element cut by a cohesive 'band'

### III.3.4 Coupling ductile damage and localization method

Traditionally, the transition from damage to localization in cohesive zone models is triggered by a stress criterion which involves the critical cohesive traction $t_0$ (prescribed as material parameter), e.g. by checking when the maximum principal tensile stress in the damaged zone attains the critical cohesive traction, see e.g. Wells [178], Remmers [136].

Though, here another indicator for localization is used relying on a stability criterion, see section III.2.4. In this case, the initial cohesive traction $t_0$ (where the cohesive separation initiates, i.e. $[\![u]\!] = 0$) rather corresponds to the current stress state $\underset{\sim}{\sigma}$ at the onset of localization satisfying the traction continuity condition $t_0 = \underset{\sim}{\sigma} \cdot \underline{n}$, see also Bordas [30] and Belytschko [19]. This implies that the initial traction is a quantity which is not a pre-defined material parameter, but results from the current stress state at localization. From that point, the gradient of the cohesive law depends on the chosen function and the work of separation (see next section).

### III.3.5 Coupling localization method and crack formation

Starting from the initial cohesive strength $t_0$, the transition from strain localization to crack propagation is supposed to be determined by the amount of energy per unit surface required to entirely counteract the cohesive traction forces at the meso-crack faces - or in a physical sense: the energy needed to break up all inter-void bonds. The decohesion energy corresponds to the area under the traction-separation law, also called work of separation per unit area $W_c$[4](unit $\frac{Nm}{m^2}$) and can be computed

[4]This energy measure is comparable to the Griffith energy release rate in brittle materials - commonly denoted as $G_f$ or $G_c$ - however here it is used in the context of ductile materials. Therefore, a different notation is used in order to not confound it with the classical fracture

from

$$W_c = \int_0^{[\![u]\!]_c} \underline{t}([\![u]\!])\,\mathrm{d}[\![u]\!]. \tag{III.26}$$

This critical work of separation is reached when the traction force becomes zero and therefore satisfies the crack initiation condition of the progressive loss of the in-band stresses from section III.2.4, see also Fig. III.6.

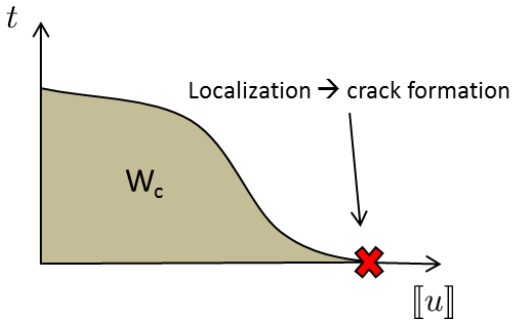


Figure III.6 – Transition from meso-crack to macro-crack

In terms of numerics, the macro-crack phase is described by the X-FEM as well. As soon as the cohesive traction approaches zero the line integrals along $\Gamma_D$ in $\mathbf{K}_{bb}$ and $\mathbf{f}_b^{int}$ cancel out and then the standard X-FEM equations describing a stress-free crack and thus pure crack opening, are naturally obtained

$$\begin{bmatrix} \int_\Omega \mathbf{B}^T\mathbf{D}^{\mathbf{t}}\mathbf{B}\,\mathrm{d}\Omega & \int_\Omega H_w\mathbf{B}^T\mathbf{D}^{\mathbf{t}}\mathbf{B}\,\mathrm{d}\Omega \\ \int_\Omega H_w\mathbf{B}^T\mathbf{D}^{\mathbf{t}}\mathbf{B}\,\mathrm{d}\Omega & \int_\Omega \mathbf{B}^T\mathbf{D}^{\mathbf{t}}\mathbf{B}\,\mathrm{d}\Omega \end{bmatrix} \begin{Bmatrix} \mathrm{d}a \\ \mathrm{d}b \end{Bmatrix} = \begin{Bmatrix} \int_{\Gamma_t} \mathbf{N}^T\mathbf{t}^*\,\mathrm{d}\Gamma \\ \int_{\Gamma_t} H_w\mathbf{N}^T\mathbf{t}^*\,\mathrm{d}\Gamma \end{Bmatrix} - \begin{Bmatrix} \int_\Omega \mathbf{B}^T\boldsymbol{\sigma}\,\mathrm{d}\Omega \\ \int_\Omega H_w\mathbf{B}^T\boldsymbol{\sigma}\,\mathrm{d}\Omega \end{Bmatrix} \tag{III.27}$$

where the stiffness term $4\int_{\Gamma_D}\mathbf{N}^T\mathbf{T}\mathbf{N}\,\mathrm{d}\Gamma$ in Eq. (III.24) and the internal force term $2\int_{\Gamma_D}\mathbf{N}^T\mathbf{t}\,\mathrm{d}\Gamma$ in Eq. (III.25d) have vanished.

## III.4 Method 2: Weak discontinuity

This method is based upon the assumption that the displacement field across the localization zone exhibits a weak discontinuity which confines the localization band.

### III.4.1 Concept

In a perspective which is different from method 1, damage and plastic deformation are assumed to concentrate inside a sharply bounded band of non-zero width. This can be argued by stating that localization goes along with void coalescence which

energy measure.

occurs in a narrow zone. This hypothesis can be corroborated by macroscopic considerations in that the meso-crack typically follows a tortuous path, as can be deduced from the micrograph in Fig. III.7. In the vicinity of the meso-crack, there are voids which have accumulated in the concentration process prior to the propagation of the meso-crack. This roughly bordered zone of high void concentration can be identified as localization band. Experimentally the band width could be quantified as the envelope of the tortuous meso-crack path in a defined volume element (right-most in Fig. III.7).

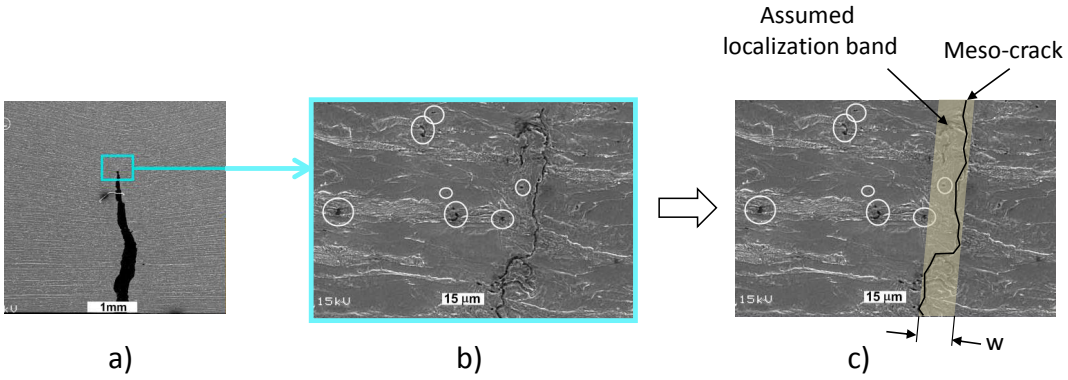


Figure III.7 – Micrograph of a meso-crack in a tensile-loaded structure (DH36): (a) macro-crack, (b) tortuous meso-crack path, (c) definition of a localization band as an envelope of the path (adapted from Geffroy [57])

The presence of a band with a finite thickness implies that the continuum stress state is maintained beyond the onset of localization - as opposed to method 1. Belytschko [20] was the first to embed a localization band into an element. In his method which is in the context of shear band modeling, the enriching dof's are computed from the requirement of stress continuity across the interface (see Fig. II.5 in chapter 2). Considering two adjacent material points, one located in the band, the other slightly outside, the former is further damaged and plastified whereas the latter undergoes elastic loading. Huespe [74] proposed (in the context of the E-FEM) to modify the shape functions of the localized element such that a strain band of finite thickness can be represented. He assumed that the GTN model is applied throughout the entire loading path, i.e. during the pre- and also the post-localization phase, until crack propagation. The initiation of a crack is indicated by a critical porosity which corresponds to the loss of the stress carrying capacity and thus the formation of a new crack surface. The band width remains constant during strain localization and the deformation is assumed to be homogeneous across the band.

In the following, we propose an X-FEM extension of the (slightly modified) E-FEM-based method of Huespe [74]. The main hypotheses are:

1. The pre-localization GTN-model is also used to determine the post-localization stress state in the localization band. Thus, it can be accounted for the hydrostatic stress dependency inside the band.

2. The predefined band width is kept constant throughout the localization process until fracture.

3. The deformations and stresses across the band (in the $\underline{n}$-direction) are homogeneous.

### III.4.2 Variational and finite element formulations

The kinematic fields across the band are characterized using a ramp function and its derivative, see also Eq. (III.3),

$$H_w(s) = \begin{cases} 1 & s \geq \frac{w}{2} \\ \frac{2}{w}s & -\frac{w}{2} \leq s < \frac{w}{2} \\ -1 & s < -\frac{w}{2} \end{cases} \quad ; \quad \delta_w(s) = \frac{\partial H_w}{\partial s} = \begin{cases} 0 & s \geq \frac{w}{2} \\ \frac{2}{w} & -\frac{w}{2} \leq s < \frac{w}{2} \\ 0 & s < -\frac{w}{2} \end{cases} \tag{III.28}$$

For the sake of a better illustration, the virtual work is first of all decomposed into a localized and a non-localized contribution

$$\int_\Omega \nabla^S(\delta u) : \underset{\sim}{\sigma}\, \mathrm{d}\Omega = \int_{\Omega_N} \nabla^S(\delta u) : \underset{\sim}{\sigma}\, \mathrm{d}\Omega + \int_{\Omega_L} \nabla^S(\delta u) : \underset{\sim}{\sigma}\, \mathrm{d}\Omega. \tag{III.29}$$

Based on the second and third hypothesis made at the beginning, the virtual work in the localized domain can be simplified to (Remmers [137])

$$\begin{aligned} \int_{\Omega_L} \nabla^S(\delta u) : \underset{\sim}{\sigma}\, \mathrm{d}\Omega &= \int_{\Gamma_D} \int_{-\frac{w}{2}}^{\frac{w}{2}} \nabla^S(\delta u) : \underset{\sim}{\sigma}\, \mathrm{d}n\, \mathrm{d}\Gamma \\ &= w \cdot \int_{\Gamma_D} \nabla^S(\delta u) : \underset{\sim}{\sigma}\, \mathrm{d}\Gamma. \end{aligned} \tag{III.30}$$

Then, a surface integral along the mean surface of the band is obtained (denoted as $\Gamma_D$ in accordance with Fig. III.3), but - and this is a difference to cohesive models - the material in the band is still regarded as a continuum. Based on the first hypothesis, the stress state in the band continues to behave according to the pre-localization GTN model. Inserting the test functions in Eqs. (III.8) and (III.9)

into the weak form of virtual work yields

$$\begin{aligned}\int_{\Omega_N} \nabla^S(\delta\hat{u}) : \underset{\sim}{\sigma}\, \mathrm{d}\Omega + \int_{\Omega_N} H_w \nabla^S(\delta\tilde{u}) : \underset{\sim}{\sigma}\, \mathrm{d}\Omega + \int_{\Omega_N} \delta_w (\delta\tilde{u} \otimes \underline{n})^S : \underset{\sim}{\sigma}\, \mathrm{d}\Omega \\ + w \cdot \int_{\Gamma_D} \nabla^S(\delta\hat{u}) : \underset{\sim}{\sigma}\, \mathrm{d}\Gamma + w \cdot \int_{\Gamma_D} H_w \nabla^S(\delta\tilde{u}) : \underset{\sim}{\sigma}\, \mathrm{d}\Gamma + w \cdot \int_{\Gamma_D} \delta_w (\delta\tilde{u} \otimes \underline{n})^S : \underset{\sim}{\sigma}\, \mathrm{d}\Gamma \\ = \int_{\Gamma_t} (\delta\hat{u} + H_w \delta\tilde{u}) \cdot \underline{t}^*\, \mathrm{d}\Gamma.\end{aligned} \tag{III.31}$$

Considering that the delta function $\delta_w$ is 0 in $\Omega_N$ and $\frac{2}{w}$ in $\Omega_L$, the third term can be eliminated and the sixth term can be simplified. Also, the ramp function $H_w$ is point symmetric with respect to $\Gamma_D$, so that by using the third hypothesis the fifth term disappears leading to

$$\begin{aligned}\int_{\Omega_N} \nabla^S(\delta\hat{u}) : \underset{\sim}{\sigma}\, \mathrm{d}\Omega + \int_{\Omega_N} H_w \nabla^S(\delta\tilde{u}) : \underset{\sim}{\sigma}\, \mathrm{d}\Omega \\ + w \cdot \int_{\Gamma_D} \nabla^S(\delta\hat{u}) : \underset{\sim}{\sigma}\, \mathrm{d}\Gamma + \cdot \int_{\Gamma_D} 2(\underset{\sim}{\sigma} \cdot \underline{n}) \delta\tilde{u}\, \mathrm{d}\Gamma = \int_{\Gamma_t} (\delta\hat{u} + H_w \delta\tilde{u}) \cdot \underline{t}^*\, \mathrm{d}\Gamma.\end{aligned} \tag{III.32}$$

Now, by the independency of the virtual variations $\delta\hat{u}$ and $\delta\tilde{u}$ and using the discretized variations of the displacements and strains, the discrete weak equilibrium equations read

$$\int_{\Omega_N} \mathbf{B}^T \boldsymbol{\sigma}\, \mathrm{d}\Omega + w \cdot \int_{\Gamma_D} \mathbf{B}^T \boldsymbol{\sigma}\, \mathrm{d}\Gamma = \int_{\Gamma_t} \mathbf{N}^T \mathbf{t}^*\, \mathrm{d}\Gamma \tag{III.33a}$$

$$\int_{\Omega_N} H_w \mathbf{B}^T \boldsymbol{\sigma}\, \mathrm{d}\Omega + 2 \int_{\Gamma_D} \mathbf{N}^T (\boldsymbol{\sigma} \cdot \mathbf{n})\, \mathrm{d}\Gamma = \int_{\Gamma_t} H_w \mathbf{N}^T \mathbf{t}^*\, \mathrm{d}\Gamma \tag{III.33b}$$

In direct comparison to Eq. (III.18) of method 1 two observations can be made: (i) in the first equation, a second volume integral appears which results from the band continuum and (ii) the second equation has the same appearance, but now the tractions are evaluated from the continuum stress in the band which is obtained from the GTN constitutive law. The stresses inside and outside the band are calculated from (hypothesis 1)

$$\dot{\boldsymbol{\sigma}}|_{\Omega_L} = \mathbf{D}^{\mathbf{t}} \dot{\boldsymbol{\varepsilon}}|_{\Omega_L} = \mathbf{D}^{\mathbf{t}} (\mathbf{B}\dot{\mathbf{a}} + H_w \mathbf{B}\dot{\mathbf{b}} + (\delta_w \mathbf{n}) \mathbf{N}\dot{\mathbf{b}}) \tag{III.34a}$$

$$\dot{\boldsymbol{\sigma}}|_{\Omega_N} = \mathbf{D}^{\mathbf{t}} \dot{\boldsymbol{\varepsilon}}|_{\Omega_N} = \mathbf{D}^{\mathbf{t}} (\mathbf{B}\dot{\mathbf{a}} + H_w \mathbf{B}\dot{\mathbf{b}}). \tag{III.34b}$$

Inserting Eq. (III.34) into Eq. (III.33) gives the discrete linearized equations in the same form as Eq. (III.23). The components of the symmetric global stiffness

matrix are computed as follows

$$\mathbf{K_{aa}} = \int_{\Omega_N} \mathbf{B}^T \mathbf{D^t} \mathbf{B} \, \mathrm{d}\Omega + w \cdot \int_{\Gamma_D} \mathbf{B}^T \mathbf{D^t} \mathbf{B} \, \mathrm{d}\Gamma \tag{III.35a}$$

$$\mathbf{K_{ab}} = \int_{\Omega_N} H_w \mathbf{B}^T \mathbf{D^t} \mathbf{B} \, \mathrm{d}\Omega + 2 \cdot \int_{\Gamma_D} \mathbf{B}^T \mathbf{D^t} \overline{\mathbf{N}} \, \mathrm{d}\Gamma \tag{III.35b}$$

$$\mathbf{K_{ba}} = \int_{\Omega_N} H_w \mathbf{B}^T \mathbf{D^t} \mathbf{B} \, \mathrm{d}\Omega + 2 \cdot \int_{\Gamma_D} \overline{\mathbf{N}}^T \mathbf{D^t} \mathbf{B} \, \mathrm{d}\Gamma \tag{III.35c}$$

$$\mathbf{K_{bb}} = \int_{\Omega_N} \mathbf{B}^T \mathbf{D^t} \mathbf{B} \, \mathrm{d}\Omega + 2 \cdot \int_{\Gamma_D} \delta_w \overline{\mathbf{N}}^T \mathbf{D^t} \overline{\mathbf{N}} \, \mathrm{d}\Gamma \tag{III.35d}$$

where $\overline{\mathbf{N}}$ is the operator such that [25]

$$\overline{\mathbf{N}}\mathbf{a} = (\mathbf{N}\mathbf{a} \otimes \mathbf{n})^S. \tag{III.36}$$

The internal and external force vectors are calculated from

$$\mathbf{f}_a^{ext} = \int_{\Gamma_t} \mathbf{N}^T \mathbf{t}^* \, \mathrm{d}\Gamma \tag{III.37a}$$

$$\mathbf{f}_b^{ext} = \int_{\Gamma_t} H_w \mathbf{N}^T \mathbf{t}^* \, \mathrm{d}\Gamma \tag{III.37b}$$

$$\mathbf{f}_a^{int} = \int_{\Omega_N} \mathbf{B}^T \boldsymbol{\sigma} \, \mathrm{d}\Omega + w \cdot \int_{\Gamma_D} \mathbf{B}^T \boldsymbol{\sigma} \, \mathrm{d}\Gamma \tag{III.37c}$$

$$\mathbf{f}_b^{int} = \int_{\Omega_N} H_w \mathbf{B}^T \boldsymbol{\sigma} \, \mathrm{d}\Omega + 2 \int_{\Gamma_D} \mathbf{N}^T (\boldsymbol{\sigma} \cdot \mathbf{n}) \, \mathrm{d}\Gamma. \tag{III.37d}$$

It can be shown that in the limit case, i.e. when $w$ goes to zero, the formulation is equivalent to a cohesive zone approach. Consider the virtual work in the band which can be transformed into terms involving surface integrals along the boundary of the band by using the divergence theorem

$$\int_{\Omega_L} \nabla^S(\delta u) : \underset{\sim}{\sigma} \, \mathrm{d}\Omega = \int_{\Gamma_D^+} \underbrace{\underset{\sim}{\sigma} \cdot \underline{n}}_{\underline{t}_{\Gamma_D}} \cdot \delta u \, \mathrm{d}\Gamma + \int_{\Gamma_D^-} \underbrace{\underset{\sim}{\sigma} \cdot (-\underline{n})}_{-\underline{t}_{\Gamma_D}} \cdot \delta u \, \mathrm{d}\Gamma, \tag{III.38}$$

where the contributions of the surface integrals along the band edges can be neglected as $w$ goes to zero. Then, using the jump variable $\delta[\![u]\!] = \delta u_{\Gamma_D^+} - \delta u_{\Gamma_D^-}$ and taking hypothesis 3 (implying that $\underline{t}_{\Gamma_D^+} = \underline{t}_{\Gamma_D^-}$), yields

$$\lim_{w \to 0} \int_{\Omega_L} \nabla^S(\delta u) : \underset{\sim}{\sigma} \, \mathrm{d}\Omega = \int_{\Gamma_D} \underline{t}_{\Gamma_D} \cdot \delta[\![u]\!] \, \mathrm{d}\Gamma. \tag{III.39}$$

This relation corresponds to the virtual work of cohesive tractions in the 'band discontinuity' $\Gamma_D$, which are induced by stresses in the band. Thus, the approach can be understood in the context of the cohesive band approach.

### III.4.3 Computational issues

The integration of the continuum terms can be employed in the same way as described in method 1, i.e. by using 64 fixed integration points. The integration of the terms concerning the localized band requires some additional reflections. Regarding the simplification made in Eq. (III.30), the integral over the localization band $\int_{\Omega_L}$ could be transformed into a surface integral over $\Gamma_D$ by still maintaining the continuum character of the localized material. This step allows to apply 1D-integration with 2 Gauss points along $\Gamma_D$, see Fig. III.8, and prevents from using any non-standard 2D-integration scheme adapted to the oriented localization band in the element.

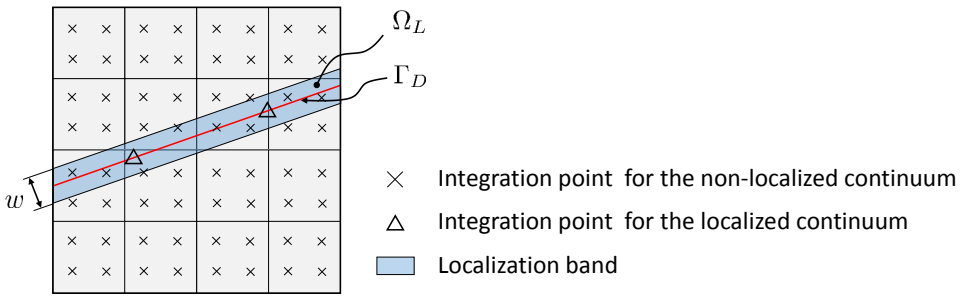


Figure III.8 – Integration scheme for a 2D quadrilateral element cut by a localization band

### III.4.4 Coupling ductile damage and localization method

As soon as localization in an element is detected, i.e. satisfying the loss of stability conditions, the localization band is introduced into the element formulation. As the inner-band material behavior is dictated by the (pre-localization) GTN model, no additional constitutive parameters need to be evaluated. The transition from the homogeneous to the inhomogeneous material is inherently involved in setting up the X-FEM equations and computing the standard and enriching dof's in the localized element such that equilibrium is obtained.

### III.4.5 Coupling localization method and crack formation

The crack is formed when the stresses in the band drop to zero and thus a stress-free crack can evolve, a condition which was defined in section III.2.4. In this case here, motivated by the argumentation in section II.3.3.3, two different criteria are proposed: using either (i) a critical porosity value or (ii) a critical energy measure,

comparable to the energy release rate used in the first method.

The first fracture criterion is widely used for Gurson-type materials, see e.g. [57], [174], [74]. The classical Gurson model [66] also involves a critical failure porosity, however does not yield realistic results [174]. Instead, Tvergaard [174] proposed an alternative failure criterion by replacing the porosity $f$ in the yield condition in Eq. (II.2) by a modified (effective) porosity which accounts for the accelerating effects of the void coalescence when $f \geq f_c$, see Fig. III.9. The material loses its stress-carrying capacity completely when the failure porosity $f_f$ is attained:

$$f^* = \begin{cases} f & f < f_c \\ f_c + K(f - f_c) & f \geq f_c \text{ with } K = \frac{f_u - f_c}{f_f - f_c};\ f_u = \frac{1}{q_1} \end{cases} \tag{III.40}$$

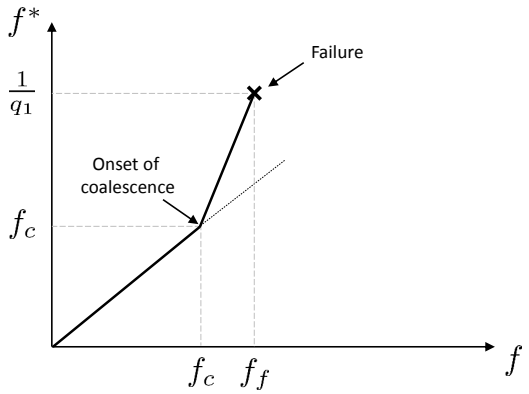


Figure III.9 – Porosity law accounting for the accelerating effects of void coalescence, proposed by Tvergaard [174]

As already noted in section II.3.3.3.1, the porosity, which is defined macroscopically in the context of a homogeneous material, is used to conclude on microscopic processes in front of the crack tip, what is not that realistic. For ductile materials, an energy-based criterion is used frequently, e.g. the energy release rate in Lemaitre-type damage mechanics models [129]. An energy-based criterion is thus proposed here which can be thought as an adaptation of the crack growth criterion which was originally proposed by Crété [46] and applied within a ductile failure model where the stage of localization was neglected. The author supposes that below a critical value of the stored energy the material is capable of accommodating plastic deformation and void-induced damage. As soon as this value is attained, a crack is necessarily formed as the only mechanism which allows for an increasing deformation.

In this present context, the stored energy criterion can be applied similarly, however it is not evaluated in a crack-tip half-circle patch, as employed by Crété, but it is calculated inside the spatially confined localization band, see Fig. III.10. Then, the stored energy is obtained from

$$W_{band} = \frac{\sum_{i=1}^{p} \omega_s^i A^i}{\sum_{i=1}^{p} A^i} \tag{III.41}$$

where $p$ represents the number of localized elements (within a defined meso-crack propagation length), $\omega_s$ is the stored plastic energy, see Eq. (II.36), averaged over the two Gauss points of the elemental band segment and $A_i$ is the area of the localization band in the element, i.e. $A_i = w \cdot l_b$, where $l_b$ denotes the length of the elemental band segment. The crack is propagating with the length $l_c$ when $W_{band} \geq W_c$.

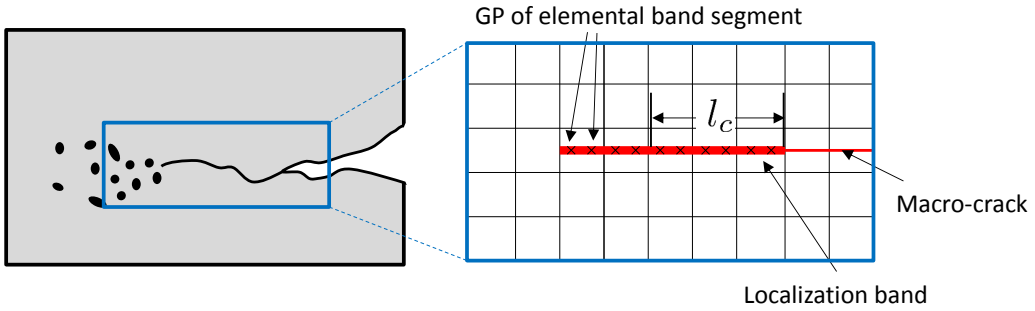


Figure III.10 – Stored energy criterion evaluated in the localization band in the defined propagation length $l_c$

However, this criterion does not provide the cancellation of the stresses so as to initiate the transition to the (stress-free crack) X-FEM. A pragmatic solution would then be to enforce the in-band stresses to zero as soon as the critical stored energy is attained what results in a sudden drop of load in the global response.

Although the loss of stress carrying capacity needs to be enforced in the second criterion, this one seems to be the preferred criterion which is used for further considerations. Then, as soon as the critical stored energy is attained, the in-band stresses are enforced to zero and thus the surface integrals along $\Gamma_D$ become zero as well leading finally to the standard X-FEM equations, see Eq. (III.27). This goes along with the opening of a new crack surface. Hence, the transition from the localization band representation to the formation of a crack is naturally obtained.

# III.5 Method 3: Regularized discontinuity

In this third method the displacement field across the localization zone is viewed as a diffuse discontinuity so that the displacement remains continuous until fracture.

## III.5.1 Concept

Here, the strains and damage are assumed to concentrate in a narrow zone. The difference to the previous method consists in that a large strain gradient prevails inside the band, with a highly localized strain peak along its center line. This idea is borrowed from the kinematic manifestation of shear bands, which can be experienced in ductile materials under highly dynamic load cases, see e.g. the test results of Roux and Longère [143] in Fig. III.11. Therein, the findings on the evolution of the shear strain across the process zone foster the idea to model the localization in a regularized (smoothed) sense, especially with regard to a prospective extension of the present work to dynamic load cases.

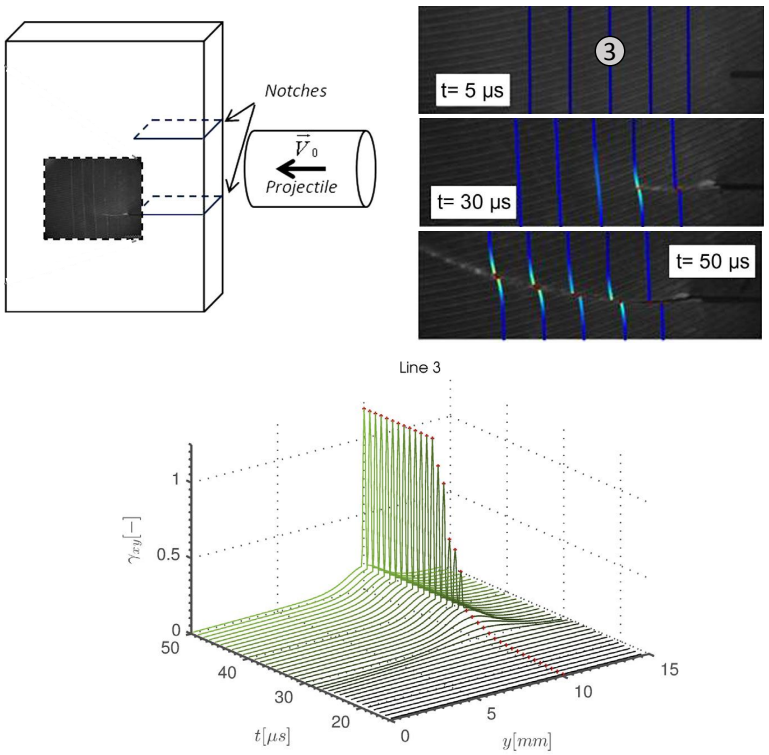


Figure III.11 – Digital image analysis during a Kalthoff and Winkler impact test [87] of a high strength steel using the line tracking method: time evolution of the shear strain along the middle line (indicated as line 3) (adapted from Roux [143])

Using the concept of the regularized discontinuity, three questions arise:

1. Which function to describe the displacement profile across the band?
2. Whether and how to define the border of the localization band?
3. Does the regularization band width remain fixed throughout localization or is it evolving?

1.) Different regularization functions can be applied. In the context of the X-FEM, Patzák [124] and Abbas [1] used a series of polynomial functions with a high gradient across the band. Benvenuti [25] proposed an exponential function to pass progressively from a continuous to a discontinuous model. In analyzing ductile materials, Areias [8], [9], Su [162] and also Roux [143] resort to a tanh-function. Here, such a tanh-based function is used due to its relevance in the context of ductile materials[5].

2.) The chosen tanh-function is $C^\infty$-continuous. In order to limit its infinite extension to a defined band width and to embed the band with a regularized strain field into the element, the function 'tail' is cut off beyond the band borders resulting in a small, artificial kink at that interface. This error is a function of the band width $w$ and of the chosen function (value at $s = \mathrm{w}/2$). The error is accepted here provided that the function is constructed such that the error is small, see Fig. III.12.

3.) At the onset of localization, an initial width is presumed. From that point, there are principally two possible approaches: (i) either the regularization width remains constant until fracture (Areias [8], [9], Huespe [74]) or (ii) the length scale gradually decreases to zero (Benvenuti [24], [25], Oliver [113]). Here, the first approach of using a constant width is used, the reasons for that choice will be explained later when discussing the transition to fracture.

Based on these considerations, the following hypotheses are suggested:

1. The GTN model is used for the pre- and post-localization response in the band, see also method 2.
2. The prescribed band width $w$ remains constant until crack formation.
3. The regularization function is cut off beyond the band borders.

[5]In literature, there are tanh-regularization functions which involve either two parameters serving to adjust the displacement gradient and the length scale, e.g. Areias [8], Benvenuti [25] or only a length scale, e.g. Patzák [124], Abbas [1], where the gradient is indirectly controlled. Here, it is preferred to control the localization width directly, so that only the second group of tanh-functions is used.

### III.5.2 Variational and finite element formulations

A tanh-based enrichment function is used which permits to control the band width, see Fig. III.12. Compared to similar functions used in the literature, e.g. Areias [8] and Roux [143], the function is adapted such that the error at the interface band/bulk, i.e. at $s = \pm w/2$, is kept small, see Fig. III.12. The regularized Heaviside and Dirac's delta distribution are then as follows

$$H_w(s) = \begin{cases} 1 & s \geq \frac{w}{2} \\ \tanh(\frac{4}{w}s) & -\frac{w}{2} \leq s < \frac{w}{2} \\ -1 & s < -\frac{w}{2} \end{cases} \quad ; \quad \delta_w(s) = \begin{cases} 0 & s \geq \frac{w}{2} \\ \frac{4}{w}[1 - \tanh^2(\frac{4}{w}s)] & -\frac{w}{2} \leq s < \frac{w}{2} \\ 0 & s < -\frac{w}{2} \end{cases} \tag{III.42}$$

what is obviously a regularized/smoothed version of the weakly discontinuous formulation (method 2). Here, both ends of the functions are cut off at the interface to the bulk, where $H_w(\frac{w}{2}) \approx 0.964$ and $H_w(-\frac{w}{2}) \approx -0.964$.

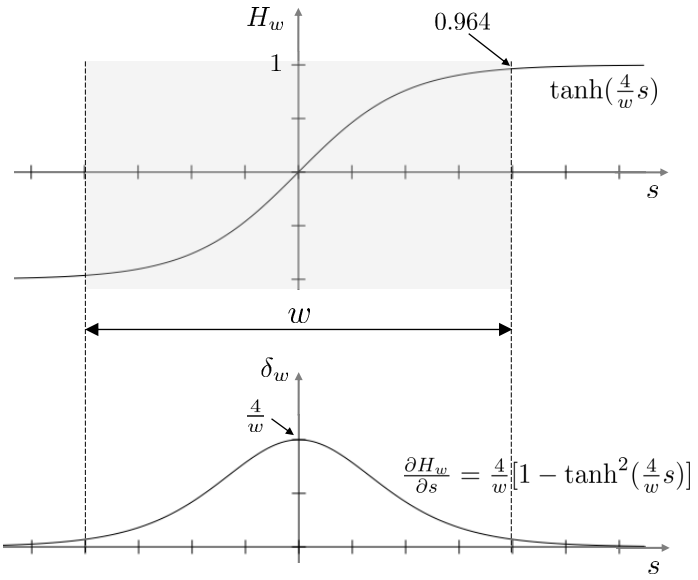


Figure III.12 – Profile of the chosen tanh-function and its derivative

Inserting the variations of displacement in Eq. (III.8) and strain in Eq. (III.9) into the equation of virtual work gives

$$\begin{aligned} \int_{\Omega_N} \nabla^S(\delta\hat{u}) : \underset{\sim}{\sigma}\, \mathrm{d}\Omega + \int_{\Omega_N} H_w \nabla^S(\delta\tilde{u}) : \underset{\sim}{\sigma}\, \mathrm{d}\Omega \\ + \int_{\Omega_L} \nabla^S(\delta\hat{u}) : \underset{\sim}{\sigma}\, \mathrm{d}\Omega + \int_{\Omega_L} H_w \nabla^S(\delta\tilde{u}) : \underset{\sim}{\sigma}\, \mathrm{d}\Omega + \int_{\Omega_L} \delta_w (\delta\tilde{u} \otimes \underline{n})^S : \underset{\sim}{\sigma}\, \mathrm{d}\Omega \\ = \int_{\Gamma_t} (\delta\hat{u} + H_w \delta\tilde{u}) \cdot \underline{t}^*\, \mathrm{d}\Gamma \end{aligned} \tag{III.43}$$

where the simplifications of the previous method do not apply here due to the non-linearity (inhomogeneity) of the stress and strain field across the band. In the same context, hypotheses have been proposed e.g. by Benvenuti [25] who assumed that the bulk strain and localized strain (which are components of the total strain, see the decomposition employed in Eq. (III.6)), and their conjugate stress fields, are mechanically uncoupled mechanisms. However, this hypothesis has been made by pure mathematical motivations, but the relation to physics remains questionable. Furthermore, it is proposed in the context of elasto-damaging materials, but no analysis has been made so far for ductile materials.

Considering that the virtual variations $\delta\hat{u}$ and $\delta\tilde{u}$ are independent and using FE discretization, the two discrete weak equilibrium equations can be written as follows

$$\int_{\Omega_N} \mathbf{B}^T\boldsymbol{\sigma}\,\mathrm{d}\Omega + \int_{\Omega_L} \mathbf{B}^T\boldsymbol{\sigma}\,\mathrm{d}\Omega = \int_{\Gamma_t} \mathbf{N}^T\mathbf{t}^*\,\mathrm{d}\Gamma \tag{III.44a}$$

$$\begin{aligned}&\int_{\Omega_N} H_w\mathbf{B}^T\boldsymbol{\sigma}\,\mathrm{d}\Omega + \int_{\Omega_L} H_w\mathbf{B}^T\boldsymbol{\sigma}\,\mathrm{d}\Omega + \int_{\Omega_L} \delta_w\overline{\mathbf{N}}^T\boldsymbol{\sigma}\,\mathrm{d}\Omega\\ =&\int_{\Gamma_t} H_w\mathbf{N}^T\mathbf{t}^*\,\mathrm{d}\Gamma.\end{aligned} \tag{III.44b}$$

Since the same constitutive assumptions as in method 2, see Eq. (III.34), are used here, the components of the discrete linearized system of equations finally read

$$\mathbf{K_{aa}} = \int_{\Omega_N} \mathbf{B}^T\mathbf{D^t}\mathbf{B}\,\mathrm{d}\Omega + \int_{\Omega_L} \mathbf{B}^T\mathbf{D^t}\mathbf{B}\,\mathrm{d}\Omega \tag{III.45a}$$

$$\mathbf{K_{ab}} = \int_{\Omega_N} H_w\mathbf{B}^T\mathbf{D^t}\mathbf{B}\,\mathrm{d}\Omega + \int_{\Omega_L} H_w\mathbf{B}^T\mathbf{D^t}\mathbf{B}\,\mathrm{d}\Omega + \int_{\Omega_L} \delta_w\mathbf{B}^T\mathbf{D^t}\overline{\mathbf{N}}\,\mathrm{d}\Omega \tag{III.45b}$$

$$\mathbf{K_{ba}} = \int_{\Omega_N} H_w\mathbf{B}^T\mathbf{D^t}\mathbf{B}\,\mathrm{d}\Omega + \int_{\Omega_L} H_w\mathbf{B}^T\mathbf{D^t}\mathbf{B}\,\mathrm{d}\Omega + \int_{\Omega_L} \delta_w\mathbf{B}^T\mathbf{D^t}\overline{\mathbf{N}}\,\mathrm{d}\Omega \tag{III.45c}$$

$$\begin{aligned}\mathbf{K_{bb}} = &\int_{\Omega_N} \mathbf{B}^T\mathbf{D^t}\mathbf{B}\,\mathrm{d}\Omega + \int_{\Omega_L} H_w^2\mathbf{B}^T\mathbf{D^t}\mathbf{B}\,\mathrm{d}\Omega + \int_{\Omega_L} H_w\delta_w\mathbf{B}^T\mathbf{D^t}\overline{\mathbf{N}}\,\mathrm{d}\Omega +\\ &\int_{\Omega_L} \delta_w H_w\overline{\mathbf{N}}^T\mathbf{D^t}\mathbf{B}\,\mathrm{d}\Omega + \int_{\Omega_L} \delta_w^2\overline{\mathbf{N}}^T\mathbf{D^t}\overline{\mathbf{N}}\,\mathrm{d}\Omega.\end{aligned} \tag{III.45d}$$

The internal and external force vectors are calculated from

$$\mathbf{f}_a^{ext} = \int_{\Gamma_t} \mathbf{N}^T\mathbf{t}^*\,\mathrm{d}\Gamma \tag{III.46a}$$

$$\mathbf{f}_b^{ext} = \int_{\Gamma_t} H_w\mathbf{N}^T\mathbf{t}^*\,\mathrm{d}\Gamma \tag{III.46b}$$

$$\mathbf{f}_a^{int} = \int_{\Omega_N} \mathbf{B}^T\boldsymbol{\sigma}\,\mathrm{d}\Omega + \int_{\Omega_L} \mathbf{B}^T\boldsymbol{\sigma}\,\mathrm{d}\Omega \tag{III.46c}$$

$$\mathbf{f}_b^{int} = \int_{\Omega_N} H_w \mathbf{B}^T \boldsymbol{\sigma} \, \mathrm{d}\Omega + \int_{\Omega_L} H_w \mathbf{B}^T \boldsymbol{\sigma} \, \mathrm{d}\Omega + \int_{\Omega_L} \delta_w \overline{\mathbf{N}}^T \boldsymbol{\sigma} \, \mathrm{d}\Omega. \tag{III.46d}$$

It can be noticed that - compared to methods 1 and 2 - there are more expressions involved and some of them contain the non-linear terms $H_w$, $H_w^2$, $H_w\delta_w$, $\delta_w$ and $\delta_w^2$. These terms provoke numerical challenges as will be seen later. It is interesting to note that the enriching dof's are evaluated at the nodes of the element and the regularized displacement profile in the element is obtained by an interpolation using the regularized tanh-function.

### III.5.3 Computational issues

In order to accurately integrate the standard X-FEM terms, where discontinuous enrichments are involved, the element is normally subdivided, see section III.3.3. As continuous enrichments are used in this method, such techniques are not necessarily required. However, in order to properly capture the high strain gradient in the localization band (consider the presence of the strongly non-linear enrichment function $H_w$ in the components of the stiffness matrix in Eq. (III.45) and the force vectors in Eq. (III.46)), many integration points have to be used for an accurate evaluation.

Benvenuti [25] extends an approach of Ventura [176] where the functions $H_w$, $H_w^2$ and $\delta_w$ are replaced by equivalent polynomial functions such that a standard (low-order) Gauss-rule can be employed. Although it gives an exact integration result, the equivalent polynomials depend on the enrichment and the element type. In the paper of Benvenuti [25], polynomials are calculated for an exponential Heaviside function, but for a tanh-function as in this case the associated polynomials have to be recalculated what can be cumbersome.

Instead, Areias [8] has proposed to capture the concentrated deformation by introducing additional Gauss points across the localization area of width $\rho$, see Fig. III.13a. The weights of the integration points are obtained from area calculations. Another method was developed by Abbas [1], where the element is subdivided with respect to the highest gradient in the band, see Fig. III.13b.

All these methods require however a mapping of the history-dependent variables from the initial Gauss points to the points in the adapted scheme. Here it remains to analyze if it is not more efficient under certain conditions to use the fixed 64-Gauss-points rule which may already provide a sufficient number of integration points.

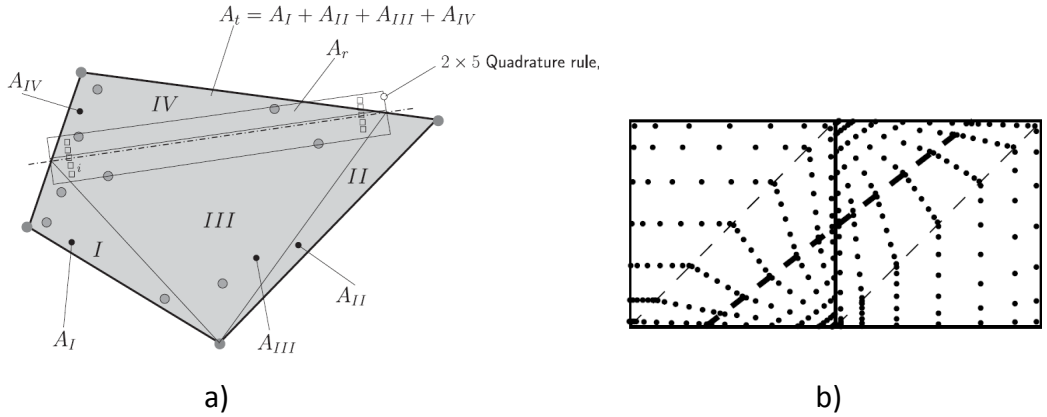


Figure III.13 – Integration schemes for regularized kinematics: a) technique of Areias [8], b) technique of Abbas [1]

## III.5.4 Coupling ductile damage and localization method

In the same manner as in method 2, the X-FEM with the regularized enrichment function is activated at the onset of localization which is triggered by the bifurcation analysis or linear perturbation method. Thereby, the displacement and strain fields remain continuous. The regularization parameter is a predefined material parameter and needs to be determined from microscopic or experimental considerations. In the context of adiabatic shear banding as a result of impact loading, an idea of the length scale can be given by the recognized Grady equation [60] which is derived from the minimization of the dissipated energy as a function of the shear band width. In the present work, quasi-static loading is assumed, so that this consideration serves for prospective extensions of the model.

## III.5.5 Coupling localization method and crack formation

Here, the point of crack initiation is determined in the same way as described in method 2, i.e. by using a stored energy criterion which is evaluated over several elements which contain the localization band. This condition and the enforcement of the loss of stress carrying capacity in the band are appropriate to this method 3 and the hypotheses considered[6].

[6]For the sake of completeness, a different approach is mentioned here which consists in progressively reducing the initial regularization parameter to zero. In the limit case, a zero-width band emerges and either a cohesive-zone model is obtained or fracture occurs directly. When the band width approaches to zero, the regularized Dirac's delta converges to the classical Dirac's delta evoking prohibitively large stresses and strains in the band. In order to avoid the unboundedness of stresses in the limit case, Simo [157], Oliver [112], Benvenuti [25] and others proposed to rather make the localized stress independent of the Dirac's delta distribution by modifying the constitutive law accordingly. For simple elasto-plastic materials the softening

## III.6 Assessment, discussion and decision for a final method

The three methods having been described one after the other, they will now be assessed and mutually compared with the aim to choose the most efficient approach. In order to make a well-grounded decision, different evaluation aspects are accounted for, namely the model hypotheses, the numerical implementation and the performance with regard to further setting up a unified failure model. The most suitable approach will accordingly be described in detail in chapter IV.

To facilitate readability, the abbreviations SDM, WDM and RDM will be used to refer to, respectively, strong, weak and regularized discontinuity method.

### III.6.1 Regarding the physics of the model hypotheses

This section discusses the question to which extent the considered model hypotheses are in agreement with physics.

In reality, strain localization can be understood as being formed in a band of non-zero width accommodating ongoing plastic deformation and damage. This is however in contradiction with the hypothesis of a zero-width length made by the SDM. But then, the introduction of cohesive tractions describing the degradation in the post-localization regime corresponds well to the experimental observation that the meso-crack does not entirely traverse the material, but exhibits areas of material cohesion. In the WDM and RDM, using the GTN model as the Gurson model corresponds quite well to the softening response in the post-localization response.

---

modulus $h$ is regularized as follows

$$\bar{h} = \delta_w^{-1} h, \tag{III.47}$$

so that by pure mathematical investigation, the Dirac's delta cancels out in the localized stress equation. However, such procedures are only found in the context of elasto-plastic or elasto-damaging materials, but for strongly non-linear ductile models, such considerations have to the author's knowledge not been employed. In the present work the distinct plasticity (exponential hardening law) smoothes the stresses which can thus not reach unbounded values. Also, in the GTN model the softening response depends not only on a single softening modulus, but on several variables so that defining a regularized softening modulus does not suffice. Different evolution laws for the band width have been proposed. Oliver [113] assumed that the band width evolves according to a simple empirical law. A decreasing law for the process zone width in concrete is given in Benvenuti [24], where the regularization parameter is made a function of the damage variable.

After all, it remains - till this day - difficult if not impossible to quantify these micro-mechanisms during strain localization in experiments and thus to draw conclusions for physical modeling. This is mainly due to a lack of high spatial resolution of the experimental devices at this micro-scale (the development of micro-tomography is yet expected to palliate this deficiency, see [100], [99], [132]) and because the crack propagates with a high velocity throughout the structure. This is probably one of the reasons why there is still no consensus on how to model strain localization in ductile materials.

In the post-localization regime the three methods are capable of describing the consequences of ductile damage induced by void growth and coalescence and ductile failure driven by distinct shearing. In the SDM this is provided by setting up a cohesive law which includes a normal and shear component, whereas in the WDM and RDM it is implied by the retained GTN constitutive model which involves the hydrostatic and deviatoric stresses as well as an additional porosity law taking into account the accelerating effects of void coalescence. In the case of the SDM, it would be also possible to implement a more specific triaxiality-dependent cohesive law, see e.g. Anvari [6], Banerjee [13] and Siegmund [153].

Moreover based on the theoretical framework of the three methods, they can be later extended to model shear banding which arises during dynamic loading - in the SDM by splitting the cohesive law into a normal and a tangential component and in the WDM and RDM by describing a localization band with a finite thickness thus corresponding to the physical appearance of the shear band.

### III.6.2 Regarding the computational issues

First of all it can be stated that the three localization methods introduce a length scale which serves as localization limiter and thus prevents the post-localization solution from severe mesh dependence. In the WDM and the RDM, the length scale obviously corresponds to the band width $w$. In the SDM, such a length scale does not appear in its inherent formulation. Yet, we propose here an effective length scale (which does not depend anymore of the mesh size) derived from the traction-separation relation

$$l_c^{eff} = \frac{W_c}{t_0}. \tag{III.48}$$

Therein, $l_c^{eff}$ can be interpreted as the effective band width of the cohesive zone which is produced when the energy $W_c$ is put into the localized cohesive band where the traction $t_0$ prevails along its interfaces to the bulk. In the case of a linear

softening law this would be $l_c^{eff} = \frac{1}{2}[\![u]\!]_{max}$ where $[\![u]\!]_{max}$ is the maximum cohesive zone separation.

Mesh dependence studies have been conducted with similar models by Wells [178] for the SDM, Huespe [74], [75] for the WDM and Areias [8], [9] for the RDM.

Concerning the numerical integration, the SDM and WDM make use of a 64-point Gauss rule to integrate the terms related to the bulk material and a 2-point Gauss rule to evaluate the line integrals of either the cohesive segment (SDM) or the band which is numerically reduced to a line (WDM). In the RDM, the numerical integration has turned out to be more difficult in so far as it is important to properly capture the high strain gradient. When the band width is chosen too small with respect to the element size, the regularized discontinuity profile cannot be properly captured by the 64 Gauss point rule. Then, specific integration schemes, as discussed in section III.5.3, have to be applied demanding for cumbersome projection techniques of the history variables.

### III.6.3 Regarding the further unified failure approach

Here the ability of the method to be incorporated into the numerical failure model involving ductile damage and crack propagation is discussed. A proper transition from the pre-localization phase of diffuse damage using standard FEM to the onset of strain localization and the straightforward passage from localization to crack propagation have to be ensured.

At the onset of localization, the enriching dof's of the X-FEM are activated in all three methods. In the SDM the initial traction force of the cohesive law in the localized element has to be determined so as to get a smooth transition. In the WDM and RDM there is no need to compute additional values as the Gurson model is furthermore used.

The transition to fracture is realized in the three methods as soon as the in-band stresses or tractions become zero. Then, for the SDM, WDM and RDM it could be shown that the equations for stress-free (standard) X-FEM are naturally obtained. In order to fulfill this condition, different energy-based approaches have been assumed - while other criteria could have been used as well. They consist in computing an energy value from the in-band stress state and compare it to a critical value, which can be thought as the maximal capacity of the material to accommodate plastic deformation and void-growth induced damage. In the SDM

the traction becomes zero when the area under the traction-separation function attains a critical fracture energy $W_c$. An energy-based criterion has also been proposed for the WDM and RDM, although the attainment of the critical value does not necessarily correspond to a vanishing stress in the localization band so that this needs to be enforced to zero and thus may result in a non-physical jump in the response.

### III.6.4 Summary and decision for the localization method

The assets and weak points of the three methods are summarized in table III.1 below according to the expressed hypotheses. Therein, the SDM clearly stands out compared to the other two methods. The SDM appears to be the most adapted method in the context of the simulation of large structures where the macromechanical consequences of localization are of great interest. Also its simplicity in terms of numerical aspects has fostered the opinion to use the cohesive zone model to describe the strain localization phase.

Combining the advantages of the presented methods, it may be possible to use the WDM or RDM after the onset of localization and to switch to the SDM at a later stage of localization. However an advanced approach raises additional questions, e.g. when to pass from WDM or RDM to SDM or how to reduce the band width towards a zero-width cohesive band? Such considerations are set aside for later research works.

Table III.1 – Assets ($\oplus$) and weak points ($\ominus$) of the strong, weak and regularized discontinuity

| Strong discontinuity | Weak discontinuity | Regularized discontinuity |
|---|---|---|
| $\oplus$ Complex micro-mechanisms collapsed into surface<br>$\oplus$ Only 1 additional parameter ($W_c$)<br>$\oplus$ Reduced mesh dependence (length scale $\frac{W_c}{t_0}$)<br>$\oplus$ Straightforward integration scheme<br>$\oplus$ Energy-based failure criterion adapted to ductile materials<br>$\oplus$ Allows for describing shear banding | $\oplus$ Reduced mesh dependence (length scale $w$)<br>$\oplus$ Straightforward integration scheme<br>$\oplus$ Post-localization behavior accounts for stress triaxiality<br>$\oplus$ Energy-based failure criterion adapted to ductile materials<br>$\oplus$ Allows for describing shear banding | $\oplus$ Reduced mesh dependence (length scale $w$)<br>$\oplus$ Post-localization behavior accounts for stress triaxiality<br>$\oplus$ Energy-based failure criterion adapted to ductile materials<br>$\oplus$ Allows for describing shear banding |
| $\ominus$ Technique to calculate initial traction $t_0$ from stress state at localization required | $\ominus$ 2 additional parameters ($w$, $W_c$)<br>$\ominus$ Failure criterion does not satisfy condition of vanishing stress | $\ominus$ 2 additional parameters ($w$, $W_c$)<br>$\ominus$ Failure criterion does not satisfy condition of vanishing stress<br>$\ominus$ Integration scheme involving variable projection necessary if band width much smaller than element size |

# III.7 Conclusion

In this chapter, three embedded-band FE approaches have been elaborated and studied from different viewpoints. Based on a profound discussion, the strong discontinuity approach using a cohesive band model has been chosen as the preferred method to describe the strain localization phase considered in this study, namely an interspersed meso-crack. The band of strain localization is accordingly represented by its median plane and its resistance in tension and shear via a cohesive law which ensures the stress continuity and the material degradation in the post-localization regime. Finally, the failure scheme from chapter 2 can be completed, see Fig. III.14.

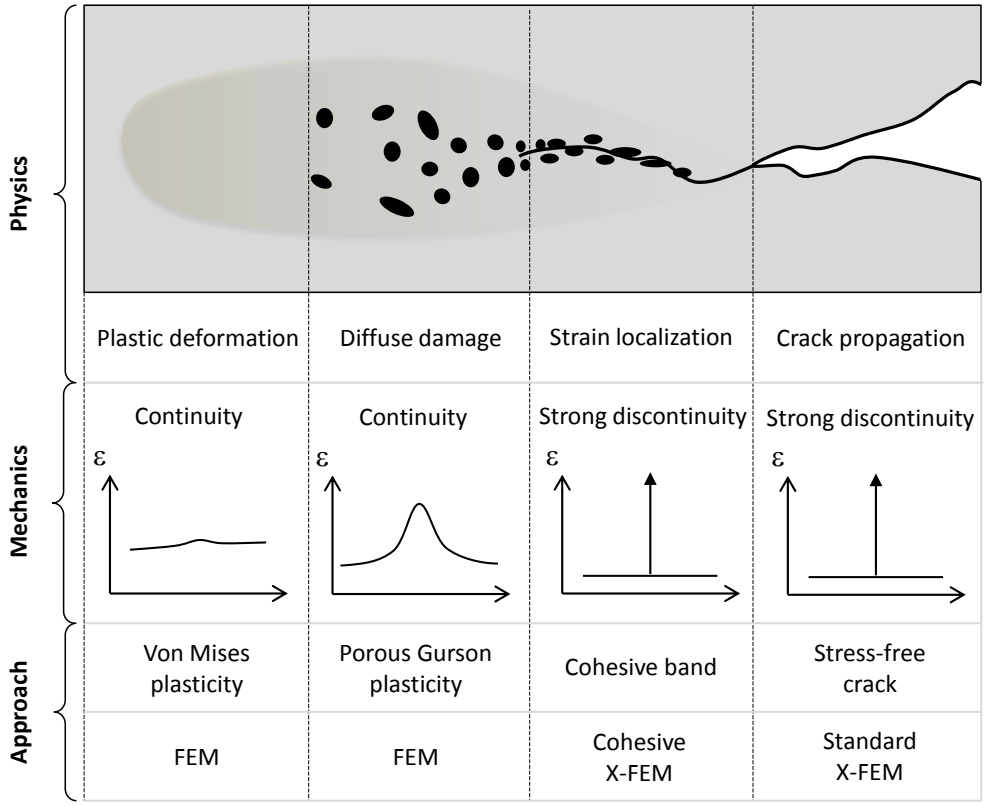


Figure III.14 – Final failure process scheme taking into account the applied approach for modeling the strain localization

# Chapter IV

# Modeling of strain localization using cohesive X-FEM

## Contents of chapter IV

# IV.1 Introduction

In this chapter a unified, physics-motivated model is proposed aiming at reproducing the successive phases of plasticity-diffuse damage, strain localization and then crack propagation. The method which has been chosen among those outlined in the previous chapter will thus be developed in detail. Thereby, the particular interest is on the application of the concept of the cohesive band model within the X-FE formulation. According to the analysis conducted in Chapter III, this combination appears indeed to be the most promising to bring together physics and numerics.

The scenario considered here is as follows, see Fig. IV.1:

1. Continuous plasticity and diffuse damage are dealt with using FEM.
2. Strongly discontinuous cracking is dealt with using X-FEM.
3. The intermediate stage (between (1) and (2)) of the strain localization considered here (meso-crack) is assumed to involve a cohesive strong discontinuity (as for a latent crack) and is accordingly dealt with using cohesive X-FEM.
4. The transition from diffuse damage (1) to strain localization (3) is assumed to result from a material bifurcation/instability.
5. The passage from strain localization (latent crack) (3) to (true) crack formation (2) is triggered by a critical work of cohesion.

# IV.2 Preliminary considerations

The main concepts are outlined in the following subsections.

## IV.2.1 Justification of using a cohesive zone model

An efficient method to model the void coalescence-induced damage accumulation band in front of the crack tip, previously introduced as the meso-crack, see Figs. II.3 and III.7, is the cohesive zone model. However, instead of describing the damage mechanisms during strain localization from a microscopic point of view, the (macroscopic) static consequences of strain softening are rather described in a phenomenological way. The degradation process during strain localization is assumed to be lumped into a sufficiently thin cohesive band. Indeed, the cohesive zone allows for a gradual transition between the onset of localization and the formation of a macro-crack. Here two different viewpoints are proposed of how to understand the physical strain localization in the context of cohesive zone modeling:

1. The first perspective is illustrated in Fig. IV.1. The meso-crack which can be observed in experiments, exhibits a very small opening which can be considered nearly constant along its propagation path, as can be concluded from the micrograph in Fig. II.3. In order to transfer this observation into a cohesive model with a progressively decreasing traction toward the macro-crack, the blunt crack-front (the first millimeters of the macro-crack) is understood as part of the meso-crack and its opening is smoothed out all over the extent of the meso-crack.

2. The second perspective is shown schematically in Fig. IV.2. This interpretation has also been used as justification in the previous chapter. Herein, the increasing effect of void coalescence, i.e. the internal necking of the inter-voids bulk material, leads to a decreasing resistance of the material. Finally, the stress carrying capacity of the material is completely lost locally and a crack can form.

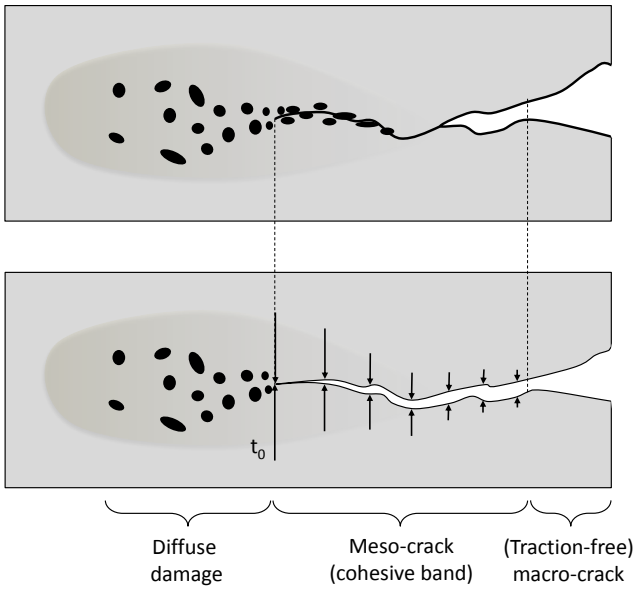


Figure IV.1 – Visualization of the first cohesive zone concept: (top) Ductile fracture model (Fig. II.1), (bottom) Introduction of cohesive tractions

In the following, the second view is adopted due to the fact that it better reflects the idea of a damage-induced strain localization which results from void coalescence.

## IV.2.2 Cohesive zone models

Cohesive models were originally proposed by Barenblatt [14], [15] and Dugdale [49] and further extended by Hillerborg [73]. Applications to ductile materials which

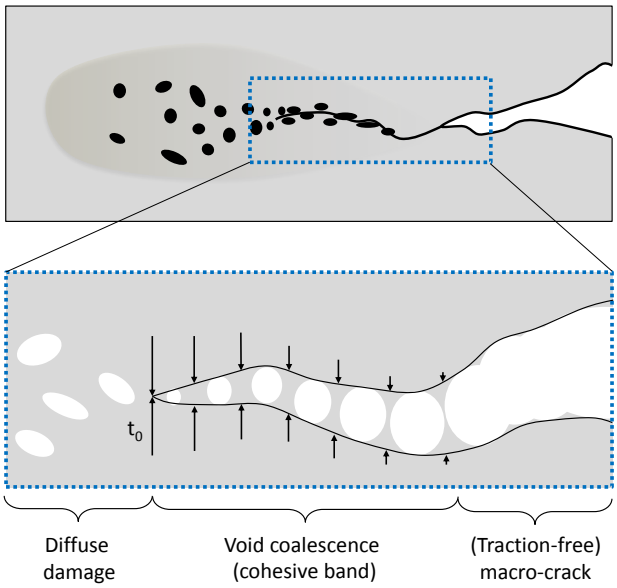


Figure IV.2 – Visualization of the second cohesive zone concept: (top) Ductile fracture model (Fig. II.1), (bottom) Introduction of cohesive tractions corresponding to the void coalescence-induced strain localization

fail from void nucleation, growth and coalescence were proposed e.g. by Needleman [110] and Siegmund [153].

Cohesive models are characterized by two constitutive relations: the classical stress-strain-relation (volumetric) describing the bulk material that remains continuous and an additional cohesive law which relates the traction force $t$ to the displacement jump $[\![u]\!]$ between the cohesive band faces, see Fig. IV.3 (explained in detail further below). The cohesive law is defined by the cohesive strength $t_0$, the decohesion energy per unit area $W_c$ and its shape.

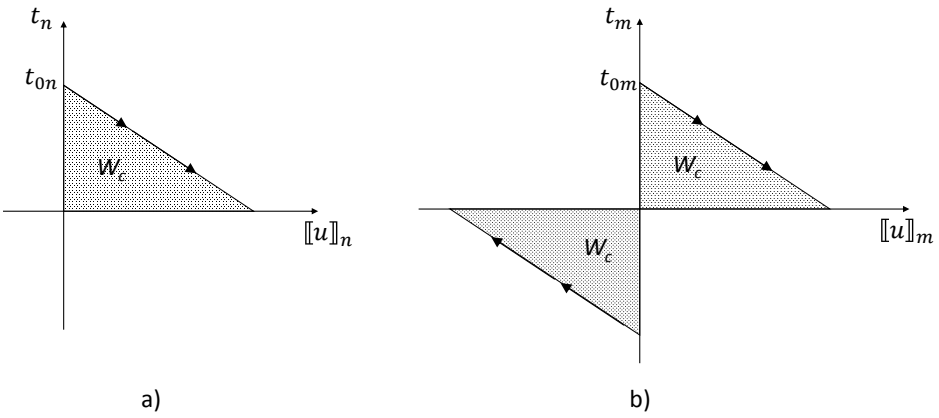


Figure IV.3 – Applied linear softening cohesive laws in the a) normal and b) tangential direction

The initiation of the progressive material separation (within the X-FEM) is usually triggered when the maximum tensile stress attains the maximum cohesive traction $t_0$. In this work, however, decohesion is assumed to initiate when a stability criterion deduced from bifurcation analysis is satisfied. In such a case, the initial cohesive strength is no longer a material parameter but rather results from the current stress state at the onset of localization so as to provide a smooth transition. Thus the activation of the cohesive band is naturally provided by the material model and accounts for the loading path.

After the onset of localization, the behavior in the cohesive band is determined from the traction-separation law. Here, the question arises whether its shape has an influence on the simulation results and which shape is the most adapted for the applied type of material. Many research works have been published so far on these questions, see e.g. Tvergaard [173], Scheider [149], Volokh [177], Alfano [4], Guinea [64], Chen [40] and Tardif [164]. There is no clear consensus on the importance of the shape of the cohesive function, but usually it is considered to be of minor relevance for the post-localization response. So using a linear or exponential law may be judged as being similar with regard to the global response of the structure. Based on these findings, **a linear softening law is adopted here** due to its simplicity and its frequent use in the context of ductile materials ([173], [93], [65]).

The unloading behavior is not particularly treated here as the applications considered in this work refer mostly to monotonically increasing loading path.

A key ingredient of the cohesive law is the fracture energy/work of separation $W_c$ which corresponds to the dissipated energy which is necessary to create a new unit stress-free crack. In the context of ductile materials it can be interpreted as the energy per unit area dissipated to make grow and coalesce voids and plastically deform the inter-void matrix in the localization band until crack formation. It is comparable to the fracture energy per unit area (critical energy release rate) used in linear elastic fracture mechanics, denoted as $G_f$. The fracture energy determines the crack opening/sliding $[\![u]\!]_c$ at the moment of crack formation. Here it is assumed that a crack is formed when the stress in the cohesive band vanishes completely, i.e. the cohesive law can be written in a general form

$$t = t_0 - \frac{t_0^2}{2W_c}[\![u]\!], \tag{IV.1}$$

where the slope of the cohesive law is $-t_0^2/(2W_c)$.

The work of separation is an important material parameter and thus it is of major interest to carefully determine its value. Three possible approaches have been identified from literature to determine the fracture energy in ductile materials:

1. *Identification of constants by experiments vs simulations comparison (inverse analysis)*, see e.g. Chen [41] and Seabra [150]. The analysis can be supported by digital image correlation, see e.g. Shen [151].

2. *FE-assisted micromechanical analysis*: Scheider [148] reports that the parameters and the shape of the cohesive law can also be found on a micromechanical basis using a RVE in a multi-scale analysis, see also Zeng [186]. Such an approach is interesting as it can be directly applied to a Gurson-based material model.

3. *Energy transfer/conservation/equivalence from damage to fracture*, originally proposed by Mazars [102], is based on thermodynamic considerations in the context of a Lemaitre-type damage model. The idea is to transform a damaged zone into an energetically equivalent crack, i.e. $\int_\Omega -Y\dot{D}\mathrm{d}\Omega = -W_c\dot{A}$, where $Y$ is the damage energy release rate (partial derivative of the free energy with respect to the damage variable $D$), $A$ is the area of the crack. Thus the work of separation can be directly deduced from the damage model, see also Cazes [36], [37] and Seabra [150].

It has been shown experimentally that in ductile materials the work of separation strongly depends on the triaxiality, see e.g. the works of Siegmund [152], [153] and Tvergaard [172]. The aforementioned authors have developed cohesive models which take into account the triaxiality in the vicinity of the crack tip. Keeping that dependence in mind, it is from now on assumed that the work of separation is determined at a given triaxiality.

It is well known that ductile damage is driven by void growth (favored by hydrostatic tension) and the ultimate stage of damage occurs in the form of void coalescence (favored by both hydrostatic tension and deviator). Therefore the propagation of the process of localization involves a cohesive law which accounts for a normal and also a (in-plane) shear component, i.e.

$$t = t_n\underline{n} + t_m\underline{m}, \tag{IV.2}$$

where $\underline{n}$ and $\underline{m}$ denote, respectively, the normal and tangential vector of the cohesive band, see Fig. IV.4.

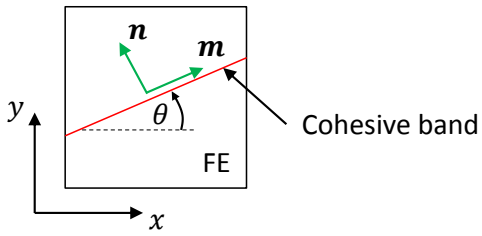


Figure IV.4 – Global and local coordinate systems of the cohesive band within the FE

Fig. IV.5 shows a post-mortem tension specimen made of ductile material. It can be seen that the opening Mode I is predominant in the specimen width whereas the shearing Mode II is predominant in the thickness. While numerically simulating such a tension test assuming 2D conditions for e.g. assessing the performance of a new development (of a constitutive model, of a numerical methodology, etc.), plane stress hypothesis (small thickness, as for the left picture of Fig. IV.5) is expected to activate Mode I crack propagation, and plane strain hypothesis (large thickness, as for the right picture of Fig. IV.5) is expected to activate Mode II crack propagation.

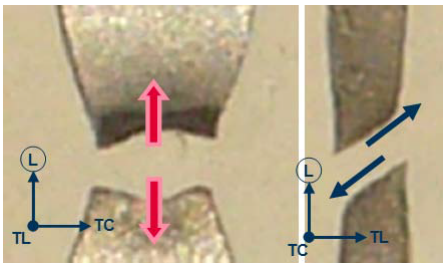


Figure IV.5 – Rupture of a ductile plate during a uni-axial tensile test: (left) rupture in the predominant opening mode in the plate width and (right) rupture in the predominant shear mode in the plate thickness [57]

Under the 2D-plane strain condition assumed in the present work (thick plate, corresponding to the right picture of Fig. IV.5), the cohesive band is supposed to cross the plate entirely in its thickness (i.e. the width of the tension specimen in Fig. IV.5). In order to be able to describe both effects of hydrostatic tension and shear on void coalescence (in the form of void impingement and localized shearing), the cohesive law has to take into account tension and shear components, see Fig. IV.3. The cohesive law considered here is expressed as

$$t_m = t_{0m} - \text{sign}(t_{0m}) \frac{t_{0m}^2}{2W_c} |[\![u]\!]_m| \tag{IV.3}$$

$$t_n = t_{0n} - \frac{t_{0n}^2}{2W_c} [\![u]\!]_n, \tag{IV.4}$$

where it is tentatively assumed that the work of separation per unit area $W_c$ is the same in normal and shear. The maximum tractions $t_{0n}$ and $t_{0m}$ are evaluated at the onset of localization from the current stress state. In the first equation the absolute value of the tangential displacement jump is used in order to model cohesive tractions in both directions of shearing. This is also reflected in Fig. IV.3 by two functions: one in the positive and one in the negative separation domain.

### IV.2.3 The extended finite element method

The principles of the classical X-FEM have already been outlined in the precedent chapters. Here, the focus is on the X-FEM formulation which is used within this chapter.

In the case of a strongly non-linear elasto-plastic ductile material, as it is the case in this work, the singular terms in the enhanced displacement formulation can be neglected, see also the considerations of Crété [45] and in the Appendix E.1 on this topic. The shifted basis formulation is applied here, originally proposed by Zi [188]. By using the shifted basis formulation, the enrichment term vanishes at the nodes and thus avoids the cumbersome use of blending elements (transition elements between the enriched elements and the standard finite elements) leading to an optimal convergence rate. Therefore only the elements containing the cohesive band are enriched and the adjacent elements are not influenced by the enrichment at all. As a consequence, the total number of enriched elements is reduced. A second advantage is that the total displacement at the nodes corresponds to the physical displacement, i.e. $u(x_i) = a_i$ what simplifies the post-processing of the displacement values. Also the displacement boundary conditions can be directly applied to the nodes. In the shifted basis approach, the Heaviside function at the nodes $H_j$ is taken into account and thus only the cut elements are enriched

$$u(x) = \sum_{i \in I} N_i(x) a_i + \sum_{j \in J} \left( H(x) - H_j \right) N_j(x) b_j. \tag{IV.5}$$

The enrichment function $H$ is calculated from the level set function $\phi$ which captures the crack trajectory and needs to be updated when the crack propagates, see Appendix E.2 for more details. The cut elements are integrated using a 64 fixed Gauss points scheme which is better adapted to strongly non-linear ductile materials, see [53], [45] and the Appendix E.3 for more information.

# IV.3 Combining cohesive models and X-FEM

The X-FEM is considered here as the more suitable method to model the cohesive band in the FE mesh. In contrast to other approaches, as e.g. the commonly used inter-element methods applied in the context of the delamination of composite materials, see e.g. Camanho [34] and Turon [167], and in the context of ductile materials, see e.g. Xu [182] and Camacho [33] (refer to the literature review in section II.3.3.1), the X-FEM does not require the a priori knowledge of the crack path on the one hand and extra cohesive elements along this crack path on the other hand. In another context, it does not need expensive remeshing. Indeed, the X-FEM, by enriching the finite element formulation, allows for incorporating the cohesive crack into the mesh independently of the mesh topology[1]. The cohesive band is inserted right at the onset of decohesion so that the problem of assigning a large stiffness to the cohesive zone from the very beginning of the simulation is avoided.

## IV.3.1 Illustration of the principle using a 1D example

The implementation of the cohesive law in X-FEM can be well explained by means of a simple 1D bar loaded in (quasi-static) tension. For the sake of simplicity, the units will be omitted in this section. Consider the model in Fig. IV.6a with an elastic material behavior. A cohesive localization band is introduced in the element center as soon as the monotonically increasing displacement at node 2 exceeds the arbitrarily chosen value $\bar{u}_2 = 0.3$. The material in the cohesive band is characterized by a linear softening traction-separation law, see Fig. IV.6b. Two Gauss points (local coordinates $\xi_1 = -1/\sqrt{3}$ and $\xi_2 = 1/\sqrt{3}$, weights $w_1 = 1$, $w_2 = 1$) are used to integrate the equilibrium equations.

Using the shifted basis formulation of the X-FEM, the displacement field is interpolated as follows

$$u(x) = \sum_{i=1}^{2} N_i(x) a_i + \sum_{j=1}^{2} (H(x) - H_j) N_j(x) b_j, \tag{IV.6}$$

where the shape functions in local coordinates $\xi$ (varying between the values $-1$ and 1) are

$$\mathbf{N}(\xi) = 0.5 \begin{bmatrix} 1-\xi & 1+\xi \end{bmatrix}. \tag{IV.7}$$

[1]There exist other numerical methods to employ the cohesive zone concept into the FE mesh. A boundary element formulation was used by Cen [39] and Saleh [145] to model cohesive crack growth. Meshless techniques as e.g. the Element-free Galerkin method were applied by Belytschko [22].

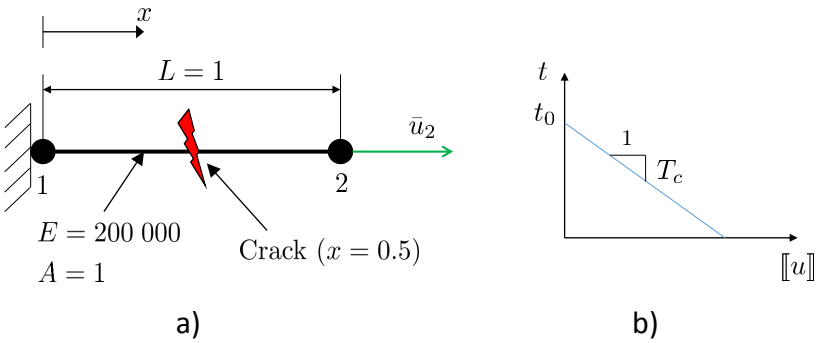


Figure IV.6 – a) 1D model of a bar with a localization in the center, b) Linear traction-separation law

The deformation at each Gauss point (GP) of the bar is computed using the B-matrix $\mathbf{B}$ and the enriched displacements $\mathbf{u}$. In global coordinates, the B-matrix is generally computed from:

$$\mathbf{B}(x) = \frac{1}{\det \mathbf{J}} \left[ \frac{\partial N_1}{\partial \xi} \quad \frac{\partial N_1}{\partial \xi}(H(x) - H_1) \quad \frac{\partial N_2}{\partial \xi} \quad \frac{\partial N_2}{\partial \xi}(H(x) - H_2) \right] \tag{IV.8}$$

where $\mathbf{J}$ is the Jacobian matrix characterizing the transformation of the variables from the local to the global coordinates; its determinant is accordingly $\det \mathbf{J} = 0.5$. The derivatives of the shape functions at the two Gauss points are $\frac{\partial N_1}{\partial \xi} = 0.5$ and $\frac{\partial N_2}{\partial \xi} = -0.5$ (independent of the position).

Now, the bar is loaded until the cohesive band is activated at $\bar{u}_2$. Until then, the enriching dof's $b_1$ and $b_2$ are zero. In the following, the internal forces in the bar are calculated at the onset of localization. First of all, the strain field is computed at the two Gauss points $x_1$ and $x_2$

$$\varepsilon(x_1) = \mathbf{B}(x_1)\mathbf{u} = \begin{bmatrix} -1 & 0 & 1 & -2 \end{bmatrix} \begin{pmatrix} a_1 = 0 \\ b_1 = 0 \\ a_2 = 0.3 \\ b_2 = 0 \end{pmatrix} = 0.3 \tag{IV.9}$$

$$\varepsilon(x_2) = \mathbf{B}(x_2)\mathbf{u} = \begin{bmatrix} -1 & -2 & 1 & 0 \end{bmatrix} \begin{pmatrix} a_1 = 0 \\ b_1 = 0 \\ a_2 = 0.3 \\ b_2 = 0 \end{pmatrix} = 0.3 \tag{IV.10}$$

Then, the stresses are

$$\sigma(x_1) = E\varepsilon(x_1) = 60000 \tag{IV.11}$$

$$\sigma(x_2) = E\varepsilon(x_2) = 60000 \tag{IV.12}$$

The internal force vector reads

$$f^{int} = \int_{\Omega^e} \mathbf{B}^T \sigma \mathrm{d}\Omega \approx \sum_{i=1}^{2} w_i \cdot A \cdot \det \mathbf{J} \cdot \mathbf{B}^T(x_i) \cdot \sigma(x_i) \tag{IV.13}$$

$$= 1 \text{ x } 1 \text{ x } 0.5 \text{ x } \begin{bmatrix} -1 \\ 0 \\ 1 \\ -2 \end{bmatrix} \text{ x } 60000 + 1 \text{ x } 1 \text{ x } 0.5 \text{ x } \begin{bmatrix} -1 \\ -2 \\ 1 \\ 0 \end{bmatrix} \text{ x } 60000 \tag{IV.14}$$

$$= \begin{bmatrix} -60000 \\ -30000 \\ 60000 \\ -30000 \end{bmatrix} \tag{IV.15}$$

Visualizing these internal forces acting at the two bar nodes (Fig. IV.7) reveals that the system is not in equilibrium due to the force contributions induced by the enriching dof's.

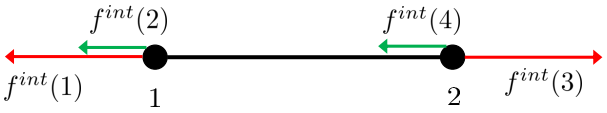


Figure IV.7 – Internal forces at the onset of localization

Considering first of all the standard X-FEM, where the crack is assumed to be traction-free, this equilibrium is obtained by calculating the enriching dof's $b_1$ and $b_2$ such that these two components are zero. As both components $f^{int}(2)$ and $f^{int}(4)$ point into the 'negative' direction, the enriching dof's would need to be positive in order to provoke a positive counteracting force, i.e. $b_1 = b_2 = \frac{1}{2}[\![u]\!] = 0.15$ (obtained by solving the equation system $\mathbf{K}\Delta\mathbf{u} = -\mathbf{f}^{int}$). After some manipulation, this enriched displacement vector then leads, to

$$\sigma(x_1) = E \cdot \begin{bmatrix} -1 & 0 & 1 & -2 \end{bmatrix} \begin{pmatrix} 0 \\ 0.15 \\ 0.3 \\ 0.15 \end{pmatrix} = 0 = \sigma(x_2). \tag{IV.16}$$

Thus the enriching dof's imply a force such that the entire bar is stress-free. These additional forces result in a sudden crack opening of $[\![u]\!] = 0.3$.

The second possibility to obtain the equilibrium in the bar without changing

the enriching dof's (aiming at crack closure at the onset of localization) is to impose cohesive forces which are associated to the enriching dof's and are oriented such that they oppose the unbalanced internal forces in Fig. IV.7, i.e.

$$\begin{bmatrix} -60000 \\ -30000 \\ 60000 \\ -30000 \end{bmatrix} + \underbrace{\begin{bmatrix} 0 \\ +30000 \\ 0 \\ +30000 \end{bmatrix}}_{=f^{coh}} = \begin{bmatrix} -60000 \\ 0 \\ 60000 \\ 0 \end{bmatrix} \tag{IV.17}$$

This example illustrates that the cohesive law introduces forces which prevent the classical X-FEM formulation from an abrupt opening. This is because the residual forces corresponding to the enriching dof's vanish and as a consequence $b_1 = b_2 = 0$, i.e. the cohesive zone remains closed. By reducing the cohesive forces progressively via a softening law, a gradual opening of the cohesive zone is realized.

This 1D model was then implemented as user element subroutine (UEL) in the finite element simulation environment Abaqus. Different traction-separation laws are applied to illustrate the working principle of the cohesive laws in combination with the X-FEM. For each simulation the evolution of the reaction force is plotted in Fig. IV.8. The following four cases are considered:

(A) Traction-free crack: $t = 0$. This provokes the immediate rupture of the element (corresponds to standard X-FEM).

(B) Cohesive traction opposed to the enriched internal force of the standard X-FEM and increasing with the applied displacement $u_2$: $t = t_0 = E \cdot \frac{u_2}{L}$. Then, the cohesive forces cancel the standard X-FEM forces associated to the enriching dof's everywhere along the loading path so that the standard FEM is obtained.

(C) Linear cohesive law: $t = t_0 + T_c \cdot [\![u]\!]$ with $T_c = -100\,000$. This law provokes a global softening response in the post-localization regime.

(D) Constant cohesive traction: $t = t_0 = E \cdot \frac{0.3}{L}$ which equals to the traction in the bar at the onset of localization. Therefore a constant resistance is maintained in the bar during the post-localization response.

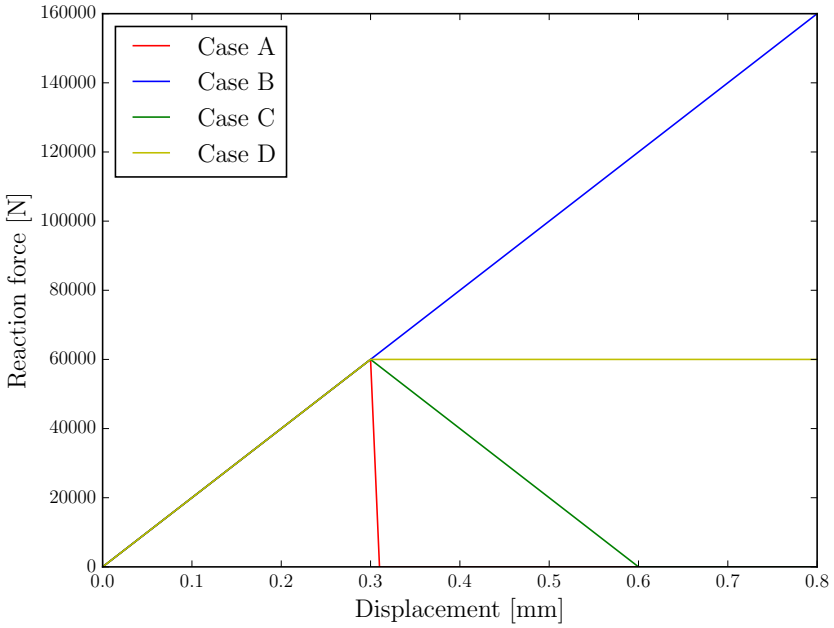


Figure IV.8 – Evolution of the reaction force in a 1D bar loaded in tension considering different cohesive laws

### IV.3.2 Aspects of numerical implementation in 2D

As indicated in section III.3 the developed set of discrete linearized equations of the X-FEM including a cohesive band is given in the following incremental form

$$\begin{bmatrix} \mathbf{K}_{aa} & \mathbf{K}_{ab} \\ \mathbf{K}_{ba} & \mathbf{K}_{bb} \end{bmatrix} \begin{Bmatrix} \mathrm{d}a \\ \mathrm{d}b \end{Bmatrix} = \begin{Bmatrix} \mathbf{f}_a^{ext} \\ \mathbf{f}_b^{ext} \end{Bmatrix} - \begin{Bmatrix} \mathbf{f}_a^{int} \\ \mathbf{f}_b^{int} \end{Bmatrix}, \tag{IV.18}$$

where the tangent stiffness matrix $\mathbf{K}$ is computed as follows

$$\mathbf{K} = \begin{bmatrix} \int_\Omega \mathbf{B}^T \mathbf{D}^{\mathbf{t}} \mathbf{B} \, \mathrm{d}\Omega & \int_\Omega \mathbf{B}^T \mathbf{D}^{\mathbf{t}} \mathbf{B}^* \, \mathrm{d}\Omega \\ \int_\Omega \mathbf{B}^{*T} \mathbf{D}^{\mathbf{t}} \mathbf{B} \, \mathrm{d}\Omega & \int_\Omega \mathbf{B}^{*T} \mathbf{D}^{\mathbf{t}} \mathbf{B}^* \, \mathrm{d}\Omega + 4 \int_{\Gamma_D} \mathbf{N}^T \mathbf{T} \mathbf{N} \, \mathrm{d}\Gamma \end{bmatrix}, \tag{IV.19}$$

where $\mathbf{T}$ is the cohesive tangent modulus as detailed in Eq. (IV.23) below. The $\mathbf{B}$-matrix contains the spatial derivatives of the shape functions $\mathbf{N}$, i.e. $\mathbf{B} = \mathbf{L}\mathbf{N}$ with $\mathbf{L}$ being the matrix differential operator

$$\mathbf{L} = \begin{bmatrix} \partial/\partial x & 0 \\ 0 & \partial/\partial y \\ \partial/\partial y & \partial/\partial x \end{bmatrix}. \tag{IV.20}$$

and $\mathbf{B}^* = \mathbf{L}\mathbf{N}^*$ with $\mathbf{N}^*$ containing the entries $N_j^* = (H(x) - H_j)N_j$ for

each node $j$ of the enriched element. The internal and external force vectors are calculated from

$$\mathbf{f}_a^{ext} = \int_{\Gamma_t} \mathbf{N}^T \mathbf{t}^* \, \mathrm{d}\Gamma \tag{IV.21a}$$

$$\mathbf{f}_b^{ext} = \int_{\Gamma_t} \mathbf{N}^{*T} \mathbf{t}^* \, \mathrm{d}\Gamma \tag{IV.21b}$$

$$\mathbf{f}_a^{int} = \int_{\Omega} \mathbf{B}^T \boldsymbol{\sigma} \, \mathrm{d}\Omega \tag{IV.21c}$$

$$\mathbf{f}_b^{int} = \int_{\Omega} \mathbf{B}^{*T} \boldsymbol{\sigma} \, \mathrm{d}\Omega + 2 \int_{\Gamma_D} \mathbf{N}^T \mathbf{t} \, \mathrm{d}\Gamma, \tag{IV.21d}$$

where the volume forces have been neglected. The stress $\boldsymbol{\sigma}$ is obtained from Eq. (III.19) in chapter III and the traction forces $\mathbf{t}$ are calculated from Eq. (III.20).

It should be noted that the cohesive tangent modulus $\mathbf{T}$ as well as the tractions $\mathbf{t}$ are defined in the local coordinate system of the oriented cohesive band. Therefore it is necessary to perform a transformation from the local to the global system. This is done by taking into account the rotation matrix $\mathbf{R}$ such that

$$\mathbf{t}^g = \mathbf{R}^T \mathbf{t}^l \text{ and } \mathbf{T}^g = \mathbf{R}^T \mathbf{T}^l \mathbf{R} \text{ ; with } \mathbf{R} = \begin{bmatrix} \cos\theta & \sin\theta \\ -\sin\theta & \cos\theta \end{bmatrix}, \tag{IV.22}$$

where g denotes the global and l the local coordinate system, see Fig. IV.4. Using the linear softening traction-separation law from section IV.2.2 yields the following (local) cohesive tangent modulus

$$\mathbf{T}^{\mathbf{l}} = \frac{\partial \mathbf{t}^l}{\partial [\![u]\!]^l} = \begin{bmatrix} \frac{\partial \mathbf{t}_m^l}{\partial [\![u]\!]_m^l} & \frac{\partial \mathbf{t}_m^l}{\partial [\![u]\!]_n^l} \\ \frac{\partial \mathbf{t}_n^l}{\partial [\![u]\!]_m^l} & \frac{\partial \mathbf{t}_n^l}{\partial [\![u]\!]_n^l} \end{bmatrix} = \begin{bmatrix} T_m^l & 0 \\ 0 & T_n^l \end{bmatrix}, \tag{IV.23}$$

where the normal and tangential traction components are assumed to be uncoupled from each other. That means that a separation in normal direction does not have an influence on the tangential direction.

The contribution of the continuum domain to the equilibrium equations of an element which is crossed by the localization band is tentatively integrated by subdividing the element into 16 rectangles which are themselves integrated by a standard 4-point Gauss rule. This 64-fixed points scheme ([53], [45]), see Fig. IV.9, is especially adapted to strongly non-linear ductile materials so as to avoid the cumbersome and numerically error-prone projection of loading- and history-dependent internal variables inherent to the classical subtriangulation methods, see e.g. Moës [106].

This method will be used tentatively. Later on, a different method is considered which is particularly efficient when further dealing with large engineering structures.

The integration of the contributions of the cohesive band to the equilibrium equations, i.e. the terms involving a line integral over $\Gamma_D$, is realized using a standard 2-point Gauss rule. Two integration points are necessary, because the displacement jump along the cohesive band is described by a linear interpolation function provided by the X-FEM. As opposed to that, the E-FEM (see e.g. [112], [74]) requires only one integration point as the enriching dof is constant over the enhanced element.

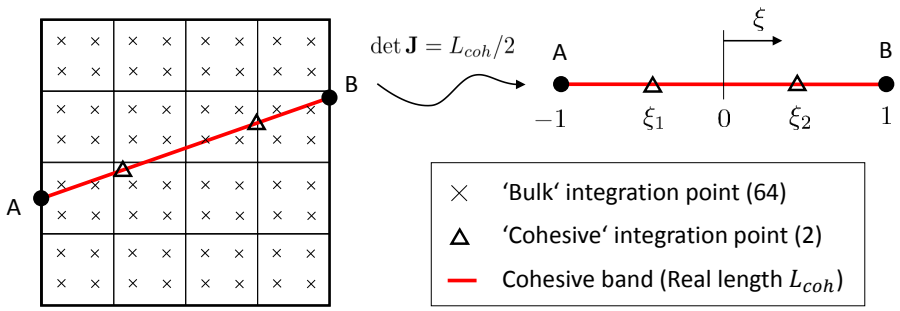


Figure IV.9 – Tentative integration scheme for a 2D quadrilateral element crossed by a cohesive band: (left) FE with 64 fixed Gauss points for the bulk part and 2 Gauss point for the cohesive part, (right) Transformed cohesive line element in the natural (local) coordinate $\xi$

In order to update the cohesive tractions at the two Gauss points, the radial return method can be applied in the same way as in the context of plasticity, see Belytschko [19], Simo [156]. The normal cohesive tractions are computed according to algorithm 1.

**Algorithm 1** Radial return method to update the (local) normal tractions from pseudo-time step $k$ to $k+1$

$[\![u]\!]_n^{k+1} = \underline{n} \cdot [\![u]\!]^{k+1} = \mathbf{n} \sum_{i=1}^{4} N_i(\xi,\eta) b_i^{k+1}$
**if** $[\![u]\!]_n^{k+1} > 0$ **then** ▷ Contact condition
  $t_y^{k+1} = t_{0n} + T_n [\![u]\!]_n^{k+1}$ ▷ Current cohesive traction
  $t_n^{trial} = t_n^k + T_n([\![u]\!]_n^{k+1} - [\![u]\!]_n^k)$ ▷ Prediction step
  $f^{k+1} = t_n^{trial} - t_y^{k+1}$ ▷ Trial cohesion function
  **if** $f^{k+1} \geq 0$ **then**
    $t_n^{k+1} = t_y^{k+1}$ ▷ Correction step
**return** $t_n^{k+1}, [\![u]\!]_n^{k+1}$

In case of contact, i.e. $[\![u]\!]_n^{k+1} \leq 0$, the cohesive band is inactive and the

material behavior is computed using the equations of motion [19][2]. The tangential tractions are calculated in the same way (index $n$ replaced by $m$), however the contact condition is not necessary as the shearing can take place in the positive and negative direction. The effect of friction during contact and gliding motion is tentatively neglected.

# IV.4 Application

The previous parts have introduced the methodology of coupling a cohesive band method with the X-FEM allowing for dealing with the progressive transition phase of strain localization. The difficulty of applying the method to non-linear ductile materials was carved out and appropriate numerical tools were proposed. The objective of this section is to apply the elaborated combination of cohesive band model and X-FEM to a test cases in order to assess its performance with regard to numerical simulations.

## IV.4.1 Modeling of localization and fracture in a ductile material

The basic numerical requirements for the subsequent applications are explained in this section.

### IV.4.1.1 Numerical environment

The choice of using the commercial FE software Abaqus has been made due to the strong interest of the industry in simulating the complex failure process in large engineering structures. Although this choice is ideal for industrial Engineers, it poses problems in terms of implementing complex scientific methodologies. Indeed there exist features to simulate failure mechanisms, but they are applicable only to simple materials. In this concern, the X-FEM is provided in Abaqus, but merely allows to use it in combination with elastic or simplistic elasto-plastic materials. Thus, it is not adapted to simulating the complex ductile failure process. Therefore, elaborated methods combining advanced constitutive modeling and X-FEM require being implemented as user element subroutine (UEL). The incorporation of the UEL, developed in the present work, into the global flow chart of Abaqus is shown in Fig. IV.10. The propagation algorithm (red-dashed box) is explained further below.

[2] A simple approach to treat contact may consist in introducing a penalty stiffness $T_n^p$ when the displacement jump is negative, i.e. $t_n = T_n^p [\![u]\!]_n$, see e.g. Remmers [136].

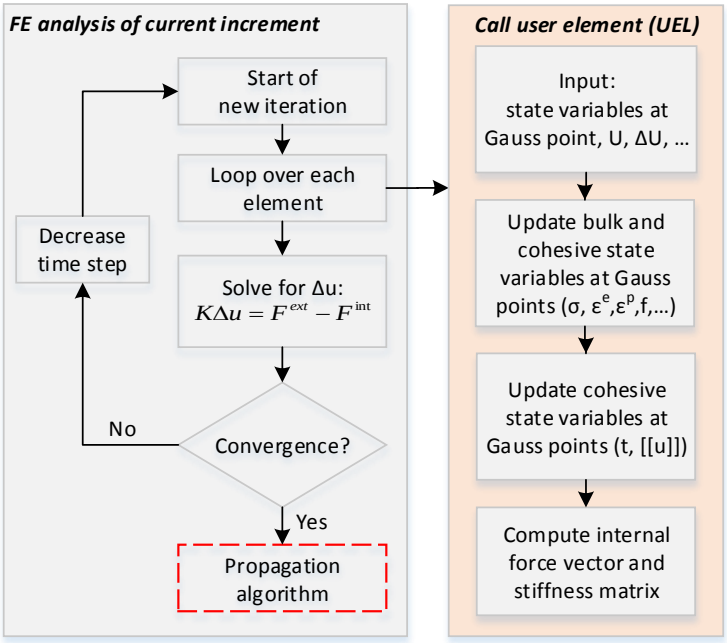


Figure IV.10 – Flow chart of FE analysis and user element (UEL) in Abaqus

In a displacement-controlled simulation, the total prescribed displacement is divided into small increments. In each increment, Abaqus loops over all finite elements of the mesh, whose behavior is determined in the UEL at each integration point. At each call of the UEL, an input database is provided (nodal displacements, increment of nodal displacements, state variables at the integration points, ...). Based on this database, the state variables at the integration points (in the bulk and along the cohesive band) are updated and the elemental stiffness matrix and the internal force vector are computed and returned to Abaqus at the end of the UEL. Abaqus carries out the assembly of the global system of equations and solves for the unknown degrees of freedom. If the solution does not converge, another iteration is performed until convergence is attained. Then, a new increment is started. This implies using an implicit integration scheme involving the return of the tangent stiffness matrix $\mathbf{K}$. This is motivated by the fact that it provides a more accurate solution compared to the explicit integration. Also, the larger computational effort of the implicit scheme compared to the explicit one is acceptable as the focus is tentatively set on quasi-static load cases in this work.

The methodology related to the propagation of the cohesive band and the crack is managed at the end of each increment, when convergence is reached. This is due to the fact that the insertion of a discontinuity in the Newton-Raphson iteration scheme reduces the order of convergence.

Table IV.1 – Parameters related to the elastic and strain hardening laws, see Eq. (II.4)

| $E$ | $\nu$ | $r_0$ | $r_{inf}$ | $k$ | $\beta$ |
|---|---|---|---|---|---|
| 200 GPa | 0.33 | 300 MPa | 350 MPa | 4.4 | 0.5 |

Table IV.2 – Parameters related to the microporous plasticity GTN model, see Eq. (II.10) together with Eqs. (II.7) - (II.9)

| $q_1$ | $q_2$ | $f_0$ | $f_N$ | $s_N$ | $\kappa_N$ | $b$ |
|---|---|---|---|---|---|---|
| 1 | 1 | $10^{-3}$ | 0.04 | 0.05 | 0.3 | $100MPa$ |

#### IV.4.1.2 Test case and parameters of the material model

In the following, a 2D test case is studied. This application example concerns a parametric study of a plate which is loaded in tension. An advanced method for the propagation of the cohesive band and crack is proposed and implemented as UEL in Abaqus. Due to purely numerical reasons, the 2D model is implemented assuming plane strain conditions. Although it might be more adapted for ductile materials to use a finite strain framework, here the deformations are assumed to remain small. The quasi-static loading is applied by displacement control.

The modified GTN model detailed in section II.3.1.2, see Eq. (II.10) and preceding Eqs. (II.4) - (II.9), is used in this model. The parameters of the material model are given in the tables IV.1 and IV.2. Therein, $E$ and $\nu$ denote, respectively, the Young's modulus and the Poisson's ratio characterizing the elastic material behavior. In Eq. (II.9) $p_r$ has been linearized in order to favor numerical stabiliy, i.e. $p_r = b(q_1 f - 1)$.

### IV.4.2 Tensile test of a 2D plate

In this section a 2D plate specimen is considered which is subjected to a quasi-static tension loading. The objective of this test case is to propose and test an algorithm for cohesive band propagation and crack formation.

#### IV.4.2.1 Problem statement

Consider the plane specimen in Fig. IV.11 which is fixed at the bottom and loaded in tension at the top (in red). The imposed displacement is increased quasi-statically up to a value $U_{max}$. The thickness of the plate is 1 mm. The plate is free of pre-cracks so that a strategy will be proposed which identifies the

position of the first nucleation of the localization band. Plane strain conditions are assumed here. The illustrations of the results are restricted to the area of interest (green box in Fig. IV.11) where the propagation of the cohesive band takes place.

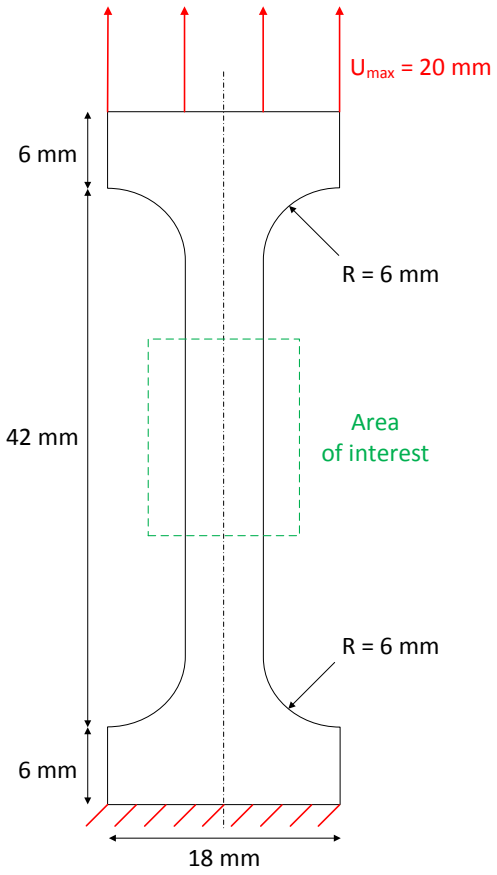


Figure IV.11 – Model of the plane uncracked specimen subjected to a quasi-static displacement loading $U_{max}$

Ten different simulations are conducted, see Tab. IV.3. In the table short cuts are assigned to the simulations (first column) serving as references for later discussion. In order to analyze the sensitivity to the mesh size, two different element sizes are used: about 0.5 mm element size for the coarse mesh and 0.25 mm for the fine mesh. Furthermore, the cohesive tangent moduli $T_m^l = T_n^l$ in Eq. (IV.23) are varying. And then, in the next section, a new propagation method combined with a 4-point Gauss rule is presented, so that simulations with 64 and also 4 GP are employed and compared. Furthermore, two simulations are employed with the GTN model without discontinuity. Finally, two simulations are conducted - one with a fine mesh and one with a coarse mesh - using the X-FEM only, i.e. without a cohesive law (CZM).

Table IV.3 – Configuration of the employed simulations (coarse mesh: element size 0.5 mm, fine mesh: element size 0.25 mm)

| Short cut | Mesh | No. of GP | $T_n^l/T_m^l[N/mm^3]$ |
|---|---|---|---|
| Sim1 | fine | 4 | $-25.0$ |
| Sim2 | fine | 4 | $-12.5$ |
| Sim3 | coarse | 64 | $-25.0$ |
| Sim4 | coarse | 64 | $-12.5$ |
| Sim5 | coarse | 4 | $-25.0$ |
| Sim6 | coarse | 4 | $-12.5$ |
| Sim7 | fine | 4 | No discontinuity |
| Sim8 | coarse | 4 | No discontinuity |
| Sim9 | fine | 4 | X-FEM without CZM |
| Sim10 | coarse | 4 | X-FEM without CZM |

#### IV.4.2.2 Description of the propagation algorithm

The propagation of the cohesive band, then the crack formation, is accomplished by the sequence of the following four steps

1. Onset and direction of propagation of the cohesive band
2. Determination of the propagation length
3. Propagation of the cohesive band
4. Onset of the macro-crack in the cohesive band wake

The methodology is explained below step by step. It is assumed that only one cohesive band can propagate throughout the structure. Branching can occur in ductile materials, but it is not considered here. A flow chart of the propagation algorithm is given at the end of this section in Fig. IV.15.

##### IV.4.2.2.1 Onset and direction of propagation of the cohesive band

As indicated in section II.3.2.3 the transition from diffuse damage to the formation of a localization band relies on finding a condition for the spontaneous occurrence of an inhomogeneous strain mode within a homogeneous material. Two common methods were discussed in the context of ductile materials: bifurcation

analysis and linear perturbation analysis, see section II.3.2.3. The analyses of the present work are limited to rate-independent materials so that the bifurcation analysis is applied here. This method consists in evaluating the orientation of the localization band $\underline{n}$ for which the determinant of the acoustic tensor $\underset{\sim}{\underset{\sim}{Q}}$ becomes zero (or numerically negative) for the first time, i.e. (see also Eq. (II.15))

$$\det \underset{\sim}{\underset{\sim}{Q}}(\underline{n}) = \det(\underline{n} \cdot \underset{\sim}{\underset{\sim}{D}}^t \cdot \underline{n}) = 0, \tag{IV.24}$$

where $\underset{\sim}{\underset{\sim}{D}}^t$ denotes the elastic-plastic tangent operator of the microporous plasticity GTN model. Normally, two solutions for $\underline{n}$ are found. The bifurcation condition is evaluated locally at an additional Gauss point which is inserted at the element center and does not contribute to the global equation system. The space between 1 and 180 degrees is swept by increments of 1 degree. For each orientation the bifurcation criterion is checked. If this criterion is fulfilled, the angle is added to a list. Then, within this list the propagation angle corresponding to the smallest determinant value is chosen. Various criteria are checked to verify if that angle is numerically and physically appropriate (e.g. if the direction would lead to overlapping of the existing band or if a crossed element would be cut twice). If the propagation angle does not fulfill these criteria, the angle with the second smallest determinant value is selected and so on until an appropriate angle is found. A different algorithm to choose the direction of propagation relying on the evaluation of the maximal plastic deformation is shown in the perspectives chapter.

The cohesive band is inserted only once the porosity at the center GP exceeds a critical value. This criterion is necessary to ensure that already some damage has evolved in the element before it is localized and thus prevents from premature artificial localization. Based on purely numerical reasons, its value is set to $f_{ini} = 0.03$ which is found to be a good compromise between numerical and physical aspects. A double criterion has thus to be satisfied for the cohesive band activation:

1. the bifurcation condition is met at the center GP of the element located in front of the current cohesive band

2. the central porosity has reached a critical value at the center GP

This is a tentative approach as it is well known that a local evaluation of the initiation criterion may lead to pathological mesh dependence [57]. A more appropriate (non-local) methodology for ductile material has been proposed by Crété [45] and may be implemented in future works.

Due to the fact that the specimen is initially free of defects or cracks, an approach is proposed which allows to find the element where the cohesive band nucleates, see Fig. IV.12. A loop over all elements identifies all those which fulfill the aforementioned criteria. If several such elements are found (what is normally the case), the cohesive band nucleates in the element with the largest porosity at the center GP.

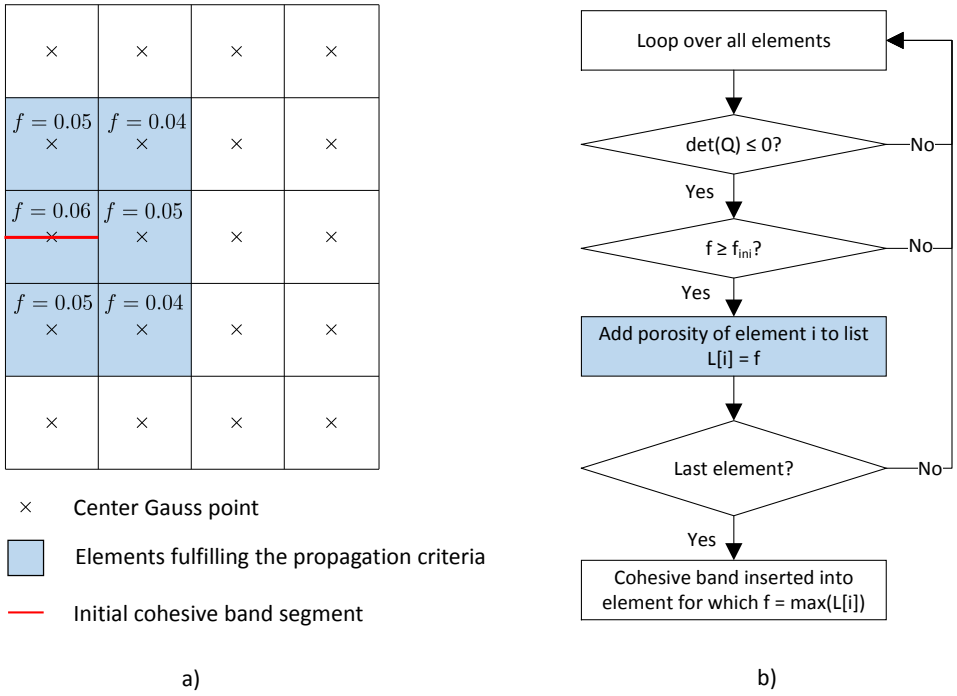


Figure IV.12 – Strategy to set the initial cohesive band: a) Situation in the FE mesh, b) Algorithm to determine the element containing the initial cohesive band

#### IV.4.2.2.2 Propagation of the cohesive band

Instead of prescribing the fracture energy, the cohesive moduli in Eq. (IV.23) are given due to a better numerical performance. The normal and tangential cohesive moduli are assumed to be equal, i.e. $T_m^l = T_n^l$.

Several modifications of the constitutive bulk behavior are made in order to better agree with physics and improve numerical performance. First of all, the void growth is enforced to stagnate at the continuum GPs in the elements which are crossed by the cohesive band. This can be justified physically because the cohesive band is assumed to be the narrow zone where all the damage and plasticity processes are henceforth concentrated. It corresponds also to the experimental

observations which suggest that around the meso-crack there are only a few small voids, see Fig. II.3. Therefore, the void growth is reduced to the elements in the process zone. This has also an important numerical advantage as it turned out that the simulation suffers from convergence problems if the void growth is not restricted.

#### IV.4.2.2.3 Determination of the propagation length

How far does the localization band propagate during one displacement increment of the monotonic loading? The characteristics of the propagation velocity for fatigue loading are well studied, see e.g. [131], [163], [90]. However, in the case of a monotonically increasing loading, far less research can be found. For a slow, quasi-static loading, experiments with the ductile material DH36 suggest that the meso-crack propagates intermittently by the length of the mesocrack (about $200 - 300\mu m$), see Fig. II.3. Modeling such a propagation length with FEs would require a prohibitively small element size compared to the structure dimensions. Therefore, the length of the intermittently propagation cohesive segment has to be adapted to the FE mesh. The procedure of that so-called exhaustion method is described below. It corresponds to the approach proposed by Crété [46] in the context of crack propagation.

The cohesive band is propagating element by element whereas its orientation does not change within an element. The front of the cohesive band is assumed to be located always on an edge. At first, the cohesive band propagates within the element in front of the current cohesive band as soon as it fulfills the propagation criteria. Then, still in the same increment and without recalculating the equilibrium, the band propagates in the next element if the criteria are fulfilled until exhaustion is attained. Due to convergence issues, the equilibrium is not recalculated when a cohesive band propagates through several elements, as it is done e.g. in the approach proposed by Pourmodheji [129].

#### IV.4.2.2.4 Onset of the macro-crack in the cohesive band wake

Instead of waiting until the residual strength of the cohesive band is completely lost, i.e. both the tractions $t_m$ and $t_n$ are zero, the crack is formed already before. This has two reasons. First of all, this corresponds to the assumption that the interrelating bonds of the coalescing voids can only stand a certain critical or rupture traction. Exceeding this traction leads to a sudden rupture of this

ligament and so to the formation of new crack surfaces. Secondly, this approach improves the convergence rate. An effective traction in the local coordinate system $t_{eff} = \sqrt{t_m^{l2} + t_n^{l2}}$ is computed and compared to a critical value, here the - up to now - arbitrary value of 100 MPa is chosen.

#### IV.4.2.2.5 Considerations on the integration scheme

Realizing that a relatively fine mesh has to be used to get reliable results, using 64 Gauss points in each FE from the beginning of the simulation (Elguedj [53], Crété [45]) tremendously slows down the calculation time, especially with regard to large structures. Also the subsequent numerical tests have revealed that using 64 GP in combination with a very fine mesh may lead to divergence of the solution. Therefore a different strategy is used here which allows reducing the number of GP tremendously and at once maintaining a still acceptable accuracy.

Here it is proposed to use the 4-point Gauss rule, what is in strong contrast to commonly used integration schemes in the X-FEM. In order to guarantee that at least one Gauss point is on both sides of the cohesive band, the new cohesive segment is forced to traverse the center of an edge. Depending on the bifurcation angle, the propagation angle can only take three possible values determined by the geometry of the element, see Fig. IV.13.

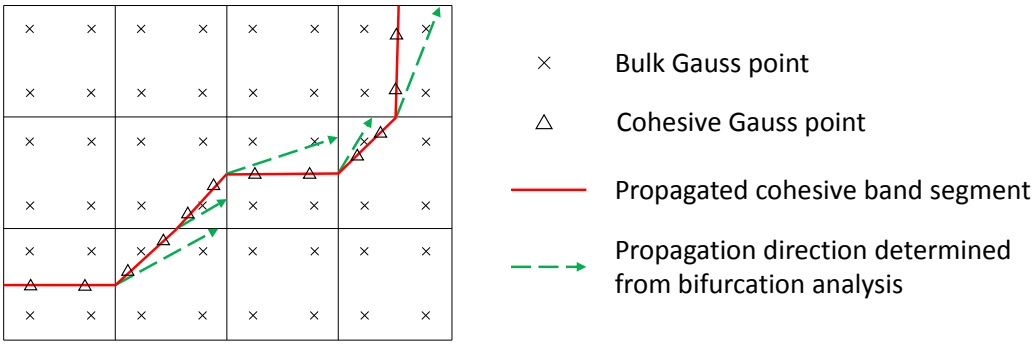


Figure IV.13 – Modified propagation algorithm using 4 GP in the continuum

The question arises in how far the accuracy of the proposed method is impaired compared to the previously recommended 64-point integration scheme. In the following, the propagation algorithm presented in this chapter is applied to the plate specimen in Fig. IV.11. In accordance with the objectives of this work, a rather coarse FE mesh is used (element size 0.5 mm). For each method two different values for the cohesive tangent modulus are considered. The results are shown in

Fig. IV.14.

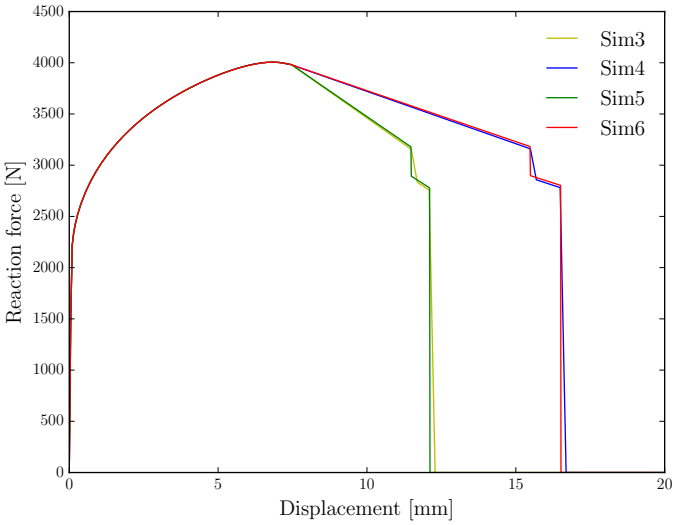


Figure IV.14 – Evolution of the reaction force with coarse mesh for Sim3, Sim4, Sim5 and Sim6, see Tab. IV.3 for the nomenclature

It can be observed that the difference between the global responses of the two approaches is slight and independent of the cohesive law. This startling finding implies that the costly use of the 64-point Gauss rule in each FE from the beginning of the simulation can be replaced by the standard 4-point rule without losing any accuracy. Although the propagation algorithm has to be slightly modified, this seems to be an efficient approach applicable to large engineering structures requiring a coarse mesh. The advantages of using 4 Gauss points instead of 64 Gauss points can be summarized as follows:

- It is considerably faster.
- It requires much less storage for the state variables on each Gauss point and thus much less time for post-processing.
- It is numerically more stable, because simulations with the 64-point rule has revealed convergence problems when applied to a very fine mesh.
- It provides still a good prediction of the global response.

The 4-point Gauss integration in combination with the described propagation algorithm is therefore used as the preferred method.

#### IV.4.2.2.6 Summary of the algorithm

The algorithm is summarized as a flow chart in Fig. IV.15. The propagation of the cohesive band and/or the crack is done at the end of a displacement increment. Therefore the introduction of a discontinuity into the unbalanced system during iteration can be avoided and the optimal convergence rate of the Newton-Raphson solution scheme can be maintained.

### IV.4.2.3 Results

The results of the simulations in Tab. IV.3 are discussed here. The visualization of the simulations is employed with the software Gmsh [59]. According to the 2D-plane strain condition assumed here, the band which will later give birth to the crack is expected to propagate following Mode II, i.e. with an angle of around 45° with respect to the normal of the loading direction, as for the right picture of Fig. IV.5 (see comments above that figure).

#### IV.4.2.3.1 Localization of damage and specimen necking using the GTN model

If the GTN model is used throughout the entire simulation without numerically treating the phase of strain localization, the damage and plasticity concentrates within a few FEs located in the center of the specimen, see Fig. IV.16. The latter shows specimen necking and no thin band of heterogeneous deformation, which is clearly in contradiction with the experimental results (see right picture of Fig. IV.5). As a consequence, the use of only a continuous model throughout the entire failure process does not allow for reproducing the phase of void coalescence-induced localization band and further Mode II-crack propagation in the specimen thickness.

#### IV.4.2.3.2 Comparison of the propagation angle

At the onset of localization, the cohesive band is inserted into the structure. It is observed that in all simulations the cohesive band nucleates in the very center of the structure and then propagates towards both sides, see Fig. IV.17.

The first two simulations a) and b) show the propagation within a fine mesh but different tangent moduli. The cohesive band propagates as one line through

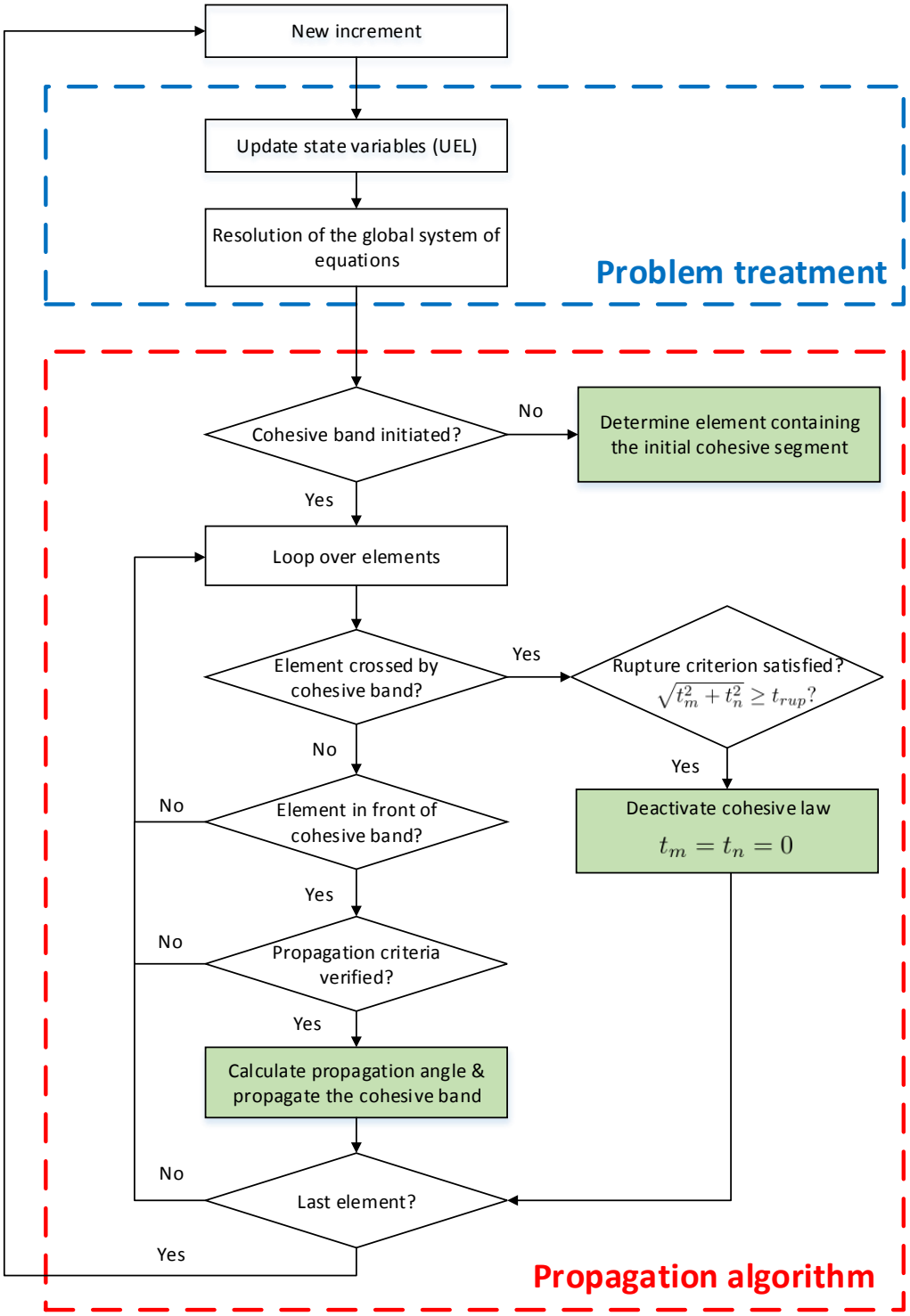


Figure IV.15 – Flow chart of propagation algorithm

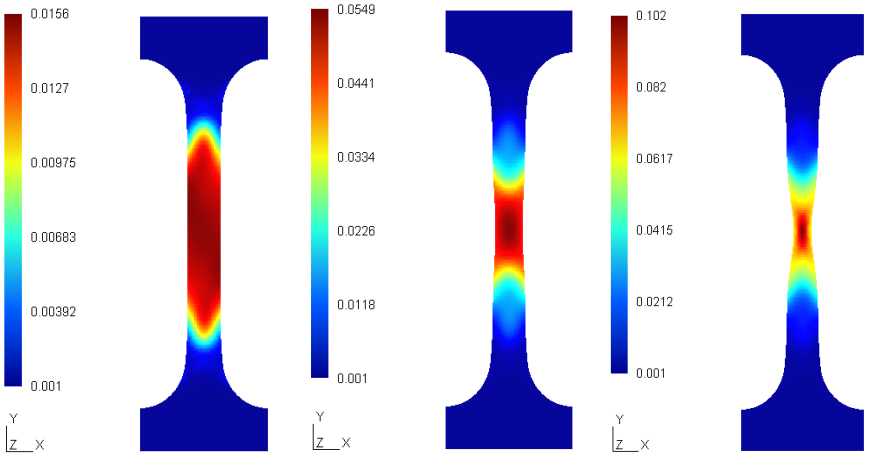


Figure IV.16 – Localization of damage $f$ with Sim7, see Tab. IV.3 for the nomenclature, at different loading states: a) $U = 7.1mm$, b) $U = 8.2mm$, c) $U = 9.9mm$

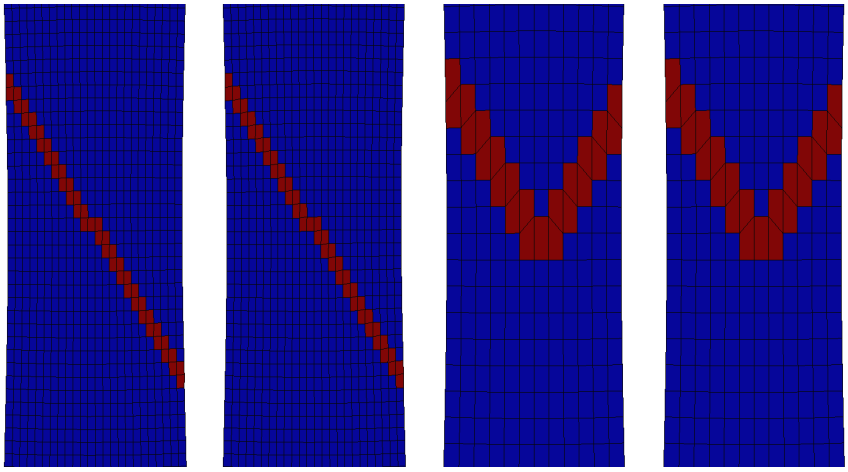


Figure IV.17 – Propagation angle of the cohesive band at an early stage of localization ($U = 7.8mm$): a) Sim1, b) Sim2, c) Sim5, d)Sim6, see Tab. IV.3 for the nomenclature

the structure and with an angle of 58° with respect to the horizontal axis as the result of the bifurcation criterion. This numerical value of 58° has to be compared with the experimental value of 45° reported previously (see above and right picture of Fig. IV.5). This discrepancy may be explained by the hypothesis of 2D-plane strain condition assumed for the numerical simulations while not being satisfied for the real loading case (the width of the tension specimen is not large enough for the plane strain condition to be met). Changing the stiffness of cohesive band does not have an influence on the propagation angle. In contrast to the fine mesh, the propagation pattern for the coarse mesh looks different and reminds of a cup and cone failure mode. These differences can be justified by the fact that the decision of the bifurcation angle in an element is purely based on the numerical determinant value of $\underset{\sim}{Q}$. A better choice may be provided by using the method of Crété [45] where the angle is chosen which yields the maximum plastic deformation.

#### IV.4.2.3.3 Comparison of the evolution of the reaction force

First of all it is worth analyzing the global response for the case when only the X-FEM, i.e. without incorporating a cohesive law ($t = 0$), in comparison to the case when the X-FEM is combined with a cohesive law. The evolution of the reaction force is shown in Fig. IV.18. In the case of using only the X-FEM without cohesive law, it can be observed that right at the onset of strain localization the structure is subjected to an abrupt drop in load to zero, i.e. an immediate formation of a crack leading to the total rupture of the structure. This abrupt drop in load reminds one of the simulation model of Crété, see Fig. I.4 in the first chapter, wherein the phase of strain localization has been neglected and a direct transition from diffuse damage (FEM) to crack propagation (X-FEM) was assumed to occur. If the X-FEM is combined with a cohesive law, this sudden drop can be retarded and the transition to crack formation takes places in a progressive manner. Then, when the critical rupture traction is reached, the propagation of a macro-crack occurs in wake of the cohesive band and the load drops to zero almost abruptly. This drop in load occurs in two steps: (i) first of all, the traction-free crack forms in a few elements (small drop in load with crack arrest in the structure) and then (ii) the crack abruptly traverses the entire structure leading to the total rupture of the structure.

It should also be paid attention to the fact that a smooth transition from the pre- to the post-localization regime can be achieved - even for the coarse mesh - mainly by computing the internal cohesive force vector from the nodal bulk forces

at the onset of localization.

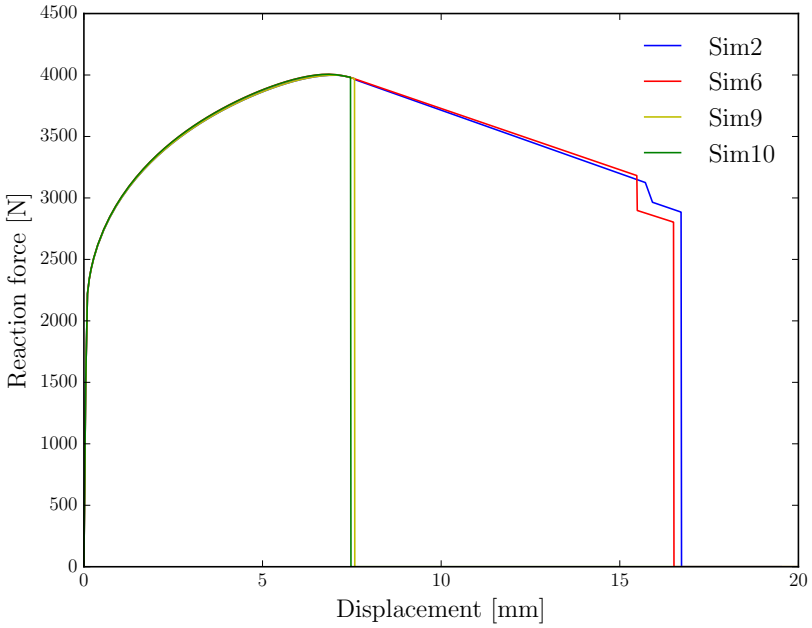


Figure IV.18 – Evolution of the reaction force for Sim2, Sim6, Sim9 and Sim10, see Tab. IV.3 for the nomenclature

It was already reported that the mesh size influences the direction of propagation. Now, the effect of the mesh size on the global response is examined, see Fig. IV.19. It can be observed that the pure use of the GTN model leads to severe mesh dependence of the global response. By contrast, the proposed cohesive band propagation method in the context of the X-FEM is nearly insensitive to the mesh size what concerns the global response.

The final graph IV.20 shows the evolution of the reaction forces for different slopes of the cohesive law, which can be well represented for the fine and coarse meshes. Due to the fact that a critical rupture traction has been used, the simulation fails earlier in the case of a larger slope.

## IV.5 Discussion and conclusion

In this chapter a methodology to couple a strain localization induced cohesive band with the X-FEM was proposed and assessed. This approach allows for passing progressively from the phase of void-growth induced damage to crack propagation in ductile materials. An appropriate cohesive law was elaborated which accounts for a normal and a tangential component. The principle and numerical aspects

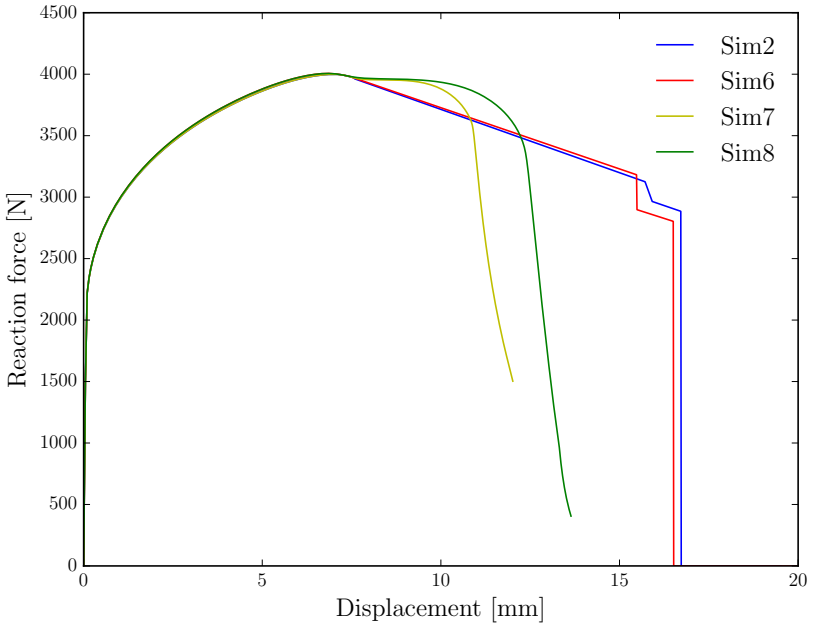


Figure IV.19 – Evolution of the reaction force for Sim2, Sim6, Sim7 and Sim8, see Tab. IV.3 for the nomenclature

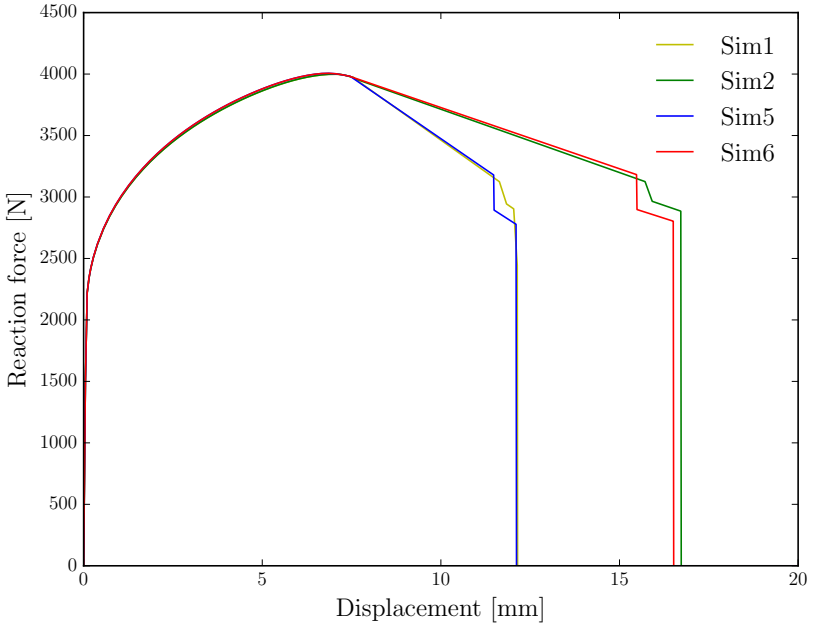


Figure IV.20 – Evolution of the reaction force for Sim1, Sim2, Sim5 and Sim6, see Tab. IV.3 for the nomenclature

of implementation of the cohesive band X-FEM were explained first in 1D, then extended to 2D. The fixed 64-point integration scheme for the bulk part was suggested as tentative method and a 2-point Gauss rule to integrate the cohesive part.

Then, a tensile test of a plate with a Gurson-based model has been presented in order to analyze the performance of the methodology. An algorithm was proposed to activate and propagate a cohesive band within the structure until rupture. This model was implemented as a UEL in the commercial FE computation code Abaqus. Several simulations with different configurations and parameters have been conducted, analyzed and compared to each other. An important observation could be made concerning the applied integration method of the bulk part in the enriched element. It could be shown that using the 4-point integration scheme merely impairs the accuracy of the simulation compared to using an expensive 64-point rule - even in a coarse mesh. The propagation method has been modified to optimally work with the new integration scheme. The calculation time and storage space can thus be reduced.

Then, the performance of the model has been tested on the one hand with a coarse and on the other hand with a fine mesh. It was observed that the propagation path differs between the two simulations. This may be traced back to the mere use of the value of the determinant as decision basis for the propagation angle. In the future, a more sophisticated methodology can be implemented, see e.g. [45]. Regarding the global response, the cohesive law allows passing progressively from diffuse damage to crack propagation and thus avoids the sudden drop in load when only using the standard X-FEM. Then it could be shown that the model behaves nearly mesh independent. Also it could be shown that the transition from diffuse damage to the onset of localization is smooth and without numerical difficulties.

A main challenge during implementation was that many sources of numerical issues have been encountered. Most of them could be solved by modifying the propagation algorithm and the constitutive laws in a physically acceptable manner. Although some issues still remain to be addressed, the cohesive band methodology in combination with a physics-motivated propagation method has been shown to produce first convincing results. In a prospective work, the parameters of the cohesive law need to be adapted to experimental results for further being used for failure analysis of engineering structures.

In the end, the final framework including the displacement field and the equilibrium equations in the three steps diffuse damage, strain localization, then crack propagation is summarized in Fig. IV.21.

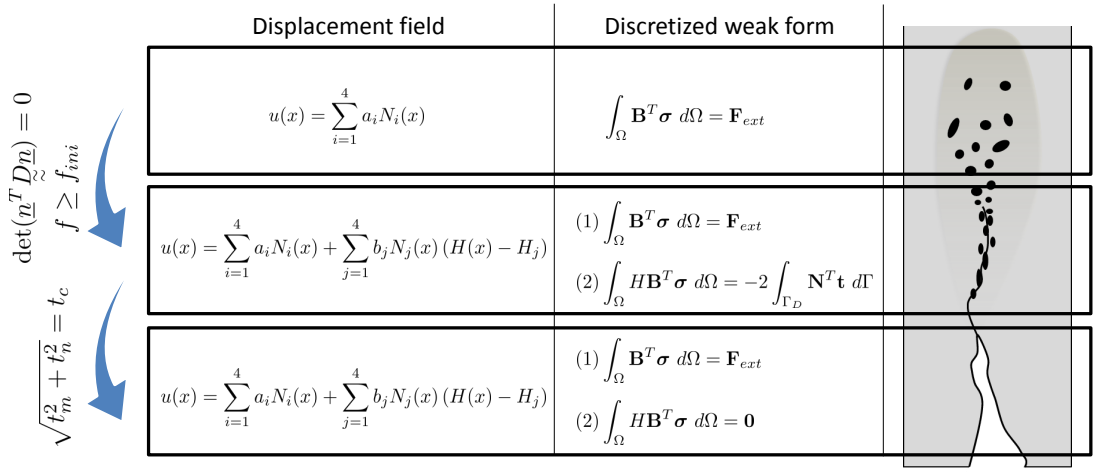


Figure IV.21 – Summary of the discretized displacement field and equilibrium equations for the steps of ductile failure

# Chapter V

# Conclusions and perspectives

## V.1 Conclusions

This work aims at contributing to the prediction of the residual strength of accidentally overloaded structures by numerical simulation (virtual testing). The challenge consists in reproducing within a unified methodology the successive (multi-scale) phases of diffuse damage (micro-scale), strain localization (meso-scale) and crack propagation (macro-scale) potentially leading to the ultimate ruin of the structure. The objective of this dissertation was to develop an appropriate (embedded band-based) method capable of reproducing the physical localization band and reducing the mesh sensitivity to a minimum.

In a first step, a material model for the pre-localization response was elaborated. The material in the undamaged state was described by a simple von Mises plasticity model. The effect of strain hardening was considered, yet the influence of viscoplasticity and thermal softening was tentatively neglected. The damaged (micro-porous) material was then described using a Gurson-type constitutive model. It was stated that mesh dependence of the structural response is a problem which comes up in the post-localization regime of softening materials or structures.

Reducing the mesh dependence in the softening regime of the material is one issue, but capturing the damage concentration and strain localization inside a narrow band is another one. The embedded-band FE method was identified to combine these two objectives in one approach. The X-FEM which allows for a precise approximation of the discontinuity path was chosen to enrich the FEs to account for the localization band kinematics. This enrichment method is also appropriate to represent a crack within the FE in the late stage of the loading process. The bifurcation analysis which is limited to rate-independent materials was identified to indicate the passage from diffuse damage to strain localization.

Three different embedded-band FE methods which enrich the kinematic field across the localization band by means of, respectively, a strong, weak or regularized discontinuity have been proposed in a common X-FEM framework. It was studied

their ability to model numerically and physically the phase of strain localization as well as the transitions from diffuse damage to localization and from localization to crack propagation in ductile materials. The strong discontinuity cohesive model appeared to be the most adapted method in the context of the simulation of large structures where the macromechanical consequences of localization are of great interest.

In order to respond to the demand of the industry to use the model for engineering applications, the model was implemented as user element (UEL) in the engineering FEM computation code Abaqus. Thereby, a constitutive model was implemented accounting for the effects of plasticity and void-growth induced damage. The X-FEM was used to describe the presence of a strong discontinuity in the enhanced elements. A methodology was shown to model a cohesive band using the X-FEM.

Then, a tensile test using a 2D plate was presented in order to assess the developed methodology. A methodology was proposed to activate and propagate the cohesive band through the structure until crack formation. This model relies on the following ingredients

- Onset and direction of propagation of the cohesive band
- Determination of the propagation length
- Propagation of the cohesive band
- Onset of the macro-crack

Controlled by ductile damage-induced softening, the strain localization was considered as the consequence of a material instability so that the onset and direction of propagation was determined from bifurcation analysis (rate independent dissipative mechanisms). If the cohesive band crosses an element, the initial cohesive force is computed such that it compensates the enrichment-related bulk force to ensure a smooth transition from the pre- to the post-localization regime. The length of propagation is determined from the exhaustion of the onset criterion within a displacement increment. The initiation of a crack is based on the comparison of the effective traction force with a critical fracture traction.

Considering the developed methodology as an attempt to describe the strain localization phase within a unified ductile failure model, the first results are quite promising from a qualitative viewpoint. It could be shown that the propagation

of the cohesive band through the structure can be reproduced in an efficient and mesh-independent way by using an adapted 4 Gauss point propagation method. Realizing a smooth transition from diffuse damage to localization, the subsequent global softening behavior during the phase of post-localization can be properly captured. Thus, the abrupt drop in load which emerged in the simulations of the model of Crété (direct transition from diffuse damage to X-FEM crack propagation), could be avoided. However, the propagation direction of the cohesive band turned out to depend on the mesh size. It is supposed that this is due to the fact that the bifurcation criterion is evaluated locally at the center of an element and based on the order of the determinant of the acoustic tensor. Furthermore, due to numerical reasons, the cohesive tangent modulus was assumed as the material constant, whereas it would be more physical to use an energy value. This explains the linear decrease of the softening response.

## V.2 Perspectives

Modeling the complex nature of ductile failure is not possible without making simplifications. This work leaves open questions and unresolved challenges even if all the main ingredients of a unified model of ductile failure have been given and first promising results have been obtained. In the following, important topics for future works are proposed and associated to short term, mid term or long term priority.

### V.2.1 Short term perspective 1: Improvement of the propagation algorithm

The results have revealed the mesh sensitivity of the propagation angle. This can be explained by the local evaluation of the bifurcation criterion at an additional Gauss point in the center of the element. Moreover, the propagation angle is determined from geometric considerations and the minimum value of the determinant of $\underset{\sim}{Q}$. However, it can be thought that these criteria are not sufficient and require advanced physical considerations.

In this concern, it may be of great interest to extend the propagation algorithm by a methodology which takes into account averaged quantities at the tip of the cohesive band. An appropriate framework was proposed by Crété [46] in order to treat the transition from diffuse damage to crack propagation in ductile materials, see Fig. V.1 for a summary.

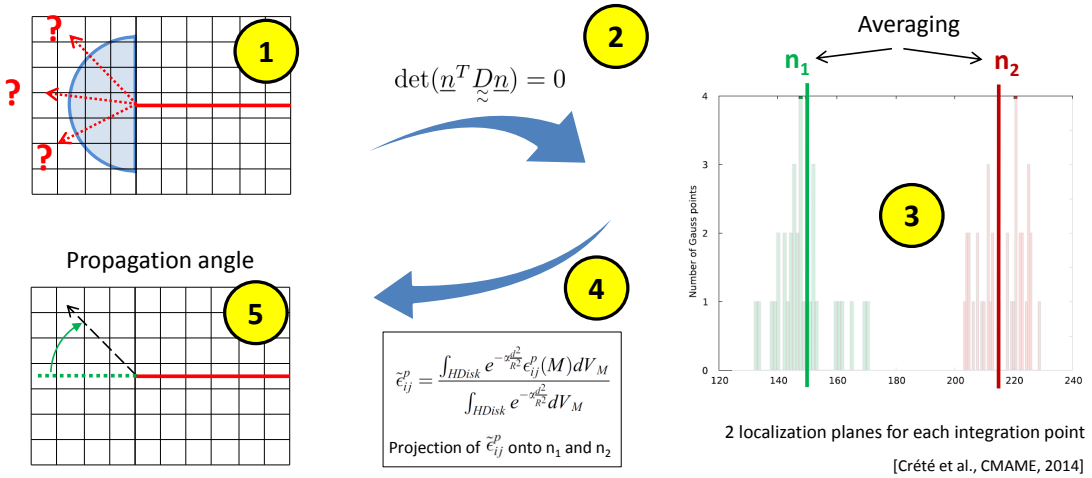


Figure V.1 – Determination of the propagation angle in the method of Crété [45] using quantities averaged over a patch

### V.2.2 Short term perspective 2: Experimental characterization of the cohesive law

Another relevant topic consists in the determination of certain parameters from experiments. First of all, the work of separation per unit area at the onset of crack propagation needs to be evaluated. Possible approaches have been presented in section IV.2.2 and involve e.g. inverse analysis ([41], [150]) or in combination with the digital image correlation ([151]), which has already been applied in our laboratory to analyze shear banding, see e.g. Roux [143].

Furthermore the influence parameters of the cohesive fracture energy with regards to the considered ductile materials (e.g. DH36) need to be identified, e.g. the effect of the triaxiality ratio or the temperature. The experiments conducted in the framework of the thesis of Geffroy [57] can serve as a first orientation.

### V.2.3 Mid term perspective: Extension of the model to dynamic loading

This work focused on the consideration of a quasi-static loading. In order to describe the failure process during accidental events as e.g. impact or explosion (dynamic loading), the model needs to be extended by several features. The treatment of dynamic loading is very complex, so that certain topics are selected and explained here:

- The effects of the strain rate and temperature on the material behavior under quasi-adiabatic conditions need to be taken into account, see the works of Geffroy [57] and Crété [45].

- The bifurcation analysis can not be applied any more, because the determinant of the acoustic tensor remains positive throughout the phase of localization. Therefore a different criterion needs to be chosen. A commonly used approach is the linear perturbation method, which is however not trivial to apply and implement.

- In highly dynamic tests and under negative triaxiality ratio, e.g. in the Kalthoff-Winkler impact test, it can be observed that crack propagation is preceded by very localized adiabatic shear banding, see Fig. V.2. As opposed to the strain localization band considered in this work, the adiabatic shear band forms first and then highly localized void-growth induced damage evolves within the band. At present, at our laboratory there are several

thesis works in progress focusing on the experimental analysis and numerical modeling of this complex phenomenon.

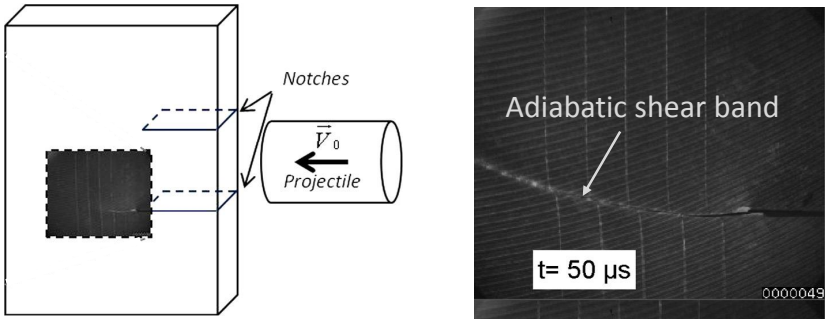


Figure V.2 – Appearance of a thin adiabatic shear band as a precursor of crack propagation in the Kalthoff-Winkler test under high-velocity impact (Roux and Longére [143])

### V.2.4 Long term perspective: Multi-scale simulation using non-intrusive coupling

The crack propagation within large scale structures can be considered as a multi-scale problem, whereas the crack-related mechanisms occur on a small scale (order of $10^{-4} - 10^{0}$ m) in a large-scale structure (order of $10^{1} - 10^{2}$ m, e.g. ships). The desired high fidelity within the local domain (strain localization and crack propagation) thus stands in contrast with a rather low fidelity computation of the global domain (entire structure using a simple FE model would involve a large number of degrees of freedom). The dissertation of Mickaël Duval [51], defended at the Institut Clément Ader in summer 2016, is an important contribution towards an efficient multi-scale computation. The proposed algorithm allows to couple a highly sophisticated research code handling the crack propagation with a commercial FE code which calculates the global domain response using a simple FE model (e.g. basic plate elements) and structure geometry. Several applications in the software Code_Aster (developed by the EDF) show the high potential of the method, see e.g. the process of non-intrusive coupling in the context of crack propagation using a linear elastic material in Fig. V.3. In the future, his simple crack propagation model could be replaced by the ductile failure model elaborated in this dissertation and further developed in prospective works.

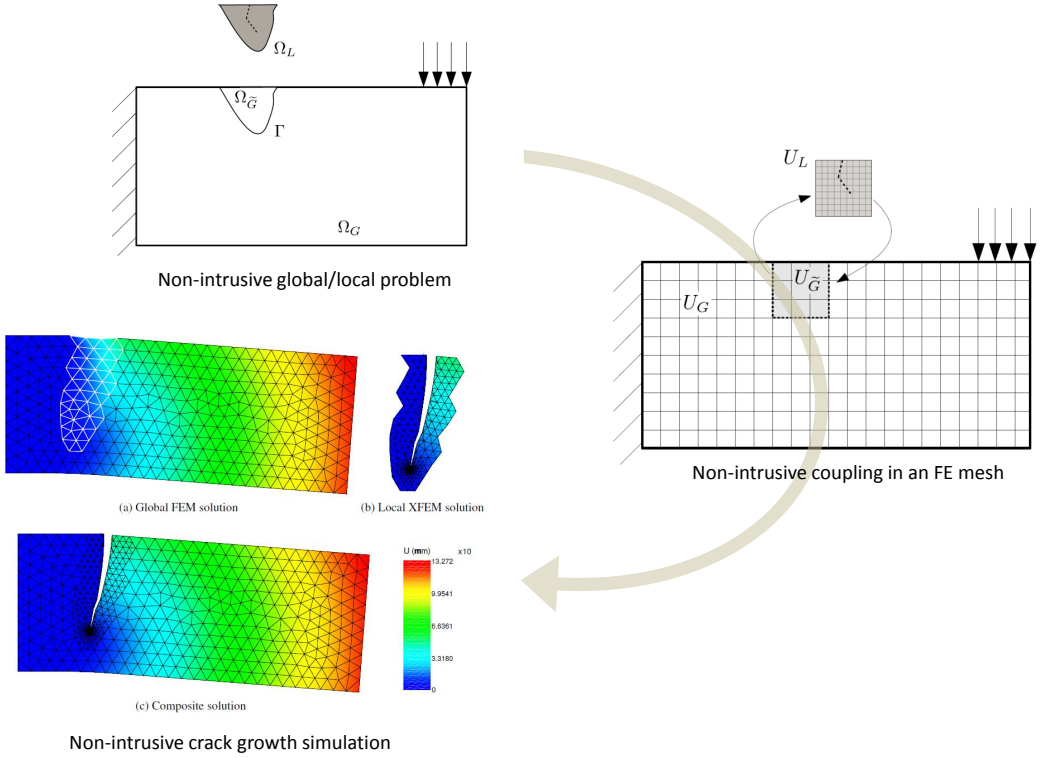


Figure V.3 – The non-intrusive coupling problem in the context of crack propagation (local domain) in a linear elastic plate (global domain)

# Appendices

# Appendix A

# Illustration of mesh sensitivity in the post-localization regime of softening materials

In order to illustrate the spurious mesh sensitivity, consider the finite element simulation of a notched 2D plate in Fig. A.1 (left) which is subjected to a prescribed vertical displacement. The material behavior is governed by the constitutive law which is shown in Fig. A.1 (right). As soon as the stress state at a material point attains the yield stress $\sigma_F$, it is assumed that it subsequently undergoes strain softening.

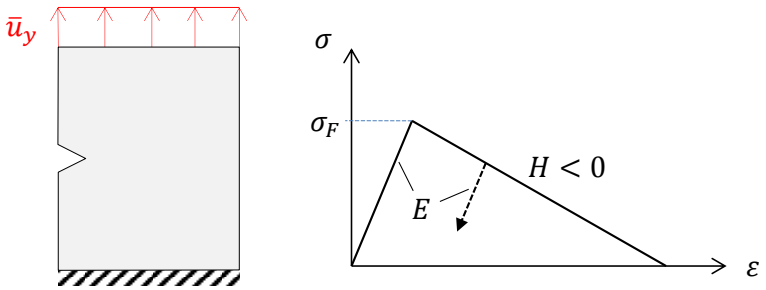


Figure A.1 – Notched plate tensile-loaded with prescribed displacement $\bar{u}_y$ (left) and bi-linear strain softening constitutive law (right)

The finite element analysis is then carried out with three different mesh refinements (implicit integration, 2D plane strain condition, standard 4-node finite element, 4-point Gauss integration). The resulting field of the equivalent softening strain for each of these meshes is shown in Fig. A.2. The corresponding global vertical force-displacement responses are plotted in Fig. A.3.

The following observations can be made:

- The plastic dissipation localizes within a band which has the size of one finite element, irrespective of the mesh size. That implies that the localization band width is not unique.
- The orientation of the localization band is not unique (and thus is not governed by the applied load case).

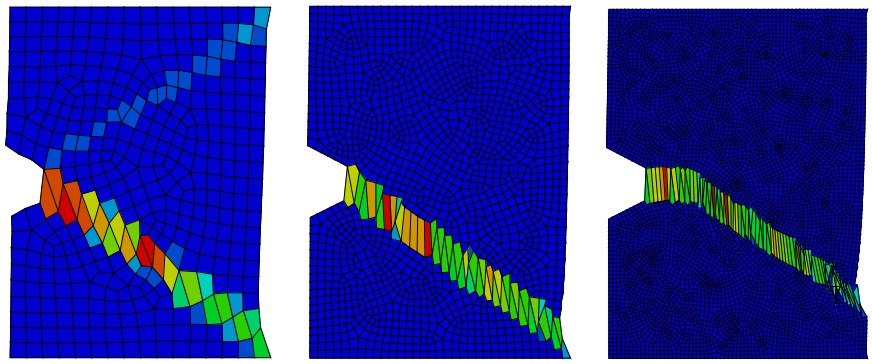

a) b) c)

Figure A.2 – Equivalent softening strain in a 2D notched plate with strain-softening material law with a a) coarse mesh, b) finer mesh and c) very fine mesh

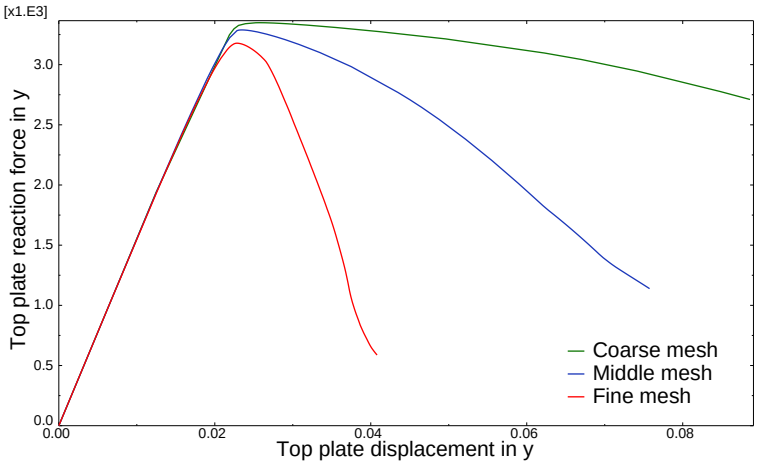


Figure A.3 – Force-displacement curves for the meshes from Fig. A.2

- The post-localization response in the force-displacement plot varies with the mesh size. Reducing the element size goes along with a softer structural behavior.

Each of these meshes represents one possible solution of the same static problem, but constituting different outcomes. In fact it can be shown that there is an infinite number of solutions - the boundary value problem is ill-posed. In the extreme case, the element size is further reduced until it is infinitely small. As a consequence, the strain localization zone becomes infinitely small what effectively corresponds to a mode of zero dissipation energy[1], see e.g. [84]. This leads to the unphysical conclusion that the structure is failing without dissipating energy. **Based on these numerical issues, a reliable estimation of the residual strength of**

[1]This conclusion results from the fact that the dissipated energy is proportional to the area of the highly deformed zone.

**the structure after failure can not be provided.**

This pathologic behavior justifies the intensive research for remedies to achieve objective mesh-independent results in the post-localization regime of the structural response of softening materials and structures.

# Appendix B

# Numerical implementation of the GTN model

The GTN model involving isotropic strain hardening is numerically integrated using the radial return algorithm, see Aravas [7]. The integration is based on a separate consideration of the deviatoric and the hydrostatic part. After mathematical manipulation of equation II.6, an incremental function $\Xi_\Delta$ can be defined

$$\Xi_\Delta = \Delta\epsilon^{pD}\frac{\partial\Phi}{\partial p_m} + \Delta\epsilon^{pM}\frac{\partial\Phi}{\partial\sigma_{eq}} = 0 \tag{B.1}$$

The integration of the following set of non-linear equations

$$\Phi = 0 \tag{B.2}$$

$$\Xi_\Delta = 0 \tag{B.3}$$

$$p_m = p_m^e + K\Delta\epsilon^{pM} \tag{B.4}$$

$$\sigma_{eq} = \sigma_{eq}^e - 3\mu\Delta\epsilon^{pD} \tag{B.5}$$

$$\Delta H = h(\Delta\epsilon^{pD}, \Delta\epsilon^{pM}, \sigma_{eq}, p_m, H) \tag{B.6}$$

can be solved for the primary unknowns $\Delta\epsilon^{pD}$ and $\Delta\epsilon^{pM}$ by applying the Newton-Raphson solution procedure. Here, $\sigma_{eq}^e$ and $p_m^e$ denote the trial functions of the equivalent stress and mean pressure, $\Delta H$ comprises the evolution equations of the state variables.

# Appendix C

# Occurrence and treatment of volumetric locking

Volumetric locking is a numerical phenomenon which occurs in low-order finite elements during (isochoric) plastic deformation leading to spurious pressure stresses at the integration points. This is especially severe for ductile materials which are subjected to a significant plastic deformation and potentially results in a wrong estimation of the residual strength of the fractured structure. Thus it is worth to shortly investigate on the possibility of the occurrence of volumetric locking using the aforementioned GTN material law.

In many material laws, the volumetric plastic deformation is supposed to remain zero as the plastic flow evolves. This is for example valid for a von Mises material where the plastic flow is only influenced by the deviatoric stresses, not by the hydrostatic stresses. That condition corresponds to a nearly-incompressibility of the material. However, when applied to fully-integrated (low-order) finite elements, which are not formulated with incompressible conditions, the pressure stresses can not be well calculated leading to wrong results.

Let us consider the tensile-loaded 2D plate at the very left of Fig. C.1. An exemplary von Mises law with the indicated values is used. The spurious stresses appear in the results of the stress component $\sigma_{xx}$ (midst of Fig. C.1), where a checkerboard-like pattern can be recognized. The stresses oscillate around the correct solution of $0MPa$ with local peaks in the order of $+/-10^5 Pa$.

The handling of that issue consists in separately treating the deviatoric and volumetric strain fields. Over the years, various techniques have been proposed, e.g. mesh refinement, higher order interpolation (see Zienkiewicz [189]), enhanced assumed strain method (Simo [158]), reduced integration with hourglass stabilization (Hughes [78]), selective reduced integration (Hughes [78]) or also the frequently used B-Bar approach (Hughes [76]). When applying the B-Bar approach in the previous plate example, the volumetric locking can be effectively avoided (see the very right of Fig. C.1).

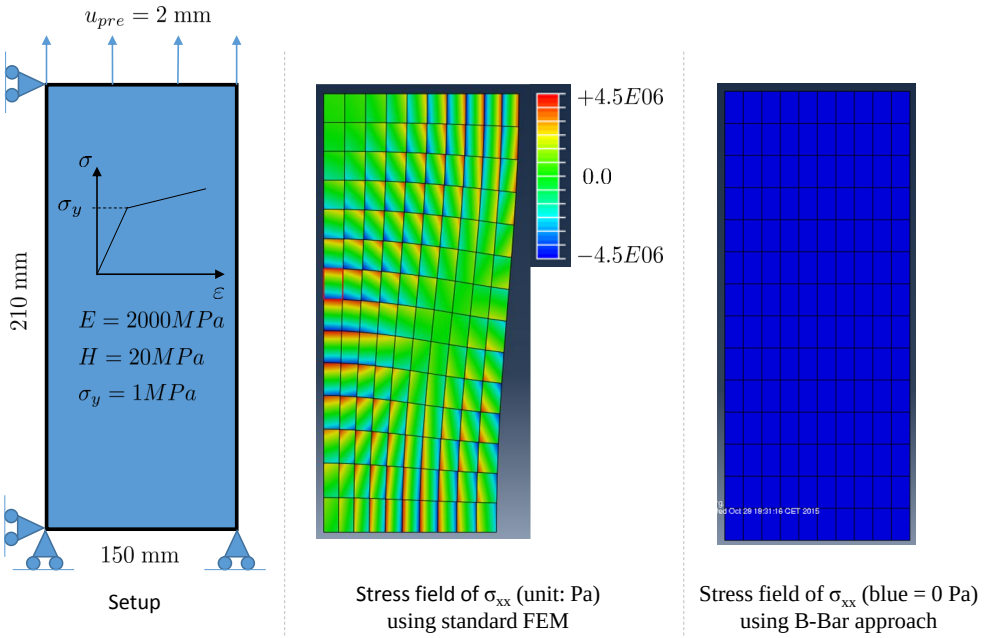


Figure C.1 – Demonstration of volumetric locking and the application of the B-Bar approach using a von Mises constitutive law

As opposed to many ductile material laws, the Gurson-type model considers the volumetric plastic deformation induced by void growth (see equation II.7). Therefore, the material does not behave incompressibly during plastic flow so that volumetric locking should not be an issue, if the Gurson model is used as sole constitutive model. Some authors recommend nevertheless to use a method to prevent volumetric locking in Gurson-type materials. In his thesis, Zhang [187] reports the occurrence of volumetric locking when using a very small initial porosity $f_0$. According to his findings, at the beginning of the damage evolution, the Gurson-type material behaves nearly like a von Mises material so that volumetric locking might be a problem.

In this work, the B-Bar approach is applied to prevent volumetric locking, which appears especially in the early stages of plastic deformation (von Mises plasticity) and damage (if a very small initial porosity is used). For the details of the B-Bar approach and its implementation, the reader is referred to the paper of Hughes [76]. However, the author is conscient about the fact that advanced techniques are necessary to apply the B-Bar approach in the context of enriched FEM during the propagation of the strain localization and the crack (see e.g. the thesis of Seabra [150] for more ideas). The extension of the B-Bar approach is however remained for future works.

# Appendix D

# Bifurcation analysis of the GTN-model

## D.1 Continuum tangent tensor

The localization analysis relies on an accurate computation of the continuum tangent operator $\underset{\approx}{D}^t$ which is derived below for the GTN model presented in section II.3.1.2, see also [147], [74] and [45] for similar solution approaches. Consider the stress-strain-rate relation

$$\dot{\underset{\sim}{\sigma}} = \underset{\approx}{C}^e : \left( \dot{\underset{\sim}{\varepsilon}} - \dot{\lambda} \frac{\partial \Phi}{\partial \underset{\sim}{\sigma}} \right) = \underset{\approx}{D}^t : \dot{\underset{\sim}{\varepsilon}}. \tag{D.1}$$

which involves the elasticity tensor $\underset{\approx}{C}^e$ and the plastic multiplier $\lambda$. Assuming plastic loading ($\dot{\lambda} > 0$), the plastic consistency condition $\dot{\lambda}\dot{\Phi} = 0$ requires that

$$\dot{\Phi}(\underset{\sim}{\sigma}, \kappa, f) = 0 = \underbrace{\frac{\partial \Phi}{\partial \underset{\sim}{\sigma}}}_{\underset{\sim}{\mathcal{N}}} : \dot{\underset{\sim}{\sigma}} + \underbrace{\frac{\partial \Phi}{\partial \kappa}}_{\mathcal{R}} : \dot{\kappa} + \underbrace{\frac{\partial \Phi}{\partial f}}_{\mathcal{F}} : \dot{f}, \tag{D.2}$$

where $\underset{\sim}{\mathcal{N}}$ denotes the direction of plastic flow. Inserting the stress rate D.1, the equivalent plastic strain rate II.5 and the porosity rate $\dot{f}$ into D.2, the plastic multiplier reads

$$\dot{\lambda} = \frac{\underset{\sim}{\mathcal{N}} : \underset{\approx}{C}^e}{\chi} : \dot{\varepsilon}, \tag{D.3}$$

using

$$\chi = \underset{\sim}{\mathcal{N}} : \underset{\approx}{C}^e : \underset{\sim}{\mathcal{N}} - \mathcal{F}(1-f)Tr(\underset{\sim}{\mathcal{N}}) - (\mathcal{F}A_n + \mathcal{R}) \frac{\underset{\sim}{\sigma} : \underset{\sim}{\mathcal{N}}}{(1-f)\sigma_y}. \tag{D.4}$$

Substituting D.4 into D.1 finally leads to the expression of the continuum tangent operator

$$\underset{\approx}{D}^t = \underset{\approx}{C}^e - \frac{(\underset{\approx}{C}^e : \underset{\sim}{\mathcal{N}}) \otimes (\underset{\sim}{\mathcal{N}} : \underset{\approx}{C}^e)}{\chi}. \tag{D.5}$$

## D.2 Analytical bifurcation analysis

An analytical expression for the result of the bifurcation criterion II.15 was elaborated by Oliver [114] and Sanchez [147]. Substituting the tangent operator D.5 into the bifurcation condition II.15 results in

$$\det(\underline{n}\cdot\underset{\sim}{D}^t\cdot\underline{n}) = \det\Bigg(\underbrace{\underline{n}\cdot\underset{\sim}{C}^e\cdot\underline{n}}_{\underset{\sim}{Q}^e} - \frac{(\underline{n}\cdot\underset{\sim}{C}^e : \underset{\sim}{\mathcal{N}})\otimes(\underset{\sim}{\mathcal{N}} : \underset{\sim}{C}^e\cdot\underline{n})}{\chi}\Bigg) = 0. \tag{D.6}$$

$$= \det(\underset{\sim}{Q}^e)\Bigg(1 - \frac{\overbrace{(\underline{n}\cdot\underset{\sim}{C}^e : \underset{\sim}{\mathcal{N}})\cdot\underset{\sim}{Q}^{e-1}\cdot(\underset{\sim}{\mathcal{N}} : \underset{\sim}{C}^e\cdot\underline{n})}^{Z(\underline{n})}}{\chi}\Bigg). \tag{D.7}$$

where $\underset{\sim}{Q}^e$ denotes the elastic acoustic tensor. Since the determinant of $\underset{\sim}{Q}^e$ ([74])

$$\det(\underset{\sim}{Q}^e) = \frac{E(1-\nu)}{(1+\nu)(1-2\nu)}\left[\frac{E}{2(1+\nu)}\right]^2 > 0 \tag{D.8}$$

is positive, the onset of localization occurs when $Z(\underline{n}) = \chi$ is satisfied for the first time. The analytical solution for the critical localization vector $\underline{n}^{crit}$ can be obtained by using a geometrical localization envelope originally developed by Benallal [23] for elasto-plastic materials and adopted for the Gurson model by [114] and Sanchez [147]. It is computed as follows

$$\underline{n}^{crit} = \cos(\theta^{crit})\underline{\Lambda}_I + \sin(\theta^{crit})\underline{\Lambda}_{III}, \tag{D.9}$$

with $\theta^{crit}$ being the critical localization angle computed from

$$\tan^2(\theta^{crit}) = -\frac{\Lambda_{III} - \gamma\Lambda_I}{\Lambda_I - \gamma\Lambda_{III}}\ ; \quad \gamma = \frac{\nu}{1-\nu} \tag{D.10}$$

where $\Lambda_1 > \Lambda_2 > \Lambda_3$ are the eigenvalues associated to the eigenvectors $\underline{\Lambda}_I, \underline{\Lambda}_{II}, \underline{\Lambda}_{III}$ of the tensor $(\underset{\sim}{C}^e : \underset{\sim}{\mathcal{N}})$ (which appears in D.7). Hence, localization analysis consists in computing $\underline{n}^{crit}$ from D.9 and D.10 for every plastic loading step and checking when $Z(\underline{n}) \geq \chi$ is fulfilled for the first time (corresponding to $\det(\underset{\sim}{Q}) \leq 0$).

Based on the expression of the acoustic tensor and advanced studies ([147]) it can be shown that the bifurcation point depends on the stress state $\underset{\sim}{\sigma}$, and the porosity $f$.

# Appendix E

# Supplementary explanations on the X-FEM

## E.1 The singular displacement field in ductile materials

In the case of a strongly non-linear ductile material, as it is the case in this work, the presented X-FEM formulation cannot be adopted directly. First of all, the singular stress at the crack tip is released over the so-called process zone which is plastically deformed. Thus, the stress field at the crack tip is attenuated so that the asymptotic enrichment functions do not apply any more. Also, the determination of the analytical functions involved in the singular enrichment term is very complex for such material so that this singular displacement term is neglected here. Elguedj [53] proposed a method which is based on the singular crack tip fields by Hutchinson, Rice and Rosengren (HRR) assuming a power-hardening material. Despite of the high accuracy of these analytical enrichment functions, the analytical stress field at the crack tip is not a priori known for a GTN material involving a non-linear material behaviour.

In his PhD thesis, Crété [45] conducted numerical tests with a ductile GTN material to analyze if the accuracy of the results significantly deteriorates if the singular enrichment functions are neglected. There, he uses two different displacement formulations:

- Heaviside enrichment to represent the jump across the crack and the asymptotic functions from LEFM to represent the singular stress field (this allows that the crack tip can also be located in the interior of an element)
- solely using the Heaviside enrichment (the asymptotic functions are neglected) whereas the crack tip is necessarily located on the element edges

For both formulations, the evolution of the equivalent stress proposed by Haboussa [68] at the crack tip was tracked in the case of a pre-cracked 2D plate which is loaded in traction. No crack propagation is allowed so that the focus is

on the influence of the stress field at the crack tip. From the results he found out that the use of the singular enrichment functions does not provide a significant difference in accuracy compared to the case where these functions are neglected. He thus proposes to neglect the singular term in the crack tip element and only use the Heaviside enrichment. This also brings another advantage. The number of degrees of freedom per element involving the singular enrichment term is 48 compared to only 16 when they are neglected. Regarding the use of the model in large-scale industrial applications, the reduction of computational costs is an immense advantage.

This simplification also seems reasonable in the case of the representation of the strain localization as a cohesive crack as the singular stress field at the crack tip is strongly attenuated and remains bounded. However we want to refer e.g. to the efforts of Moës [105] who proposed in the case of cohesive cracks non-singular enrichment functions at the crack tip which are proportional to $r^2$ instead of $\sqrt{r}$.

## E.2 Representation of the crack by the level-set method

The enrichment functions $H$ and $F$ are calculated from the coordinates $\phi$ and $\psi$ which capture the crack trajectory and the crack tip position and need to be updated when the crack propagates. Here we use the usually applied concept of level set, first proposed by Osher and Sethian [120] and later adopted also in other domains as e.g. fluid mechanics or fluid-structure interaction (see e.g. Baumgärtner and Wolf [16]). This function is necessary to align the FE mesh with the crack discontinuity by assigning a signed distance value of each node to the discontinuity which represents the trajectory of value zero. The signed distance function $\phi$ of the crack path is defined as follows

$$\phi(\mathbf{x}) = ||\mathbf{x} - \mathbf{x}^*|| sgn\Big(\mathbf{n}(\mathbf{x}^*)(\mathbf{x} - \mathbf{x}^*)\Big) \tag{E.1}$$

where $\mathbf{x}$ represents a material point in the domain, $\mathbf{x}^*$ is the closest-point projection of $\mathbf{x}$ onto the discontinuity and $\mathbf{n}$ is the normal vector of the trajectory. It can be shown that the gradient of $\phi$ is collinear with the normal vector $\mathbf{n}$. In a FE mesh, the (discretized) level set function is computed from the signed distance values of the four nodes of an element $\phi_{i=\{1,2,3,4\}}$

$$\phi^h(\mathbf{x}) = \sum_{i \in I} N_i(\mathbf{x}) \phi_i. \tag{E.2}$$

The crack tip is represented by a second level set function $\psi$ which is computed from the tangential vector at the crack tip $\mathbf{t}$

$$\psi(\mathbf{x}) = (\mathbf{x} - \mathbf{x}')\mathbf{t}(\mathbf{x}') \tag{E.3}$$

whereas $\mathbf{x}'$ is the crack tip point. In the same manner, $\psi$ is discretized in a FE mesh as follows

$$\psi^h(\mathbf{x}) = \sum_{i \in I} N_i(\mathbf{x})\psi_i. \tag{E.4}$$

This function is thus orthogonal to $\phi$ at the crack tip. It should be noted that the Heaviside function is then a direct function of $\phi$ ($H(\mathbf{x}) = sign(\phi(\mathbf{x}))$ and the singular enrichment functions $F$ are direct functions of $\phi$ and $\psi$. The two level set functions need to be updated when the crack propagates, which is normally done by numerically integrating two modified Hamilton-Jacobi equations, one for $\phi$ and one for $\psi$, see e.g. Gravouil [61] for more information. However, here we use a simplified approach, also applied by Stolarska [161] and Crété [45], in which the level set is updated geometrically based on the crack propagation angle and the distance of crack propagation per increment (velocity).

## E.3 Numerical integration

This section discusses the choice of an appropriate integration scheme of the X-FEM considering the use of a non-linear Gurson-type constitutive model.

The standard Gauss integration rule is not precise enough for integration of the discontinuous functions appearing in the computation of the stiffness matrix and the internal force vector.

The most common technique, proposed by Moës [106] consists in subdividing the cut element into triangles and applying the standard Gauss rule to each of these triangles (see Fig. E.1). When a crack passes through an element, a mapping of the state variables at each of the standard Gauss points to the new Gauss points of the subdivided triangles needs to be performed.

Although this method provides an accurate integration of the element, it is not suitable for ductile materials with a significant phase of plastification. For this type of materials, the state variables at each Gauss point are history-dependent. This implies that the mapping of the state variables from the Gauss points of the regular FE to the Gauss points of the triangles of the subdivided element is not trivial at all and is accompanied with numerical challenges. Furthermore the conservation

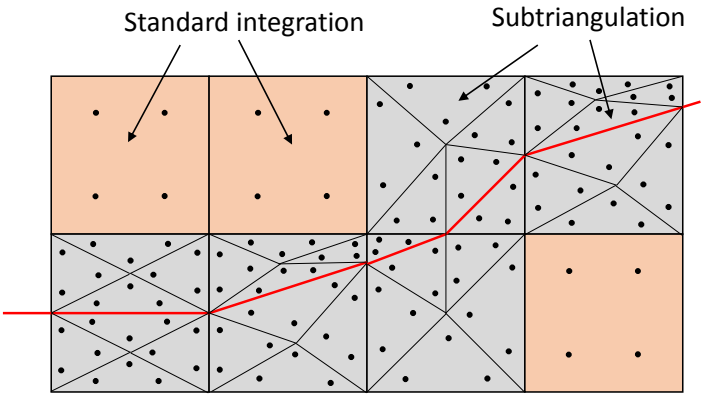


Figure E.1 – Subdivision of the cut elements into triangles which are integrated using standard Gauss rule. All the other elements use 4-point Gauss integration.

of energy during the projection of the state variables is not guaranteed. On top of that, the application of such mapping is in contradiction with the powerful advantage of the X-FEM to avoid cumbersome remeshing and projection. An alternative approach for elasto-plastic materials was proposed by Elguedj [53] which is based on a subdivision into 16 regular quadrilaterals (see Fig. E.2). Each of these quadrilaterals is integrated using a standard 4-point integration rule giving in total 64 fixed Gauss points per cut element. This approach provides a reasonable approximation of the integrals involving discontinuous functions.

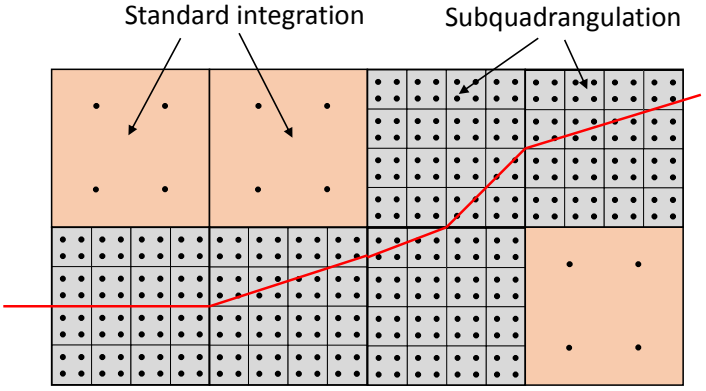


Figure E.2 – Subdivision of the cut elements into 16 quadrilaterals which are integrated using standard 4-point integration rule.

This integration scheme with a largely increased number of points was also applied in the PhD thesis of Crété [45] in the context of a GTN-material. In order to avoid the projection of the fields from the 4-point scheme to the 64-point scheme, he uses the 64-point scheme already from the beginning of the simulation in all those elements which might possibly undergo cracking throughout the simulation. To this end, he defines already in the design phase a zone where cracking will

probably occur. All elements in this zone are then integrated with the 64-point rule throughout the entire simulation, although it might be possible that some elements won't crack.

That integration method is well suited for ductile materials, but it is extremely costly in terms of computational time, especially with regard to large structure in the industrial context. Alternatively, Ventura [176] proposed a method which works without subdivision. That method relies on replacing the integrals involving the discontinuous functions by continuous polynomial functions which can be integrated using standard integration rules. Benvenuti [25] exploited the Ventura integration scheme to integrate regularized discontinuities. Though this applies to triangular elements and not for quadrilaterals.

# Bibliography


[1] S. Abbas, A. Alizada, and T.-P. Fries. The xfem for high-gradient solutions in convection-dominated problems. *International Journal for Numerical Methods in Engineering*, 82:1044–1072, 2010.

[2] H. Ahmadian, S. H. Ardakani, and S. Mohammadi. Strain-rate sensitivity of unstable localized phase transformation phenomenon in shape memory alloys using a non-local model. *International Journal of Solids and Structures*, 63:167–183, 2015.

[3] J. Alfaiate, A. Simone, and L. J. Sluys. Non-homogeneous displacement jumps in strong embedded discontinuities. *International Journal of Solids and Structures*, 40(21):5799–5817, 2003.

[4] G. Alfano. On the influence of the shape of the interface law on the application of cohesive-zone models. *Composites Science and Technology*, 66(6):723–730, 2006.

[5] M. Ambati, T. Gerasimov, and L. De Lorenzis. Phase-field modeling of ductile fracture. *Computational Mechanics*, 55(5):1017–1040, 2015.

[6] M. Anvari, I. Scheider, and C. Thaulow. Simulation of dynamic ductile crack growth using strain-rate and triaxiality-dependent cohesive elements. *Engineering Fracture Mechanics*, 73:2210–2228, 2006.

[7] N. Aravas. On the numerical integration of a class of pressure-dependent plasticity models. *International Journal for Numerical Methods in Engineering*, 24(7):1395–1416, 1987.

[8] P. Areias and T. Belytschko. Two-scale shear band evolution by local partition of unity. *International Journal for Numerical Methods in Engineering*, 66(5):878–910, 2006.

[9] P. Areias and T. Belytschko. Two-scale method for shear bands: thermal effects and variable bandwidth. *International Journal for Numerical Methods in Engineering*, 72(6):658–696, 2007.

[10] F. Armero and K. Garikipati. An analysis of strong discontinuities in multiplicative finite strain plasticity and their relation with the numerical simulation of strain localization in solids. *International Journal of Solids and Structures*, 33(20):2863–2885, 1996.

[11] H. Autenrieth, V. Schulze, N. Herzig, and L. W. Meyer. Ductile failure model for the description of aisi 1045 behavior under different loading conditions. *Mechanics of Time-Dependent Materials*, 13(3):215–231, 2009.

[12] Y. L. Bai. Thermo-plastic instability in simple shear. *Journal of the Mechanics and Physics of Solids*, 30:195–207, 1982.

[13] A. Banerjee and R. Manivasagam. Triaxiality dependent cohesive zone model. *Engineering Fracture Mechanics*, 76:1761–1770, 2009.

[14] G. I. Barenblatt. The formation of equilibrium cracks during brittle fracture. general ideas and hypotheses. axially-symmetric cracks. *Journal of Applied Mathematics and Mechanics*, 23(3):622–636, 1959.

[15] G. I. Barenblatt. The mathematical theory of equilibrium cracks in brittle fracture. *Advances in Applied Mechanics*, 7:55–129, 1962.

[16] D. Baumgärtner, J. Wolf, R. Rossi, R. Wüchner, and P. Dadvand. *Contribution to the fluid-structure interaction analysis of ultra-lightweight structures using an embedded approach*. CIMNE, 1 edition, 2015.

[17] Z. P. Bažant, T. Belytschko, and T.-P. Chang. Continuum theory for strain-softening. *Journal of Engineering Mechanics*, 110(12):1666–1692, 1984.

[18] T. Belytschko and T. Black. Elastic crack growth in finite elements with minimal remeshing. *International Journal for Numerical Methods in Engineering*, 45(5):601–620, 1999.

[19] T. Belytschko, H. Chen, J. Xu, and G. Zi. Dynamic crack propagation based on loss of hyperbolicity and a new discontinuous enrichment. *International Journal for Numerical Methods in Engineering*, 58(12):1873–1905, 2003.

[20] T. Belytschko, J. Fish, and B. E. Engelman. A finite element with embedded localization zones. *Computer Methods in Applied Mechanics and Engineering*, 70:59–89, 1988.

[21] T. Belytschko, Y. Y. Lu, and L. Gu. Element-free galerkin methods. *International Journal for Numerical Methods in Engineering*, 37(2):229–256, 1994.

[22] T. Belytschko, D. Organ, and C. Gerlach. Element-free galerkin methods for dynamic fracture in concrete. *Computer Methods in Applied Mechanics and Engineering*, 187(3):385–399, 2000.

[23] A. Benallal and C. Comi. Localization analysis via a geometrical method. *International Journal of Solids and Structures*, 33(1):99–119, 1996.

[24] E. Benvenuti and A. Tralli. Simulation of finite-width process zone in concrete-like materials by means of a regularized extended finite element model. *Computational Mechanics*, 50:479–497, 2012.

[25] E. Benvenuti, A. Tralli, and G. Ventura. A regularized xfem model for the transition from continuous to discontinuous displacements. *International Journal for Numerical Methods in Engineering*, 74(6):911–944, 2008.

[26] A. A. Benzerga. Micromechanics of coalescence in ductile fracture. *Journal of the Mechanics and Physics of Solids*, 50(6):1331–1362, 2002.

[27] A. A. Benzerga, J. Besson, and A. Pineau. Coalescence-controlled anisotropic ductile fracture. *Journal of Engineering Materials and Technology*, 121(2):221–229, 1999.

[28] A. H. Berends, L. J. Sluys, and R. de Borst. Discontinuous modelling of mode-i failure. In D.R.J. Owen, E. Onate, and E. Hinton, editors, *Computational Plasticity: Fundamentals and Applications*, volume 1, pages 751–758. International Center for Numerical Methods in Engineering, 1997.

[29] J. Besson, D. Steglich, and W. Brocks. Modeling of plane strain ductile rupture. *International Journal of Plasticity*, 19(10):1517–1541, 2003.

[30] S. Bordas, T. Rabczuk, and G. Zi. Three-dimensional crack initiation, propagation, branching and junction in non-linear materials by an extended meshfree method without asymptotic enrichment. *Engineering Fracture Mechanics*, 75(5):943–960, 2008.

[31] P.-O. Bouchard, F. Bay, Y. Chastel, and I. Tovena. Crack propagation modelling using an advanced remeshing technique. *Computer Methods in Applied Mechanics and Engineering*, 189(3):723–742, 2000.

[32] P. Broumand and A. R. Khoei. X-fem modeling of dynamic ductile fracture problems with a nonlocal damage-viscoplasticity model. *Finite Elements in Analysis and Design*, 99:49–67, 2015.

[33] G. T. Camacho and M. Ortiz. Computational modelling of impact damage in brittle materials. *International Journal of Solids and Structures*, 33(20):2899–2938, 1996.

[34] P. P. Camanho and C. G. Dávila. Mixed-mode decohesion finite elements for the simulation of delamination in composite materials. Technical report, NASA, 2002.

[35] B. J. Carter, P. A. Wawrzynek, and A. R. Ingraffea. Automated 3-d crack growth simulation. *International Journal for Numerical Methods in Engineering*, 47(1-3):229–253, 2000.

[36] F. Cazes, M. Coret, A. Combescure, and A. Gravouil. A thermodynamic method for the construction of a cohesive law from a nonlocal damage model. *International Journal of Solids and Structures*, 46(6):1476–1490, 2009.

[37] F. Cazes, A. Simatos, M. Coret, and A. Combescure. A cohesive zone model which is energetically equivalent to a gradient-enhanced coupled damage-plasticity model. *European Journal of Mechanics-A/Solids*, 29(6):976–989, 2010.

[38] Cedre. Limburg, 05 2016.

[39] Z. Cen and G. Maier. Bifurcations and instabilities in fracture of cohesive-softening structures: a boundary element analysis. *Fatigue and Fracture of Engineering Materials and Structures*, 15(9):911–928, 1992.

[40] C. R. Chen, O. Kolednik, J. Heerens, and F. D. Fischer. Three-dimensional modeling of ductile crack growth: Cohesive zone parameters and crack tip triaxiality. *Engineering Fracture Mechanics*, 72(13):2072–2094, 2005.

[41] X. Chen, X. Deng, M. A. Sutton, and P. Zavattieri. An inverse analysis of cohesive zone model parameter values for ductile crack growth simulations. *International Journal of Mechanical Sciences*, 79:206–215, 2014.

[42] G. P. Cherepanov. Crack propagation in continuous media. *Journal of Applied Mathematics and Mechanics*, 31(3):503–512, 1967.

[43] C. C. Chu and A. Needleman. Void nucleation effects in biaxially stretched sheets. *Journal of Engineering Materials and Technology*, 102(3):249–256, 1980.

[44] R. J. Clifton. Material response to ultra-high loading rates. *NRC National Material Advisory Board (US) Report*, 356:129–142, 1980.

[45] J.-P. Crété. *Traitement numérique de la fissuration d'une structure navale*. PhD thesis, Université de Bretagne Sud, 2013.

[46] J.-P. Crété, P. Longère, and J.-M. Cadou. Numerical modelling of crack propagation in ductile materials combining the GTN model and X-FEM. *Computer Methods in Applied Mechanics and Engineering*, 275:204–233, 2014.

[47] D. Dias-da Costa, J. Alfaiate, L. J. Sluys, and E. N. B. S. Júlio. Towards a generalization of a discrete strong discontinuity approach. *Computer Methods in Applied Mechanics and Engineering*, 198(47):3670–3681, 2009.

[48] D. Dias-da Costa, J. Alfaiate, L. J. Sluys, and E. N. B. S. Júlio. A comparative study on the modelling of discontinuous fracture by means of enriched nodal and element techniques and interface elements. *International Journal of Fracture*, 161(1):97–119, 2010.

[49] D. S. Dugdale. Yielding of steel sheets containing slits. *Journal of the Mechanics and Physics of Solids*, 8:100–108, 1960.

[50] P. Dumstorff and G. Meschke. Crack propagation criteria in the framework of x-fem-based structural analyses. *International Journal for Numerical and Analytical Methods in Geomechanics*, 31(2):239–259, 2007.

[51] M. Duval. *Apports du couplage non-intrusif en mécanique non-linéaire des structures*. PhD thesis, UPS Toulouse, 2016.

[52] E. N. Dvorkin, A. M. Cuitiño, and G. Gioia. Finite elements with displacement interpolated embedded localization lines insensitive to mesh size and distortions. *International Journal for Numerical Methods in Engineering*, 30(3):541–564, 1990.

[53] T. Elguedj, A. Gravouil, and A. Combescure. Appropriate extended functions for x-fem simulation of plastic fracture mechanics. *Computer Methods in Applied Mechanics and Engineering*, 195(7):501–515, 2006.

[54] C. Feist and G. Hofstetter. An embedded strong discontinuity model for cracking of plain concrete. *Computer Methods in Applied Mechanics and Engineering*, 195(52):7115–7138, 2006.

[55] T.-P. Fries and T. Belytschko. The extended/generalized finite element method: an overview of the method and its applications. *International Journal for Numerical Methods in Engineering*, 84(3):253–304, 2010.

[56] W. M. Garrison and N. R. Moody. Ductile fracture. *Journal of Physics and Chemistry of Solids*, 48(11):1035–1074, 1987.

[57] A.-G. Geffroy. *Modélisation numérique de la rupture de structures navales sous l'effet d'explosions au contact*. PhD thesis, Université de Bretagne Sud, 2010.

[58] A.-G. Geffroy, P. Longère, and B. Leblé. Fracture analysis and constitutive modelling of ship structure steel behaviour regarding explosion. *Engineering Failure Analysis*, 18(2):670–681, 2011.

[59] C. Geuzaine and J.-F. Remacle. Gmsh: A 3-d finite element mesh generator with built-in pre- and post-processing facilities. *International Journal for Numerical Methods in Engineering*, 79(11):1309–1331, 2009.

[60] D. E. Grady. Dissipation in adiabatic shear bands. *Mechanics of Materials*, 17:289–293, 1994.

[61] A. Gravouil, N. Moës, and T. Belytschko. Non-planar 3d crack growth by the extended finite element and level sets - part ii: Level set update. *International Journal for Numerical Methods in Engineering*, 53(11):2569–2586, 2002.

[62] J. P. Gray and J. J. Monaghan. Numerical modelling of stress fields and fracture around magma chambers. *Journal of Volcanology and Geothermal Research*, 135(3):259–283, 2004.

[63] A. A. Griffith. The phenomena of rupture and flow in solids. *Philosophical Transactions of the Royal Society of London. Series A*, 221:163–198, 1921.

[64] G. V. Guinea, M. Elices, and J. Planas. On the initial shape of the softening function of cohesive materials. *International Journal of Fracture*, 87(2):139–149, 1997.

[65] A. S. Gullerud, X. Gao, R. H. Dodds, and R. Haj-Ali. Simulation of ductile crack growth using computational cells: numerical aspects. *Engineering Fracture Mechanics*, 66(1):65–92, 2000.

[66] A. L. Gurson. Continuum theory of ductile rupture by void nucleation and growth: Part i - yield criteria and flow rules for porous ductile media. *Journal of Engineering Materials and Technology*, 99(1):2–15, 1977.

[67] D. Haboussa, T. Elguedj, B. Leblé, and A. Combescure. Simulation of the shear-tensile mode transition on dynamic crack propagations. *International Journal of Fracture*, 178(1-2):195–213, 2012.

[68] D. Haboussa, D. Grégoire, T. Elguedj, H. Maigre, and A. Combescure. X-fem analysis of the effects of holes or other cracks on dynamic crack propagations. *International Journal for Numerical Methods in Engineering*, 86(4-5):618–636, 2011.

[69] J. Hadamard. Sur les problèmes aux dérivées partielles et leur signification physique. *Princeton University Bulletin*, 13:49–52, 1902.

[70] J. W. Hancock and A. C. Mackenzie. On the mechanisms of ductile failure in high-strength steels subjected to multi-axial stress-states. *Journal of the Mechanics and Physics of Solids*, 24:147–160, 1976.

[71] R. Hill. A general theory of uniqueness and stability in elastic-plastic solids. *Journal of the Mechanics and Physics of Solids*, 6:236–249, 1958.

[72] R. Hill. Acceleration waves in solids. *Journal of the Mechanics and Physics of Solids*, 10:1–16, 1962.

[73] A. Hillerborg, M. Modéer, and P.-E. Petersson. Analysis of crack formation and crack growth in concrete by means of fracture mechanics and finite elements. *Cement and Concrete Research*, 6:773–782, 1976.

[74] A. E. Huespe, A. Needleman, J. Oliver, and P. J. Sanchez. A finite thickness band method for ductile fracture analysis. *International Journal of Plasticity*, 25(12):2349–2365, 2009.

[75] A. E. Huespe, A. Needleman, J. Oliver, and P. J. Sánchez. A finite strain, finite band method for modeling ductile fracture. *International Journal of Plasticity*, 28:53–69, 2012.

[76] T. J. R. Hughes. Generalization of selective integration procedures to anisotropic and nonlinear media. *International Journal for Numerical Methods in Engineering*, 15(9):1413–1418, 1980.

[77] T. J. R. Hughes. Multiscale phenomena: Green's functions, the Dirichlet-to-Neumann formulation, subgrid scale models, bubbles and the origins of stabilized methods. *Computer Methods in Applied Mechanics and Engineering*, 127(1):387–401, 1995.

[78] T. J. R. Hughes, W. K. Liu, and A. Brooks. Finite element analysis of incompressible viscous flows by the penalty function formulation. *Journal of Compuational Physics*, 30:1–60, 1979.

[79] G. R. Irwin. Analysis of stresses and strains near the end of a crack traversing a plate. *Journal of Applied Mechanics*, 24:361–364, 1957.

[80] Y. Jan. *Modélisation de la propagation de fissure sur des structures minces, soumises à des sollicitations intenses et rapides, par la méthode X-FEM.* PhD thesis, INSA de Lyon, 2016.

[81] M. Jirásek. Comparative study on finite elements with embedded discontinuities. *Computer Methods in Applied Mechanics and Engineering*, 188:307–330, 2000.

[82] M. Jirásek. Conditions of uniqueness for finite elements with embedded cracks. In *European Congress on Computational Methods in Applied Sciences and Engineering*, 2000.

[83] M. Jirásek. Objective modeling of strain localization. *Revue française de génie civil*, 6(6):1119–1132, 2002.

[84] M. Jirásek. Mathematical analysis of strain localization. *Revue européenne de génie civil*, 11(7-8):977–991, 2007.

[85] M. Jirásek and T. Belytschko. Computational resolution of strong discontinuities. In H.A. Mang, F.G. Rammerstorfer, and J. Eberhardsteiner, editors, *Fifth World Congress on Computational Mechanics*, Vienna, 2002.

[86] G. R. Johnson and W. H. Cook. Fracture characteristics of three metals subjected to various strains, strain rates, temperatures and pressures. *Engineering Fracture Mechanics*, 21(1):31–48, 1985.

[87] J. F. Kalthoff and S. Winkler. Failure mode transition at high rates of shear loading. *DGM Informationsgesellschaft mbH, Impact Loading and Dynamic Behavior of Materials*, 1:185–195, 1988.

[88] M. Klisinski, K. Runesson, and S. Sture. Finite element with inner softening band. *Journal of Engineering Mechanics*, 117(3):575–587, 1991.

[89] K. Komori. Proposal and use of a void model for the simulation of ductile fracture behavior. *Acta Materialia*, 47(10):3069–3077, 1999.

[90] U. Krupp. *Fatigue crack propagation in metals and alloys: microstructural aspects and modelling concepts*. John Wiley & Sons, 2007.

[91] R. Larsson, K. Runesson, and S. Sture. Embedded localization band in undrained soil based on regularized strong discontinuity - theory and fe-analysis. *International Journal of Solids and Structures*, 33(20):3081–3101, 1996.

[92] J. Lemaitre. A continuous damage mechanics model for ductile fracture. *Journal of Engineering Materials and Technology*, 107(1):83–89, 1985.

[93] H. Li and N. Chandra. Analysis of crack growth and crack-tip plasticity in ductile materials using cohesive zone models. *International Journal of Plasticity*, 19(6):849–882, 2003.

[94] W. B. Lievers, A. K. Pilkey, and M. J. Worswick. The co-operative role of voids and shear bands in strain localization during bending. *Mechanics of Materials*, 35(7):661–674, 2003.

[95] P. Longère, A. Dragon, H. Trumel, T. de Resseguier, X. Deprince, and E. Petitpas. Modelling adiabatic shear banding via damage mechanics approach. *Archives of Mechanics*, 55:3–38, 2003.

[96] P. Longère, A. Dragon, H. Trumel, and X. Deprince. Adiabatic shear banding-induced degradation in a thermo-elastic/viscoplastic material under dynamic loading. *International Journal of Impact Engineering*, 32(1):285–320, 2005.

[97] P. Longère, A.-G. Geffroy, B. Leblé, and A. Dragon. Modeling the transition between dense metal and damaged (microporous) metal viscoplasticity. *International Journal of Damage Mechanics*, 21(7):1020–1063, 2012.

[98] H. R. Lotfi and P. B. Shing. Embedded representation of fracture in concrete with mixed finite elements. *International Journal for Numerical Methods in Engineering*, 38(8):1307–1325, 1995.

[99] E. Maire, O. Bouaziz, M. Di Michiel, and C. Verdu. Initiation and growth of damage in a dual-phase steel observed by x-ray microtomography. *Acta Materialia*, 56(18):4954–4964, 2008.

[100] E. Maire, J.-Y. Buffiere, L. Salvo, J. J. Blandin, W. Ludwig, and J. M. Letang. On the application of x-ray microtomography in the field of materials science. *Advanced Engineering Materials*, 3(8):539–546, 2001.

[101] J. Mandel. Conditions de stabilité et postulat de Drucker. In J. Kravtchenko and P. Sirieys, editors, *Rhéologie et mécanique des sols*. Springer-Verlag, 1966.

[102] J. Mazars and G. Pijaudier-Cabot. From damage to fracture mechanics and conversely: a combined approach. *International Journal of Solids and Structures*, 33(20):3327–3342, 1996.

[103] J. M. Melenk and I. Babuška. The partition of unity finite element method: Basic theory and applications. *Computer Methods in Applied Mechanics and Engineering*, 139(1):289–314, 1996.

[104] T. Menouillard. *Dynamique explicite pour la simulation numérique de propagation de fissure par la méthode des éléments finis étendus*. PhD thesis, INSA de Lyon, 2007.

[105] N. Moës and T. Belytschko. Extended finite element method for cohesive crack growth. *Engineering Fracture Mechanics*, 69(7):813–833, 2002.

[106] N. Moës, J. Dolbow, and T. Belytschko. A finite element method for crack growth without remeshing. *International Journal for Numerical Methods in Engineering*, 46:131–150, 1999.

[107] N. Moës, C. Stolz, P.-E. Bernard, and N. Chevaugeon. A level set based model for damage growth: the thick level set approach. *International Journal for Numerical Methods in Engineering*, 86(3):358–380, 2011.

[108] A. Molinari. Instabilité thermo-visco-plastique en cisaillement simple. *Journal de Mécanique Théorique et Appliquée*, 4:659–684, 1985.

[109] T. F. Morgeneyer, M. J. Starink, and I. Sinclair. Evolution of voids during ductile crack propagation in an aluminium alloy sheet toughness test studied by synchrotron radiation computed tomography. *Acta Materialia*, 56(8):1671–1679, 2008.

[110] A. Needleman. A continuum model for void nucleation by inclusion debonding. *Journal of Applied Mechanics*, 54(3):525–531, 1987.

[111] A. Needleman and V. Tvergaard. On the finite element analysis of localized plastic deformation. In J.T. Oden and G. Carey, editors, *Finite Elements - Special Problems in Solid Mechanics*, pages 94–157. Prentice-Hall, 1983.

[112] J. Oliver. Modeling strong discontinuities in solid mechanics viq strain softening constitutive equations. part 1: Fundamentals. part 2: Numerical simulation. *International Journal for Numerical Methods in Engineering*, 39:3575–3624, 1996.

[113] J. Oliver and A. E. Huespe. Continuum approach to material failure in strong discontinuity settings. *Computer Methods in Applied Mechanics and Engineering*, 193:3195–3220, 2004.

[114] J. Oliver and A. E. Huespe. Theoretical and computational issues in modelling material failure in strong discontinuity scenarios. *Computer Methods in Applied Mechanics and Engineering*, 193(27):2987–3014, 2004.

[115] J. Oliver, A. E. Huespe, S. Blanco, and D. L. Linero. Stability and robustness issues in numerical modeling of material failure with the strong discontinuity approach. *Computer Methods in Applied Mechanics and Engineering*, 195(52):7093–7114, 2006.

[116] J. Oliver, A. E. Huespe, and J. C. Cante. An implicit/explicit integration scheme to increase computability of non-linear material and contact/friction problems. *Computer Methods in Applied Mechanics and Engineering*, 197:1865–1889, 2008.

[117] J. Oliver, A. E. Huespe, and P. J. Sanchez. A comparative study on finite elements for capturing strong discontinuities: E-fem vs. x-fem. *Computer Methods in Applied Mechanics and Engineering*, 195:4732–4752, 2006.

[118] M. Ortiz and A. Pandolfi. Finite-deformation irreversible cohesive elements for three-dimensional crack-propagation analysis. *International Journal for Numerical Methods in Engineering*, 44(9):1267–1282, 1999.

[119] M. Ortiz, Leroy Y., and A. Needleman. A finite element method for localized failure analysis. *Computer Methods in Applied Mechanics and Engineering*, 61:189–214, 1987.

[120] S. Osher and J. A. Sethian. Fronts propagating with curvature-dependent speed: algorithms based on hamilton-jacobi formulations. *Journal of Computational Physics*, 79(1):12–49, 1988.

[121] N. S. Ottosen and K. Runesson. Properties of discontinuous bifurcation solutions in elasto-plasticity. *International Journal of Solids and Structures*, 27(4):401–421, 1991.

[122] T. Pardoen, I. Doghri, and F. Delannay. Experimental and numerical comparison of void growth models and void coalescence criteria for the prediction of ductile fracture in copper bars. *Acta Materialia*, 46(2):541–552, 1998.

[123] T. Pardoen and J. W. Hutchinson. An extended model for void growth and coalescence. *Journal of the Mechanics and Physics of Solids*, 48(12):2467–2512, 2000.

[124] B. Patzák and M. Jirásek. Process zone resolution by extended finite elements. *Engineering Fracture Mechanics*, 70(7):957–977, 2003.

[125] Agenzia Nazionale per la Sicurezza del Volo (ANSV). Rapporto d'inchiesta - inconveniente grave occorso all'aeromobile boeing 767-432-er, marche n834mh. Technical report, ANSV, 2007.

[126] P. Perzyna. Stability of flow processes for dissipative solids with internal imperfections. *Zeitschrift für angewandte Mathematik und Physik*, 35(6):848–867, 1984.

[127] G. Pijaudier-Cabot and Z. Bažant. Nonlocal damage theory. *Journal of Engineering Mechanics*, 113(10):1512–1533, 1987.

[128] A. Portela, M. H. Aliabadi, and D. P. Rooke. The dual boundary element method: effective implementation for crack problems. *International Journal for Numerical Methods in Engineering*, 33(6):1269–1287, 1992.

[129] R. Pourmodheji and M. Mashayekhi. Improvement of the extended finite element method for ductile crack growth. *Materials Science and Engineering*, 551:255–271, 2012.

[130] B. Prabel. *Modélisation avec la méthode X-FEM de la propagation dynamique et de l'arrêt de fissure de clivage dans un acier de cuve REP*. PhD thesis, INSA de Lyon, 2007.

[131] N. Pugno, M. Ciavarella, P. Cornetti, and A. Carpinteri. A generalized Paris law for fatigue crack growth. *Journal of the Mechanics and Physics of Solids*, 54(7):1333–1349, 2006.

[132] L. Qian, H. Toda, K. Uesugi, T. Kobayashi, T. Ohgaki, and M. Kobayashi. Application of synchrotron x-ray microtomography to investigate ductile fracture in al alloys. *Applied Physics Letters*, 87(24):241907, 2005.

[133] G. N. Rabotnov and S. A. Shesterikov. Creep stability of columns and plates. *Journal of the Mechanics and Physics of Solids*, 6:27–34, 1957.

[134] R. F. Recht. Catastrophic thermoplastic shear. *Journal of Applied Mechanics*, 31(2):189–193, 1964.

[135] J. J. C. Remmers, R. de Borst, and A. Needleman. A cohesive segments method for the simulation of crack growth. *Computational Mechanics*, 31(1-2):69–77, 2003.

[136] J. J. C. Remmers, R. de Borst, and A. Needleman. The simulation of dynamic crack propagation using the cohesive segments method. *Journal of the Mechanics and Physics of Solids*, 56(1):70–92, 2008.

[137] J. J. C. Remmers, R. de Borst, C. V. Verhoosel, and A. Needleman. The cohesive band model: a cohesive surface formulation with stress triaxiality. *International Journal of Fracture*, 181(2):177–188, 2013.

[138] J. Réthoré, A. Gravouil, and A. Combescure. A stable numerical scheme for the finite element simulation of dynamic crack propagation with remeshing. *Computer Methods in Applied Mechanics and Engineering*, 193(42):4493–4510, 2004.

[139] J. R. Rice. A path independent integral and the approximate analysis of strain concentration by notches and cracks. *Journal of Applied Mechanics*, 35(2):379–386, 1968.

[140] J. R. Rice. The localization of plastic deformation. In W.T. Koiter, editor, *Theoretical and Applied Mechanics*, volume 1, pages 207–220, North-Holland, Amsterdam, 1976.

[141] C. Roucoules, P. D. Hodgson, S. Yue, and J. J. Jonas. Softening and microstructural change following the dynamic recrystallization of austenite. *Metallurgical and Materials Transactions A*, 25(2):389–400, 1994.

[142] G. Rousselier. Ductile fracture models and their potential in local approach of fracture. *Nuclear Engineering and Design*, 105(1):97–111, 1987.

[143] E. Roux, P. Longère, O. Cherrier, T. Millot, D. Capdeville, and J. Petit. Analysis of asb assisted failure in a high strength steel under high loading rate. *Materials & Design*, 75:149–159, 2015.

[144] J. W. Rudnicki and J. R. Rice. Conditions for the localization of deformation in pressure-sensitive dilatant materials. *Journal of the Mechanics and Physics of Solids*, 23:371–394, 1975.

[145] A. L. Saleh and M. H. Aliabadi. Crack growth analysis in concrete using boundary element method. *Engineering Fracture Mechanics*, 51(4):533–545, 1995.

[146] E. Samaniego and T. Belytschko. Continuum-discontinuum modelling of shear bands. *International Journal for Numerical Methods in Engineering*, 62:1857–1872, 2005.

[147] P. J. Sánchez, A. E. Huespe, and J. Oliver. On some topics for the numerical simulation of ductile fracture. *International Journal of Plasticity*, 24:1008–1038, 2008.

[148] I. Scheider. Derivation of separation laws for cohesive models in the course of ductile fracture. *Engineering Fracture Mechanics*, 76(10):1450–1459, 2009.

[149] I. Scheider and W. Brocks. The effect of the traction separation law on the results of cohesive zone crack propagation analyses. In *Key Engineering Materials*, volume 251, pages 313–318, 2003.

[150] M. R. R. Seabra. *Continuous-Discontinuous Approach for the Modelling of Ductile Fracture*. PhD thesis, University of Porto, 2012.

[151] B. Shen and G. H. Paulino. Direct extraction of cohesive fracture properties from digital image correlation: a hybrid inverse technique. *Experimental Mechanics*, 51(2):143–163, 2011.

[152] T. Siegmund and W. Brocks. *Tensile decohesion by local failure criteria*. GKSS-Forschungszentrum, 1999.

[153] T. Siegmund and W. Brocks. A numerical study on the correlation between the work of separation and the dissipation rate in ductile fracture. *Engineering Fracture Mechanics*, 67(2):139–154, 2000.

[154] A. Simatos. *Méthode XFEM pour la modélisation de grandes propagations de fissure en déchirure ductile*. PhD thesis, INSA de Lyon, 2010.

[155] D. C. Simkins and S. Li. Meshfree simulations of thermo-mechanical ductile fracture. *Computational Mechanics*, 38(3):235–249, 2006.

[156] J. C. Simo and T. J. R. Hughes. *Computational Inelasticity*, volume 7. Springer Science & Business Media, 2006.

[157] J. C. Simo and J. Oliver. A new approach to the analysis and simulation of strain softening in solids. In Z.P. Bažant, Z. Bittnar, M. Jirásek, and J. Mazars, editors, *Fracture and damage in quasi-brittle structures*, pages 25–39, London, 1994. E & FN Spon.

[158] J. C. Simo and M. S. Rifai. A class of mixed assumed strain methods and the method of incompatible modes. *International Journal for Numerical Methods in Engineering*, 29:1595–1638, 1990.

[159] L. J. Sluys. Discontinuous modeling of shear banding. In D.R.J Owen, E. Onate, and E. Hinton, editors, *Computational Plasticity COMPLAS V*. CIMNE., Barcelona, Spain, 1997.

[160] J.-H. Song, H. Wang, and T. Belytschko. A comparative study on finite element methods for dynamic fracture. *Computational Mechanics*, 42(2):239–250, 2008.

[161] M. Stolarska, D. L. Chopp, N. Moës, and T. Belytschko. Modelling crack growth by level sets in the extended finite element method. *International Journal for Numerical Methods in Engineering*, 51(8):943–960, 2001.

[162] S. Su and L. Stainier. Energy-based variational modeling of adiabatic shear bands structure evolution. *Mechanics of Materials*, 80:219–233, 2015.

[163] N. Sukumar, D. L. Chopp, and B. Moran. Extended finite element method and fast marching method for three-dimensional fatigue crack propagation. *Engineering Fracture Mechanics*, 70(1):29–48, 2003.

[164] N. Tardif. *Étude du comportement à haute température d'une fissuration instable dans l'acier 16MND5 et application au calcul de la rupture d'un fond de cuve en cas d'accident grave*. PhD thesis, INSA de Lyon, 2009.

[165] T. Y. Thomas. Extended compatibility conditions for the study of surfaces of discontinuity in continuum mechanics. *Journal of Mathematics and Mechanics*, 6:311–322, 1957.

[166] P. F. Thomason. A theory for ductile fracture by internal necking of cavities. *Journal of the Institute of Metals*, 96(12):360–365, 1968.

[167] A. Turon, C. G. Davila, P. P. Camanho, and J. Costa. An engineering solution for mesh size effects in the simulation of delamination using cohesive zone models. *Engineering Fracture Mechanics*, 74:1665–1682, 2007.

[168] V. Tvergaard. Influence of voids on shear band instabilities under plane strain conditions. *International Journal of Fracture*, 17(4):389–407, 1981.

[169] V. Tvergaard. Material failure by void coalescence in localized shear bands. *International Journal of Solids and Structures*, 18(8):659–672, 1982.

[170] V. Tvergaard. On localization in ductile materials containing spherical voids. *International Journal of Fracture*, 18(4):237–252, 1982.

[171] V. Tvergaard. Material failure by void growth to coalescence. *Advances in Applied Mechanics*, 27:83–151, 1989.

[172] V. Tvergaard. Crack growth predictions by cohesive zone model for ductile fracture. *Journal of the Mechanics and Physics of Solids*, 49(9):2191–2207, 2001.

[173] V. Tvergaard and J. W. Hutchinson. The relation between crack growth resistance and fracture process parameters in elastic-plastic solids. *Journal of the Mechanics and Physics of Solids*, 40:1377–1397, 1992.

[174] V. Tvergaard and A. Needleman. Analysis of the cup-cone fracture in a round tensile bar. *Acta Metallurgica*, 32(1):157–169, 1984.

[175] H. Ulmer, M. Hofacker, and C. Miehe. Phase field modeling of brittle and ductile fracture. *PAMM*, 13(1):533–536, 2013.

[176] G. Ventura. On the elimination of quadrature subcells for discontinuous functions in the extended finite-element method. *International Journal for Numerical Methods in Engineering*, 66(5):761–795, 2006.

[177] K. Y. Volokh. Comparison between cohesive zone models. *Communications in Numerical Methods in Engineering*, 20(11):845–856, 2004.

[178] G. N. Wells and L. J. Sluys. A new method for modelling cohesive cracks using finite elements. *International Journal for Numerical Methods in Engineering*, 50(12):2667–2682, 2001.

[179] H. G. F. Wilsdorf. The ductile fracture of metals: a microstructural viewpoint. *Materials Science and Engineering*, 59(1):1–39, 1983.

[180] T. W. Wright and R. C. Batra. The initiation and growth of adiabatic shear bands. *International Journal of Plasticity*, 1:205–212, 1985.

[181] J.-Y. Wu. Unified analysis of enriched finite elements for modeling cohesive cracks. *Computer Methods in Applied Mechanics and Engineering*, 200(45):3031–3050, 2011.

[182] X.-P. Xu and A. Needleman. Numerical simulations of fast crack growth in brittle solids. *Journal of the Mechanics and Physics of Solids*, 42(9):1397–1434, 1994.

[183] L. Xue and T. Wierzbicki. Ductile fracture initiation and propagation modeling using damage plasticity theory. *Engineering Fracture Mechanics*, 75(11):3276–3293, 2008.

[184] H. Yamamoto. Conditions for shear localization in the ductile fracture of void-containing materials. *International Journal of Fracture*, 14(4):347–365, 1978.

[185] A. M. Yan and H. Nguyen-Dang. Multiple-cracked fatigue crack growth by bem. *Computational Mechanics*, 16(5):273–280, 1995.

[186] X. Zeng and S. Li. A multiscale cohesive zone model and simulations of fractures. *Computer Methods in Applied Mechanics and Engineering*, 199(9):547–556, 2010.

[187] Y. Zhang. *Modélisation et simulation numérique robuste de l'endommagement ductile*. PhD thesis, MINES ParisTech, 2016.

[188] G. Zi and T. Belytschko. New crack-tip elements for xfem and applications to cohesive cracks. *International Journal for Numerical Methods in Engineering*, 57(15):2221–2240, 2003.

[189] O. C. Zienkiewicz and R. L. Taylor. *The Finite Element Method*, volume 5. McGraw-Hill London, 1977.

[190] M. A. Zikry, M. R. Pothier, and J. N. Baucom. High strain-rate shear-strain localization in f.c.c. crystalline materials: a perturbation analysis. *International Journal of Solids and Structures*, 37:6177–6202, 2000.

Université Fédérale

Toulouse Midi-Pyrénées

# THÈSE

**En vue de l'obtention du**

## DOCTORAT DE L'UNIVERSITÉ DE TOULOUSE

**Délivré par :**

Institut Supérieur de l'Aéronautique et de l'Espace

---

**Présentée et soutenue par :**
**Johannes WOLF**

**le** mercredi 14 décembre 2016

**Titre :**

Traitement numérique de la fissuration dans les matériaux structuraux ductiles sous l'effet de sollicitations sévères

Numerical treatment of crack propagation in ductile structural materials under severe conditions

---

**École doctorale et discipline ou spécialité :**

ED MEGeP : Génie mécanique, mécanique des matériaux

**Unité de recherche :**

Institut Clément Ader

**Directeur(s) de Thèse :**

M. Patrice LONGERE (directeur de thèse)
M. Jean-Marc CADOU (co-directeur de thèse)

**Jury :**

André DRAGON Directeur de recherche CNRS émérite, Pprime - Président
Alain COMBESCURE Professeur émérite, INSA, Lyon - Rapporteur
Laurent STAINIER Professeur, ECN, Nantes - Rapporteur
Milan JIRASEK Professeur, CTU, Prague Examinateur
Hélène WELEMANE Maître de conférences, ENI, Tarbes Examinatrice
Patrice LONGERE Professeur, ISAE-SUPAERO, Toulouse - Directeur de thèse
Jean-Marc CADOU Maître de conférences, UBS, Lorient - Co-directeur de thèse

# Table des matières

# Nomenclature

GTN Gurson-Tvergaard-Needleman

MEF Méthode des Éléments Finis

PG Point de Gauss

X-FEM Extended Finite Element Method

# Chapitre I

# Introduction

## Contents of chapter I

# I.1 Contexte de l'étude

## I.1.1 Contexte industriel

Le travail présenté s'inscrit dans la conception de grandes structures fabriquées en matériaux ductiles vis-à-vis d'évènements accidentels, par exemple de la collision de navires, de l'impact des oiseaux en aviation ou du crash dans l'industrie automobile, qui peut potentiellement mener à la rupture finale de la structure. Considérons l'exemple du navire pétrolier Limburg lors d'une attaque terroriste, voir Fig. I.1. Un bateau équipé d'explosif causa une détonation aux abords du navire et engendra un grand trou dans la coque. Cet accident entraîna une marée noire.

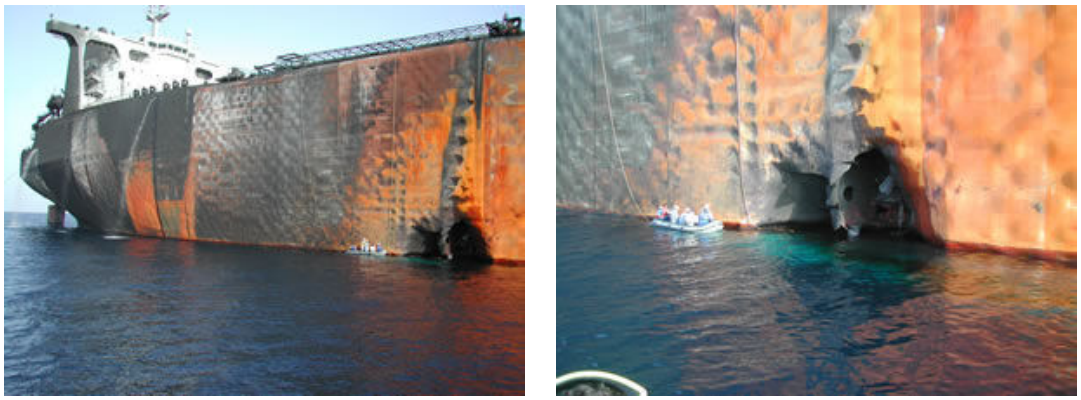

a) b)

FIGURE I.1 – Navire pétrolier Limburg après attaque terroriste : a) navire endommagé [15] et b) vue proche [15]

Un cas d'endommagement fréquemment reporté dans l'aéronautique est l'ingestion des oiseaux dans les moteurs des avions qui peut mener à des déformations plastiques sévères et de la fissuration des ailettes, voir Fig. I.2. De tels évènements ont déjà causé de nombreux crash d'avions.

Un défaut *local* peut avoir des conséquences catastrophiques à l'échelle *globale* de la structure. Prédire la résistance résiduelle de la structure surchargée est d'un grand intérêt pour la préservation des fonctions principales et l'intégrité des zones sensibles. Réaliser des essais à grande échelle engendreraient des coûts inacceptables. A la place, il est plus favorable d'analyser des éprouvettes *de petite échelle* prélevées dans la structure *de grande échelle* qui sont exposées à des conditions similaires et d'identifier les mécanismes fondamentaux qui mènent à la propagation d'une fissure. Basé sur les observations expérimentales et faisant des hypothèses, le but de ce travail est de mettre en place un modèle numérique.

a) b)

FIGURE I.2 – Ingestion d'oiseaux dans les moteurs des avions menant à l'endommagement des ailettes : a) Plusieurs fissures à travers des ailettes [38] et b) déformation plastique large [38]

**Ce travail est consacré au développement d'un modèle numérique basé le plus possible sur la physique permettant de conduire des essais virtuels pouvant mener à rupture en utilisant la méthode des éléments finis (MEF).**

## I.2 Problèmes posés et verrous scientifiques

Décrire le processus de la déformation jusqu'à la rupture dans des matériaux ductiles implique la prise en compte de mécanismes complexes dont la compréhension reste - à ce jour - imparfaite. On peut distinguer les étapes successives suivantes (souvent considérées indépendamment) : déformation plastique, endommagement plus ou moins diffus, concentration de l'endommagement (coalescence des cavités) et la localisation de la déformation et finalement la formation et propagation de la fissure, voir Fig. I.3. Le but final est de les allier dans un modèle unifié qui devra être implémenté dans un code de calcul.

### I.2.1 Modélisation et enjeux numériques

#### I.2.1.1 Endommagement diffus et dépendance au maillage

A la suite de l'endommagement diffus induit par la croissance des cavités, les propriétés du matériau subissent une dégradation progressive. Afin de reproduire les conséquences de l'endommagement ductile, plusieurs modèles constitutifs ont été proposés, par exemple par Gurson [25], Lemaitre [28], Rousselier [42] et aussi

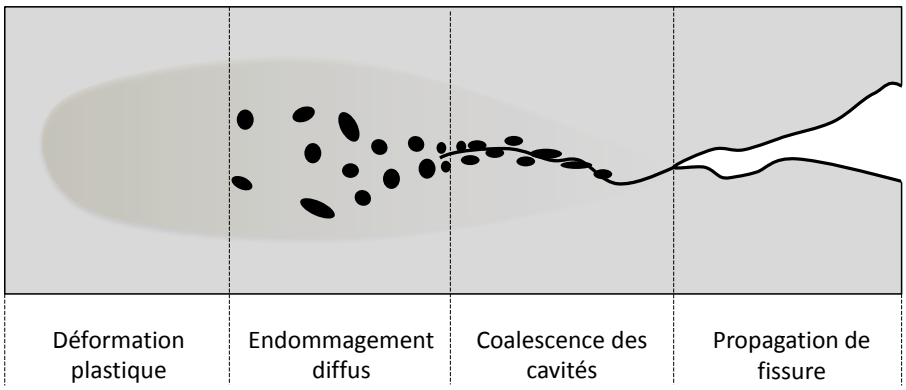


FIGURE I.3 – Mécanismes principaux du processus de la fissuration ductile

Longère [30]. Après une importante évolution de l'endommagement la réponse globale de la structure entre dans un régime adoucissant (au lieu du régime durcissant qui le précède). Ce comportement adoucissant est accompagné de la concentration de la déformation plastique et de l'endommagement dans une bande étroite.

Si on utilise la MEF standard, on observe la localisation de la déformation et de l'endommagement dans une couche de la taille d'un élément fini. A cause de cette dépendance pathologique au maillage une prédiction fiable de la résistance résiduelle de la structure après surcharge ne peut pas être assurée. La modélisation complémentaire de la phase "post-localisation" est donc indispensable.

#### I.2.1.2 Concentration de l'endommagement et localisation de la déformation

Les modèles constitutifs locaux n'arrivent pas à décrire la concentration de l'endommagement et la localisation de la déformation dans une bande étroite et la propagation de fissure potentielle. Une approche corrective consiste à contrôler la localisation de la déformation numérique dans le maillage EF afin de permettre la capture de la localisation de la déformation réelle. La dépendance au maillage qui est le résultat de la localisation de la déformation peut être gérée en introduisant une longueur caractéristique dans la formulation qui sert de limiteur de la localisation. Des techniques non-locales (par exemple celles de Bažant [5] et Pijaudier-Cabot [39]) peuvent être appliquées pour atténuer la pathologie, mais des résultats exacts demandent un maillage très fin et ainsi un effort de calcul conséquent pour de grandes structures. En outre la localisation de la déformation physique elle-même comme précurseur possible de la formation d'une fissure ne peut pas être représentée proprement.

Une approche prometteuse consiste à utiliser des EFs relativement larges et incorporer la bande fine de déformation fortement localisée dans l'EF, par exemple en enrichissant la formulation de la cinématique de l'EF (Ortiz [35], Belytschko [7]) ou le modèle constitutif du matériau (Longère [29]). **Le développement d'une méthode de bande incorporée appropriée capable de reproduire la bande de localisation physique et de réduire la sensibilité au maillage au minimum est un objectif important de cette thèse.**

#### I.2.1.3 Formation et propagation d'une fissure

La MEF standard n'est pas appropriée à reproduire la cinématique discontinue de la fissure. Des techniques complémentaires comme la méthode de suppression des éléments (Song [48], Autenrieth [3]) et la méthode inter-élément (Xu [53]) peuvent être utilisées pour décrire la propagation de fissure mais elles sont dépendantes du maillage. Des techniques de remaillage adaptatif ont été montrées comme permettant de mieux reproduire la propagation de fissure, voir par exemple Bouchard [11], par contre elles exigent un effort de calcul très conséquent.

Similaire à l'approche de bande incorporée pour traiter la localisation de la déformation (numérique et physique), la fissure peut être incluse dans l'élément fini en enrichissant la formulation cinématique de l'EF, comme il est fait dans la MEF étendue (X-FEM) (Belytschko [6]). Des travaux dédiés à montrer la performance de la X-FEM pour représenter la rupture de structures élastiques-(quasi) fragiles sont nombreux dans la littérature (Moës [33], Dumstorff [20]), cependant des travaux s'inscrivant dans le contexte des structures ductiles et fortement non-linéaires sont toujours peu abondants (Crété [18], Broumand [12]). En plus la méthode des EFs incorporés permet d'utiliser un maillage grossier et pour cette raison elle est plus adaptée à la simulation de grandes structures.

### I.2.2 Vers une approche unifiée

Le défi consiste à reproduire dans une méthodologie unifiée les étapes successives de l'endommagement diffus, localisation de la déformation et propagation de fissure aboutissant à la rupture finale de la structure. Cela demande la définition d'une cinématique spécifique et des critères motivés par la physique pour traiter le passage d'une phase à l'autre aussi compatible que possible. **A cet effet on étudie ici la capacité de trois différentes méthodes d'EF avec bande incorporée pour modéliser la phase de transition critique entre endommagement plus ou moins diffus (mécanique des milieux continus) et propagation de fissure**

**(mécanique de la rupture), à savoir la localisation de la déformation. La plus prometteuse des trois approches étudiées est ensuite élaborée en détail et des critères basés le plus possible sur la physique sont proposés afin de passer de l'endommagement diffus à la localisation de la déformation, puis de la localisation de la déformation à la propagation de fissure.**

## I.3 Hypothèses principales pour le traitement numérique

Les hypothèses les plus pertinentes qui sont supposées pour les développements numériques dans le cadre de cette thèse sont :

- Le focus de ce travail est sur le phénomène de la localisation de la déformation qui est déclenché par l'endommagement induit par la croissance des cavités.
- Le chargement est supposé augmenter de manière monotone et quasi-statique. Pour cette raison, les influences de la température et vitesse de la déformation seront négligées provisoirement. De plus cela implique que la phase de déchargement ne sera pas traitée.
- La domaine de la structure est discrétisée en utilisant des éléments finis 2D avec une formulation de déformation plane.
- Il est supposé que la déformation reste suffisamment petite (hypothèse des petites perturbations), tout en étant conscient du fait que la fissuration ductile implique de grandes déformations locales.

# Chapitre II

# Performance de méthodes sélectionnées pour décrire la localisation de la déformation

## Contents of chapter II

# II.1 Introduction

La fissuration ductile est considérée comme le résultat de la concentration des cavités dans une bande d'endommagement localisé. Le focus dans ce travail est sur la modélisation de la phase de la localisation de la déformation, donc la troisième phase dans Fig. II.1 et la transition (i) de la phase précédente de l'endommagement plus ou moins diffus à la localisation de la déformation et (ii) de la localisation de la déformation à la phase suivante de la formation d'une fissure.

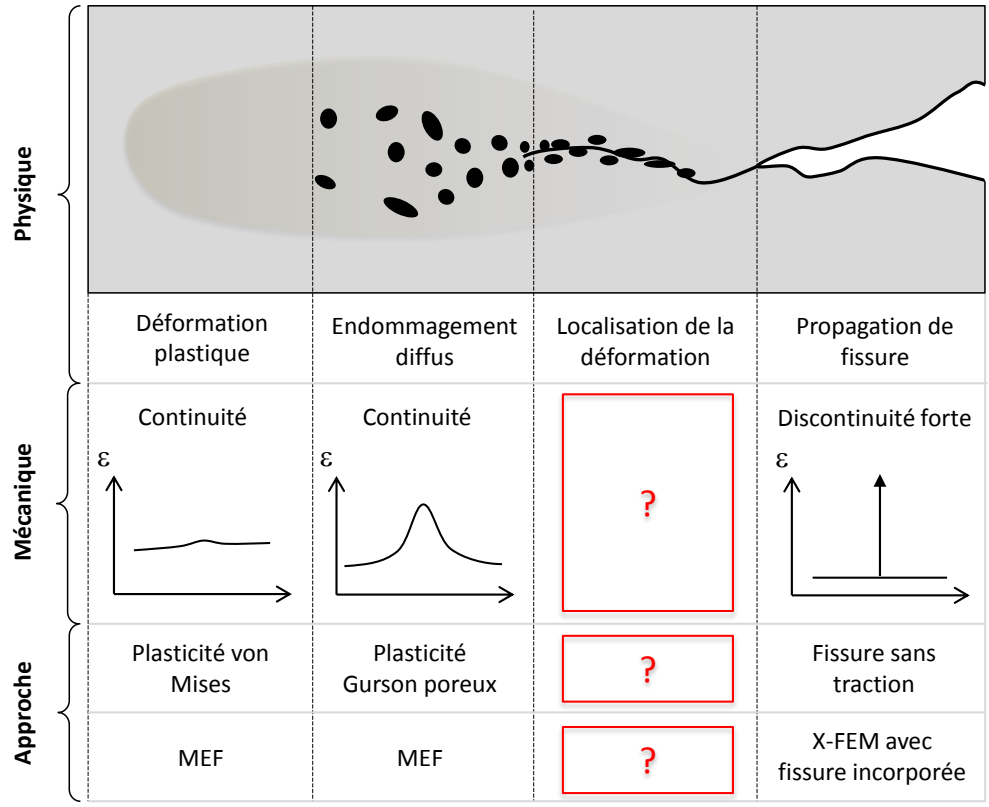


FIGURE II.1 – Processus de la fissuration où on cherche à modéliser la phase de la localisation de la déformation (en boites rouges)

Dans cette partie, on va étudier la performance de trois méthodes différentes avec une bande incorporée dans l'EF (discontinuité forte, faible et régularisée à travers de la bande) pour modéliser la phase de la localisation de la déformation dans des matériaux ductiles. La plus prometteuse de ces approches étudiées sera développée en détail dans le chapitre prochain.

Il n'y a pas de consensus dans la littérature sur la façon de modéliser la phase critique de la localisation de la déformation. Des approches continues essaient de

décrire les effets de la coalescence de cavités sur le matériau continu, voir par exemple les travaux de Pardoen ([36], [37]), Benzerga ([9], [10]) et Tvergaard ([50], [51]). Une approche alternative consiste à reproduire les conséquences cinématiques de la bande étroite de déformation fortement localisée dans une approche comme présentée dans la suite.

Par définition, une discontinuité forte implique une discontinuité du champ de déplacement/vitesse, tandis qu'une discontinuité faible implique une discontinuité du champ du gradient de déplacement/vitesse.

## II.2 Considérations préliminaires

On considère un champ de déplacement continu $\hat{u}(x)$ qui est enrichi par un champ discontinu $\tilde{u}(x)$ qui représente la cinématique de la bande de localisation. La superposition de ces deux champs donne le champ de déplacement total $u(x)$

$$u(x) = \hat{u}(x) + H_w(s)\tilde{u}(x) \tag{II.1}$$

où la fonction $H_w(s)$ est une version adaptée de la fonction Heaviside classique ; $s$ est la fonction de distance par rapport à la ligne centrale de la bande, voir Fig. II.2). La fonction Heaviside modifiée est choisie selon la cinématique désirée de chacune des trois méthodes :

- Discontinuité forte : $H_w(s) = \begin{cases} 1 & s \geq 0 \\ -1 & s < 0 \end{cases}$ (II.2)

- Discontinuité faible : $H_w(s) = \begin{cases} 1 & s \geq \frac{w}{2} \\ \frac{2}{w}s & -\frac{w}{2} \leq s < \frac{w}{2} \\ -1 & s < -\frac{w}{2} \end{cases}$ (II.3)

- Discontinuité régularisée : $H_w(s) = \begin{cases} 1 & s \geq \frac{w}{2} \\ \tanh(\frac{4}{w}s) & -\frac{w}{2} \leq s < \frac{w}{2} \\ -1 & s < -\frac{w}{2} \end{cases}$ (II.4)

où $w$ est l'épaisseur caractéristique de la bande de localisation. Ces fonctions sont visualisées dans le diagramme de la Fig. II.2.

Ces trois profils de déplacement différents viennent d'interprétations physiques différentes du mécanisme de la localisation de la déformation :

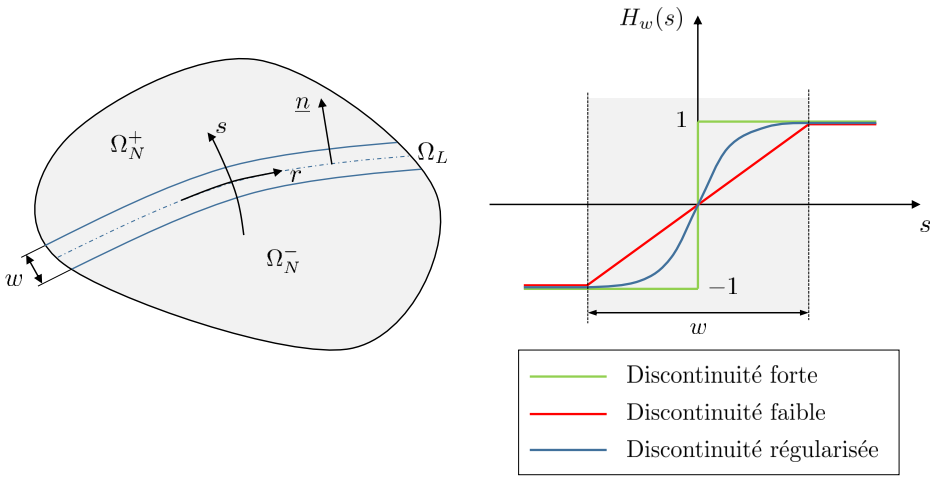


FIGURE II.2 – Comparaison qualitative de la discontinuité forte, faible et régularisée

— *Discontinuité forte :* On suppose que les micro-mécanismes complexes qui se déroulent pendant la localisation de la déformation sont concentrés dans une surface qui correspond à l'observation expérimentale de la présence d'une méso-fissure. Dans un contexte similaire on trouve par exemple les travaux de Dvorkin [22], Moës [32], Oliver [34] et Remmers [40].

— *Discontinuité faible :* La phase de localisation est accompagnée de la coalescence de cavités qui se déroule dans une zone fine avec une déformation constante à travers la bande. Des exemples de la littérature sont les travaux de Belytschko [7], Huespe [27], Ortiz [35] et Sluys [47].

— *Discontinuité régularisée :* On peut aussi supposer que la localisation de la déformation ne peut pas apparaître dans une bande clairement délimitée. Donc le champ de déformation à travers la bande est plutôt vue d'une manière continue et lissée. On peut citer les travaux d'Abbas [1], Areias [2], Benvenuti [8] et Su [49].

Ces trois points de vue de la bande de localisation seront étudiés dans la suite. On va utiliser la méthode de la X-FEM pour représenter la cinématique au sein de l'élément fini. Donc le champ de déplacement discret peut être écrit

$$\mathbf{u} = \mathbf{Na} + H_w \mathbf{Nb}, \tag{II.5}$$

où $\mathbf{N}$ est la matrice des fonctions de forme et $\mathbf{a}$ et $\mathbf{b}$ sont, respectivement, les champs de déplacement régulier et enrichi.

Dans un premier temps, on va supposer que l'amorçage de la bande de localisation est calculé via l'analyse de bifurcation. Ensuite, la bande de localisation est incorporée dans l'EF et les degrés de liberté enrichis de la X-FEM sont activés.

La transition vers la phase de la propagation de fissure se fait naturellement par un critère qui permet de progressivement annuler la contrainte dans la bande de localisation. Dans ce cas limite, la contribution du domaine localisé au système des équations globales disparaît et la formulation de la X-FEM classique est obtenue.

## II.3 Méthode 1 : Discontinuité forte

Les mécanismes d'endommagement importants se déroulent sur une échelle très petite comparée aux dimensions de la structure. Cette méthode consiste donc à représenter d'une manière macro-mécanique le processus de la dégradation dans une bande de localisation avec une approche cohésive (Barenblatt [4], Dugdale [19], Hillerborg [26]) où une loi de traction-séparation adoucissante ($t$-$[\![u]\!]$) est introduite, voir Fig. II.3.

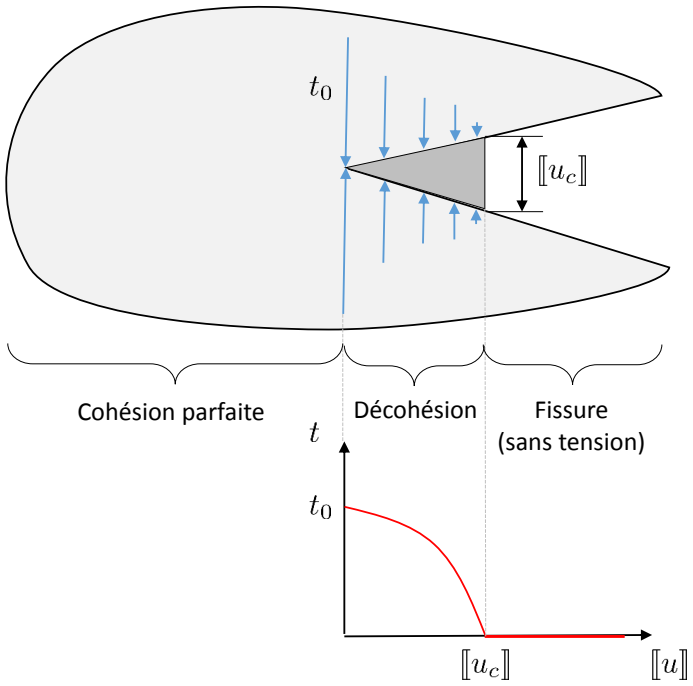


FIGURE II.3 – Cohesive zone model for mode I

Des fissure cohésives ont été incorporé dans la X-FEM par exemple par Moës [32] et Wells [52] dans le contexte des matériaux quasi-fragiles et par Seabra [45] et Simatos [46] pour des matériaux ductiles.

En prenant la formulation du champ de déplacement de l'équation (II.2) on peut montrer que l'équilibre dans le système peut être décrit par les deux équations

suivantes

$$\int_{\Omega} \mathbf{B}^T \boldsymbol{\sigma} \, \mathrm{d}\Omega = \int_{\Gamma_t} \mathbf{N}^T \mathbf{t}^* \, \mathrm{d}\Gamma \tag{II.6a}$$

$$\int_{\Omega} H_w \mathbf{B}^T \boldsymbol{\sigma} \, \mathrm{d}\Omega + 2 \int_{\Gamma_D} \mathbf{N}^T \mathbf{t} \, \mathrm{d}\Gamma = \int_{\Gamma_t} H_w \mathbf{N}^T \mathbf{t}^* \, \mathrm{d}\Gamma \tag{II.6b}$$

La première équation constitue l'équilibre dans le milieu continu et la deuxième équation est la continuité de traction à travers la discontinuité dans une formulation faible. Après discrétisation, on peut finalement écrire le système des équations discrètes dans une formulation incrémentale

$$\begin{bmatrix} \mathbf{K}_{aa} & \mathbf{K}_{ab} \\ \mathbf{K}_{ba} & \mathbf{K}_{bb} \end{bmatrix} \begin{Bmatrix} \mathrm{d}a \\ \mathrm{d}b \end{Bmatrix} = \begin{Bmatrix} \mathbf{f}_a^{ext} \\ \mathbf{f}_b^{ext} \end{Bmatrix} - \begin{Bmatrix} \mathbf{f}_a^{int} \\ \mathbf{f}_b^{int} \end{Bmatrix}, \tag{II.7}$$

où la matrice de rigidité tangente est calculée comme suit

$$\mathbf{K} = \begin{bmatrix} \int_{\Omega} \mathbf{B}^T \mathbf{D}^{\mathbf{t}} \mathbf{B} \, \mathrm{d}\Omega & \int_{\Omega} H_w \mathbf{B}^T \mathbf{D}^{\mathbf{t}} \mathbf{B} \, \mathrm{d}\Omega \\ \int_{\Omega} H_w \mathbf{B}^T \mathbf{D}^{\mathbf{t}} \mathbf{B} \, \mathrm{d}\Omega & \int_{\Omega} \mathbf{B}^T \mathbf{D}^{\mathbf{t}} \mathbf{B} \, \mathrm{d}\Omega + 4 \int_{\Gamma_D} \mathbf{N}^T \mathbf{T} \mathbf{N} \, \mathrm{d}\Gamma \end{bmatrix} \tag{II.8}$$

et les vecteurs de force interne et externe sont

$$\mathbf{f}_a^{ext} = \int_{\Gamma_t} \mathbf{N}^T \mathbf{t}^* \, \mathrm{d}\Gamma \tag{II.9a}$$

$$\mathbf{f}_b^{ext} = \int_{\Gamma_t} H_w \mathbf{N}^T \mathbf{t}^* \, \mathrm{d}\Gamma \tag{II.9b}$$

$$\mathbf{f}_a^{int} = \int_{\Omega} \mathbf{B}^T \boldsymbol{\sigma} \, \mathrm{d}\Omega \tag{II.9c}$$

$$\mathbf{f}_b^{int} = \int_{\Omega} H_w \mathbf{B}^T \boldsymbol{\sigma} \, \mathrm{d}\Omega + 2 \int_{\Gamma_D} \mathbf{N}^T \mathbf{t} \, \mathrm{d}\Gamma. \tag{II.9d}$$

L'incorporation d'une discontinuité dans un élément en utilisant la X-FEM demande l'application d'une technique d'intégration spéciale dans le milieu continu des éléments coupés. A cause de la présence d'un matériau fortement non-linéaire, on va utiliser l'intégration par 64 points de Gauss fixes, voir aussi Crété [18], au lieu de la méthode classique de la sous-triangulation de Moës [33]. Les contributions de la bande cohésive sont intégrées par 2 points de Gauss positionnés au long du segment cohésif.

La transition entre endommagement et localisation est déclenchée par le critère de bifurcation. Il est important de noter que la traction initiale de la loi cohésive doit être déterminée au moment de l'amorçage afin d'assurer une transition douce.

L'amorçage de la fissure est indiqué par un critère énergétique. La fissure se forme si l'aire sous la courbe traction-séparation dépasse une certaine valeur $W_c$, voir Fig. II.4

$$W_c = \int_0^{[\![u]\!]_c} \underline{t}([\![u]\!])\,\mathrm{d}[\![u]\!]. \tag{II.10}$$

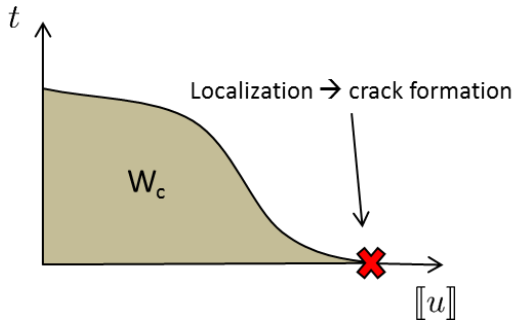


FIGURE II.4 – Transition de localisation à la formation d'une fissure

Dans ce cas, la traction dans la bande cohésive atteint le valeur zéro et la formulation de la X-FEM classique est obtenue.

## II.4 Méthode 2 : Discontinuité faible

Cette méthode est basée sur l'hypothèse que le champ de déplacement à travers la zone de localisation présente une discontinuité faible, donc une bande de localisation clairement délimitée. Dans cette partie, on va proposer une extension de la méthode X-FEM présentée par Huespe [27]. Les hypothèses principales sont :

1. Le modèle de Gurson dans la phase de pré-localisation est également utilisé pour déterminer l'état de contrainte de post-localisation dans la bande de localisation. Ce faisant, on peut prendre en compte la dépendance de la contrainte hydrostatique dans la bande.
2. L'épaisseur de la bande pré-définie est maintenue constante pendant le processus de localisation jusqu'à la rupture.
3. Les déformations et contraintes à travers la bande (dans la direction normale) sont homogènes.

En utilisant l'équation (II.3) avec l'équation du travail virtuel on arrive aux équations d'équilibre suivantes (Remmers [41])

$$\begin{aligned}\int_{\Omega_L} \nabla^S(\delta u) : \underset{\sim}{\sigma}\,\mathrm{d}\Omega &= \int_{\Gamma_D}\int_{-\frac{w}{2}}^{\frac{w}{2}} \nabla^S(\delta u) : \underset{\sim}{\sigma}\,\mathrm{d}n\,\mathrm{d}\Gamma \\ &= w \cdot \int_{\Gamma_D} \nabla^S(\delta u) : \underset{\sim}{\sigma}\,\mathrm{d}\Gamma.\end{aligned} \tag{II.11}$$

où $\Gamma_D$ dénote la surface moyenne de la bande. Après quelques manipulations mathématiques, on peut écrire les équations discrètes dans la même forme que Eq. (II.7). Les composantes de la matrice de rigidité tangente sont comme suit

$$\mathbf{K_{aa}} = \int_{\Omega_N} \mathbf{B}^T \mathbf{D^t} \mathbf{B} \, \mathrm{d}\Omega + w \cdot \int_{\Gamma_D} \mathbf{B}^T \mathbf{D^t} \mathbf{B} \, \mathrm{d}\Gamma \tag{II.12a}$$

$$\mathbf{K_{ab}} = \int_{\Omega_N} H_w \mathbf{B}^T \mathbf{D^t} \mathbf{B} \, \mathrm{d}\Omega + 2 \cdot \int_{\Gamma_D} \mathbf{B}^T \mathbf{D^t} \overline{\mathbf{N}} \, \mathrm{d}\Gamma \tag{II.12b}$$

$$\mathbf{K_{ba}} = \int_{\Omega_N} H_w \mathbf{B}^T \mathbf{D^t} \mathbf{B} \, \mathrm{d}\Omega + 2 \cdot \int_{\Gamma_D} \overline{\mathbf{N}}^T \mathbf{D^t} \mathbf{B} \, \mathrm{d}\Gamma \tag{II.12c}$$

$$\mathbf{K_{bb}} = \int_{\Omega_N} \mathbf{B}^T \mathbf{D^t} \mathbf{B} \, \mathrm{d}\Omega + 2 \cdot \int_{\Gamma_D} \delta_w \overline{\mathbf{N}}^T \mathbf{D^t} \overline{\mathbf{N}} \, \mathrm{d}\Gamma \tag{II.12d}$$

où $\overline{\mathbf{N}}$ est l'operateur [8]

$$\overline{\mathbf{N}}\mathbf{a} = (\mathbf{N}\mathbf{a} \otimes \mathbf{n})^S. \tag{II.13}$$

Les vecteurs de force interne et externe sont calculés grâce à

$$\mathbf{f}_a^{ext} = \int_{\Gamma_t} \mathbf{N}^T \mathbf{t}^* \, \mathrm{d}\Gamma \tag{II.14a}$$

$$\mathbf{f}_b^{ext} = \int_{\Gamma_t} H_w \mathbf{N}^T \mathbf{t}^* \, \mathrm{d}\Gamma \tag{II.14b}$$

$$\mathbf{f}_a^{int} = \int_{\Omega_N} \mathbf{B}^T \boldsymbol{\sigma} \, \mathrm{d}\Omega + w \cdot \int_{\Gamma_D} \mathbf{B}^T \boldsymbol{\sigma} \, \mathrm{d}\Gamma \tag{II.14c}$$

$$\mathbf{f}_b^{int} = \int_{\Omega_N} H_w \mathbf{B}^T \boldsymbol{\sigma} \, \mathrm{d}\Omega + 2 \int_{\Gamma_D} \mathbf{N}^T (\boldsymbol{\sigma} \cdot \mathbf{n}) \, \mathrm{d}\Gamma. \tag{II.14d}$$

L'intégration de la partie continue de l'élément coupé se fait de la même façon que pour la méthode 1, c'est-à-dire en utilisant 64 points de Gauss fixes. L'intégration des termes concernant la bande de localisation peut être faite aussi avec 2 points de Gauss le long de la discontinuité $\Gamma_D$ puisque l'intégrale sur la bande de localisation peut être transformée en une intégrale de surface.

Puisque le modèle de Gurson est appliqué dans la bande de localisation, la transition de la phase de l'endommagement à la phase de la localisation de la déformation se produit automatiquement en activant les degrés de liberté de la X-FEM. Il n'est pas nécessaire d'évaluer des paramètres supplémentaires.

La fissure se forme quand la contrainte dans la bande atteint la valeur zéro, une condition qui était définie dans la partie II.2. Ici on va utiliser un critère basé sur l'énergie stockée dans la bande de localisation, voir Fig. II.5. Dans ce cas, l'énergie

stockée se calcule comme suit

$$W_{bande} = \frac{\sum_{i=1}^{p} \omega_s^i A^i}{\sum_{i=1}^{p} A^i} \tag{II.15}$$

où $p$ représente le numéro des éléments localisés, $\omega_s$ est l'énergie plastique stockée moyennée sur les deux points de Gauss du segment cohésif de l'élément et $A_i$ est l'aire de la bande de localisation dans l'élément, donc $A_i = w \cdot l_b$, où $l_b$ dénote la longueur du segment cohésif. La fissure se propage avec la longueur $l_c$ si $W_{bande} \geq W_c$. Dès que la valeur critique $W_c$ est atteinte, la contrainte dans la bande est mise à zéro.

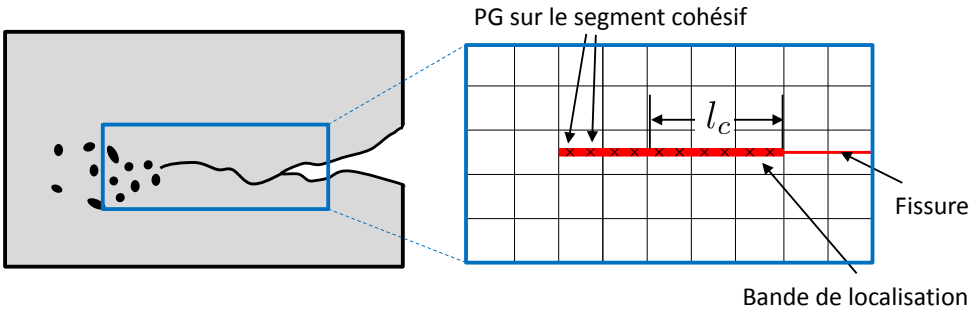


FIGURE II.5 – Critère d'énergie stockée évalué dans la bande de localisation

## II.5 Méthode 3 : Discontinuité régularisée

Dans cette troisième méthode le champ de déplacement à travers la zone de localisation est vue comme une discontinuité diffuse, donc le déplacement reste continu jusqu'à la rupture.

On va considérer les hypothèses suivantes :

1. Le modèle GTN est utilisé pour la réponse de la pré- et post-localisation dans la bande, voir aussi méthode 2.
2. L'épaisseur de la bande prescrite $w$ reste constante jusqu'à rupture.
3. La fonction de régularisation (profil en tanh) est coupée au-delà des bords de la bande.

Une fonction d'enrichissement tanh est utilisée, voir Eq. (II.4) (Areias [2], Roux [43]). Si on met le champ de déplacement dans la formulation de travail virtuel, on

obtient

$$\begin{aligned}\int_{\Omega_N} \nabla^S(\delta\hat{u}) : \underset{\sim}{\sigma}\, \mathrm{d}\Omega + \int_{\Omega_N} H_w \nabla^S(\delta\tilde{u}) : \underset{\sim}{\sigma}\, \mathrm{d}\Omega \\ + \int_{\Omega_L} \nabla^S(\delta\hat{u}) : \underset{\sim}{\sigma}\, \mathrm{d}\Omega + \int_{\Omega_L} H_w \nabla^S(\delta\tilde{u}) : \underset{\sim}{\sigma}\, \mathrm{d}\Omega + \int_{\Omega_L} \delta_w (\delta\tilde{u} \otimes \underline{n})^S : \underset{\sim}{\sigma}\, \mathrm{d}\Omega \\ = \int_{\Gamma_t} (\delta\hat{u} + H_w \delta\tilde{u}) \cdot \underline{t}^*\, \mathrm{d}\Gamma\end{aligned} \tag{II.16}$$

Avec les fonctions d'interpolation, les composantes de la matrice de rigidité tangente peuvent être écrites

$$\mathbf{K_{aa}} = \int_{\Omega_N} \mathbf{B}^T \mathbf{D^t} \mathbf{B}\, \mathrm{d}\Omega + \int_{\Omega_L} \mathbf{B}^T \mathbf{D^t} \mathbf{B}\, \mathrm{d}\Omega \tag{II.17a}$$

$$\mathbf{K_{ab}} = \int_{\Omega_N} H_w \mathbf{B}^T \mathbf{D^t} \mathbf{B}\, \mathrm{d}\Omega + \int_{\Omega_L} H_w \mathbf{B}^T \mathbf{D^t} \mathbf{B}\, \mathrm{d}\Omega + \int_{\Omega_L} \delta_w \mathbf{B}^T \mathbf{D^t} \overline{\mathbf{N}}\, \mathrm{d}\Omega \tag{II.17b}$$

$$\mathbf{K_{ba}} = \int_{\Omega_N} H_w \mathbf{B}^T \mathbf{D^t} \mathbf{B}\, \mathrm{d}\Omega + \int_{\Omega_L} H_w \mathbf{B}^T \mathbf{D^t} \mathbf{B}\, \mathrm{d}\Omega + \int_{\Omega_L} \delta_w \mathbf{B}^T \mathbf{D^t} \overline{\mathbf{N}}\, \mathrm{d}\Omega \tag{II.17c}$$

$$\begin{aligned}\mathbf{K_{bb}} = &\int_{\Omega_N} \mathbf{B}^T \mathbf{D^t} \mathbf{B}\, \mathrm{d}\Omega + \int_{\Omega_L} H_w^2 \mathbf{B}^T \mathbf{D^t} \mathbf{B}\, \mathrm{d}\Omega + \int_{\Omega_L} H_w \delta_w \mathbf{B}^T \mathbf{D^t} \overline{\mathbf{N}}\, \mathrm{d}\Omega + \\ &\int_{\Omega_L} \delta_w H_w \overline{\mathbf{N}}^T \mathbf{D^t} \mathbf{B}\, \mathrm{d}\Omega + \int_{\Omega_L} \delta_w^2 \overline{\mathbf{N}}^T \mathbf{D^t} \overline{\mathbf{N}}\, \mathrm{d}\Omega.\end{aligned} \tag{II.17d}$$

Les vecteurs de force interne et externe sont calculés comme suit

$$\mathbf{f}_a^{ext} = \int_{\Gamma_t} \mathbf{N}^T \mathbf{t}^*\, \mathrm{d}\Gamma \tag{II.18a}$$

$$\mathbf{f}_b^{ext} = \int_{\Gamma_t} H_w \mathbf{N}^T \mathbf{t}^*\, \mathrm{d}\Gamma \tag{II.18b}$$

$$\mathbf{f}_a^{int} = \int_{\Omega_N} \mathbf{B}^T \boldsymbol{\sigma}\, \mathrm{d}\Omega + \int_{\Omega_L} \mathbf{B}^T \boldsymbol{\sigma}\, \mathrm{d}\Omega \tag{II.18c}$$

$$\mathbf{f}_b^{int} = \int_{\Omega_N} H_w \mathbf{B}^T \boldsymbol{\sigma}\, \mathrm{d}\Omega + \int_{\Omega_L} H_w \mathbf{B}^T \boldsymbol{\sigma}\, \mathrm{d}\Omega + \int_{\Omega_L} \delta_w \overline{\mathbf{N}}^T \boldsymbol{\sigma}\, \mathrm{d}\Omega. \tag{II.18d}$$

Pour évaluer les intégrales, il n'est pas nécessaire d'appliquer la méthode de la sous-triangulation, qui est traditionnellement utilisé dans la X-FEM, parce que on utilise seulement des termes d'enrichissement continus. Cependant, il n'est pas trivial de capturer le gradient de la déformation large dans la bande de localisation, donc un grand nombre de points d'intégration doivent être utilisés. On peut citer des approches de Benvenuti [8] et d'Areias [2], mais ils exigent une projection des variables d'état qui dépendent de l'histoire. C'est pourquoi on va proposer ici d'utiliser 64 points de Gauss fixes qui permettent une évaluation suffisamment précise.

La transition de la phase pré- à la phase post-localisation peut se produire de la même façon que pour la méthode 2, parce que on va maintenir le modèle GTN au-delà de l'amorçage de la localisation. Aussi le critère d'amorçage d'une fissure peut être retenu, c'est-à-dire avec un critère basé sur l'énergie stockée dans la bande de localisation. Cette condition et le critère de l'annulation de la contrainte dans la bande sont appropriés pour cette méthode 3 et les hypothèses prises en compte.

## II.6 Discussion

Les points forts et faibles de ces trois méthodes présentées sont récapitulées dans le tableau II.1 en bas selon les hypothèses exprimées. Le tableau suggère que la méthode de la discontinuité forte sort clairement du lot en comparaison avec les deux autres méthodes. La méthode de la discontinuité forte semble la méthode la plus adaptée à une simulation de grandes structures où les conséquences macro-mécaniques de la localisation sont de grand intérêt. Aussi sa simplicité en terme d'aspects numériques a motivé le choix d'utiliser un modèle de zone cohésive pour décrire la phase de la localisation de la déformation.

TABLE II.1 – Points forts ($\oplus$) et faibles ($\ominus$) des méthodes de discontinuité forte, faible et régularisée

| Discontinuité forte | Discontinuité faible | Discontinuité régularisée |
|---|---|---|
| $\oplus$ Des micro-mécanismes complexes sont concentrés dans une surface<br>$\oplus$ Seulement un paramètre supplémentaire ($W_c$)<br>$\oplus$ Dépendance au maillage réduite (longueur caractéristique $\frac{W_c}{t_0}$)<br>$\oplus$ Méthode d'intégration standard<br>$\oplus$ Critère de rupture basé sur l'énergie est adapté aux matériaux ductiles<br>$\oplus$ Permet de décrire une bande de cisaillement | $\oplus$ Dépendance au maillage réduite (longueur caractéristique $w$)<br>$\oplus$ Méthode d'intégration standard<br>$\oplus$ Comportement post-localisation prend en compte la triaxialité de la contrainte<br>$\oplus$ Critère de rupture basé sur l'énergie est adapté aux matériaux ductiles<br>$\oplus$ Permet de décrire une bande de cisaillement | $\oplus$ Dépendance au maillage réduite (longueur caractéristique $w$)<br>$\oplus$ Comportement post-localisation prend en compte la triaxialité de la contrainte<br>$\oplus$ Critère de rupture basé sur l'énergie est adapté aux matériaux ductiles<br>$\oplus$ Permet de décrire une bande de cisaillement |
| $\ominus$ Technique pour calculer la traction initiale $t_0$ à partir de l'état de contrainte au moment de l'amorçage de la localisastion est nécessaire | $\ominus$ 2 paramètres additionnels ($w$, $W_c$)<br>$\ominus$ Critère de rupture ne satisfait pas la condition de l'annulation de la contrainte | $\ominus$ 2 paramètres additionnels ($w$, $W_c$)<br>$\ominus$ Critère de rupture ne permet pas d'annuler la contrainte<br>$\ominus$ Méthode d'intégration implique une projection de variables nécessaire si l'épaisseur de la bande est beaucoup plus petite que la taille de l'EF |

# II.7 Conclusion

Dans ce chapitre, on a étudié trois approches d'élément fini avec une bande incorporée avec différents points de vue. Basée sur une discussion profonde, l'approche d'une discontinuité forte avec un modèle de bande cohésive a été choisie comme la méthode préférée pour décrire la phase de la localisation de la déformation considérée dans cette étude, soit une méso-fissure entrecoupée de matière. La bande de localisation de la déformation est donc représentée par son plan moyen et sa résistance en tension et cisaillement via une loi cohésive qui assure la continuité de traction et la dégradation du matériau dans le régime de la post-localisation. Finalement, le schéma de fissuration de Fig. II.1 peut être complété, voir Fig. II.6.

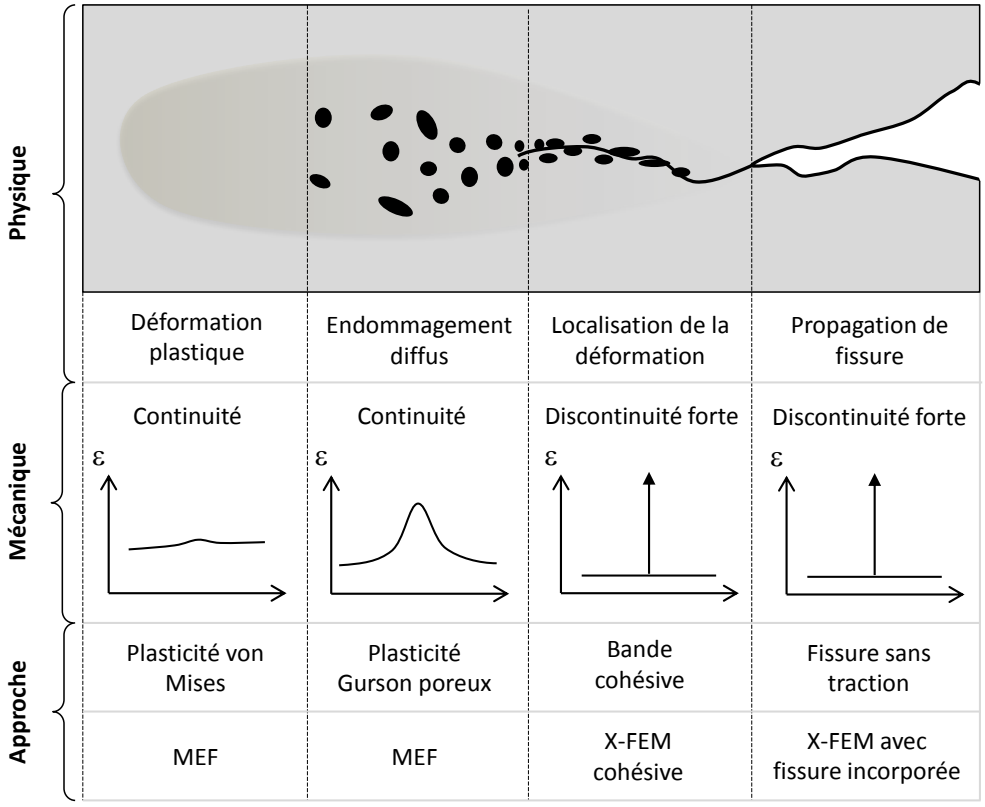


FIGURE II.6 – Processus final de la fissuration prenant en compte l'approche appliquée pour modéliser la localisation de la déformation

# Chapitre III

# Modélisation de la localisation de la déformation en utilisant la X-FEM cohésive

## Contents of chapter III

# III.1 Introduction

Dans ce chapitre on va proposer un modèle unifié et motivé par la physique avec le but de reproduire les phases successives de plasticité-endommagement diffus, localisation de la déformation et puis propagation de fissure. La méthode qui a été choisie parmi celles discutées dans le dernier chapitre sera développée en détail. L'intérêt particulier est sur l'application du concept de modèle de bande cohésive dans une formulation X-FEM. Selon les analyses effectuées dans le chapitre II, cette combinaison semble effectivement la plus prometteuse pour allier la physique et numérique.

Le scénario considéré ici est comme suit, voir Fig. III.1 :

1. Plasticité continue et endommagement diffus sont traités avec la MEF.
2. Fissuration à discontinuité forte est traitée avec la X-FEM.
3. La phase intermédiaire (entre (1) et (2)) de la localisation de la déformation considérée ici (méso-fissure) est supposée introduire une discontinuité forte cohésive et est traitée avec la X-FEM cohésive.
4. La transition de l'endommagement diffus (1) à la localisation de la déformation (3) est supposée le résultat d'une bifurcation/instabilité du matériau.
5. Le passage de la localisation de la déformation (3) à la formation de la (vraie) fissure (2) est piloté par un travail critique de cohésion.

# III.2 Considérations préliminaires

On peut interpréter la bande cohésive comme l'effet progressif de la coalescence des cavités, c'est-à-dire la striction interne du matériau inter-cavités, qui mène à une résistance décroissante du matériau jusqu'à la rupture, voir Fig. III.1.

On va adopter en bas une loi cohésive linéaire adoucissante de la forme

$$t = t_0 - \frac{t_0^2}{2W_c}[\![u]\!], \tag{III.1}$$

où la pente de la loi cohésive est $-t_0^2/(2W_c)$, voir Fig. III.2.

Pour prendre en compte le comportement en tension et cisaillement, la traction est décomposée comme suit

$$t = t_n \underline{n} + t_m \underline{m}, \tag{III.2}$$

où $\underline{n}$ and $\underline{m}$ dénotent, respectivement, la composante normale et tangentielle dans la bande cohésive, voir Fig. Fig. III.3.

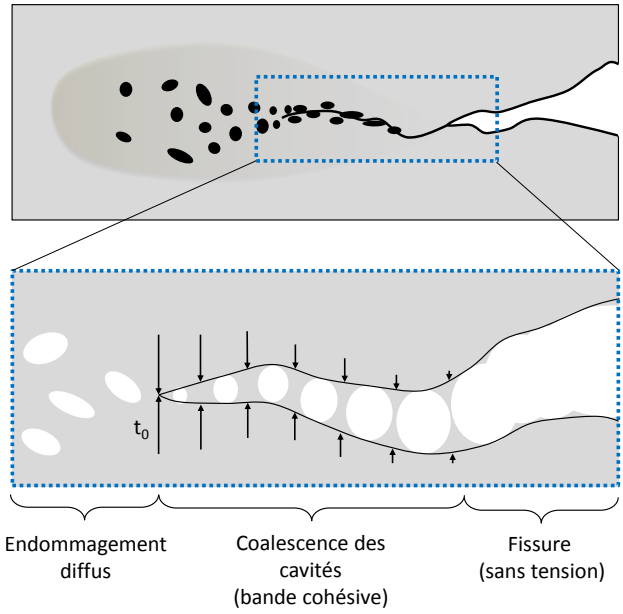


FIGURE III.1 – Visualisation du concept 'bande cohésive' : (en haut) Modèle de rupture ductile (Fig. II.6), (en bas) Introduction de tractions cohésives associées à la localisation de la déformation induite par la coalescence des cavités

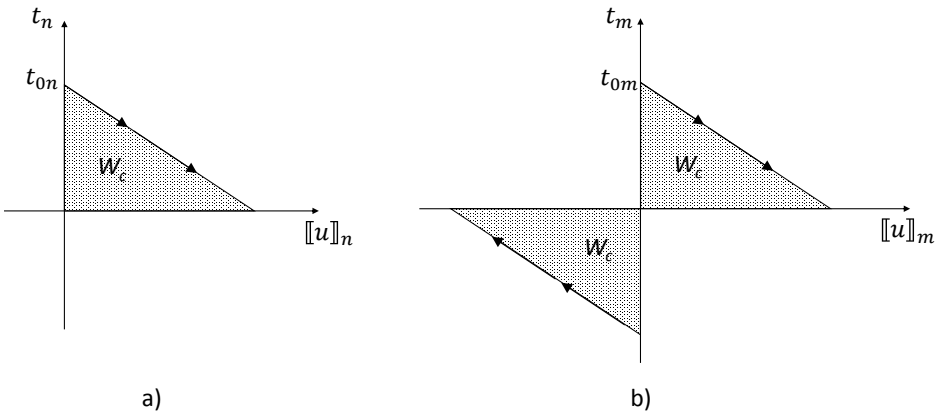


FIGURE III.2 – Loi cohésive linéaire adoucissante dans la direction a) normale et b) tangentielle

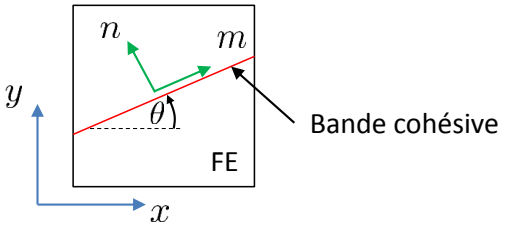


FIGURE III.3 – Repères global et local de la bande cohésive dans un EF

Pour déterminer le travail à séparation, il existe plusieurs méthodes dans la littérature, on va en citer trois qui sont appliquées dans le contexte des matériaux ductiles :

1. Identification des constants via une comparaison entre essais vs simulations (analyse inverse), voir par exemple Chen [16] et Seabra [45].
2. Analyse micro-mécanique assistée par des EFs, voir par exemple Scheider [44] pour des matériaux de type Gurson
3. Transfert/conservation/équivalence de l'énergie de l'endommagement à la fissure, voir par exemple Mazars [31], Cazes [13], [14] et Seabra [45] dans le contexte des matériaux de type Lemaitre

## III.3 Combiner modèle de bande cohésive et X-FEM

On va utiliser ici l'approche de la base décalée pour la X-FEM, qui a été proposée par Zi [54]. Cette approche consiste à prendre en compte dans le champ de déplacement enrichi la fonction d'Heaviside $H_j$ sur les nœuds

$$u(x) = \sum_{i \in I} N_i(x) a_i + \sum_{j \in J} \left( H(x) - H_j \right) N_j(x) b_j. \tag{III.3}$$

Les éléments coupés sont intégrés par 64 points de Gauss, une méthode qui est mieux adaptée aux matériaux fortement non-linéaires, voir Elguedj [23] et Crété [17].

Comme indiqué dans le chapitre précédent dans la section II.3 le système des équations linéarisées discrètes de la X-FEM avec une bande cohésive incorporée est donné comme suit

$$\begin{bmatrix} \mathbf{K}_{aa} & \mathbf{K}_{ab} \\ \mathbf{K}_{ba} & \mathbf{K}_{bb} \end{bmatrix} \begin{Bmatrix} \mathrm{d}a \\ \mathrm{d}b \end{Bmatrix} = \begin{Bmatrix} \mathbf{f}_a^{ext} \\ \mathbf{f}_b^{ext} \end{Bmatrix} - \begin{Bmatrix} \mathbf{f}_a^{int} \\ \mathbf{f}_b^{int} \end{Bmatrix}, \tag{III.4}$$

où la matrice de rigidité tangente $\mathbf{K}$ est calculée comme suit

$$\mathbf{K} = \begin{bmatrix} \int_\Omega \mathbf{B}^T \mathbf{D}^{\mathbf{t}} \mathbf{B} \, \mathrm{d}\Omega & \int_\Omega \mathbf{B}^T \mathbf{D}^{\mathbf{t}} \mathbf{B}^* \, \mathrm{d}\Omega \\ \int_\Omega \mathbf{B}^{*T} \mathbf{D}^{\mathbf{t}} \mathbf{B} \, \mathrm{d}\Omega & \int_\Omega \mathbf{B}^{*T} \mathbf{D}^{\mathbf{t}} \mathbf{B}^* \, \mathrm{d}\Omega + 4 \int_{\Gamma_D} \mathbf{N}^T \mathbf{T} \mathbf{N} \, \mathrm{d}\Gamma \end{bmatrix}, \tag{III.5}$$

où $\mathbf{T}$ est le module tangent cohésif comme détaillé en Eq. (III.9) en bas. La matrice $\mathbf{B}$ contient les dérivées des fonctions de forme $\mathbf{N}$, donc $\mathbf{B} = \mathbf{L}\mathbf{N}$ avec $\mathbf{L}$

étant l'opérateur différentiel

$$\mathbf{L} = \begin{bmatrix} \partial/\partial x & 0 \\ 0 & \partial/\partial y \\ \partial/\partial y & \partial/\partial x \end{bmatrix}. \tag{III.6}$$

et $\mathbf{B}^* = \mathbf{L}\mathbf{N}^*$ avec $\mathbf{N}^*$ contenant les entrées $N_j^* = (H(x) - H_j)N_j$ pour chaque nœud $j$ de l'élément enrichi. Les vecteurs de force interne et externe sont calculés comme suit

$$\mathbf{f}_a^{ext} = \int_{\Gamma_t} \mathbf{N}^T \mathbf{t}^* \, \mathrm{d}\Gamma \tag{III.7a}$$

$$\mathbf{f}_b^{ext} = \int_{\Gamma_t} \mathbf{N}^{*T} \mathbf{t}^* \, \mathrm{d}\Gamma \tag{III.7b}$$

$$\mathbf{f}_a^{int} = \int_{\Omega} \mathbf{B}^T \boldsymbol{\sigma} \, \mathrm{d}\Omega \tag{III.7c}$$

$$\mathbf{f}_b^{int} = \int_{\Omega} \mathbf{B}^{*T} \boldsymbol{\sigma} \, \mathrm{d}\Omega + 2 \int_{\Gamma_D} \mathbf{N}^T \mathbf{t} \, \mathrm{d}\Gamma, \tag{III.7d}$$

Il faut noter que le module tangent cohésif $\mathbf{T}$ ainsi que les tractions $\mathbf{t}$ sont définies dans le repère local de la bande cohésive. Donc il est nécessaire de transformer ces variables d'un repère local à un repère global. Cela est effectué avec la matrice de rotation $\mathbf{R}$ en sorte que

$$\mathbf{t}^g = \mathbf{R}^T \mathbf{t}^l \text{ and } \mathbf{T}^g = \mathbf{R}^T \mathbf{T}^l \mathbf{R} \text{ ; with } \mathbf{R} = \begin{bmatrix} \cos\theta & \sin\theta \\ -\sin\theta & \cos\theta \end{bmatrix}, \tag{III.8}$$

où g denote le repère global et l le repère local, voir Fig. III.3. Considérant la loi cohésive linéaire de la section III.2 on peut écrire le module tangent cohésif

$$\mathbf{T^l} = \frac{\partial \mathbf{t}^l}{\partial [\![u]\!]^l} = \begin{bmatrix} \frac{\partial \mathbf{t}_m^l}{\partial [\![u]\!]_m^l} & \frac{\partial \mathbf{t}_m^l}{\partial [\![u]\!]_n^l} \\ \frac{\partial \mathbf{t}_n^l}{\partial [\![u]\!]_m^l} & \frac{\partial \mathbf{t}_n^l}{\partial [\![u]\!]_n^l} \end{bmatrix} = \begin{bmatrix} T_m^l & 0 \\ 0 & T_n^l \end{bmatrix}. \tag{III.9}$$

L'intégration des contributions de la bande cohésive dans les équations d'équilibre, donc les termes impliquant une intégrale de ligne sur $\Gamma_D$, est effectuée par deux points de Gauss qui sont mis sur le segment cohésif de l'élément, voir Fig. III.4.

## III.4 Application

Dans la partie précédente on a introduit une méthodologie de couplage entre une méthode de bande cohésive et la X-FEM permettant de traiter la phase de

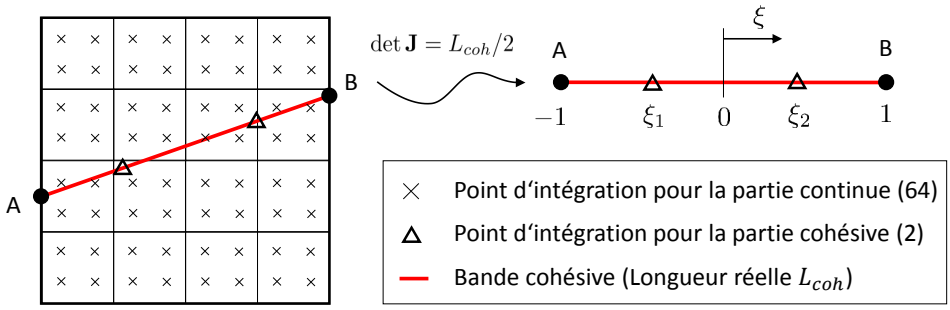


FIGURE III.4 – Méthode d'intégration pour un élément rectangulaire 2D coupé par une bande cohésive : (gauche) EF avec 64 points de Gauss fixes pour la partie du milieu continu et 2 points de Gauss pour la partie cohésive, (droit) Élément cohésif 1D transformé dans le repère naturel avec la coordonnée $\xi$

transition progressive de la localisation de la déformation. L'objectif de cette partie est d'appliquer la combinaison élaborée du modèle de bande cohésive et de la X-FEM à deux cas test afin d'apprécier la performance au regard de simulations numériques.

### III.4.1 Modélisation de la localisation et de la rupture dans un matériau ductile

Pour mettre en œuvre les méthodes présentées en bas on a fait le choix d'utiliser le code de calcul par éléments finis Abaqus. Ce choix est motivé par l'intérêt fort de l'industrie de simuler le processus complexe de la fissuration dans de grandes structures.

Dans la suite, deux modèles en 2D différents sont étudiés. Le premier est un cas de test simple considérant un seul EF qui permet de mieux comprendre la méthodologie et analyser des problèmes numériques éventuels. Le deuxième cas test s'intéresse à une étude paramétrique d'une plaque qui est chargée en tension. On va supposer des conditions de déformation plane et on assume que la déformation reste petite.

Dans les deux cas tests le modèle de GTN modifié est retenu. Les paramètres du comportement du matériau sain et aussi du matériau endommagé sont donnés dans les tableaux III.1 et III.2.

TABLE III.1 – Paramètres du modèle constitutif du matériau sain

| $E$ | $\nu$ | $r_0$ | $r_{inf}$ | $k$ | $\beta$ |
|---|---|---|---|---|---|
| 200 GPa | 0.33 | 300 MPa | 350 MPa | 4.4 | 0.5 |

TABLE III.2 – Paramètres du modèle GTN de plasticité microporeuse

| $q_1$ | $q_2$ | $f_0$ | $f_N$ | $s_N$ | $\kappa_N$ | $b$ |
|---|---|---|---|---|---|---|
| 1 | 1 | $10^{-3}$ | 0.04 | 0.05 | 0.3 | $100MPa$ |

### III.4.2 Essai de traction avec un EF 2D seul

On considère l'EF 2D seul dans Fig. III.5

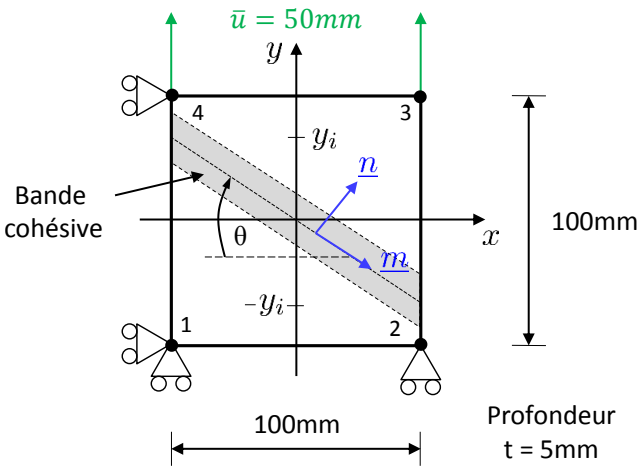


FIGURE III.5 – Essai en traction avec un EF 2D seul avec une bande cohésive inclinée au moment de l'amorçage de la localisation

On va supposer qu'une bande cohésive sera incorporée dans l'EF si le critère de bifurcation est satisfait. Si c'est la cas, la bande cohésive est incluse dans l'EF, mais avec une orientation arbitraire (donc non basée sur l'analyse de bifurcation), par exemple $\theta = 0°, 20°, 40°$. Les modules tangents de la loi cohésive sont $T_m^l = T_n^l = -15\frac{N}{mm^3}$.

Dans un premier essai, la bande cohésive est orientée horizontalement ($\theta = 0°$). L'évolution de la force verticale au nœud 3 est montrée dans Fig. III.6. A titre de comparaison, les courbes d'une simulation avec la X-FEM standard (fissure sans tension) et une simulation sans discontinuité sont montrées.

La simulation avec la X-FEM standard mène à une chute brutale de la force

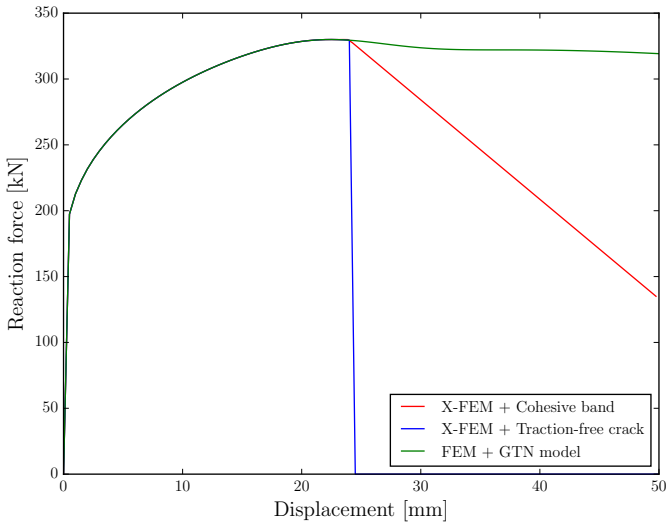


FIGURE III.6 – Evolution de la force verticale au nœud 3

dans l'EF. Cependant l'introduction des tractions cohésives permet la décroissance progressive de la résistance résiduelle de l'EF à zéro.

Si on incline maintenant la bande cohésive, on peut constater que la solution ne converge plus. Après de nombreuses considérations numériques et mathématiques, on pense que c'est la formulation de la X-FEM qui cause ces problèmes numériques. Pour expliquer cette supposition, on va tout d'abord considérer l'équation de la continuité de contrainte faible à travers la bande de l'Eq. (III.7d)

$$\int_{\Omega} \mathbf{B}^{*T} \boldsymbol{\sigma} \, \mathrm{d}\Omega + 2 \int_{\Gamma_D} \mathbf{N}^T \mathbf{t}^g \, \mathrm{d}\Gamma = 0. \tag{III.10}$$

La contrainte dans l'EF est

$$\boldsymbol{\sigma} = \begin{bmatrix} \sigma_{xx} \\ \sigma_{yy} \\ \tau_{xy} \end{bmatrix} = \begin{bmatrix} 0 \\ \sigma_{yy} \\ 0 \end{bmatrix}. \tag{III.11}$$

Désormais on va se concentrer sur l'équilibre de la force verticale au nœud 3. La contribution de la partie continue est obtenue de

$$f_{3y}^{bulk} = \int_{\Omega} (H(x,y) - H_3) \cdot B_{3y}^T(x,y) \sigma_{yy} \, d\Omega \tag{III.12}$$

où $B_{3y}^T(x,y) = 1 + x$. Si la base décalée est utilisée, l'intégrale sur le côté positif est nulle et seulement l'intégrale sur la côté négative n'est pas zéro. Cette intégrale

peut être évaluée analytiquement :

$$\begin{aligned} f_{3y}^{bulk} &= -2\int_{x=-1}^{x=1}\int_{y=-1}^{y=y_I x}(1+x)\sigma_{yy}\; dx\; dy \\ &= -2\sigma_{yy}(\frac{2}{3}y_I + 2) \end{aligned} \tag{III.13}$$

où $y_I$ dénote la coordonnée en y des points d'intersection $A(x=-1|y=-y_I)$ et $B(x=+1|y=+y_I)$ de la bande cohésive avec les bords de l'élément, voir Fig. III.5. La contribution de la bande cohésive est obtenue de

$$f_{3y}^{coh} = 2\int_{\Gamma_D} \mathbf{N}^T \mathbf{t}^g \, \mathrm{d}\Gamma \tag{III.14}$$

La traction cohésive initiale le long de l'interface dans le repère global est calculée de la condition de la continuité de traction

$$\underline{t}^g = \underset{\sim}{\sigma} \cdot \underline{n}, \tag{III.15}$$

où $\underline{n} = \{\sin\theta; \cos\theta\}$ est le vecteur normal avec $\sin\theta = (2y_i)/L_{coh}$ et $\cos\theta = 2/L_{coh}$, où $L_{coh}$ est la longueur de la bande cohésive. Puis, les tractions en forme matricielle s'écrivent

$$\mathbf{t}^g = \begin{bmatrix} 0 \\ 2\sigma_{yy}/L_{coh} \end{bmatrix}. \tag{III.16}$$

On va limiter les considérations à une bande cohésive qui est incorporée à l'amorçage de la localisation et qui porte les tractions cohésive initiales qui sont supposées constantes tout le long de la bande cohésive pour maintenir la fermeture totale. Puis, l'intégrale de ligne (III.14) se simplifie à

$$f_{3y}^{coh} = 2 \cdot L_{coh} \cdot 2\sigma_{yy}/L_{coh} = 4\sigma_{yy}. \tag{III.17}$$

Avec les équations (III.13), (III.17) et (III.10) on arrive à la condition de la continuité de traction

$$-2\sigma_{yy}(\frac{2}{3}y_i + 2) + 4\sigma_{yy} = 0, \tag{III.18}$$

qui donne finalement $y_i = 0$. C'est-à-dire que la X-FEM satisfait la continuité de traction uniquement si la bande cohésive est horizontale ($\theta = 0°$). Si la bande est inclinée, il y aura une différence entre la force interne de la X-FEM et la force interne de la bande cohésive associées aux degrés de liberté enrichis. Dans les simulations, cela a l'effet que le saut de la force introduit des oscillations sévères dans la procédure de résolution et le solveur n'arrive plus à converger.

Une approche pour surmonter ce problème numérique retenue dans la suite consiste à calculer les forces cohésive de telle façon qu'ils compensent les forces du milieu continu associées aux degrés de liberté $b$ :

$$\mathbf{f}_b^{int,0} = \underbrace{\int_\Omega \mathbf{B}^{*T}\boldsymbol{\sigma}\,\mathrm{d}\Omega}_{\mathbf{f}_b^{xfem,0}} + \underbrace{2\int_{\Gamma_D} \mathbf{N}^T\mathbf{t}^g\,\mathrm{d}\Gamma}_{\mathbf{f}_b^{coh,0}}. \tag{III.19}$$

Afin d'assurer une transition douce, il faut que : $\mathbf{f}_b^{coh,0} = -\mathbf{f}_b^{xfem,0}$. La loi cohésive doit donc être modifiée pour qu'elle ne contienne plus la traction cohésive initiale $t_0$, voir Fig. III.7. Finalement, la force interne de la bande cohésive peut être écrite dans la forme

$$\mathbf{f}_b^{coh} = -\mathbf{f}_b^{xfem,0} + \Delta\mathbf{f}_b^{coh} \;;\text{ with } \Delta\mathbf{f}_b^{coh} = 2\int_{\Gamma_D} \mathbf{N}^T\mathbf{t}^g\,\mathrm{d}\Gamma \tag{III.20}$$

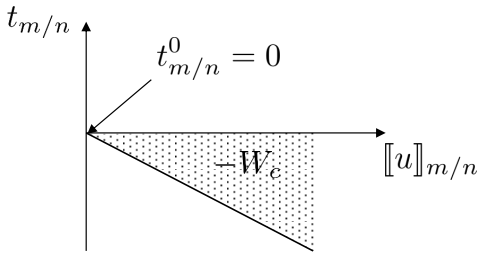


FIGURE III.7 – Loi cohésive modifié pour forcer une transition douce de l'endommagement à la localisation de la déformation

### III.4.3 Essai de traction d'une éprouvette plane 2D

Dans cette section on va considérer une éprouvette plane 2D chargée en traction, voir Fig. III.8.

Les simulations avec les configurations selon table III.3 sont effectuées. Dans le maillage grossier, la taille de l'EF est 0.5 mm et dans le maillage fin, elle est 0.25 mm.

#### III.4.3.1 Description de l'algorithme de propagation

Pour mieux comprendre les explications suivantes, l'algorithme est résumé dans le diagramme de la Fig. III.9.

La propagation de la bande cohésive, puis la formation de la fissure, est déterminée par la séquence des quatre étapes suivantes

1. Amorçage et direction de propagation de la bande cohésive

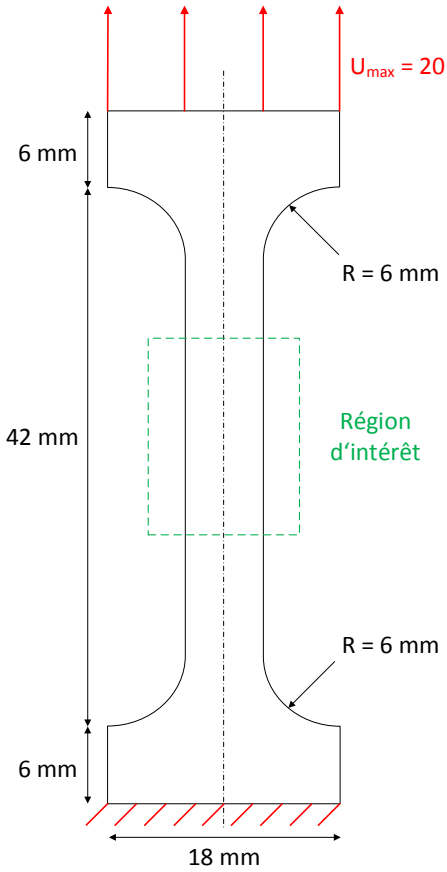


FIGURE III.8 – Modèle de l'éprouvette plane initialement non-fissurée chargée en traction

TABLE III.3 – Configuration des simulations effectuées

| Abbrev. | Maillage | Num. de PG | $T_n^l/T_m^l$ |
|---|---|---|---|
| Sim1 | fin | 4 | $-25.0$ |
| Sim2 | fin | 4 | $-12.5$ |
| Sim3 | grossier | 64 | $-25.0$ |
| Sim4 | grossier | 64 | $-12.5$ |
| Sim5 | grossier | 4 | $-25.0$ |
| Sim6 | grossier | 4 | $-12.5$ |
| Sim7 | fin | 4 | Pas de discontinuité |
| Sim8 | grossier | 4 | Pas de discontinuité |
| Sim9 | fin | 4 | X-FEM sans loi cohésive |
| Sim10 | grossier | 4 | X-FEM sans loi cohésive |

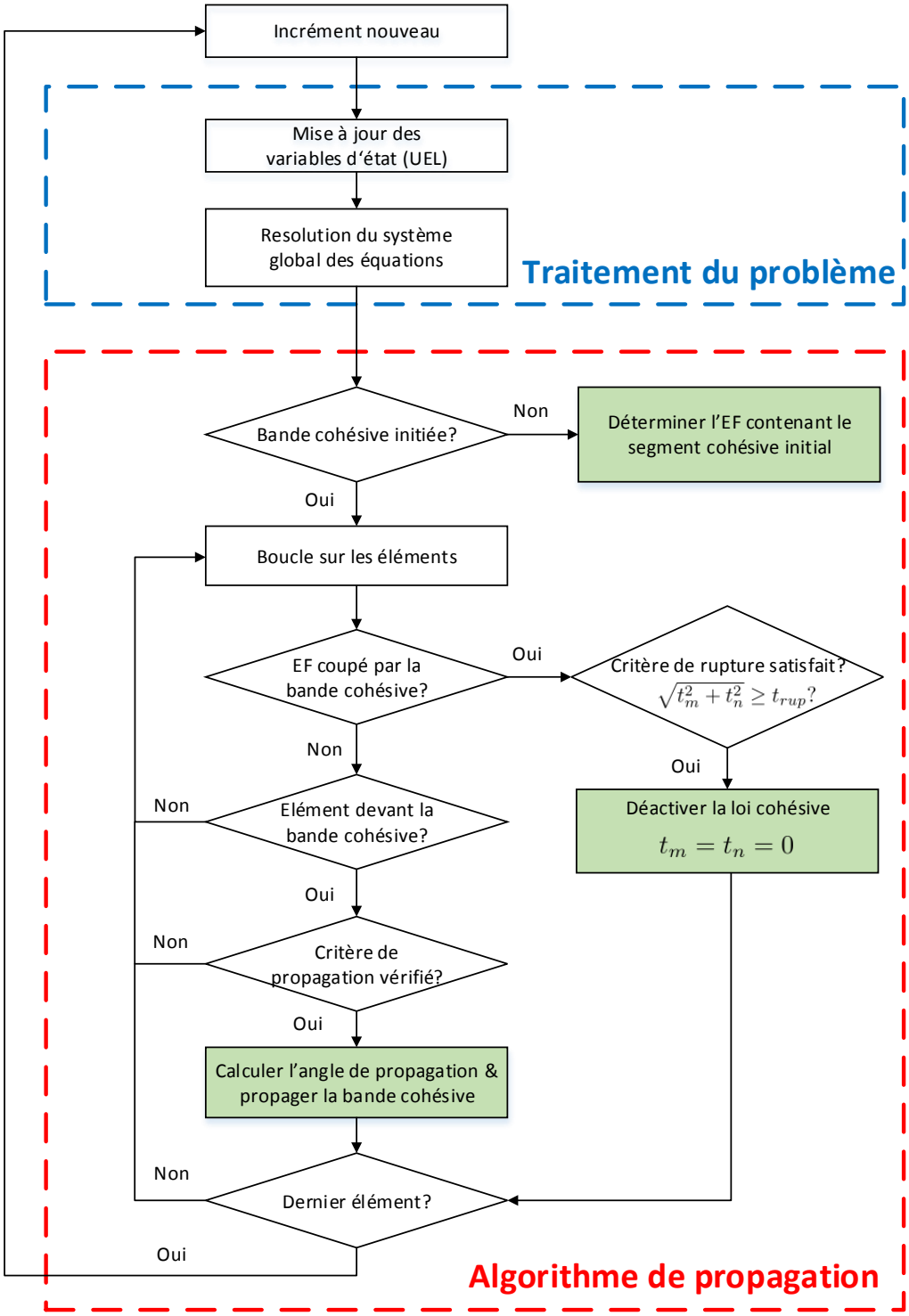


FIGURE III.9 – Diagramme de l'algorithme de propagation

2. Détermination de la longueur de propagation
3. Propagation de la bande cohésive
4. Amorçage de la fissure

L'amorçage de la bande cohésive est conditionné par l'analyse de bifurcation. Cette méthode consiste à trouver l'orientation de la bande de localisation $\underline{n}$ pour laquelle le déterminant du tenseur acoustique $\underset{\approx}{Q}$ devient zéro ou négatif pour la première fois

$$\det \underset{\approx}{Q}(\underline{n}) = \det(\underline{n} \cdot \underset{\approx}{D}^t \cdot \underline{n}) = 0, \tag{III.21}$$

où $\underset{\approx}{D}^t$ est l'opérateur tangent du modèle GTN microporeux. Normalement, on trouve deux solutions pour $\underline{n}$. La solution retenue est celle qui donne la valeur du déterminant minimale. Pour des raisons purement numériques, la bande cohésive ne se propage que si aussi la porosité évaluée sur un point de Gauss supplémentaire (au centre de l'EF) dépasse une valeur critique. Ici on choisit la valeur $f_{ini} = 0.03$ qui est un bon compromis entre numérique et physique.

Pour détecter l'EF dans lequel le premier segment de la bande cohésive va être amorcée, on cherche l'EF qui satisfait les deux critères précédente et - si cela concerne plusieurs éléments - qui a une valeur de porosité maximale.

La longueur de la bande dans un incrément est déterminée par la méthode d'épuisement, voir Crété [18]. Dans cette méthode la bande cohésive se propage jusqu'à ce que les critères de propagation ne sont plus satisfaits.

L'amorçage d'une fissure est piloté par un critère de traction au lieu d'un critère d'énergie pour améliorer les propriétés de convergence. La fissure se forme si la traction effective $t_{eff} = \sqrt{{t_m^l}^2 + {t_n^l}^2}$ atteint une valeur critique, ici on utilise une valeur arbitrairement choisie pour le moment de 100 MPa.

### III.4.3.2 Considérations sur la méthode d'intégration

On peut constater que la méthode d'intégration à 64 points de Gauss coûte très chère en terme de temps de calcul, particulièrement en regard de structures larges. Ici on va proposer une stratégie à 4 points de Gauss qui permet de réduire le temps de calcul. Si on n'utilise que 4 points de Gauss, il faut garantir qu'au moins un point de Gauss est situé sur les deux côtés de la bande cohésive. Donc ce qu'on va faire est de forcer le nouveau segment cohésif à traverser le centre d'un bord de l'EF. En fonction de l'angle calculé par l'analyse de bifurcation, l'angle de propagation peut seulement prendre trois valeurs différentes déterminées par la

géométrie de l'EF, voir Fig. III.10.

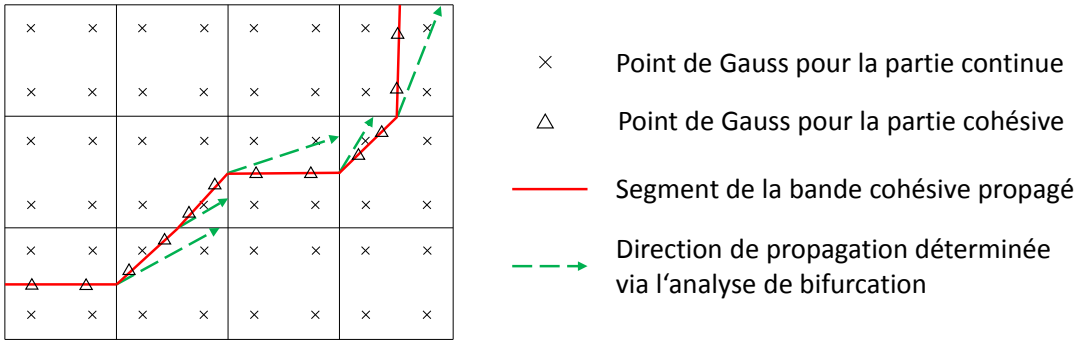


FIGURE III.10 – Algorithme de propagation modifié avec 4 PG dans le milieu continu

Il se pose la question de savoir si cette méthode est assez précise pour l'utiliser ici. Donc on applique l'algorithme de propagation à l'éprouvette plane de la Fig. III.8. Un maillage grossier est utilisé (taille de l'EF 0.5 mm). Les résultats sont montrés dans Fig. III.11.

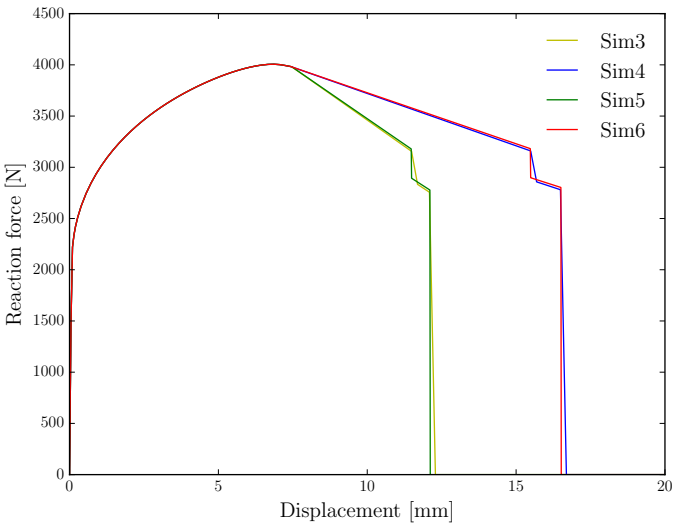


FIGURE III.11 – Evolution de la force avec un maillage grossier pour Sim3, Sim4, Sim5 et Sim6, voir nomenclature dans le tableau III.3

On peut observer que la différence entre les réponses globales des deux approches est insignifiante et indépendante de la loi cohésive. Cette observation implique que l'utilisation coûteuse de 64 points de Gauss dans chaque EF dès le début de la simulation peut être remplacée par une méthode d'intégration plus économique à 4

points de Gauss sans perdre de la précision. Les avantages de cette méthodes sont donc :

— Elle est considérablement plus rapide.

— Elle demande moins d'espace pour stocker les variables d'état sur chaque point de Gauss et donc beaucoup moins de temps pour le post-traitement.

— Elle est numériquement plus stable, parce que les simulations avec 64 points de Gauss ont dévoilé des problèmes de convergence quand elle est appliquée à un maillage très fin.

— Elle permet encore une bonne prédiction de la réponse globale.

#### III.4.3.3 Résultats

On discute ici les résultats des simulations dans le tableau III.3. On va en particulier vérifier si les approches sont capables de reproduire une propagation selon un angle de 45° comme observé expérimentalement dans l'épaisseur d'une éprouvette de traction (point de vue correspondant à un état de déformations planes).

##### III.4.3.3.1 Localisation de l'endommagement dans le modèle GTN

Si le modèle GTN est utilisé pendant toute la simulation sans traitement numérique de la phase de localisation, l'endommagement se concentre dans quelques EFs au centre de l'éprouvette, voir Fig. III.12.

##### III.4.3.3.2 Comparaison de l'angle de propagation

On peut constater que dans toute les simulations la bande cohésive s'active dans le centre de la structure et ensuite se propage vers les deux côtés, voir Fig. III.13.

Dans les deux premières simulations a) et b) la bande cohésive se propage avec un angle de 58° par rapport à l'axe horizontale comme résultat du critère de bifurcation. Cette valeur numérique de 58° est à comparer à la valeur expérimentale de 45°. Cette différence peut s'expliquer par l'hypothèse de déformations planes supposée dans les simulations tout en n'étant pas satisfaite dans le cas de chargement réel (la largeur de l'éprouvette n'est en effet pas assez grande). Pour un maillage plus

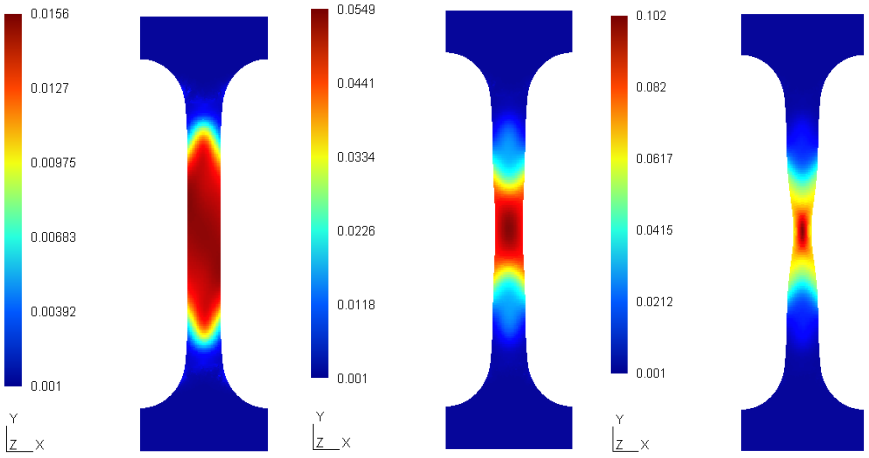


FIGURE III.12 – Localisation de l'endommagement $f$ avec Sim7, voir nomenclature dans le tableau III.3, à des chargements différents : a) $U = 7.1mm$, b) $U = 8.2mm$, c) $U = 9.9mm$

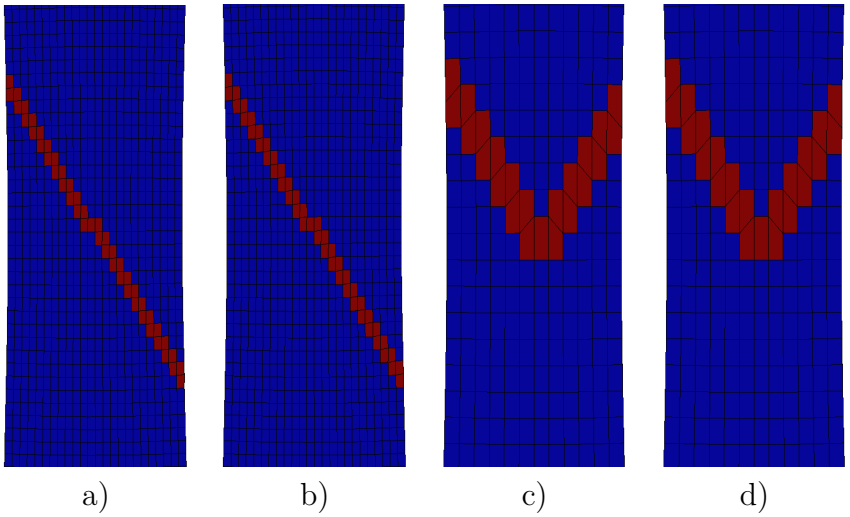


FIGURE III.13 – Angle de propagation de la bande cohésive ($U = 7.8mm$) : a) Sim1, b) Sim2, c) Sim5, d)Sim6, voir nomenclature dans le tableau III.3

fin (c et d) la bande se propage de la même façon vers la gauche, mais vers la droite la bande se propage différemment en comparaison avec un maillage grossier. Cette différence peut être justifiée par la méthode de décision de l'angle. Le choix de l'angle dans l'analyse de bifurcation est fait seulement à partir de la valeur du déterminant $Q$. Une approche plus physique serait de choisir la direction qui produit une déformation plastique maximale, voir Crété [17].

#### III.4.3.3.3 Comparaison de l'évolution de la force de réaction

D'abord on va analyser la réponse globale pour le cas si la X-FEM seule est utilisée en comparaison avec la X-FEM cohésive, voir Fig. III.14. La X-FEM sans loi cohésive mène à une chute brutale de la force au moment de l'amorçage de la localisation. Cependant dans le cas de la X-FEM cohésive, la force décroît progressivement après l'amorçage de la localisation avant de chuter à zéro en deux phases (en escalier) après l'amorçage de la fissure. La chute brutale de la force que l'on peut observer dans le cas de la X-FEM standard est donc retardée.

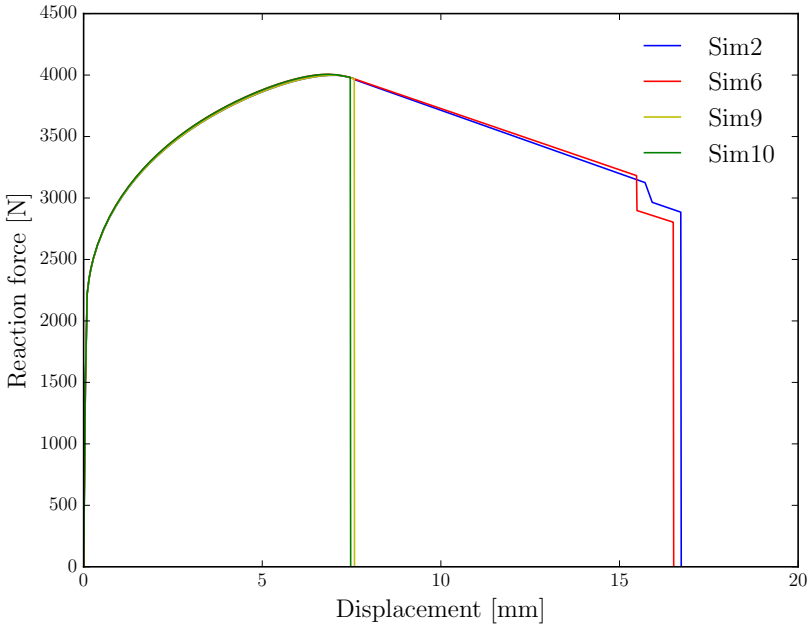


FIGURE III.14 – Évolution de la force de réaction pour Sim2, Sim6, Sim9 et Sim10, voir nomenclature dans le tableau III.3

Maintenant, l'effet de la taille sur la réponse globale est analysé voir Fig. III.15. On peut observer que le modèle GTN sans traitement numérique de la localisation mène à une dépendance forte au maillage. Cependant, l'utilisation de la bande cohésive avec la méthode de propagation permet de presque éviter cette dépendance

au maillage.

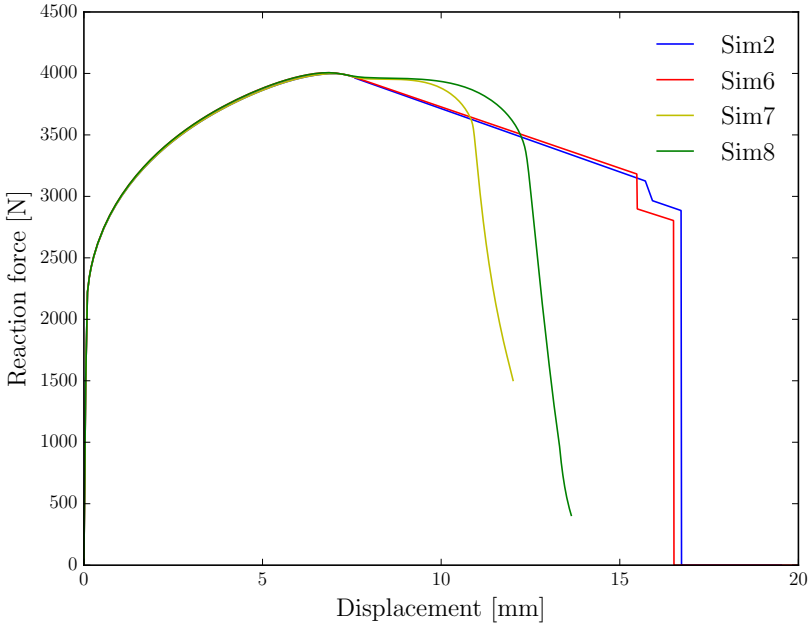


FIGURE III.15 – Évolution de la force de réaction pour Sim2, Sim6, Sim7 et Sim8, voir nomenclature dans le tableau III.3

Le graphe final III.16 montre l'évolution de la force pour des pentes de la loi cohésive différentes, qui peuvent être bien représentées.

## III.5 Conclusion

Dans ce chapitre on a proposé et étudié une méthodologie pour coupler une bande cohésive induite par la localisation de la déformation avec la X-FEM. Cette approche permet de passer progressivement de la phase de l'endommagement induit par la croissance des cavités à la propagation de fissure dans des matériaux ductiles. Deux applications différentes avec un modèle GTN ont été présentées : une essai de traction avec un EF 2D seul et un essai de traction d'une éprouvette plate.

L'essai de traction avec un EF 2D seul a dévoilé que la X-FEM cohésive ne permet pas de satisfaire la continuité de traction. Une solution a été proposée : en modifiant la loi cohésive, une force cohésive initiale est calculée qui oppose la force de la partie continue associée aux degrés de liberté.

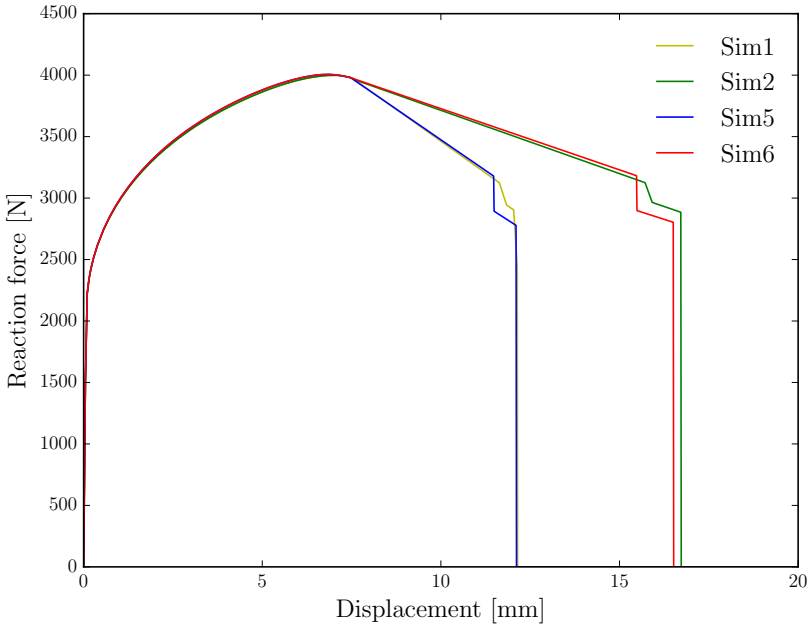


FIGURE III.16 – Évolution de la force de réaction pour Sim1, Sim2, Sim5 et Sim6, voir nomenclature dans le tableau III.3

Pour la deuxième application un algorithme de propagation a été proposé. On a montré qu'on peut utiliser une méthode d'intégration par 4 points de Gauss au lieu de 64 points de Gauss sans perdre de la précision. Puis, la performance du modèle a été testée. On a observé que le trajet de la fissure est différent pour un maillage grossier et un maillage fin. Ça peut s'expliquer par l'utilisation seule du déterminant du tenseur acoustique pour choisir l'angle de propagation. Dans l'avenir une méthodologie plus sophistiquée peut être implémentée, voir par example [17]. Concernant la réponse globale la loi cohésive permet de progressivement passer de l'endommagement diffus à la localisation de la formation d'une fissure et cette méthode évite la chute brutale qui est constatée dans le cas de l'utilisation de la X-FEM seule.

Bien que quelques problèmes devraient être améliorer dans la suite, la méthodologie de bande cohésive en combinaison avec une méthode de propagation motivée par la physique a été montrée comme produisant des résultats prometteurs. Enfin, la méthodologie adoptée pour tout le processus de la fissuration est résumée en Fig. III.17.

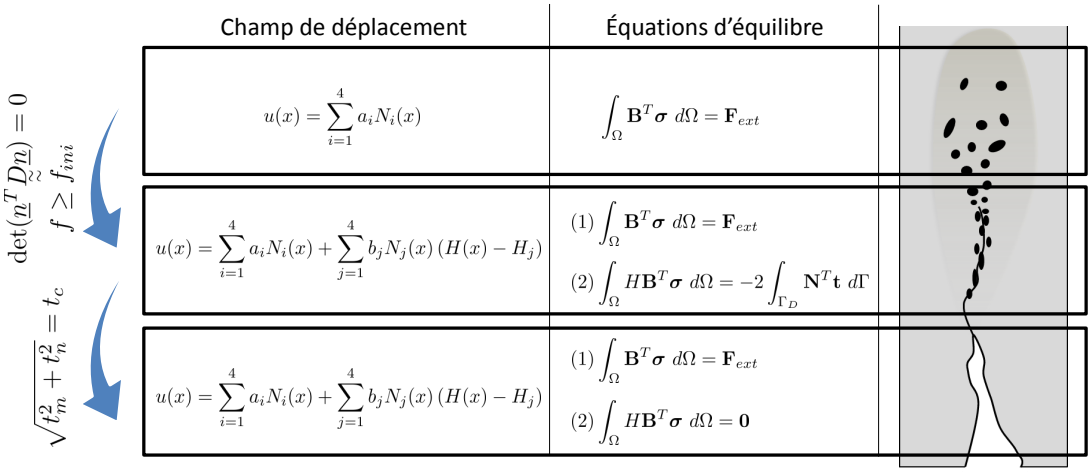


FIGURE III.17 – Synthèse des champs de déplacement et des équations d'équilibre pour les phases de la fissuration ductile

# Chapitre IV

# Conclusions et perspectives

## IV.1 Conclusions

Ce travail vise à contribuer à la prédiction de la résistance résiduelle de structures surchargées en utilisant la simulation numérique (essais virtuels). Le défi consiste à reproduire dans une méthodologie unifiée les phases successives de l'endommagement diffus (micro-échelle), localisation de la déformation (méso-échelle) et propagation de fissure (macro-échelle) menant potentiellement à la rupture finale de la structure. L'objective de cette thèse était de développer une méthode (basée sur une bande incorporée) appropriée capable de reproduire la bande de localisation physique et réduire ainsi la sensibilité au maillage à un minimum.

On a étudié trois approches d'élément fini avec une bande incorporée de différents points de vue. Basé sur une discussion profonde, l'approche d'une discontinuité forte avec un modèle de bande cohésive a été choisie comme la méthode préférée pour décrire la phase de la localisation de la déformation considérée dans cette étude, soit une méso-fissure entrecoupée de matière. La bande de localisation de la déformation est donc représentée par son plan moyen et sa résistance en tension et cisaillement via une loi cohésive qui assure la continuité de traction et la dégradation du matériau dans le régime de post-localisation.

Ensuite on a développé et étudié cette méthodologie pour coupler une bande cohésive induite par la localisation de la déformation avec la X-FEM. Cette approche permet de passer progressivement de la phase de l'endommagement induit par la croissance des cavités à la propagation de fissure dans des matériaux ductiles. Deux applications différentes avec un modèle GTN ont été présentées : un essai de traction avec un EF 2D seul et un essai de traction d'une éprouvette plate.

Afin de répondre à la demande de l'industrie d'utiliser le modèle pour des applications techniques, le modèle a été implémenté dans une routine (UEL) dans le code de calcul par EFs Abaqus. Un modèle constitutif a été implémenté qui prend en compte les effets de la plasticité et de l'endommagement induit par la croissance des cavités. La X-FEM a été utilisée pour représenter une discontinuité forte dans un EF.

L'essai de traction avec un EF 2D seul a dévoilé que la X-FEM cohésive ne permet pas de satisfaire la continuité de traction. Une solution a été proposée : en modifiant la loi cohésive, une force cohésive initiale est calculée qui oppose la force de la partie continue associée aux degrés de liberté.

Pour la deuxième application un algorithme de propagation a été proposé. On a montré qu'on peut utiliser une méthode d'intégration par 4 points de Gauss au lieu de 64 points de Gauss sans perdre de la précision. Puis, la performance du modèle a été testée. On a observé que le trajet de la fissure est différent pour un maillage grossier et un maillage fin. Ça peut s'expliquer par l'utilisation seule du déterminant du tenseur acoustique pour choisir l'angle de propagation. Dans l'avenir une méthodologie plus sophistiquée peut être implémentée, voir par exemple [17]. Concernant la réponse globale la loi cohésive permet de progressivement passer de l'endommagement diffus à la localisation de la déformation et de la localisation de la déformation à la fissure. Cette méthode évite la chute brutale qui est constatée dans le cas de l'utilisation de la X-FEM seule.

Si on considère que la méthodologie développée est une tentative pour décrire la phase de localisation de la déformation dans un modèle unifié de la rupture ductile, les premiers résultats sont prometteurs d'un point de vue qualitatif.

# IV.2 Perspectives

Ce travail laisse des questions ouvertes et des problèmes non résolus en suspend. Dans la suite on va donc proposer des sujets importants pour des développements futurs.

## IV.2.1 Perspective à court terme 1 : Améliorer l'algorithme de propagation

Les résultats ont dévoilé la sensibilité au maillage de l'angle de propagation. Un critère plus physique pour déterminer l'angle de propagation est la méthode de Crété [18]. Cette méthode consiste à prendre en compte des quantités moyennées dans une pastille devant le front de la fissure, voir Fig. IV.1 pour une synthèse.

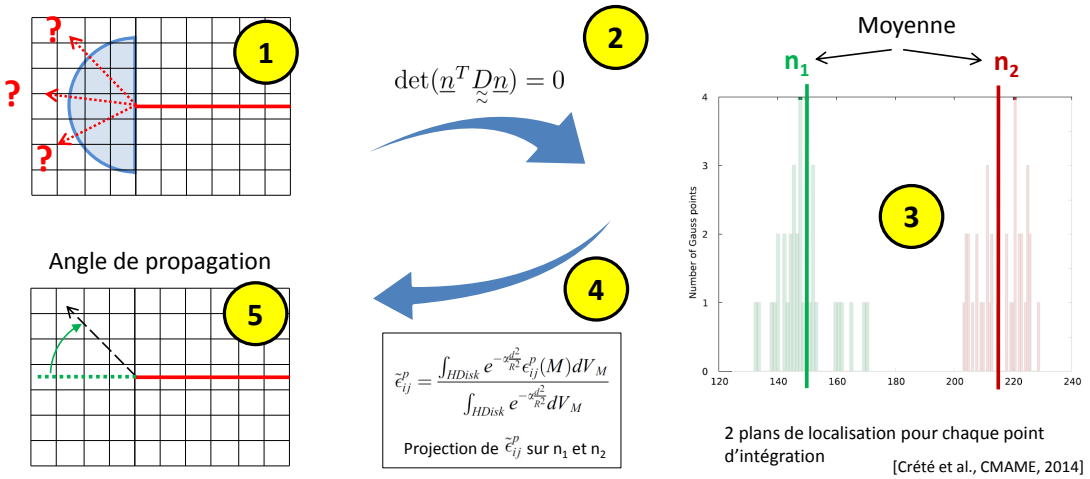


FIGURE IV.1 – Détermination de l'angle de propagation dans la méthode de Crété [17]

## IV.2.2 Perspective à court terme 2 : Caractérisation expérimentale de la loi cohésive

Un autre sujet important concerne la détermination des paramètres caractéristiques à partir d'essais. Premièrement, le travail de séparation à la formation d'une fissure doit être évalué, par exemple par analyse inverse ([16], [45]). On peut aussi citer le concept de l'énergie d'équivalence, voir Cazes [13]. En outre les paramètres d'influence de l'énergie à rupture en vue des matériaux ductiles considérés doivent être identifiés, par exemple l'effet de la triaxialité ou de la température.

### IV.2.3 Perspective à moyen terme : Extension du modèle à un chargement dynamique

Cette thèse s'est concentrée sur un chargement quasi-statique. L'extension du modèle à un chargement dynamique est très complexe, donc on va regarder quelques sujets choisis :

— Les effets de la vitesse de déformation et de la température sur le comportement du matériau doivent être pris en compte, voir les travaux de Geffroy [24] and Crété [17].

— L'analyse de bifurcation est limitée aux matériaux qui sont indépendants de la vitesse de chargement. L'approche des perturbations linéaires est par exemple plus adaptée à un chargement dynamique, mais plus difficile à mettre en œuvre.

— Dans l'essai d'impact de Kalthoff-Winkler on peut constater la formation d'une bande de cisaillement adiabatique, un phénomène complexe, voir Fig. IV.2. Contrairement à la bande de localisation traitée dans ce travail, la bande de cisaillement adiabatique se forme d'abord et puis l'endommagement évolue dans la bande.

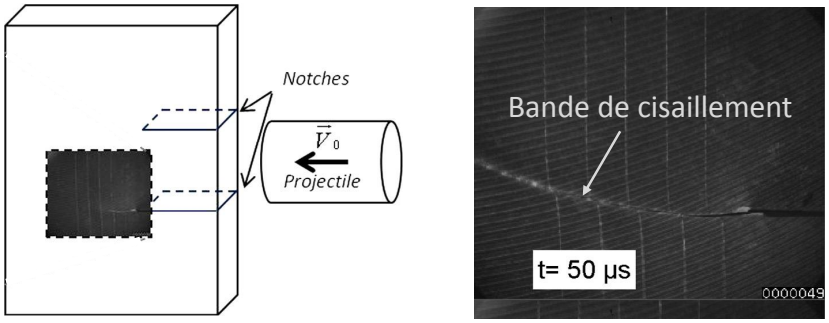


FIGURE IV.2 – Bande de cisaillement adiabatique comme précurseur de la propagation de fissure dans l'essai d'impact de Kalthoff-Winkler (Roux et Longére [43])

### IV.2.4 Perspective à longue terme : Simulation multi-échelle

La propagation de fissure dans une structure large peut être considérée comme un problème multi-échelle. La haute fidélité souhaitée dans le domaine local (localisation de la déformation et propagation de fissure) contraste le calcul à une faible fidélité dans le domaine global (structure entière utilisant un modèle 2D simple impliquant un grand nombre d'EFs). La thèse de Duval [21] est une contribution importante vers une simulation multi-échelle efficace. L'algorithme proposé permet

de coupler un code de recherche sophistiqué traitant le problème de propagation de fissure avec un code de calcul par EFs commercial qui calcule la structure globale avec un modèle utilisant des EFs simple, voir Fig. IV.3.

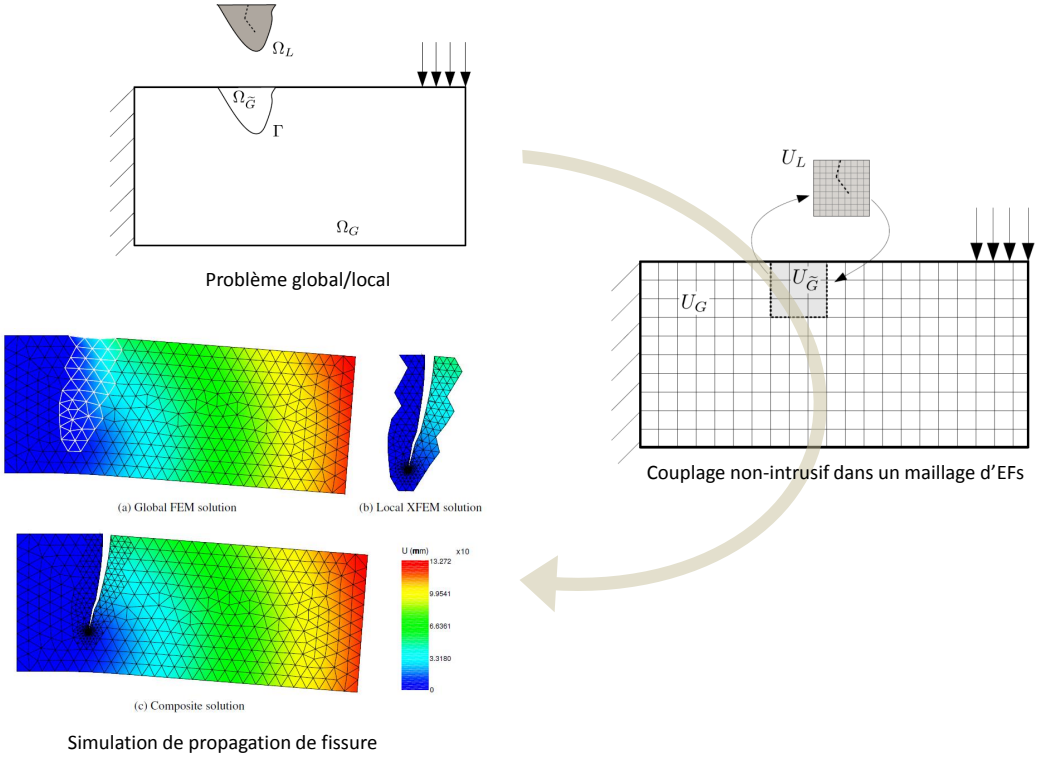


FIGURE IV.3 – Couplage non-intrusif dans le contexte de la propagation de fissure (domaine local) dans une plaque élastique (domaine global)

# Bibliographie


[1] S. Abbas, A. Alizada, and T.-P. Fries. The xfem for high-gradient solutions in convection-dominated problems. *International Journal for Numerical Methods in Engineering*, 82 :1044–1072, 2010.

[2] P. Areias and T. Belytschko. Two-scale shear band evolution by local partition of unity. *International Journal for Numerical Methods in Engineering*, 66(5) :878–910, 2006.

[3] H. Autenrieth, V. Schulze, N. Herzig, and L. W. Meyer. Ductile failure model for the description of aisi 1045 behavior under different loading conditions. *Mechanics of Time-Dependent Materials*, 13(3) :215–231, 2009.

[4] G. I. Barenblatt. The mathematical theory of equilibrium cracks in brittle fracture. *Advances in Applied Mechanics*, 7 :55–129, 1962.

[5] Z. P. Bažant, T. Belytschko, and T.-P. Chang. Continuum theory for strain-softening. *Journal of Engineering Mechanics*, 110(12) :1666–1692, 1984.

[6] T. Belytschko and T. Black. Elastic crack growth in finite elements with minimal remeshing. *International Journal for Numerical Methods in Engineering*, 45(5) :601–620, 1999.

[7] T. Belytschko, J. Fish, and B. E. Engelman. A finite element with embedded localization zones. *Computer Methods in Applied Mechanics and Engineering*, 70 :59–89, 1988.

[8] E. Benvenuti, A. Tralli, and G. Ventura. A regularized xfem model for the transition from continuous to discontinuous displacements. *International Journal for Numerical Methods in Engineering*, 74(6) :911–944, 2008.

[9] A. A. Benzerga. Micromechanics of coalescence in ductile fracture. *Journal of the Mechanics and Physics of Solids*, 50(6) :1331–1362, 2002.

[10] A. A. Benzerga, J. Besson, and A. Pineau. Coalescence-controlled anisotropic ductile fracture. *Journal of Engineering Materials and Technology*, 121(2) :221–229, 1999.

[11] P.-O. Bouchard, F. Bay, Y. Chastel, and I. Tovena. Crack propagation modelling using an advanced remeshing technique. *Computer Methods in Applied Mechanics and Engineering*, 189(3) :723–742, 2000.

[12] P. Broumand and A. R. Khoei. X-fem modeling of dynamic ductile fracture problems with a nonlocal damage-viscoplasticity model. *Finite Elements in Analysis and Design*, 99 :49–67, 2015.

[13] F. Cazes, M. Coret, A. Combescure, and A. Gravouil. A thermodynamic method for the construction of a cohesive law from a nonlocal damage model. *International Journal of Solids and Structures*, 46(6) :1476–1490, 2009.

[14] F. Cazes, A. Simatos, M. Coret, and A. Combescure. A cohesive zone model which is energetically equivalent to a gradient-enhanced coupled damage-plasticity model. *European Journal of Mechanics-A/Solids*, 29(6) :976–989, 2010.

[15] Cedre. Limburg, 05 2016.

[16] X. Chen, X. Deng, M. A. Sutton, and P. Zavattieri. An inverse analysis of cohesive zone model parameter values for ductile crack growth simulations. *International Journal of Mechanical Sciences*, 79 :206–215, 2014.

[17] J.-P. Crété. *Traitement numérique de la fissuration d'une structure navale*. PhD thesis, Université de Bretagne Sud, 2013.

[18] J.-P. Crété, P. Longère, and J.-M. Cadou. Numerical modelling of crack propagation in ductile materials combining the GTN model and X-FEM. *Computer Methods in Applied Mechanics and Engineering*, 275 :204–233, 2014.

[19] D. S. Dugdale. Yielding of steel sheets containing slits. *Journal of the Mechanics and Physics of Solids*, 8 :100–108, 1960.

[20] P. Dumstorff and G. Meschke. Crack propagation criteria in the framework of x-fem-based structural analyses. *International Journal for Numerical and Analytical Methods in Geomechanics*, 31(2) :239–259, 2007.

[21] M. Duval. *Apports du couplage non-intrusif en mécanique non-linéaire des structures*. PhD thesis, UPS Toulouse, 2016.

[22] E. N. Dvorkin, A. M. Cuitiño, and G. Gioia. Finite elements with displacement interpolated embedded localization lines insensitive to mesh size and distortions. *International Journal for Numerical Methods in Engineering*, 30(3) :541–564, 1990.

[23] T. Elguedj, A. Gravouil, and A. Combescure. Appropriate extended functions for x-fem simulation of plastic fracture mechanics. *Computer Methods in Applied Mechanics and Engineering*, 195(7) :501–515, 2006.

[24] A.-G. Geffroy. *Modélisation numérique de la rupture de structures navales sous l'effet d'explosions au contact*. PhD thesis, Université de Bretagne Sud, 2010.

[25] A. L. Gurson. Continuum theory of ductile rupture by void nucleation and growth : Part i - yield criteria and flow rules for porous ductile media. *Journal of Engineering Materials and Technology*, 99(1) :2–15, 1977.

[26] A. Hillerborg, M. Modéer, and P.-E. Petersson. Analysis of crack formation and crack growth in concrete by means of fracture mechanics and finite elements. *Cement and Concrete Research*, 6 :773–782, 1976.

[27] A. E. Huespe, A. Needleman, J. Oliver, and P. J. Sanchez. A finite thickness band method for ductile fracture analysis. *International Journal of Plasticity*, 25(12) :2349–2365, 2009.

[28] J. Lemaitre. A continuous damage mechanics model for ductile fracture. *Journal of Engineering Materials and Technology*, 107(1) :83–89, 1985.

[29] P. Longère, A. Dragon, H. Trumel, T. de Resseguier, X. Deprince, and E. Petitpas. Modelling adiabatic shear banding via damage mechanics approach. *Archives of Mechanics*, 55 :3–38, 2003.

[30] P. Longère, A.-G. Geffroy, B. Leblé, and A. Dragon. Modeling the transition between dense metal and damaged (microporous) metal viscoplasticity. *International Journal of Damage Mechanics*, 21(7) :1020–1063, 2012.

[31] J. Mazars and G. Pijaudier-Cabot. From damage to fracture mechanics and conversely : a combined approach. *International Journal of Solids and Structures*, 33(20) :3327–3342, 1996.

[32] N. Moës and T. Belytschko. Extended finite element method for cohesive crack growth. *Engineering Fracture Mechanics*, 69(7) :813–833, 2002.

[33] N. Moës, J. Dolbow, and T. Belytschko. A finite element method for crack growth without remeshing. *International Journal for Numerical Methods in Engineering*, 46 :131–150, 1999.

[34] J. Oliver. Modeling strong discontinuities in solid mechanics viq strain softening constitutive equations. part 1 : Fundamentals. part 2 : Numerical simulation. *International Journal for Numerical Methods in Engineering*, 39 :3575–3624, 1996.

[35] M. Ortiz, Leroy Y., and A. Needleman. A finite element method for localized failure analysis. *Computer Methods in Applied Mechanics and Engineering*, 61 :189–214, 1987.

[36] T. Pardoen, I. Doghri, and F. Delannay. Experimental and numerical comparison of void growth models and void coalescence criteria for the prediction of ductile fracture in copper bars. *Acta Materialia*, 46(2) :541–552, 1998.

[37] T. Pardoen and J. W. Hutchinson. An extended model for void growth and coalescence. *Journal of the Mechanics and Physics of Solids*, 48(12) :2467–2512, 2000.

[38] Agenzia Nazionale per la Sicurezza del Volo (ANSV). Rapporto d'inchiesta - inconveniente grave occorso all'aeromobile boeing 767-432-er, marche n834mh. Technical report, ANSV, 2007.

[39] G. Pijaudier-Cabot and Z. Bažant. Nonlocal damage theory. *Journal of Engineering Mechanics*, 113(10) :1512–1533, 1987.

[40] J. J. C. Remmers, R. de Borst, and A. Needleman. The simulation of dynamic crack propagation using the cohesive segments method. *Journal of the Mechanics and Physics of Solids*, 56(1) :70–92, 2008.

[41] J. J. C. Remmers, R. de Borst, C. V. Verhoosel, and A. Needleman. The cohesive band model : a cohesive surface formulation with stress triaxiality. *International Journal of Fracture*, 181(2) :177–188, 2013.

[42] G. Rousselier. Ductile fracture models and their potential in local approach of fracture. *Nuclear Engineering and Design*, 105(1) :97–111, 1987.

[43] E. Roux, P. Longère, O. Cherrier, T. Millot, D. Capdeville, and J. Petit. Analysis of asb assisted failure in a high strength steel under high loading rate. *Materials & Design*, 75 :149–159, 2015.

[44] I. Scheider. Derivation of separation laws for cohesive models in the course of ductile fracture. *Engineering Fracture Mechanics*, 76(10) :1450–1459, 2009.

[45] M. R. R. Seabra. *Continuous-Discontinuous Approach for the Modelling of Ductile Fracture*. PhD thesis, University of Porto, 2012.

[46] A. Simatos. *Méthode XFEM pour la modélisation de grandes propagations de fissure en déchirure ductile*. PhD thesis, INSA de Lyon, 2010.

[47] L. J. Sluys. Discontinuous modeling of shear banding. In D.R.J Owen, E. Onate, and E. Hinton, editors, *Computational Plasticity COMPLAS V*. CIMNE., Barcelona, Spain, 1997.

[48] J.-H. Song, H. Wang, and T. Belytschko. A comparative study on finite element methods for dynamic fracture. *Computational Mechanics*, 42(2) :239–250, 2008.

[49] S. Su and L. Stainier. Energy-based variational modeling of adiabatic shear bands structure evolution. *Mechanics of Materials*, 80 :219–233, 2015.

[50] V. Tvergaard. Material failure by void coalescence in localized shear bands. *International Journal of Solids and Structures*, 18(8) :659–672, 1982.

[51] V. Tvergaard. Material failure by void growth to coalescence. *Advances in Applied Mechanics*, 27 :83–151, 1989.

[52] G. N. Wells and L. J. Sluys. A new method for modelling cohesive cracks using finite elements. *International Journal for Numerical Methods in Engineering*, 50(12) :2667–2682, 2001.

[53] X.-P. Xu and A. Needleman. Numerical simulations of fast crack growth in brittle solids. *Journal of the Mechanics and Physics of Solids*, 42(9) :1397–1434, 1994.

[54] G. Zi and T. Belytschko. New crack-tip elements for xfem and applications to cohesive cracks. *International Journal for Numerical Methods in Engineering*, 57(15) :2221–2240, 2003.